Spherical Harmonic Inductive Detection Coils and their use In Dynamic Pre-emphasis for Magnetic Resonance Imaging

by

Karl T. Edler

A Thesis submitted to the Faculty of Graduate Studies of

The University of Manitoba

in partial fulfilment of the requirements of the degree of

DOCTOR OF PHILOSOPHY

Department of Physics and Astronomy

University of Manitoba

Winnipeg

Spherical Harmonic Inductive Detection Coils and their use in Dynamic Pre-emphasis for Magnetic Resonance Imaging

by

Karl T. Edler

Abstract

Spherical Harmonic Inductive Detection Coils and their use in Dynamic Pre-emphasis for Magnetic Resonance Imaging

by

Karl T. Edler

Doctor of Philosophy in Medical Physics

University of Manitoba, Department of Physics and Astronomy

D. I. Hoult, Chair

The issue of eddy currents induced by the rapid switching of magnetic field gradients is a long-standing problem in magnetic resonance imaging. A new method for dealing with this problem is presented whereby spatial harmonic components of the magnetic field are continuously sensed, through their temporal rates of change, and corrected. In this way, the effects of the eddy currents on multiple spatial harmonic components of the magnetic field can be detected and corrections applied during the rise time of the gradients.

Sensing the temporal changes in each spatial harmonic is made possible with specially designed detection coils. However to make the design of these coils possible, general relationships between the spatial harmonics of the field, scalar potential, and vector potential are found within the quasi-static approximation. These relationships allow the vector potential to be found from the field – an inverse curl operation – and may be of use beyond the specific problem of detection coil design.

Using the detection coils as sensors, methods are developed for designing a negative feedback system to control the eddy current effects and optimizing that system with respect to image noise and distortion. The design methods are successfully tested in a series of proof-of-principle experiments which lead to a discussion of how to incorporate similar designs into an operational MRI.

Keywords: magnetic resonance imaging, eddy currents, dynamic shimming, negative feedback, quasi-static fields, vector potential, inverse curl

Acknowledgements

The Natural Sciences and Engineering Research Council of Canada (NSERC) is acknowledged for providing the bulk of the funds for this research and Canada's National Research Council (NRC-CNRC) for allowing me access to their facilities.

Thanks go to my supervisor David Hoult for providing the initial idea for this research – that it should be possible to use Faraday induction to sense the harmonics of the magnetic field thereby making control feasible – and for his excellent guidance along the way.

Special mention also goes to Glen Kolansky who patiently answered so very many practical questions both electrical and mechanical.

Finally, without the support and encouragement of my wife Beckie I might not have had the persistence to relate the harmonics of the fields to those of the potentials and this work might never have been completed.

Contents

List of Tables

List of Figures

List of Symbols

Constants

$\hbar = 6.62606896 \times 10^{-34}$ J·s/2π	reduced Plank constant
$\epsilon_0 = 8.854187817 \times 10^{-12}$ $A^2 \cdot s^2 \cdot m^{-2} \cdot N^{-1}$	electric permittivity of free space
$\mu_0 = 4\pi \times 10^{-7}$ $N \cdot A^{-2}$	magnetic permeability of free space
$c = 1/\sqrt{\mu_0 \epsilon_0}$	speed of light in free space
$m_p = 1.672621637 \times 10^{-27}$ kg	proton mass
$k = 1.3806504 \times 10^{-23}$ J·K^{-1}	Boltzmann constant

Coordinates

r	cylindrical or spherical radial coordinate
$\mathbf{r}$	position vector (field point)
$\mathbf{r_o}$	position vector (source point)
θ	spherical declination angle
ϕ	cylindrical or spherical azimuthal angle
x, y, z	Cartesian coordinates
$\hat{\mathbf{x}}, \hat{\mathbf{y}}, \hat{\mathbf{z}}$	Cartesian unit vectors
dV	volume element
$d\mathbf{a}$	area element
$d\mathbf{l}$	line element
t	time
τ	time interval
Δt	discrete time step
ω	angular frequency

Electromagnetics

$\mathbf{B}$	magnetic field
$\mathbf{E}$	electric field
ρ	charge density
$\mathbf{J}$	current density
Θ	electric scalar potential
Ψ	magnetic scalar potential
$\mathbf{A}$	magnetic vector potential
V	voltage
$M_{a,b}$	mutual inductance between paths a and b
Φ	magnetic flux linkage density
Φ_T	total magnetic flux linkage
σ	material conductivity
$\delta(\mathbf{r})$	Dirac delta
δ	skin depth
$\mathbf{M}$	magnetization
$\mathbf{P}$	polarization
ϵ_r	relative dielectric constant of a material
χ_m	magnetic susceptibility of a material

Basic Electronics and Control Systems

R	resistance
L	inductance
C	capacitance
Z	impedance
V	voltage
I	current
A, B, C, T	process, sensor, feedback compensator, and combined feedback transfer functions
ϕ_m	phase margin
s	Laplace variable
$j = \sqrt{-1}$	imaginary number
ω_n, ζ	natural frequency and damping ratio
Λ	open loop transfer function

Nuclear Magnetic Resonance (NMR)

γ	gyromagnetic ratio
γ_p	gyromagnetic ratio for a proton
γ_{pc}	classically predicted gyromagnetic ratio for a proton
g	Landé g-factor
ω_s	classical spin angular frequency of atomic nucleus
ω_r	angular frequency of rotating frame
ω_0	angular frequency of freely precessing magnetization
$\Delta\omega$	angular frequency of freely precessing magnetization in a frame rotating at ω_r
$\omega_1, \omega_{1x}, \omega_{1y}$	$\omega_1 = -\gamma B_1, \quad \omega_{1x} = \omega_1 \cos\psi, \quad \omega_{1y} = \omega_1 \sin\psi$
$\mathbf{m}$	magnetic moment
$\mathbf{L}$	angular momentum
$\Delta q(\mathbf{r}), \Delta m(\mathbf{r})$	classical atomic charge and mass distributions
$\mathbf{\Gamma}$	torque per unit volume
U	potential energy
B_0	static z-directed magnetic field
$\mathbf{B_1}, B_1$	transverse magnetic field and its magnitude
ψ	phase shift
$\mathbf{B}'$	magnetic field in a frame rotating at ω_r
$\mathbf{B}'_\mathbf{1}, B'_1$	transverse magnetic field and its magnitude in a frame rotating at ω_r
$\mathbf{B}'_\mathbf{z}$	axial magnetic field in a rotating frame at ω_r
T_1	characteristic spin-lattice relaxation time
T_2	characteristic spin-spin relaxation time
T_2^*	characteristic transverse relaxation time
M_x, M_y, M_z	Cartesian components of magnetization
M'_x, M'_y, M'_z	Cartesian components of magnetization in a frame rotating at ω_r
M_{xy}	transverse magnetization
M_0	equilibrium magnetization

Thermal Physics

T	absolute temperature in kelvin
$B_{therm}(t)$	microscopic magnetic field which fluctuates due to thermal interaction
$J(\omega)$	spectral density function
$K(t)$	lattice state auto-correlation function
E_a, E_r, E_0	energy of a system, a reservoir in thermal contact with it, and the total energy respectively
$\Omega_A, \Omega_R, \Omega_0$	states accessible to: a system A, a reservoir in contact with A, and the combined system respectively
P_s	the probability that a system has an energy E_s
ω_c	critical frequency
P_+^0, P_-^0	equilibrium probability that a proton is in the higher energy state or the lower energy state respectively
N	protons per unit volume
N_+, N_-	protons per unit volume in the higher energy state and the lower energy state respectively
N^0, N_+^0, N_-^0	same as above but at thermal equilibrium
n	average number of excess aligned protons per unit volume
W_+, W_-	rate which protons flip from aligned to anti-aligned and the rate at which the opposite occurs

Magnetic Resonance Imaging (MRI)

T_E	echo time
T_{Acq}	duration of signal acquisition
G_x, G_y, G_z	alternative names for harmonic coefficients $B_{za,1,1}$, $B_{zb,1,1}$, and $B_{za,1,0}$
$I(x, y, z)$	image function
S	total signal
PSF	point spread function
BW	receiver bandwidth

Spherical Harmonics

$T_{n,m}, T'_{n,m}$	azimuthally symmetric and antisymmetric components of the spherical harmonics
$P_{n,m}(\cos\theta)$	associated Legendre polynomials
$\delta_{n,m}$	Kroneker delta
n, m	order and degree indicies
$C_{a,n,m}, C_{b,n,m}$	arbitrary symmetric and antisymmetric spherical harmonic coefficients
$B_{xa,n,m}, B_{xb,n,m}$	symmetric and antisymmetric spherical harmonic coefficients for the B_x field
$B_{ya,n,m}, B_{yb,n,m}$	symmetric and antisymmetric spherical harmonic coefficients for the B_y field
$B_{za,n,m}, B_{zb,n,m}$	symmetric and antisymmetric spherical harmonic coefficients for the B_z field
$B_{zab,n,m}$	combined notation for either $B_{za,n,m}$ or $B_{zb,n,m}$
$A_{xa,n,m}, A_{xb,n,m}$	spherical harmonic coefficients for the A_x vector potential component
$A_{ya,n,m}, A_{yb,n,m}$	spherical harmonic coefficients for the A_y vector potential component
$A_{za,n,m}, A_{zb,n,m}$	spherical harmonic coefficients for the A_z vector potential component

Spherical Harmonic Inductive Detection Coil Design

$\mathbf{W}, W$	vector winding density and its magnitude
$F_j(z), G_j(z)$	axial and azimuthal winding functions for Fourier component j of the winding density
$\Phi_{n,m}$	flux linkage due to B_z field harmonic $B_{za,n,m}$
$\mathbf{\Phi_d}$	harmonic flux linkage vector
$\mathbf{D}$	winding coefficient vector
$\mathbf{S}$	harmonic flux linkage matrix
R	coil former radius
L	coil former length
Γ	stream function
V_T	total induced voltage
n_{max}	the maximum harmonic order explicitly rejected by a detection coil design
$\kappa_{a,n,m}$	spherical harmonic weights used in detection coil design

Spherical Harmonic Control Systems

ω_I	characteristic angular frequency of the electronic integrator
ω_Q	optimal feedback path cross-over frequency
ω_L	characteristic angular frequency of the low-pass filter connected to the sense resistor
R	resistance of current sense resistor
i_c	current in the field production coil
H	magnitude and phase of the harmonic under control
K_c	gain of the harmonic production coil
D, F_I, F_L	transfer functions of the detection coil, electronic integrator, and low-pass filter
K_D, K_I, K_L	constants associated with the above transfer functions
$R_e, L_e, \omega_e, \omega_{es}, \xi$	eddy current parameters
K_D, R_D, C_D, L_D, V_D	gain, resistance, capacitance, inductance, and voltage of a harmonic detection coil
K_S, ω_S, F_S	current amplifier gain, cut-off angular frequency, and transfer function
K_{Cmp}, ω_{Cmp}	compensator gain and cut-off angular frequency
ω_M	angular frequency at which the two stages of the electronic integrator mesh
$\zeta = \omega_e/\omega_I$	eddy current cross-over ratio
Δ_{fb}	feedback deviation

Part I

Introduction and Background

Chapter 1

Introduction

Our ancestors, afflicted with both sickness and injury, did not simply bear these things. Instead, believing that their maladies could be remedied, treatments were devised. In ages past, understanding the body's internal structure and operation required either the dissection of corpses or the risks of exploratory surgery. However, in the twentieth century an array of medical imaging tools was devised allowing physicians to peer into a living body without surgery. The insights gained from this enhanced perception have accelerated medical progress.

One of these tools is magnetic resonance imaging (MRI) which excites, by means of magnetic fields, protons in the body and then uses the excitation to form an image. MRI stands out from other medical imaging modalities in its excellent soft tissue contrast and the lack of lasting physiological effect[1] [119]. Moreover, its tissue contrast mechanisms allow images of internal anatomy, blood flow, heart motion, and brain function [67, 90]; as well as tissue temperature [96, 22], chemical composition [4, 9], and mechanical elasticity [89, 83]. However, a major challenge in MRI is to determine a sequence of magnetic fields with which to excite the patient's protons and then to design equipment capable of producing that sequence.

This thesis focuses on a new way to control a subset of the magnetic fields used in MRI – the gradient fields which vary at audio frequencies. In a nutshell, this time-dependent subset is distorted by interaction with nearby metal and the distortions must be corrected for successful image formation since the metal may not be removed. Although there are existing solutions to this problem, they use *a priori* calibrations rather than detection and correction of the distortions as they occur. Thus we present the hypothesis that coils of wire can be shaped to sense the field distortions and that the resulting information can be used to correct the distortions as they unfold. The hope is that, at least in some circumstances, this new method will be preferable to existing solutions.

[1] Temporary effects of the electromagnetic fields are usually not observed but may include a tapping/tingling sensation or a slight feeling of nausea. However, since the patient must lie in a narrow tube, claustrophobia is a common problem [119].

1.1 Scope of the Thesis

The thesis develops the method mentioned above and explores how it may be used in future MRI systems. In part I, chapter 2 reviews the relevant background in electromagnetism (section 2.1), nuclear magnetic resonance (NMR) (section 2.2) and MRI (section 2.3). In chapter 3, the technology used to produce gradient fields (section 3.1) is presented with the negative feedback control theory (section 3.2) that is used to decide precisely how to correct field distortions.

With the background established, part II develops a theory applicable to dynamic detection and correction of the field distortions. Chapter 4 describes the design of spherical harmonic detection coils such that each coil detects the changes in a single harmonic component of the gradient field. This is done by decomposing the gradient distortions into the spherical harmonics of equation 2.1.31 (section 4.1) and using the decomposition to determine wire patterns (section 4.2). Chapter 5 designs a complete system around the coils using negative feedback for each harmonic (section 5.2) and this system is then optimized with respect to the MRI image (section 5.3). To verify the technique, part III presents an inexpensive experimental method (chapter 6) and its results (section 6.4).

Part IV then discusses the scaling of this proof-of-concept experimental method to actual MRI imaging. As part of that discussion chapter 7 presents the importance of isolation between control systems for various harmonics as well as how to specify performance parameters. Regarding these parameters, chapter 8 covers some practical considerations required to generate acceptable detection coils. Finally, chapter 9 closes the thesis by proposing a path for future harmonic control system development.

Chapter 2

Required Physics

2.1 Relevant Electromagnetism

As Sir Isaac Newton's (1623-1727) laws of motion provided a theoretical foundation for the engines of the industrial revolution, James Clerk Maxwell's (1831-1879) equations unifying electricity, magnetism, and optics are a foundation for many of the technologies of the 20th century including NMR and MRI. Since all subsequent parts of this thesis depend on them, we start by taking a moment to consider Maxwell's four equations:

$$\nabla \cdot \mathbf{E} = \frac{\rho}{\epsilon_0} \tag{2.1.1}$$

$$\nabla \times \mathbf{B} = \mu_0 \mathbf{J} + \frac{1}{c^2}\frac{\partial}{\partial t}\mathbf{E} \tag{2.1.2}$$

$$\nabla \cdot \mathbf{B} = 0 \tag{2.1.3}$$

$$\nabla \times \mathbf{E} + \frac{\partial}{\partial t}\mathbf{B} = 0 \tag{2.1.4}$$

which explain how the source charge and current densities ρ and $\mathbf{J}$ give rise to electric and magnetic vector fields $\mathbf{E}$ and $\mathbf{B}$. In these equations, ∇ is a differential operator as defined in table 2.1 while μ_0, ϵ_0, and the speed of light *in vacuo* $c = 1/\sqrt{\mu_0\epsilon_0}$ are merely constants that depend on the system of units employed. Although we could choose units such that these constants are unity[1], we shall exclusively use the international system of units (SI) which measures space in meters (m), time in seconds (s), current in amperes (A),

[1] Arranging the constants in Maxwell's equations such that:

$$\begin{array}{ll} \nabla \cdot \mathbf{E} = \frac{\rho}{\epsilon_0} & \nabla \times (c\mathbf{B}) = c\mu_o \mathbf{J} + \frac{\partial}{c\partial t}\mathbf{E} \\ \nabla \cdot (c\mathbf{B}) = 0 & \nabla \times \mathbf{E} + \frac{\partial}{c\partial t}(c\mathbf{B}) = 0 \end{array}$$

makes it clear that the constants can be dropped by adjusting the units of charge, current, time, and magnetic field.

and the electric and magnetic fields in volts per meter ($\mathrm{V} \cdot \mathrm{m}^{-1}$) and webers per square meter ($\mathrm{Wb} \cdot \mathrm{m}^{-2}$) respectively; in this system $\epsilon_0 = 8.854187817 \times 10^{-12}\ \mathrm{A}^2 \cdot \mathrm{s}^2 \cdot \mathrm{m}^{-2} \cdot \mathrm{N}^{-1}$ and $\mu_0 = 4\pi \times 10^{-7}\ \mathrm{N} \cdot \mathrm{A}^{-2}$.

The fields not only arise from charged particles, they also exert a force on each particle

$$\mathbf{F} = q\,(\mathbf{E} + \mathbf{v} \times \mathbf{B}) \tag{2.1.5}$$

called the Lorentz force that depends on the particle's velocity $\mathbf{v}$ and charge q. Moreover, since current density arises from the motion of charges, ρ and $\mathbf{J}$ are related by the continuity equation:

$$\frac{\partial}{\partial t}\rho + \nabla \cdot \mathbf{J} = 0 \tag{2.1.6}$$

derived by first taking the divergence of Ampère's law (equation 2.1.2) and then by inserting Gauss's Law for electric field (equation 2.1.1) and Gauss's Law for magnetic field (equation 2.1.3). An important implication of equation 2.1.3 is that magnetic fields always exist in closed loops; they have no sources or sinks. This means that any magnetic field gradient along a given direction is accompanied by a perpendicular concomitant field gradient.

Although these equations encompass all of classical electromagnetism, potentials are often more convenient to use than fields. Following Jackson [52, pg 239], we note that since $\nabla \cdot \mathbf{B} = 0$ the magnetic field may be expressed as the curl of a vector potential $\mathbf{A}$

$$\nabla \times \mathbf{A} = \mathbf{B} \tag{2.1.7}$$

transforming equation 2.1.4 into

$$\nabla \times (\mathbf{E} + \frac{\partial}{\partial t}\mathbf{A}) = 0.$$

This allows the entity $\mathbf{E} + \frac{\partial}{\partial t}\mathbf{A}$ to be written as the gradient of a scalar potential Θ

$$\mathbf{E} + \frac{\partial}{\partial t}\mathbf{A} = -\nabla\Theta. \tag{2.1.8}$$

and application of equation 2.1.1 then reduces Maxwell's original four equations into two equivalent equations regarding potentials rather than fields:

$$\nabla^2\Theta + \frac{\partial}{\partial t}(\nabla \cdot \mathbf{A}) = -\frac{\rho}{\epsilon_0} \tag{2.1.9}$$

$$\nabla^2\mathbf{A} - \frac{1}{c^2}\frac{\partial^2}{\partial t^2}\mathbf{A} - \nabla\left(\nabla \cdot \mathbf{A} + \frac{1}{c^2}\frac{\partial}{\partial t}\Theta\right) = -\mu_0\mathbf{J}. \tag{2.1.10}$$

Derivative	Number
$\nabla \equiv \hat{\boldsymbol{x}}\frac{\partial}{\partial x} + \hat{\boldsymbol{y}}\frac{\partial}{\partial y} + \hat{\boldsymbol{z}}\frac{\partial}{\partial z}$	0
$\nabla \times \nabla\psi = 0$	1
$\nabla \cdot (\nabla \times \mathbf{A}) = 0$	2
$\nabla \times (\nabla \times \mathbf{A}) = \nabla(\nabla \cdot \mathbf{A}) - \nabla^2\mathbf{A}$	3
$\nabla^2\psi \equiv \nabla \cdot (\nabla\psi)$	4
$\nabla \cdot (\psi\mathbf{A}) = \mathbf{A} \cdot \nabla\psi + \psi\nabla \cdot \mathbf{A}$	5
$\nabla \times (\psi\mathbf{A}) = \nabla\psi \times \mathbf{A} + \psi\nabla \times \mathbf{A}$	6
$\nabla(\mathbf{A} \cdot \mathbf{B}) = (\mathbf{A} \cdot \nabla)\mathbf{B} + (\mathbf{B} \cdot \nabla)\mathbf{A} + \mathbf{A} \times (\nabla \times \mathbf{B}) + \mathbf{B} \times (\nabla \times \mathbf{A})$	7
$\nabla \cdot (\mathbf{A} \times \mathbf{B}) = \mathbf{B} \cdot (\nabla \times \mathbf{A}) - \mathbf{A} \cdot (\nabla \times \mathbf{B})$	8
$\nabla \times (\mathbf{A} \times \mathbf{B}) = \mathbf{A}(\nabla \cdot \mathbf{B}) - \mathbf{B}(\nabla \cdot \mathbf{A}) + (\mathbf{B} \cdot \nabla)\mathbf{A} - (\mathbf{A} \cdot \nabla)\mathbf{B}$	9
$\nabla(\psi\phi) = \psi(\nabla\phi) + \phi(\nabla\psi)$	10
$\psi\nabla^2\psi = \nabla \cdot (\psi\nabla\psi) - (\nabla\psi \cdot \nabla\psi)$	11
$\nabla^2\left(\frac{1}{\mathbf{r}-\mathbf{r_o}}\right) = -4\pi\delta^3(\mathbf{r} - \mathbf{r_o})$	12
$\delta^3(\mathbf{r} - \mathbf{r_o}) = \begin{cases} 0 \mid \mathbf{r} \neq \mathbf{r_o} \\ \infty \mid \mathbf{r} = \mathbf{r_o} \end{cases}$	13
$\nabla\left(\frac{1}{\lvert\mathbf{r}-\mathbf{r_o}\rvert}\right) = -\frac{\mathbf{r}-\mathbf{r_o}}{\lvert\mathbf{r}-\mathbf{r_o}\rvert^3}$ [52, pg 29]	14

Table 2.1: Vector derivatives. In the definition of the differential operator ∇ on line 0, the variables $\hat{\boldsymbol{x}}, \hat{\boldsymbol{y}}$, and $\hat{\boldsymbol{z}}$ are unit vectors along the Cartesian axes.

Theorem Name	Theorem
Gradient Theorem	$\int_{\mathbf{a}}^{\mathbf{b}} (\nabla\psi) \cdot d\mathbf{l} = f(\mathbf{b}) - f(\mathbf{a})$
Divergence Theorem (Gauss's theorem)	$\int (\nabla \cdot \mathbf{A})\, dv = \oint \mathbf{A} \cdot d\mathbf{a}$
Curl Theorem (Stokes's theorem)	$\int (\nabla \times \mathbf{A}) \cdot d\mathbf{a} = \oint \mathbf{A} \cdot d\mathbf{l}$

Table 2.2: Fundamental theorems

An important quantity related to the potentials is voltage, the line integral of electric field along some path from **a** to **b**

$$V = -\int_{\mathbf{a}}^{\mathbf{b}} \mathbf{E} \cdot d\mathbf{l} \tag{2.1.11}$$

and by applying the gradient theorem from table 2.2 to equation 2.1.8, voltage may be expressed as

$$V = (\Theta(\mathbf{b}) - \Theta(\mathbf{a})) + \frac{\partial}{\partial t}\int_{\mathbf{a}}^{\mathbf{b}} \mathbf{A} \cdot d\mathbf{l} \tag{2.1.12}$$

where the quantity

$$\Phi_T = -\int_{\mathbf{a}}^{\mathbf{b}} \mathbf{A} \cdot d\mathbf{l} \tag{2.1.13}$$

is a measure of the total flux linkage. Note that if the path is a closed loop, $\mathbf{a} = \mathbf{b}$ and $\Theta(\mathbf{a}) = \Theta(\mathbf{b})$ which causes equation 2.1.12 to reduce to Faraday's law $V_{loop} = -\frac{\partial}{\partial t}\Phi_{T_{loop}}$. By Stokes's theorem (table 2.2), the total flux linkage is the total magnetic field passing through any area that has the closed loop as its boundary; expressed mathematically this is

$$\Phi_{T_{loop}} = \oint \mathbf{A} \cdot d\mathbf{l} = \int (\nabla \times \mathbf{A}) \cdot d\mathbf{a} = \int \mathbf{B} \cdot d\mathbf{a}. \tag{2.1.14}$$

The voltage is useful for calculating the current in a material with conductivity σ where the current density obeys the simple relationship

$$\mathbf{J} = \sigma\mathbf{E} \tag{2.1.15}$$

arising from the Lorentz force of equation 2.1.5 and electron collisions in matter. By integrating along a path of length l from **a** to **b** with constant **J**, σ, and area da we can re-write equation 2.1.15 as

$$I = \frac{\sigma da}{l} V = V/R$$

where the resistance is $R = \frac{l}{\sigma da}$, the current is $I = \mathbf{J} \cdot d\mathbf{a}$, and V is the voltage from equation 2.1.12.

2.1.1 Material Properties

Materials are composed of charged particles in constant motion giving rise to tumultuously fluctuating microscopic fields. So, in order to find the field in or near a material we must know the field contributions of the charges in that material. From basic chemistry, these charges are either constrained within a certain vicinity; perhaps as part of an atomic nucleus, electron orbital, or chemical bond; or may move to any location in the material, possibly by hopping from bond to bond as in semi-conductors. We thus model material charges in two groups: the bound charges and associated currents which may be perturbed by external fields but remain attached to a certain location; and the free charges which redistribute themselves throughout the material by flowing as free currents, often obeying equation 2.1.15.

If we are interested only in macroscopic fields we can consider a large number – an ensemble – of atoms or molecules over which the tumultuous quantum-scale fluctuations average away. In such an ensemble average, the net bound charge is everywhere zero but, distributed throughout the material, there may be both separations of bound charge as well as bound current loops. We model the average, but still microscopic, bound charge separations as a distribution of electric dipoles called the polarization $\mathbf{P}$ and the bound current loops as a distribution of magnetic dipoles called the magnetization $\mathbf{M}$. An electric dipole is the product $\mathbf{p} = q\mathbf{d}$ of charges $\pm q$ separated by a very small vector $\mathbf{d}$ and a magnetic dipole is the product $\mathbf{m} = I\mathbf{a}$ of a current I flowing around a very small area[2] $\mathbf{a}$.

In this scheme, the field and potential contributions from polarization and magnetization are added to those from the free charge and current. Also, the polarization and magnetization can, in general, be functions of the whole history of the material, as in ferro-electric and ferro-magnetic materials. However, in many materials, including those of the human body, the polarization at a point is linearly related to the electric field pulling bound charges apart and the magnetization is linearly related to the magnetic field causing the magnetic dipoles to either align (paramagnetism) or change their magnitudes depending on their orientations so as to oppose the external field (diamagnetism) [37, 6.1.3]. In these linear materials, the polarization and magnetization obey the relations $\mathbf{P} = \epsilon_0 (\epsilon_r - 1)\mathbf{E}$ and $\mathbf{M} = \frac{\chi_m}{\mu_0(1+\chi_m)}\mathbf{B}$ [37, pg 180, 274] respectively where ϵ_r is the relative dielectric constant and $\frac{\chi_m}{\mu_0(1+\chi_m)}$ is just a constant related to the magnetic susceptibility χ_m of the material[3]. The result of placing a material with these properties in a homogeneous field is that the material produces, by means of its bound charges and currents, local field distortions proportional to the strength of the external field.

2.1.2 Coulomb Gauge

Since the potentials are defined such that they produce fields when differentiated, any aspect of a potential that disappears under the prescribed differentiations does not contribute to the field and can be chosen arbitrarily. For example, the gradient of any scalar function f can be added to the vector potential ($\mathbf{A}' = \mathbf{A} + \nabla f$) without influencing the magnetic field since the curl of a gradient is zero ($\nabla \times \mathbf{A}' = \nabla \times \mathbf{A} + \nabla \times \nabla f = \nabla \times \mathbf{A} = \mathbf{B}$). This freedom allows the condition $\nabla \cdot \mathbf{A} = 0$ to be specified by replacing $\mathbf{A}$ with $\mathbf{A}' = \mathbf{A} + \nabla f$ where $\nabla \cdot \mathbf{A}' = \nabla \cdot \mathbf{A} + \nabla^2 f = 0$. A vector potential satisfying this condition is said to belong to the Coulomb gauge [52, pg 241]. Clearly, the vector potential associated with a magnetic field is not unique even if is a member of the Coulomb gauge since any such vector potential may have a function ∇g added to it without violating the condition $\nabla \cdot \mathbf{A} = 0$ provided $\nabla^2 g = 0$.

For potentials within the Coulomb gauge, equations 2.1.9 and 2.1.10 simplify [52, pg 242] to

[2] The vector nature of the area denotes its orientation.

[3] Although it is not ideal to write a simple constant as $\frac{\chi_m}{\mu_0(1+\chi_m)}$, the standard definitions of magnetic susceptibility χ_m and relative magnetic permeability $\mu_r \equiv (1 + \chi_m)$ do not permit a relation like $\mathbf{M} = \frac{1}{\mu_0}(1 + a_r)\mathbf{B}$ which would be symmetric with the electric case.

$$\nabla^2\Theta = -\frac{\rho}{\epsilon_0} \tag{2.1.16}$$

$$\frac{1}{c^2}\frac{\partial^2}{\partial t^2}\mathbf{A} - \nabla^2\mathbf{A} = \mu_0\mathbf{J} - \frac{1}{c^2}\nabla\frac{\partial}{\partial t}\Theta. \tag{2.1.17}$$

Therefore the Coulomb gauge reduces Maxwell's equations to Poisson's equation for the electric scalar potential and the inhomogeneous wave equation for the magnetic vector potential.

2.1.3 Quasi-statics

In a region of interest, whether near or far from sources, which is small enough that the actual current $\mathbf{J}$ dominates over the field derivatives, we have[4] $\mu_0\mathbf{J} \gg \frac{1}{c^2}\left(\frac{\partial^2}{\partial t^2}\mathbf{A} + \nabla\frac{\partial}{\partial t}\Theta\right)$ so equations 2.1.16 and 2.1.17 reduce to

$$\nabla^2\Theta = -\frac{\rho}{\epsilon_0} \tag{2.1.18}$$

$$\nabla^2\mathbf{A} = -\mu_0\mathbf{J}. \tag{2.1.19}$$

Note that equations 2.1.18 and 2.1.19 imply [52, pg 180]

$$\Theta = \frac{1}{4\pi\epsilon_0}\int\frac{\rho}{|\mathbf{r}-\mathbf{r_o}|}dV + \Theta_o \tag{2.1.20}$$

$$\mathbf{A} = \frac{\mu_0}{4\pi}\int\frac{\mathbf{J}}{|\mathbf{r}-\mathbf{r_o}|}dV + \nabla\psi \tag{2.1.21}$$

($\nabla\psi$ and Θ_o are constants of integration) leading directly[5] to the well known Biot-Savart law [52, pg 175] through vector derivatives 1, 6 and 13 in table 2.1:

$$\mathbf{B} = \nabla\times\mathbf{A} = \frac{\mu_0}{4\pi}\int\frac{\mathbf{J}(\mathbf{r_o})\times(\mathbf{r}-\mathbf{r_o})}{|\mathbf{r}-\mathbf{r_o}|^3}dV + \frac{\mu_0}{4\pi}\int\frac{\nabla\times\mathbf{J}(\mathbf{r_o})}{|\mathbf{r}-\mathbf{r_o}|}dV \tag{2.1.22}$$

$$\mathbf{B} = \frac{\mu_0}{4\pi}\int\frac{\mathbf{J}(\mathbf{r_o})\times(\mathbf{r}-\mathbf{r_o})}{|\mathbf{r}-\mathbf{r_o}|^3}dV. \tag{2.1.23}$$

So in this so-called "quasi-static region" the potentials can be computed directly from the sources even though the fields are still inter-related.

[4] It could also be stated that the maximum size of the region r is much less than the minimum wavelength λ of the potentials or fields ($r \ll \lambda$). Another way of imposing this criteria is to say that $\frac{1}{c^2}\frac{\partial^2}{\partial t^2}\mathbf{A} \ll \nabla^2\mathbf{A}$ and $\mu_0\mathbf{J} \gg \frac{1}{c^2}\nabla\frac{\partial}{\partial t}\Theta$.

[5] In equation 2.1.22, $\nabla\times\mathbf{J}(\mathbf{r_o}) = 0$ because $\mathbf{J}(\mathbf{r_o})$ depends on the location of the source point $\mathbf{r_o}$ over which we are integrating rather than on the field point $\mathbf{r}$ over which the differentiation ∇ takes place.

2.1.3.1 Mutual- and Self-Inductance

In a quasi-static region, current density alone gives rise to the vector potential $\mathbf{A}$ through equation 2.1.19. This means that the voltage along some path $\mathbf{a}_1 \rightarrow \mathbf{b}_1$ in equation 2.1.12 depends on the potential Θ as well as the flux linkages from all currents $\mathbf{a}_n \rightarrow \mathbf{b}_n$ including itself. Since the flux linkages are geometrically complex but linear with current (equation 2.1.21), it is common to express the flux linkage between current paths p and q as

$$\Phi_{q,p} = M_{q,p} I_p$$

where $M_{p,q} = M_{q,p}$ is the mutual inductance between the paths and $M_{q,q} = L_q$ is a path's self-inductance. The voltage in path q is then:

$$V_q = \Big(\Theta(\mathbf{b}_q) - \Theta(\mathbf{a}_q)\Big) - \sum_p M_{q,p} \frac{\partial}{\partial t} I_p \tag{2.1.24}$$

and if the paths are closed circuits, equation 2.1.21 produces the Neumann equation [38, pg 8] for mutual inductance:

$$M_{q,p} = \frac{\mu_0}{4\pi} \oint_q \oint_p \frac{d\mathbf{q} \cdot d\mathbf{p}}{|\mathbf{r_q} - \mathbf{r_p}|}. \tag{2.1.25}$$

2.1.3.2 Eddy Currents

Within a quasi-static region filled with conductive material such that current density is proportional to electric field, equations 2.1.15 and 2.1.8 yield

$$\mathbf{J} = -\sigma \left(\frac{\partial}{\partial t} \mathbf{A} + \nabla \Theta \right) \tag{2.1.26}$$

which, when used with equation 2.1.19, forms an inhomogeneous diffusion equation

$$\frac{1}{\mu_0} \nabla^2 \mathbf{A} - \sigma \frac{\partial}{\partial t} \mathbf{A} = \sigma \nabla \Theta. \tag{2.1.27}$$

In situations where the region is not exposed to conservative electric fields, such as those caused by connecting a conductor to a laboratory current source, $\nabla\Theta = 0$ and equation 2.1.27 simplifies to the homogeneous diffusion equation [52, pg 219]

$$\nabla^2 \mathbf{A} = \mu_0 \sigma \frac{\partial}{\partial t} \mathbf{A}. \tag{2.1.28}$$

which has solutions of the form $e^{i(\omega \pm r/\delta)t} e^{\mp r/\delta}$ where ω is the angular frequency of the vector potential and

$$\delta = \sqrt{\frac{2}{\mu_0 \sigma \omega}} \tag{2.1.29}$$

is the skin depth, a measure of how far the vector potential at the conductor surface diffuses into the material. Thus each vector component of the vector potential diffuses into electrical conductors as heat does into thermal conductors. The spatial variation in vector potential is caused by induced eddy currents [128, pg 4] $\mathbf{J} = -\sigma\frac{\partial}{\partial t}\mathbf{A}$ distributed throughout the material which may be computed once equation 2.1.28 has been solved using either analytical or numerical methods.

2.1.4 Source-Free Region and Spherical Harmonics

If the region of interest has no current or charge sources ($\mathbf{J} = 0$, $\rho = 0$) then $\nabla(\nabla\cdot\mathbf{B}) - \nabla\times(\nabla\times\mathbf{B}) = \nabla^2\mathbf{B} = 0$ and a magnetic scalar potential Ψ may be introduced such that $\nabla^2\Psi = 0$, $\nabla\Psi = \mathbf{B}$. In this source-free region, equations 2.1.18 and 2.1.19 both reduce to Laplace's equation so that[6]:

$$\begin{aligned} \nabla^2\Theta = 0 \ , \ \ \nabla^2\Psi = 0 \\ \nabla^2\mathbf{A} = 0 \ , \ \ \nabla^2\mathbf{B} = 0 \end{aligned} \ . \tag{2.1.30}$$

In a spherical region with coordinates (r, θ, ϕ), the solution to any of these equations may be written as a sum of spherical harmonics [117, 15, 88] $\sum_{m=0}^{\infty}\sum_{n=m}^{\infty} C_{a,n,m}T_{n,m} + C_{b,n,m}T'_{n,m}$ where the azimuthally symmetric and antisymmetric components of the spherical harmonics with respect to azimuth $\phi = 0$ are

$$T_{n,m} = r^n P_{n,m}(\cos\theta)\cos m\phi \quad T'_{n,m} = r^n P_{n,m}(\cos\theta)\sin m\phi, \tag{2.1.31}$$

$P_{n,m}$ are the associated Legendre polynomials defined [1, pg 332,785] by

$$P_{n,m}(x) = \frac{(1-x^2)^{\frac{m}{2}}}{(-1)^n 2^n n!}\frac{d^m}{dx^m}\frac{d^n}{dx^n}\left[(1-x^2)^n\right], \tag{2.1.32}$$

and $C_{a,n,m}$ and $C_{b,n,m}$ are constants. The subscripts a and b on these constants denote that they are for $T_{n,m}$ and $T'_{n,m}$ respectively. Following the nomenclature of Morse and Feshbach [88], we refer to zonal harmonics as those where $m = 0$, sectoral harmonics as those where $n = m$, and call the rest tesseral harmonics.

In electrodynamics the potentials and fields are often differentiated with respect to spatial coordinates. This motivated the development of the *Cartesian* derivatives of the spherical harmonics [111, 18, pg 111] which are summarized in table 2.3 as adapted to the notation of equation 2.1.31.

2.2 Nuclear Magnetic Resonance (NMR)

Magnetic resonance imaging [18, 73] is based on a physical effect known as nuclear magnetic resonance (NMR) [122]. This effect arises because atomic nuclei are electrically charged and, provided their charge and mass numbers are not both even[7], have spin. The co-incidence of nuclear spin and charge

[6] The electric field also satisfies the Laplace equation $\nabla^2\mathbf{E} = 0$.

[7] Nuclei with odd mass numbers have half-integral spin while those with even mass numbers but odd charge numbers have integral spin [73, pg 60].

$\frac{\partial T_{n,m}}{\partial x} = \frac{1}{2}\left\{-(1+\delta_{m,0})T_{n-1,m+1} + (1-\delta_{m,0})(n+m)(n+m-1)T_{n-1,m-1}\right\}$	1
$\frac{\partial T_{n,m}}{\partial y} = \frac{1}{2}\left\{-(1+\delta_{m,0})T'_{n-1,m+1} - (1-\delta_{m,0})(n+m)(n+m-1)T'_{n-1,m-1}\right\}$	2
$\frac{\partial T_{n,m}}{\partial z} = (n+m)T_{n-1,m}$	3
$\frac{\partial T'_{n,m}}{\partial x} = \frac{1}{2}\left\{-(1+\delta_{m,0})T'_{n-1,m+1} + (1-\delta_{m,0})(n+m)(n+m-1)T'_{n-1,m-1}\right\}$	4
$\frac{\partial T'_{n,m}}{\partial y} = \frac{1}{2}\left\{(1+\delta_{m,0})T_{n-1,m+1} + (1-\delta_{m,0})(n+m)(n+m-1)T_{n-1,m-1}\right\}$	5
$\frac{\partial T'_{n,m}}{\partial z} = (n+m)T'_{n-1,m}$	6
$\delta_{n,m} = \begin{cases} 1 \mid n = m \\ 0 \mid n \neq m \end{cases}$	7

Table 2.3: Cartesian derivatives of spherical harmonics.

produces a magnetic moment for which it is energetically favourable to align with an external magnetic field. In an attempt to measure the nuclear magnetic moment, early workers subjected beams of atoms to both a large static magnetic field and, at right angles, a much smaller oscillating magnetic field [106, 105]. Since the behaviour of the nuclei in these experiments was strongly affected at a specific oscillatory frequency, the effect was called nuclear magnetic resonance and it was soon realized that atomic nuclei exhibit similar effects in bulk materials [104, 36], such as the human body, and these effects were eventually used for imaging [69].

2.2.1 Precession of a Proton Ensemble in a Magnetic Field

Classically, the proton may be modelled, like any nucleus, as a sphere with charge $\Delta q(\mathbf{r})$ and mass $\Delta m(\mathbf{r})$ distributions spinning at an angular frequency ω_s about some axis. Considering an elemental volume dV at position $\mathbf{r}$ in the proton, its contribution to angular momentum is $d\boldsymbol{L} = \boldsymbol{\omega_s} r^2 \Delta m(\mathbf{r}) dV$ where r is the radial distance from the axis of rotation to position $\mathbf{r}$ and the direction of the vector $\boldsymbol{\omega_s}$ is such that the proton spins counter-clockwise when viewed from the vector tip. Furthermore, the contribution of this elemental volume to the proton's magnetic moment is just the product of the current due to the charge in that volume and the area swept out in a singe rotation: $d\boldsymbol{m} = \Delta q(\mathbf{r}) dV \frac{\omega_s}{2\pi} \pi r^2$. Performing the integral over the entire proton we find a total angular momentum $\boldsymbol{L} = \boldsymbol{\omega_s} \int r^2 \Delta m(\mathbf{r}) dV$ and total magnetic moment $\boldsymbol{m} = \boldsymbol{\omega_s} \frac{1}{2} \int r^2 \Delta q(\mathbf{r}) dV$. Provided the distributions remain constant, the angular momentum and magnetic moment are related to each other by

$$\mathbf{m} = \gamma \mathbf{L} \tag{2.2.1}$$

where γ is the gyromagnetic ratio.

However, the proton is so small that this simplistic picture breaks down and quantum mechanics must be applied. First of all, since the proton's charge is distributed in space and thus has centripetal acceleration, classical physics predicts that the spin energy will be radiated in the form of electromagnetic

waves until the spinning eventually stops; but in actuality the proton continues to spin indefinitely. Moreover, the classical expectation for the proton's gyromagnetic ratio is just half its charge to mass ratio $\gamma_{pc} = \frac{q}{2m_p} = 4.789 \times 10^7\ \mathrm{T^{-1}s^{-1}}$ but in actuality it is $\gamma_p = g\frac{q}{2m_p} = 2.675 \times 10^8\ \mathrm{T^{-1}s^{-1}}$ [26, 135, 136] where $g = 5.5857$ can be computed from relativistic quantum mechanics [24] and the internal quark structure of the proton [102, pg 74].

Even more strange is the behaviour of the proton's spin angular momentum [114, ch 3]. This angular momentum has a fixed total value of $\sqrt{3}\hbar/2$ but its component along an axis can only ever be $\pm\hbar/2$ in any interaction or measurement; $\hbar = \frac{h}{2\pi}$ is the reduced Planck constant. If the proton has an angular momentum α, either $\pm\hbar/2$, along some axis A_1 and then the angular momentum is measured along another axis A_2, the value along this axis becomes either $\pm\hbar/2$ **completely at random**. The measurement along A_2 changes the proton's state such that a subsequent measurement along A_1 no longer reveals an angular momentum component α but rather a random value of either $\pm\hbar/2$. Note that a measurement need not imply an observer [85, pg 687], since any interaction involving the angular momentum's component along an axis effectively measures that component. However, despite this random behaviour, the results are not entirely beyond prediction since the probabilities for the two values along A_2 can be predicted from the previous angular momentum α along A_1, the angle between A_1 and A_2, and the time between the interactions. So although a single proton is inherently unpredictable, the average behaviour of a large number of protons is predictable in that it samples deterministic probabilities. Moreover, although a single proton can only project an angular momentum of $\pm\hbar/2$ along one axis at a time, a large number of protons can produce a well defined, and seemingly continuously variable, angular momentum vector with components along all three spatial dimensions.

Now the majority of the behaviour exploited in MRI is the result of a macroscopic (μm − cm) distribution of hydrogen nuclei (protons) ~ and there are approximately 6.7×10^{22} hydrogen nuclei in a millilitre of water ~ so we can easily take an ensemble of several billion such nuclei as our smallest scale of consideration. For such a large number of protons, quantum behaviour averages away and, as an aid to comprehension, we may revive the classical proton model. We either imagine each proton as a classical spinning ball, realizing that this is only valid so long as we work only with the ensemble, or we imagine the ensemble as a classical spinning ball with the state of individual protons contributing to the expected magnetic moment. In either case we must not take the classical analogy too far since the charge does not damp the spinning motion through radiation and the gyromagnetic ratio is the one observed in experiment and predicted by quantum mechanics. Although subsequent discussion will focus on hydrogen nuclei, there are other nuclei of interest in MRI and the gyromagnetic ratios for some of these are given in table 2.4.

Continuing with the classical model, the ensemble average magnetic moment per unit volume is a magnetization which experiences a torque per unit volume $\mathbf{\Gamma} = \mathbf{M} \times \mathbf{B}$ in a magnetic field $\mathbf{B}$ due to the Lorentz force (equation 2.1.5). Using equation 2.2.1, and remembering that torque is the rate of change of

Z	Isotope	spin number: I	Abundance (%)	$\frac{\gamma}{2\pi}$ (MHz/T)
1	^{1}H	1/2	99.9850	42.5775
1	^{2}H	1	0.0115	6.5359
6	^{13}C	1/2	1.07	10.7084
8	^{17}O	5/2	0.038	5.7742
11	^{23}Na	3/2	100	11.2688
15	^{31}P	1/2	100	17.2515

Table 2.4: Gyromagnetic ratios, natural abundance, and nuclear spin numbers for several isotopes [74, 9-92].

angular momentum, gives the magnetization's time evolution in a magnetic field

$$\frac{d\mathbf{M}}{dt} = \gamma \mathbf{M} \times \mathbf{B}. \tag{2.2.2}$$

This is the Larmor equation describing precession of the magnetization about the direction of the applied magnetic field – an analogous motion to that of a spinning top in the presence of gravity – and the magnetization has a potential energy per unit volume defined by

$$U = -\mathbf{M} \cdot \mathbf{B}. \tag{2.2.3}$$

Since the motion is clockwise when viewed from the tip of $\mathbf{B}$, the angular frequency defined in the Larmor equation:

$$\boldsymbol{\omega} = -\gamma \mathbf{B} \tag{2.2.4}$$

is defined with a negative sign so the motion is counter-clockwise about the tip of $\boldsymbol{\omega}$ and the familiar right-hand rule can be applied. Note that for convenience, the negative sign in this equation is omitted either because only the magnitude is important or the direction of precession does not change any pertinent result.

NMR experiments, including MRI, involve both static and oscillating magnetic fields and it is useful to split the magnetic field of equation 2.2.2 into a static B_0 defining the z-direction and a perpendicular component B_1 rotating at angular frequency ω_r

$$\mathbf{B} = B_1 \cos(\omega_r t + \psi)\hat{\boldsymbol{x}} + B_1 \sin(\omega_r t + \psi)\hat{\boldsymbol{y}} + B_0 \hat{\boldsymbol{z}} = \mathbf{B}_1 + B_0 \hat{\boldsymbol{z}}. \tag{2.2.5}$$

In order to consider a stationary $\mathbf{B}_1$, rather than one that rotates at ω_r, a new coordinate frame is introduced and denoted with a prime. In this new frame shown in figure 2.1, the rotation of B_1 matches that of the coordinate frame and thus $\mathbf{B}_1$ is stationary. However, in the absence of B_1, magnetization in the $x'y'$-plane now precesses with angular frequency $\Delta\omega = \omega_0 - \omega_r$ where $\omega_0 = -\gamma B_0$ and since the magnetization is precessing at angular frequency $\Delta\omega$, there must be a field in this frame: $B'_z = -\frac{1}{\gamma}\Delta\omega$ [122, pg 12]. Thus with B_1 engaged, the magnetic field in the rotating frame is the vector sum:

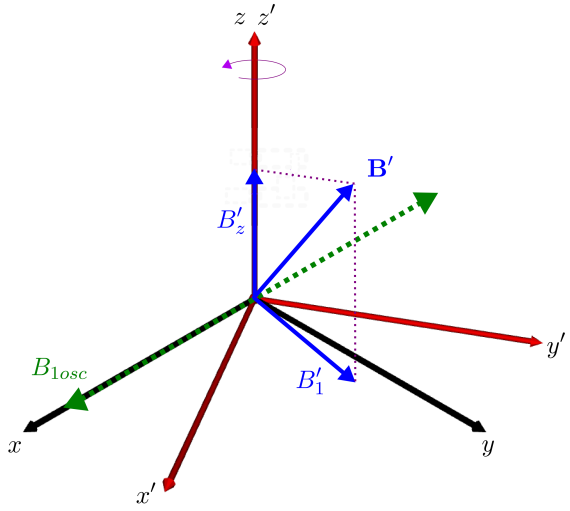

Figure 2.1: In a reference frame that rotates with angular frequency ω_r about the lab frame's z-direction, the rotating magnetic field $\mathbf{B_1}$ has a fixed orientation $\mathbf{B}'_1$.

$$\mathbf{B}' = \mathbf{B}'_\mathbf{1} + \mathbf{B}'_\mathbf{z} = -\frac{1}{\gamma}\left(\omega_{1x}\hat{\mathbf{x}} + \omega_{1y}\hat{\mathbf{y}} + \Delta\omega\hat{\mathbf{z}}\right) \tag{2.2.6}$$

where $\omega_{1x} = \omega_1\cos(\psi)$, $\omega_{1y} = \omega_1\sin(\psi)$ and $\omega_1 = -\gamma B_1$. Despite being in a new reference frame, the magnetization still experiences a torque and we rewrite equation 2.2.2 as

$$\frac{d}{dt}\begin{bmatrix} M'_x \\ M'_y \\ M'_z \end{bmatrix} = \begin{bmatrix} 0 & -\Delta\omega & \omega_{1y} \\ \Delta\omega & 0 & -\omega_{1x} \\ -\omega_{1y} & \omega_{1x} & 0 \end{bmatrix}\begin{bmatrix} M'_x \\ M'_y \\ M'_z \end{bmatrix} \tag{2.2.7}$$

where the magnetization moves about the effective magnetic field B' in the rotating frame with angular frequency $|\gamma\mathbf{B}'|$.

Equation 2.2.7 is useful in that the motion of $\mathbf{M}'$ can be visualized using the matrix parameters set by the magnitude, phase, and frequency (relative to ω_0) of $\mathbf{B}_1$. If the applied $\mathbf{B}_1$ field is on-resonance, $\Delta\omega = 0$ and the magnetization simply nutates about $\mathbf{B}'_\mathbf{1}$ with the solution to equation 2.2.7 taking the form

$$\begin{aligned} M'_x &= M_0\sin(\theta(t))\sin(\psi) \\ M'_y &= -M_0\sin(\theta(t))\cos(\psi) \\ M'_z &= M_0\cos(\theta(t)) \\ \theta(t) &= \int_0^t \omega_1(t')dt' \end{aligned} \tag{2.2.8}$$

where ψ is the phase of B_1 from equation 2.2.5, the initial condition is $M'_z = M_0$, and $\theta(t)$ is the flip angle produced by $\omega_1(t) = -\gamma B_1(t)$. Although $\mathbf{B}'_\mathbf{1}$ is confined to the $x'y'$-plane, the application of short on-resonance B_1 *pulses* with correct duration and orientation may be used to nutate magnetization to any

orientation in the rotating frame. For example, suppose all the magnetization is aligned with B_0 and a resonant pulse ($\Delta\omega = 0$) with magnitude B_1 and duration τ such that $\omega_1\tau = -\gamma B_1\tau = \frac{\pi}{2}$ is applied. The result of this 90° pulse is that the magnetization is flipped into the transverse plane.

For a pulse where $\Delta\omega \gg \omega_1$, however, the effective field in the rotating frame is overwhelmingly in the z-direction so the magnetization cannot be arbitrarily re-oriented. In short, the system is resonant because the magnetization reacts appreciably only if $\omega_1 > \Delta\omega$ which only occurs when $\omega_r \simeq \omega_0$. Between externally applied B_1 pulses, $\omega_1 \simeq 0$ and any initial transverse magnetization $M'_{xy\,0}$ in the $x'y'$-plane merely rotates about the z-axis as

$$\begin{aligned} M'_x &= M'_{xy\,0}\cos(\theta(t)) \\ M'_y &= M'_{xy\,0}\sin(\theta(t)) \\ M'_{xy} &= M'_x + iM'_y = M_{xy\,0}e^{i\theta(t)} \\ \theta(t) &= \int_0^t \Delta\omega(t')dt' + \psi \end{aligned} \tag{2.2.9}$$

where ψ is the initial phase of the transverse magnetization and we may optionally express the transverse magnetization M'_{xy} with complex numbers where $i = \sqrt{-1}$. We have written $\Delta\omega$ to depend on time since the z-directed field may have a slight offset $\Delta B_z(t)$ in addition to the static component B_0 such that $B_z = \Delta B_z(t) + B_0$ and thus $\Delta\omega = -\gamma\Delta B_z(t) + \omega_o - \omega_r$. In section 2.3 we shall see that these slight offsets, which may vary spatially as well as temporally, have an important role in imaging.

2.2.2 Relaxation

We have seen that the nuclear magnetization is influenced by B_0 and B_1 fields. However, in a biological sample the protons experience magnetic fields from each other, especially from those in the same molecule, and from both the motion and spin of electrons [122, pg 87] in addition to those fields externally applied. Thermal motion causes relatively free molecules to experience Brownian motion – random shifts of position and orientation – while molecules fixed in a lattice vibrate therein. In this tumult, conservative electric fields mediate collisions while magnetic fields influence the proton ensemble's magnetization through equation 2.2.7. However, due to their microscopic size and chaotic nature, the magnetic fields are not known precisely and thus the equation cannot be directly applied.

2.2.2.1 Spectral Density Function

Imagine, however, that we are somehow able to measure the microscopic thermal fluctuations $B_{therm}(t)$ superimposed on the field in an arbitrary direction – we assume the fluctuations are independent of direction. Now as long as the temperature remains constant, the mean value and standard deviation of the fluctuations do not change. Therefore, $B_{therm}(t)$ is a stationary random process [101, 2.7.4] with the property that its Fourier transform (table 2.5) has a specific magnitude at every frequency even though the

$F(\omega) \equiv \mathfrak{F}[f(t)] \equiv \int_{-\infty}^{\infty} f(t)e^{-i\omega t}dt$
$\mathfrak{F}^{-1}[F(\omega)] = f(t) = \frac{1}{2\pi}\int_{-\infty}^{\infty} F(\omega)e^{i\omega t}d\omega$

Table 2.5: Fourier transforms can be defined in various ways; we define them as above [101, Table 2.3].

phases at each frequency vary randomly with time. The square of these magnitudes can be expressed as a power spectrum [93, ch 14] $J(\omega) = F(\omega)F^*(\omega)$, also known as a spectral density function, where $F(\omega)$ is the Fourier transform and the superscript denotes complex conjugation. Taking the inverse Fourier transform of the power spectrum and remembering that $B_{therm}(t)$ is a real valued function yields

$$K(t) = \int_{-\infty}^{\infty} B_{therm}(\tau)B_{therm}(\tau + t)d\tau$$

which is an auto-correlation function showing the extent to which $B_{therm}(t)$ is related to itself over time.

A crude estimate for the auto-correlation function, and thus the spectral density function, can be made by assuming $B_{therm}(\tau)$ arises as a result of the various states that each of the molecular contributors to B_{therm} have at time τ. Then if ω_c is the probability per second that a contributor leaves its state, the number of unchanged contributors N obeys the differential equation $dN/dt = -\omega_c N$. Assuming the auto-correlation $K(t)$ is proportional to $N(t)$, it takes the form $K(t) \propto e^{-pt}$ as long as $t \geq \tau$. Now if we look at what must have happened before time τ, the same probability per second is at work but now changing the contributors to the states that they have at time τ rather than away from them. Thus the auto-correlation has the form

$$K(t) \propto e^{-\omega_c|t|}$$

and its Fourier transform reveals an estimated spectral density[8]

$$J(\omega) = \mathfrak{F}^{-1}\left[K(t)\right] \propto 1/\left(1 + \omega^2/\omega_c^2\right). \tag{2.2.10}$$

Therefore the energy associated with thermal fluctuations in the magnetic field is constant over a wide bandwidth; that is, the fluctuations produce white noise on the magnetic field. However, above some critical frequency $f_c = \omega_c/(2\pi)$, possibly associated with molecular tumbling or vibration, the power drops rapidly to zero. The importance of these results is not that they are strictly correct – the material may have many critical frequencies or other complexities that do not fit this model – but rather that the fluctuating magnetic field along each axis has contributions over a wide range of frequencies including the resonant frequency $\omega_0 = -\gamma B_0$. As can be seen in equation 2.2.7, low frequency changes to B_z influence $M'_{x,y}$ while transverse fields near ω_0 flip magnetization either toward or away from the z-axis, providing a mechanism for energy transfer between the proton ensemble and thermal motion in the material. It is to these effects that we now turn.

[8]This is precisely the spectral density function presented by Farrar and Becker [31, ch 4].

2.2.2.2 The Origin of Bulk Magnetization and T_1

Returning to individual protons rather than the ensemble, interactions with the B_0 field cause the proton's spin-state to take on either an angular momentum $\hbar/2$ aligned along B_0 with energy $-\mu B_0$ or anti-aligned with energy μB_0 where $\mu = \gamma\frac{\hbar}{2}$ is the z-component of the proton's magnetic moment. Although it is energetically favourable for the z-component of spin angular momentum to be aligned with the field, thermal interactions along axes in the transverse plane flip the protons out of alignment. However, if left undisturbed and at a constant temperature, an equilibrium is established in the ensemble between these two tendencies. To examine the properties of this equilibrium, we employ Boltzmann statistics as described by Pathria [93, p 12, p 43].

Let us consider a system A (which we will shortly identify as a single proton) in thermal equilibrium with an energy reservoir R consisting of an ensemble of many copies of that system. The combined energy of A and R is just the sum of their individual energies $E_0 = E_a + E_r$ where $E_0 \simeq E_r$ since the reservoir is much larger than A. The number of quantum states accessible to any system is a function of its energy so that the number of states accessible to the system A, the reservoir R, and the combination of the two are $\Omega_A(E_a)$, $\Omega_R(E_r)$, and $\Omega_0(E_a) = \Omega_A(E_a)\Omega_R(E_r)$ respectively. Now in thermal equilibrium, the entropy $S = k\ \ln\Omega$, and thus the total number of accessible states Ω_0, is at a maximum so that

$$\frac{\partial\Omega_0}{\partial E_a} = 0 = \Omega_R\frac{\partial\Omega_A}{\partial E_a} + \Omega_A\frac{\partial\Omega_R}{\partial E_r}\frac{\partial E_r}{\partial E_a} \rightarrow \frac{\partial \ln\Omega_A}{\partial E_a} = \frac{\partial \ln\Omega_R}{\partial E_r}$$

where $\frac{\partial \ln\Omega}{\partial E} = \frac{1}{kT}$ since, keeping all other properties constant, we have $\frac{\partial S}{\partial E} = \frac{1}{T}$ where k is Boltzmann's constant and T is absolute temperature in kelvin of the reservoir or system. Now if we assume that any accessible state has the same probability as any other, the probability P_s that system A has an energy E_s is just the number of ways in which the reservoir can take take the energy $E_r = E_0 - E_a$ over the total number of the reservoir's accessible states:

$$P_s = \frac{\Omega_R(E_r)}{\sum_r \Omega_R(E_r)}.$$

Since $E_0 \simeq E_r$ we can expand $\ln(\Omega_R(E_r))$ as a Taylor series about $E_r = E_0$

$$\ln(\Omega_R(E_r)) = \ln(\Omega_R(E_0)) + (E_r - E_0)\frac{\partial \ln\Omega_R}{\partial E_r}|_{E_r=E_0} + ...$$

which allows us to approximate $\Omega_R(E_r)$ as $\Omega_R(E_r) \simeq \xi e^{-\frac{E_s}{kT}}$ where ξ is just a constant and we have used the relationship $\frac{\partial \ln\Omega}{\partial E} = \frac{1}{kT}$. In this approximation, the probability that the system A in thermal equilibrium takes on an energy E_s is

$$P_s = \frac{e^{-\frac{E_s}{kT}}}{\sum_s e^{-\frac{E_s}{kT}}} \tag{2.2.11}$$

where the constants ξ have cancelled out[9].

Now, if the system A is a proton in a magnetic field B_0 the energies of the two possible states with respect to this field are $-\mu B_0$ and μB_0 as above. Therefore, from equation 2.2.11, the ratio of the probability of a proton being in the higher energy state P_+^0 – in an interaction with the B_0 field – to the probability of it being in the lower state P_-^0 is [63, p 57-61]

$$\frac{P_+^0}{P_-^0} = \frac{e^{-\mu B_0/kT}}{e^{\mu B_0/kT}} = e^{-2\mu B_0/kT} \tag{2.2.12}$$

and following Slichter [122, pg 4-9], if there are N protons per unit volume, and N_+ of these protons are anti-aligned with energy μB_o, then the remaining protons

$$N_- = N - N_+ \tag{2.2.13}$$

are in the state $-\mu B_o$ where the difference between these populations

$$n = N_- - N_+ \tag{2.2.14}$$

is the average number of excess aligned protons per unit volume; that is $M_z = \mu n$. In equilibrium, denoted with a superscript, the ratio of these two populations must be the same as the ratio of the probabilities in equation 2.2.12

$$\frac{N_+^0}{N_-^0} = e^{-2\mu B_0/kT} = \frac{P_+^0}{P_-^0}.$$

Whether equilibrium has been established or not, there is an average rate W_+ at which an individual proton flips from aligned to anti-aligned and another average rate W_- at which the opposite occurs. The total transition rate in either direction depends on the populations in each state and this provides a differential equation for the number of aligned protons per unit volume

$$\frac{dN_-}{dt} = N_+ W_- - N_- W_+. \tag{2.2.15}$$

However at steady state, $\frac{dN_-}{dt} = 0$ so

$$\frac{N_+^0}{N_-^0} = \frac{W_+}{W_-} = e^{-2\mu B_0/kT} \tag{2.2.16}$$

which gives the ratio of transition rates. Desiring to express equation 2.2.15 in terms of M_z, we assume $\frac{dN}{dt} = 0$ and then use equations 2.2.13 and 2.2.14 to find $\frac{dM_z}{dt} = 2\mu\frac{dN_-}{dt} = \mu N(W_- - W_+) - M_z(W_+ + W_-)$. This equation may then be re-arranged and expressed using the equilibrium magnetization M_0 instead of transition rates:

[9] At low temperatures Boltzmann statistics fails and one must use either Fermi-Dirac or Bose-Einstein statistics depending on the properties of the particles [39, pg 75].

Tissue Material	T_1 (ms)
cerebrospinal fluid (CSF)	4000+
blood (arterial)	1200
brain grey matter	920
brain white matter	790
skeletal muscle	870
lipids (fat)	260

Table 2.6: Approximate T_1 values at 1.5 T [8, pg 961]

$$\frac{d}{dt}M_z = \frac{1}{T_1}\left(M_0 - M_z\right) \tag{2.2.17}$$

where

$$M_0 = \mu N\left(\frac{W_- - W_+}{W_+ + W_-}\right) \quad T_1 = \frac{1}{W_+ + W_-}. \tag{2.2.18}$$

Now since the average transition rates are not directly known, it is useful to express the equilibrium magnetization as

$$M_0 = \mu N\left(\frac{e^{\mu B_o/kT} - e^{-\mu B_o/kT}}{e^{\mu B_o/kT} + e^{-\mu B_o/kT}}\right)$$

using equations 2.2.16 and 2.2.18. However, $\mu B_0/kT$ is small thus allowing M_0 to be approximated using a Taylor expansion such that

$$M_0 \simeq N\frac{\gamma^2\hbar^2 B_0}{4kT}. \tag{2.2.19}$$

Returning to M_z, the solution to equation 2.2.17 is that the difference from equilibrium $M_0 - M_z$ decays with a characteristic time known as T_1 according as

$$M_z = M_0\left(1 - e^{-t/T_1}\right). \tag{2.2.20}$$

Therefore if the magnetization is not aligned with B_0, possibly as a result of an externally applied B_1 pulse, the system of protons transfers its energy to the material as heat and M_z eventually attains its equilibrium value M_0 – this process is called spin-lattice relaxation since the arrangement of molecules is often loosely referred to as the 'lattice' even if the molecules do not form a regular array but move about freely in a liquid. Now T_1 depends on transitions between spin states and these transitions are mediated by molecular B_1 fields fluctuating at angular frequency $\omega_0 = -\gamma B_0$. Therefore T_1 should be proportional to the value of the spectral density $J(\omega)$ at ω_0 [18, pg 31] and is thus a function of the externally applied field B_0 [31, ch 4] as well as the material properties; some practical values can be found in table 2.6.

2.2.2.3 The Origin of T_2

Having seen the effect of thermal interactions on M_z, we turn our attention to their influence over transverse magnetization. Now the considerations of the previous section are of no use here since M_{xy} is energetically neutral with respect to B_0 and there is usually[10] no appreciable exchange of energy with the surrounding material. However, low frequency thermal fluctuations in B_z, due to molecular motion as described in section 2.2.2.1, produce a succession of random shifts to the precession frequency, making it either faster or slower than ω_0, and thus causing the transverse magnetization M_{xy} to exhibit small random phase changes slightly modifying its deterministic precession. These fluctuations are local to each proton such that conceptually dividing the ensemble into smaller parts, but not down to individual protons, reveals that each part experiences its own independent random phase walk. The result is that, over time, the individual contributions to M_{xy} dephase and eventually the absolute value $\left|M_{xy}\right|$ relaxes to zero quite apart from any spin-lattice interaction. Moreover, the dephasing of magnetic moments, also called spin-spin relaxation, is irreversible since it is caused by random thermal fluctuations.

Although spin-spin relaxation cannot be reversed, the individual magnetic moments are conserved and eventually the system settles such that there is a small average alignment with B_0 as predicted by equation 2.2.20. At this point a B_1 pulse can once more flip magnetization so that it undergoes precession and spin-spin relaxation. Thus while the re-growth of M_z does not reverse dephasing, alignment along z causes previous transverse phase differences to become irrelevant. Since the individual proton magnetic moments are conserved, spin-spin relaxation cannot cause transverse magnetization to disappear more slowly than spin-lattice relaxation causes M_z to re-grow. Therefore, provided spin-spin relaxation is at work, $M_0 \geq \sqrt{M_{xy}^2 + M_z^2}$ where the magnetization is equal to M_0 only in equilibrium when $M_z = M_0$ or immediately after a flip from equilibrium.

Since M_{xy} depends on the precise phase of each of its contributors, the actual time course of $\left|M_{xy}\right|$ may be quite complicated [18, pg 22]. However, since the phase spread increases as time goes on, spin-spin relaxation may be approximated with an exponential decay $\left|M'_{xy}(t)\right| = \left|M'_{xy}(0)\right| e^{-t/T_2}$ allowing us to write the differential equations

$$\frac{d}{dt}M'_x = -\frac{1}{T_2}M'_x, \quad \frac{d}{dt}M'_y = -\frac{1}{T_2}M'_y. \tag{2.2.21}$$

where conservation of magnetic moment ensures that $T_2 \leq T_1$. Although this model is fairly accurate for typical experimental behaviour in liquids (see table 2.7 for some values) and is used throughout the NMR and MRI literature, many materials, such as citrate [137], demonstrate non-exponential spin-spin relaxation.

[10] To see situations where there *is* appreciable energy exchange, see Slichter [122, pg 34 and ch 6].

Tissue Material	T_2 (ms)
cerebrospinal fluid (CSF)	~ 2000
blood (venus)	50
brain grey matter	100
brain white matter	90
skelatal muscle	50
lipids (fat)	80

Table 2.7: Approximate T_2 values at 1.5 T [8, pg 961]

2.2.2.4 Phenomenological Bloch Equations

We now modify the predicted motion of a proton ensemble's magnetization vector to include both spin-spin and spin-lattice relaxation. Since equations 2.2.17 and 2.2.21 are independent of externally applied B_1 fields, they apply in both the laboratory and rotating frames and may be incorporated into equation 2.2.7 such that

$$\frac{d}{dt}\begin{bmatrix} M'_x \\ M'_y \\ M'_z \end{bmatrix} = \begin{bmatrix} -\frac{1}{T_2} & -\Delta\omega & \omega_{1y} & 0 \\ \Delta\omega & -\frac{1}{T_2} & -\omega_{1x} & 0 \\ -\omega_{1y} & \omega_{1x} & -\frac{1}{T_1} & \frac{1}{T_1} \end{bmatrix} \begin{bmatrix} M'_x \\ M'_y \\ M'_z \\ M_0 \end{bmatrix}. \tag{2.2.22}$$

where the rows in this matrix generate the Bloch equations [10, 11] describing the magnetization vector's motion. Because of the approximations required to write equation 2.2.21, these equations are 'phenomenological' in that they describe the typical behaviour but may not capture the intricacies of a particular situation. Now since T_1 and T_2 take into account the thermal field fluctuations, the terms ω_{1x} and ω_{1y} arise entirely from an externally applied B_1 field and not the microscopic field. Therefore, unless otherwise noted, any further mention of the B_1 field shall refer only to the externally applied field and not the thermally fluctuating microscopic field.

On the other hand, $\Delta\omega$ arises not only from the externally applied B_0 but also from the average field resulting from the material's bulk magnetic susceptibility and the precise local field at a particular position in a molecule produced by the motion of electrons within that molecule. This local molecular field produces a "chemical shift" in $\Delta\omega$ depending on the chemical structure in which a proton is embedded. These shifts are static since the magnetic moments associated with the electrons remain in equilibrium and are not perturbed by external B_1 fields tuned to resonate with the protons.

This modified equation of motion (equation 2.2.22) still describes precession about the effective magnetic field B'_1 but now unperturbed magnetization re-aligns at a rate $\frac{1}{T_1}$ to form an equilibrium z-magnetization M_0 while M_{xy} decays to zero at a faster rate $\frac{1}{T_2}$. In the absence of an external B_1 pulse, $\omega_{1x} = \omega_{1y} = 0$ and the solution

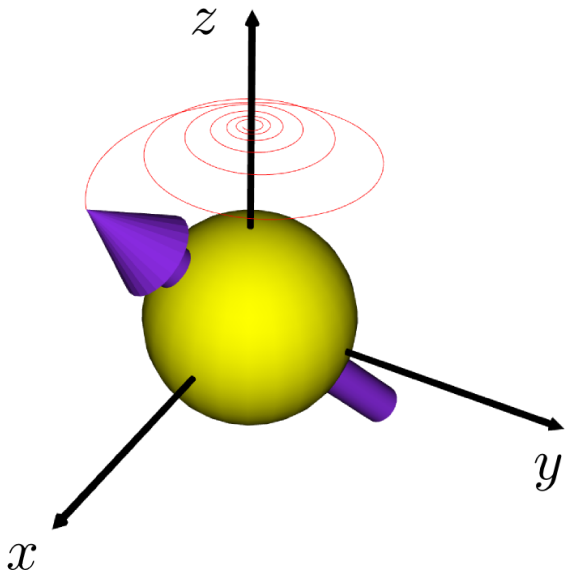

Figure 2.2: As seen from the laboratory frame, equation 2.2.23 shows that the bulk magnetization (arrow) for a certain ensemble (sphere) precesses clock-wise about the z-axis as it slowly relaxes and aligns with that same axis. The path traversed by the arrow's tip is traced.

$$\begin{aligned} M'_x &= M_0 \sin(\alpha)\cos(\theta(t))e^{-t/T_2} \\ M'_y &= M_0 \sin(\alpha)\sin(\theta(t))e^{-t/T_2} \\ M'_{xy} &= M'_x + iM'_y = M_0 \sin(\alpha)e^{-t/T_2}e^{i\theta(t)} \\ M'_z &= M_0\left(1-(1-\cos(\alpha))\,e^{-t/T_1}\right) \\ \theta(t) &= \int_0^t \Delta\omega(\tau)d\tau + \psi \end{aligned} \tag{2.2.23}$$

is visualized in figure 2.2. Moreover, when a B_1 pulse has a duration much shorter than T_2, equation 2.2.8 still applies.

Although finding a general analytical solution to equation 2.2.22 is quite difficult, a numerical solution may be sought using the algorithm

$$\begin{bmatrix} M'_x \\ M'_y \\ M'_z \end{bmatrix}^{j+1} = \Delta t \begin{bmatrix} -\frac{1}{T_2} & -\Delta\omega & \omega_{1y} & 0 \\ \Delta\omega & -\frac{1}{T_2} & -\omega_{1x} & 0 \\ -\omega_{1y} & \omega_{1x} & -\frac{1}{T_1} & \frac{1}{T_1} \end{bmatrix} \begin{bmatrix} M'_x \\ M'_y \\ M'_z \\ M_0 \end{bmatrix}^{j} + \begin{bmatrix} M'_x \\ M'_y \\ M'_z \end{bmatrix}^{j} \tag{2.2.24}$$

where Δt is the time step, M_0 is the constant equilibrium magnetization, and j denotes the magnetization at time $j\Delta t$. To reduce numerical error, Δt must be chosen such that the small change to the magnetization vector during each step is much smaller than M_0.

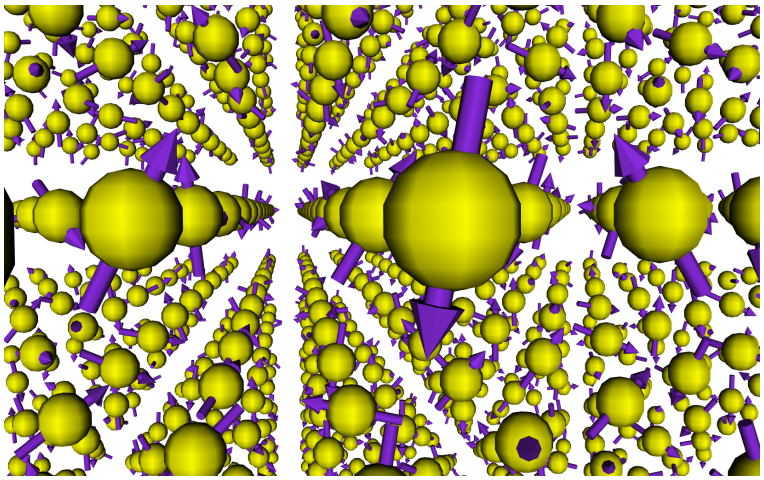

Figure 2.3: Since an isochromat is an ensemble of protons with a single resonant frequency, we can imagine a regular lattice of isochromats even though molecules in a liquid have no regular arrangement.

2.2.3 Echoes and the Free Induction Decay

Thus far we have considered a proton ensemble at a specific position with a single resonant frequency. However, as shown in figure 2.3, we can consider a distribution of proton ensembles where each ensemble has its own magnetization vector and parameters M_0, T_1, T_2, $\Delta\omega$, ω_{1x}, and ω_{1y} – proton ensembles are usually referred to as isochromats in reference to their independent resonant frequencies. Most of the differences between isochromats arise primarily from material properties, but the resonant frequencies are also influenced by physical location in a spatially inhomogeneous B_z field. Regardless of cause, the spread of resonant frequency causes deterministic dephasing between isochromats unlike the random dephasing resulting in the spin-spin relaxation of a single isochromat.

After a B_1 pulse, equilibrium isochromats flipped into the transverse plane rapidly dephase with respect to one another, as shown in figure 2.4. Now just as spin-spin relaxation can cause $\left|M_{xy}\right|$ to be a complicated function of time for a single isochromat, dephasing between isochromats can make the total transverse magnetization's disappearance complicated as well. However, as in section 2.2.2.3, this complexity is often masked by assuming that the total transverse magnetization takes the form $\left|M_{Txy}\right| = \left|M_{Txy}(0)\right| e^{-t/T_2^*}$ where T_2^* expresses the time it takes for transverse magnetization to dephase both by reversible and irreversible processes. By assuming that dephasing of any kind produces an exponential decay we can write $1/T_2^* = (1/T_2) + (1/T_2')$ where T_2' is a time constant related only to dephasing between isochromats and T_2 is the spin-spin relaxation time from above. Although this greatly simplifies theoretical calculations and has some validity in many experimental situations, it is a very coarse approximation and may break down depending on the materials used and the precise geometry of the field inhomogeneities. Using this approximation, the transverse magnetization evolves according as

$$M_{Tx,y}(t) = M_{Tx,y}(0)e^{j\omega_0 t}e^{-t/T_2^*}. \tag{2.2.25}$$

Since the dephasing between isochromats is deterministic, it can be reversed to form an echo. As shown in figure 2.5, suppose the isochromats are initially aligned with B_0 and then a 90° pulse flips them into the transverse plane where each precesses at its own frequency – this 90° pulse is often called an excitation pulse because it changes relaxed magnetization into precessing magnetization. Directly after this pulse the isochromats produce a free induction decay and each isochromat accumulates phase proportional to its own precession frequency. Then at a time τ, a 180° B_1 pulse – known as an inversion pulse – flips all the transverse magnetization such that an isochromat with phase $\theta_{a-} = \tau\Delta\omega_a$ before inversion acquires a phase $\theta_{a+} = -\tau\Delta\omega_a$ afterwards. Therefore at time 2τ, every isochromat returns to its original phase and briefly contributes to a bulk alignment of nuclear magnetic moment known as a spin-echo [40]. Although the isochomats re-phase with respect to one another, each isochromat has experienced spin-spin relaxation during the time 2τ so the echo magnitude is reduced by a factor $e^{-2\tau/T_2}$ with respect to the initial transverse magnetization.

Although in the case of spin echoes the spread in $\Delta\omega$ is beyond our control, arising from susceptibility effects, chemical shifts, or magnet imperfections; we can, as shown in figure 2.6, intentionally introduce a B_z field gradient along the x direction such that $B_z = B_0 + G_x x$ and $\Delta\omega = -\gamma G_x x$ where $G_x = \frac{dB_Z}{dx}$. If this gradient is applied for a time τ then the phase accumulated in the rotating frame by an isochromat at position x is $-\gamma G_x x\tau$. Then, by reversing the gradient such that $B_z = B_0 - G_x x$ for a subsequent time τ, the isochromats re-phase at time 2τ forming a gradient echo. Unlike a spin echo, however, phases accumulated due to B_0 field inhomogeneity and chemical shift are not re-phased and the gradient echo is weighted by a factor $e^{-2\tau/T_2^*}$ rather than $e^{-2\tau/T_2}$. In general, gradient echoes can be formed more quickly than spin echoes since phasing and dephasing may be accelerated by employing stronger gradients. However, these gradients must be super-imposed over a very homogeneous B_0 field since otherwise T_2^* is short and the gradient echoes are weak.

2.2.4 Signal Detection

Having seen how externally applied B_1 fields can manipulate the isochromats of nuclear magnetization, we now turn our attention to detecting these isochromats. Each isochromat is a magnetic moment which, when changing with time, can both induce a voltage in a length of wire by Faraday's Law and also produce freely propagating electromagnetic waves. Thus isochromats precessing in the transverse plane are of special importance because they produce the NMR signal – the so-called "free induction decay" or FID.

We follow Hoult and Ginsberg [48] and use the model shown in figure 2.7 to gain further insight. In this model an isochromat precessing in the transverse plane is represented by two orthogonal current

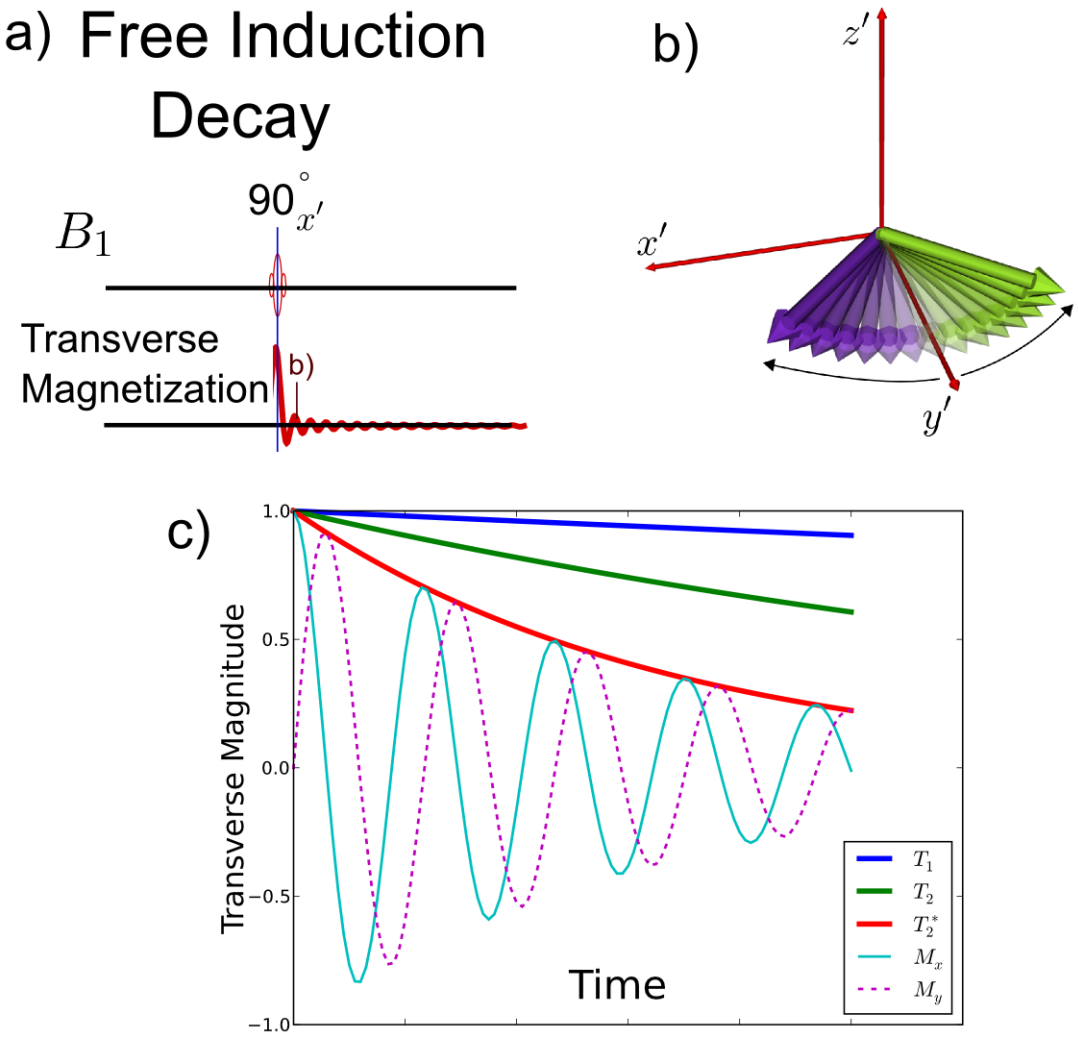

Figure 2.4: In a) we see that transverse magnetization is excited after a B_1 pulse but then rapidly decays. Part b) shows how the isochromats at the time labelled in part a) appear in the rotating frame; this dephasing causes the decay. In c) the M_x and M_y components of the transverse magnetization during the FID are shown in detail under the T_2^* decay of equation 2.2.25; the decay rate relative to the precession frequency has been exaggerated so that both effects can be clearly seen.

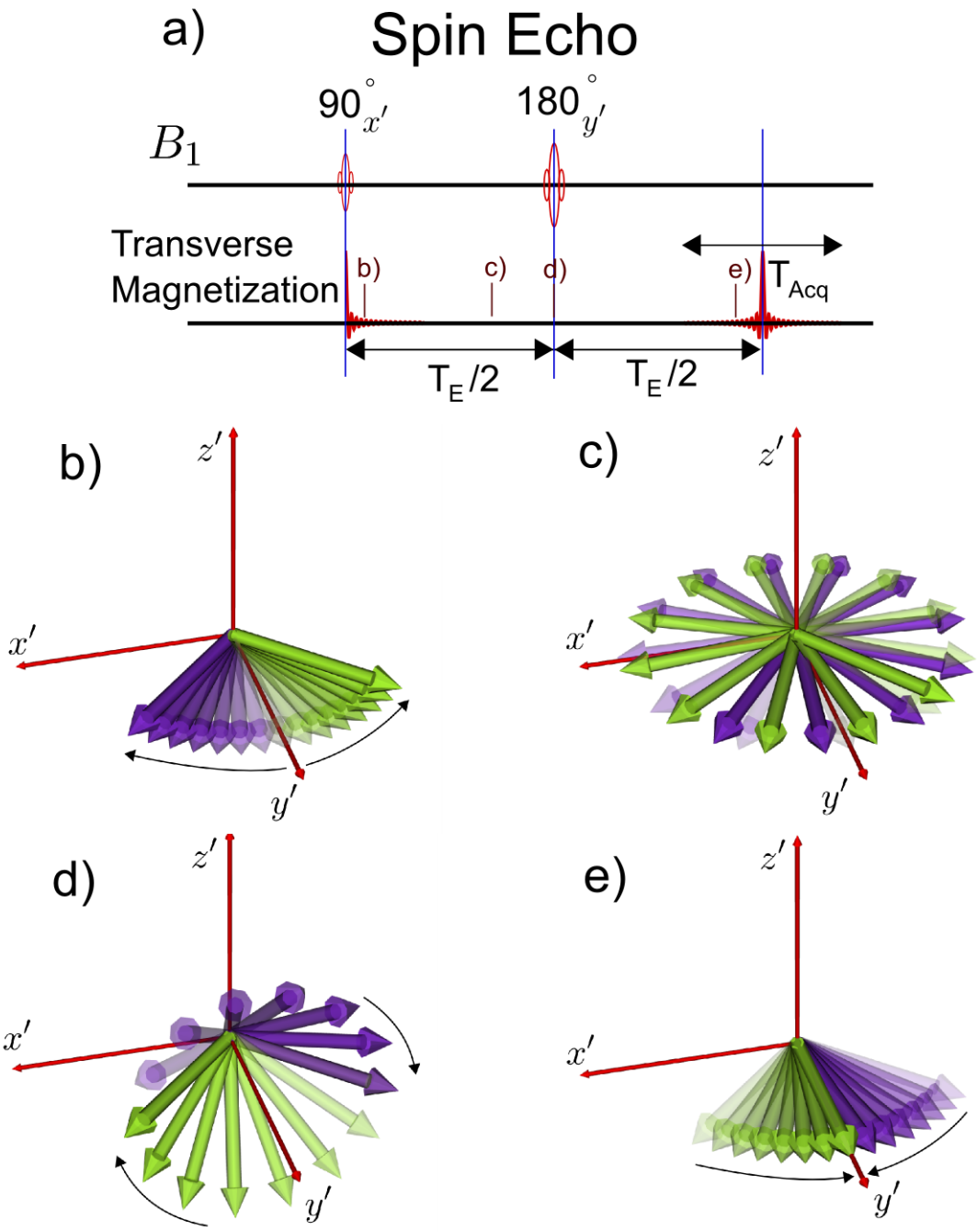

Figure 2.5: In a) we see a schematic of a spin-echo sequence where each of the four time points (b,c,d,e) has a corresponding isochromat schematic. In b), the newly flipped isochromats begin to dephase immediately after the 90° pulse. Over time the isochromats evenly distribute themselves and the average transverse magnetization is zero c). In d) the path of only two isochromats is seen during the 180° pulse about y'; before the pulse the isochromat starting on the left had a phase $-\psi$ while the other isochromat had a phase ψ such that the inversion pulse causes them to switch positions. As shown in e), the isochromats finally re-phase at time T_E causing a spin-echo.

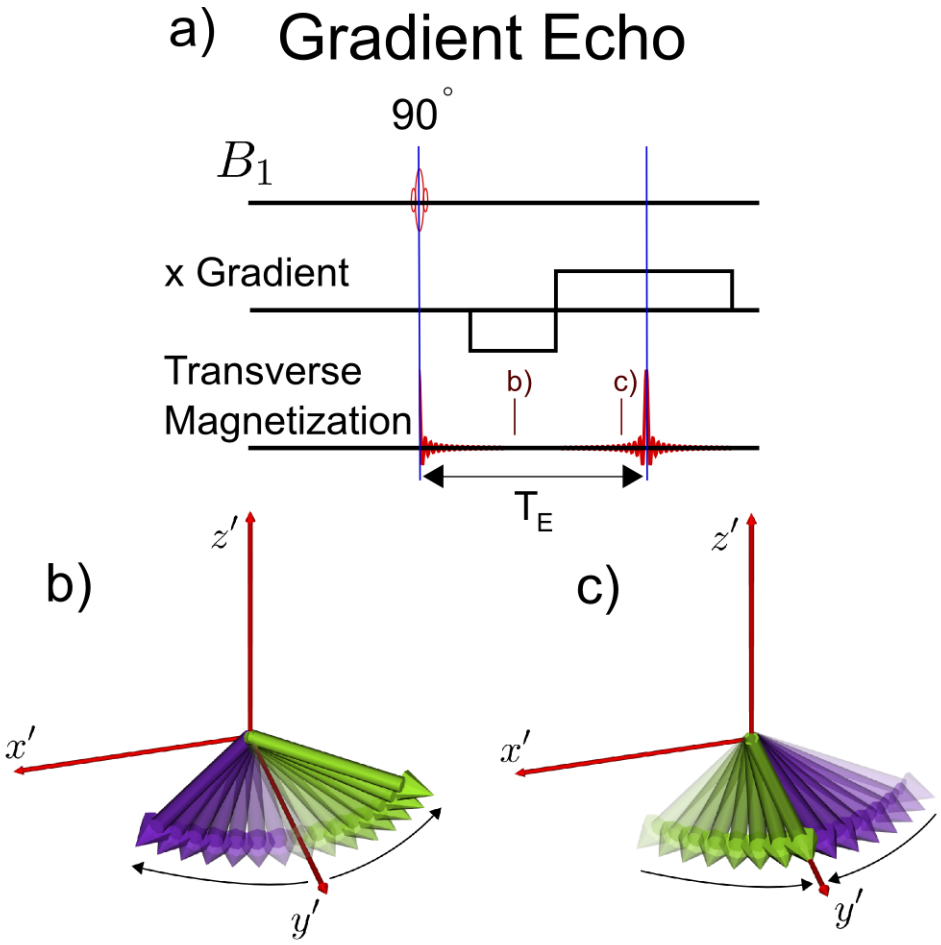

Figure 2.6: Part a) shows a simple gradient-echo schematic indicating the times at which the isochromat schematics b) and c) take place. The negative lobe of the gradient causes isochromats to dephase b) while the positive lobe causes them to re-phase c), form an echo, and dephase once more.

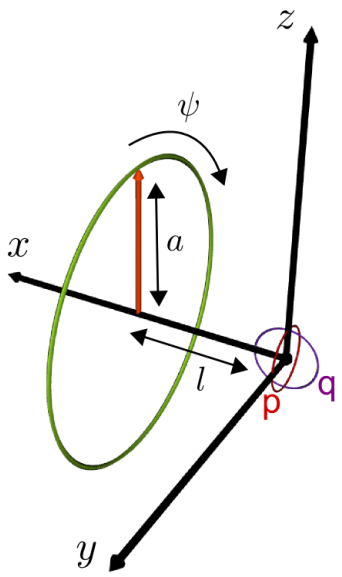

Figure 2.7: A model for signal reception. Two infinitesimal rings of oscillating current are placed at the origin and oriented such that one is about the x-axis and the other about the y-axis. A wire ring of radius a is placed a distance l along the x-axis and the voltage induced in it is the detected NMR signal.

loops p and q in which equal currents oscillate at the same frequency but are separated in phase by $\pi/2$. The total magnetic moment $\mathbf{m}$ is merely the vector sum of the oscillating magnetic moments from the two loops

$$\mathbf{m} = \mathbf{m}_p + \mathbf{m}_q$$
$$m = m_0 e^{i\omega t}$$
$$\mathbf{m}_p = \mathrm{Re}\,(m)\,\hat{\mathbf{x}} \quad \mathbf{m}_q = \mathrm{Im}\,(m)\,\hat{\mathbf{y}}$$

where complex numbers are a mathematical convenience; that is, we may perform computations with $e^{i\omega t}$ with the understanding that the real and imaginary parts correspond to the physical x and y components of the magnetic moment respectively. Note that in this calculation it is assumed that the magnitude of the transverse magnetization m_0 changes very slowly compared to the precession frequency – a good approximation since echoes and free induction decays last tens to hundreds of milliseconds while a period of nuclear precession takes only a fraction of a microsecond.

The electromagnetic analysis of an oscillating magnetic moment is standard fare in electrodynamics texts [52, 37, 91] which state that the vector potential at a point $\mathbf{r}$ due to a magnetic moment at the origin is

$$\boldsymbol{A} = -\frac{\mu_0}{4\pi r^3}\left(\mathbf{r} \times \left([\mathbf{m}] + \frac{r}{c}\frac{\partial}{\partial t}[\mathbf{m}]\right)\right)$$

where the square brackets indicate that the magnetic moment is evaluated at the retarded time $t \rightarrow t - r/c$ where c is the speed of light in a vacuum. Since there are no free charges in this situation, $\nabla\Theta = 0$ and thus

the vector potential and electric field (equation 2.1.8) associated with $\mathbf{m}_p$ are

$$\mathbf{A}_p = \frac{m_0\mu_0 \sin(\theta')}{4\pi r^2}\left(1 - i\frac{r}{c}\omega\right)e^{i\omega(t-r/c)}\hat{\boldsymbol{\phi}}'$$

and

$$\mathbf{E}_p = -\frac{\partial}{\partial t}\mathbf{A}_p - \nabla\Theta = -\frac{im_0\mu_0 \sin(\theta')\omega}{4\pi r^2}\left(1 + i\frac{r\omega}{c}\right)e^{i\omega(t-r/c)}\hat{\boldsymbol{\phi}}'$$

where the real parts are the physical quantities, θ' is the angle from the x-axis, and ϕ' is the rotation angle about it – analogous to the usual spherical polar coordinates where θ and ϕ are related to the z-axis. Integrating the time averaged value of $\mathbf{S}_p = \frac{\mathrm{Re}(\mathbf{E}_p)\cdot\mathrm{Re}(\mathbf{E}_p)}{\mu_o c}$ over a sphere centred on the magnetic moment but with radius in the far field ($r \gg \frac{c}{\omega}$) gives the well known power radiated by electromagnetic waves emanating from the oscillating magnetic moment. Since our model has two oscillating magnetic moments, the total power escaping as radiation is just twice this value

$$P_{rad} = \frac{\mu_0 m_0^2 \omega^4}{6\pi c^3}.$$

Now, as shown in figure 2.7, we use a wire ring of radius a about the x-axis placed a distance l from the magnetic moment as a simple model for a signal reception coil. The voltage induced in this ring

$$V_{ring} = \frac{\partial}{\partial t}\int_{ring}\mathbf{A}\cdot d\mathbf{l} = -\int_0^{2\pi} E_p\, a\, d\psi$$

$$V_{ring} = i\frac{m_0\mu_0 a\, \sin(\alpha)\omega}{2f^2}\left(1 + i\frac{f\omega}{c}\right)e^{i\omega(t-f/c)} \tag{2.2.26}$$

is computed using equation 2.1.12 where $f^2 = a^2 + l^2$, $f\,\sin(\alpha) = a$, and the voltage is entirely due to $\mathbf{m}_p$ since the electric field arising from $\mathbf{m}_q$ is everywhere perpendicular to the wire ring. Still following Hoult and Ginsberg [48], provided the ring is placed in the near field where $f \ll \frac{c}{\omega}$ and V_{ring} can be approximated with a Taylor expansion in f

$$\begin{aligned} V_{ring} &\simeq \tfrac{\mu_0 a^2\omega}{2f^3} m_0\left(1 + \tfrac{f^2\omega^2}{2c^2}\right)e^{i(\omega t+\pi/2)} \simeq \tfrac{\mu_0 a^2}{2f^3}\tfrac{N\gamma\hbar^2 dV}{4kT}\left(\omega^2 + \tfrac{f^2\omega^4}{2c^2}\right)e^{i(\omega t+\pi/2)} \\ \text{Signal} = \mathrm{Re}(V_{ring}) &\simeq \tfrac{\mu_0 a^2\omega}{2\left(a^2+l^2\right)^{3/2}} m_0\left(1 + \tfrac{(a^2+l^2)\omega^2}{2c^2}\right)\sin(\omega t) \simeq \tfrac{\mu_0 a^2}{2\left(a^2+l^2\right)^{3/2}}\tfrac{N\gamma\hbar^2 dV}{4kT}\left(\omega^2 + \tfrac{(a^2+l^2)\omega^4}{2c^2}\right)\sin(\omega t) \end{aligned} \tag{2.2.27}$$

where $m_0 \simeq N\gamma\hbar^2\omega\, dV/4kT$ in a small valume dV. By comparing equations 2.2.26 and 2.2.27, we see that the term proportional to ω^2 is entirely due to the near field while the term proportional to ω^4 is a first-order correction taking voltage due to electromagnetic waves into account. From this simple model we glean that, beyond heating the material through spin-lattice relaxation, there are two additional transfers of energy from the nuclear magnetic moment: energy is transferred to nearby conductive paths if they are present and is also

radiated as electromagnetic waves. Now since the average power P_{av} transferred to the ring is just the time average of $P = \mathrm{Re}(V_{ring})^2/R$ where R is the resistance of the ring, setting $R = \infty$ removes the conductive path and thus the detected NMR signal. Moreover there are two separate mechanisms, in the two separate terms in equation 2.2.26, by which energy is coupled to the conductive path: Faraday induction, which dominates the coupling and only removes energy from the protons when a receiving coil is present, and the slight interaction of this coil with the freely propagating electromagnetic radiation that leaves the protons with or without the coil.

Let us compare the peak values for the various energy transfers. Considering equations 2.2.3 and 2.2.20, the peak power transfer to the lattice within a small volume ΔV is (divide in half for RMS power)

$$P_{sl\,max} = \frac{M_0 B_0}{T_1}\Delta V$$

while the maximum powers transferred to the ring and radiated to the far field are

$$P_{ring\,max} \simeq \frac{\mu_o^2 M_0^2 a^4 \omega^2}{8R\left(a^2+l^2\right)^3}(\Delta V)^2\left(1+\frac{\left(a^2+l^2\right)\omega^2}{c^2}\right)$$

and

$$P_{rad\,max} = \frac{\mu_o M_0^2 \omega^4}{6\pi c^3}(\Delta V)^2$$

where M_0 is computed from equation 2.2.19 and $\omega = \gamma B_0$. For protons in one millilitre of water at temperature 37°C with $T_1 \sim 500$ ms in a magnetic field of 3 T near a wire ring with radius $a = 10$ cm and resistance of 1 Ω placed such that $l = 10$ cm, we have that $M_0\Delta V = 9.3\times10^{-9}$ J/T, $\omega/2\pi = 127.74$ MHz and the respective powers are $P_{sl\,max} = 55.7\times10^{-9}$ W, $P_{ring\,max} \simeq 137(1+0.14)\times10^{-12}$ W, and $P_{rad\,max} = 88.4\times10^{-15}$ W. So although there is some radiation, and a signal ($\sim 18\,\mu$V) can be detected in the wire ring; both these effects are trivial compared to the transfer of energy into heat within the water. Moreover, the power transferred to the wire ring is primarily a result of near-field inductive coupling, rather than electromagnetic waves. The signal detection coil, which we modelled with a wire ring, is usually called an RF-coil referring to the frequency of interaction (radio frequency) rather than the reception of electromagnetic waves.

From the view point of quantum mechanics, electromagnetic waves are photons; but since the contribution of waves to the detected NMR signal is small, photons are not primarily responsible. A plausible quantum explanation is that near-field interactions are mediated by virtual photons [47, 46] which do not have the normal photon energy $E = \hbar\omega$ but rather take on other energy values as permitted by Heisenberg's uncertainty principle $\Delta E\Delta t \sim \hbar$ [114, 24, p 80, p 97]. As an indication that this is the case, consider virtual photons with uncertain energies between 0 and $\hbar\omega$ over a time $\Delta t \sim \hbar/\Delta E = 1/\omega$. If the virtual photons travel at the speed of light then in this short time they may act over a limited radius $\Delta r \sim c/\omega$ which is precisely the range of the classical near-field interaction. Despite this indication, no definitive evidence of

virtual photons giving rise to the NMR signal has been found to date; all we have is the negative evidence that freely moving photons, emitted either spontaneously or through stimulation, are not primarily responsible[11]. Thus for most practical purposes, such as the computation of signal induced in a receiving coil, it is preferable to remain within the realm of classical electrodynamics where inductive coupling is a simple matter.

2.2.5 Signal and Quadrature Phase Sensitive Detection

From the detected NMR signal voltage we wish to acquire a digital representation of the transverse magnetization components M'_x and M'_y in the rotating frame (equation 2.2.22). For the purposes of this thesis, a key component in this process is the quadrature phase sensitive detector shown in figure 2.8 which is able to recover the complex transverse magnetization M_{xy} from the real signal induced in a coil while reducing the frequency to make it amenable to digital acquisition. Note however that digital signal processing methods often sample an intermediate frequency.

Since any device sensitive to the magnetization signal with angular frequency ω_0 is also sensitive to the much larger B_1 pulses with approximately the same frequency, signal acquisition is usually restricted to times when $B_1 = 0$. In this case, equation 2.2.23 shows that the transverse magnetization of an ensemble of protons with a single resonant frequency and T_2 within a small volume dV, known as a voxel, precesses and decays as:

$$\begin{aligned} M'_{xy} &= \Im(x, y, z) e^{-t/T_2} e^{i(\theta(t)+\phi_0)} \\ M'_{xy} &= M'_x + iM'_y \end{aligned} \tag{2.2.28}$$

where ϕ_0 is the initial phase and $\Im(x, y, z)$ is the initial magnetization flipped into the transverse plane. Within every voxel there may be multiple isochromats obeying equation 2.2.28 where each isochromat is associated with an ensemble of protons experiencing a different chemical environment (chemical shift, T_1, T_2).

From equation 2.2.27 we know that the pre-amplified voltage induced in a nearby RF-coil due to this one isochromat in a voxel is

$$S = \beta \Im(x, y, z) e^{-t/T_2} \sin(\omega_0 t + \theta(t) + \phi_0)\, dV \equiv S_0 \sin(\omega_0 t + \kappa_0)$$

where β encapsulates the effects of a specific coil geometry (which is probably not a simple ring), the signal frequency dependence, and the pre-amplifier.

The first step in the quadrature phase sensitive detection process is to feed the signal, along with reference signals mentioned below, into two separate mixers. A mixer produces at its output the product

[11] The long-held belief that the NMR signal arises from coherent spontaneous emission [23] can be shown to be false since the radiated power predicted for this mechanism is exactly the radiated power predicted classically and not the signal detected in the coil [48].

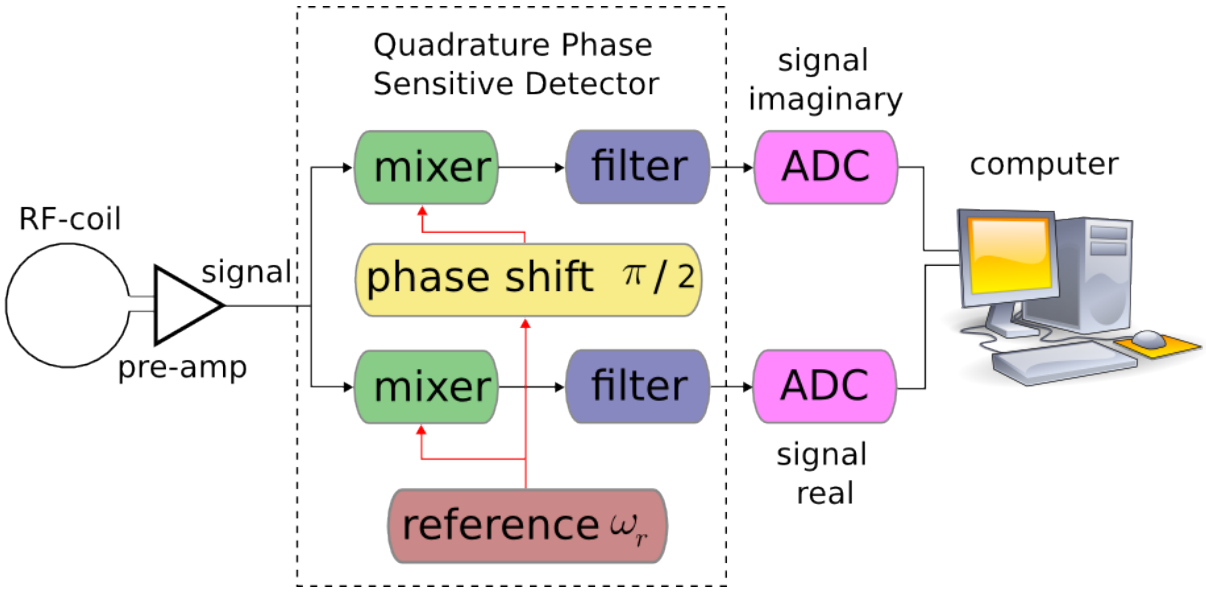

Figure 2.8: Signal from the RF-coil is amplified and sent into the quadrature phase sensitive detector to be demodulated and split into real and imaginary parts. The result is sampled by analog to digital converters (ADC) and stored in a computer. Alternatively the signal may be sampled directly after the pre-amp and the quadrature phase sensitive detector implemented in software [121].

of its inputs, so if the inputs to a mixer are the NMR signal $S = S_0 \sin(\omega_0 t + \kappa_0)$ and a reference signal $R = R_0 \sin(\omega_r t + \kappa_r)$ then the mixer output is

$$SR = \frac{1}{2} S_0 R_0 \left(\cos\left((\omega_0 - \omega_r)t + \kappa_0 - \kappa_r\right) - \cos\left((\omega_0 + \omega_r)t + \kappa_0 + \kappa_r\right)\right)$$

and after using a low-pass filter, only the low-frequency component $\frac{1}{2} S_0 R_0 \cos((\omega_0 - \omega_r)t + \kappa_0 - \kappa_r)$ remains – note that $S_0 = \beta \Im(x, y, z) e^{-t/T_2} dV$ and $\kappa_0 = \theta(t) + \phi_0$. The key to the quadrature phase sensitive detector is that there are two mixers with separate references that are $\pi/2$ out of phase

$$R_a = R_0 \sin(\omega_r t + \kappa_r), \quad R_b = -R_0 \cos(\omega_r t + \kappa_r)$$

so that after filtering, the two output signals are

$$s_a = \frac{1}{2} R_0 S_0 \cos((\omega_0 - \omega_r)\, t + \kappa), \quad s_b = \frac{1}{2} R_0 S_0 \sin((\omega_0 - \omega_r)\, t + \kappa)$$

where $\kappa = \kappa_0 - \kappa_r$. Using complex numbers, these signals are compactly represented as

$$s = s_a + i s_b = \frac{1}{2} R_0 S_0 e^{i((\omega_o - \omega_r)t + \kappa)}$$

and if we set the reference frequency and phase such that $\omega_r = \omega_0$ and $\kappa_r = \phi_0$, the signal from a single voxel after quadrature phase sensitive detection is

$$\begin{aligned} s &= \alpha \Im(x,y,z) e^{-t/T_2} e^{i\theta(t)} \\ \theta(t) &= \int_0^t \Delta\omega(\tau) d\tau + \psi \end{aligned} \tag{2.2.29}$$

where α is a constant that depends on the electronic hardware.

These output signals, which can be acquired using analog to digital converters (ADC) and stored on a computer, precisely describe the motion of both components of the transverse magnetization as given in equation 2.2.28. The quadrature phase sensitive detector has recovered the complex representation of transverse magnetization from the purely real voltage induced in the coil. For this reason, all further references to signal will refer to the complex signal as presented at the output of a quadrature phase sensitive detector. Also note that the signal from the entire sample is found using the volume integral $S = \int_{sample} sdV$.

2.3 Magnetic Resonance Imaging (MRI)

As we have seen, a distribution of precessing isochromats induces a detectable signal voltage in a nearby coil. In magnetic resonance imaging the total signal is separated into contributions from each small voxel[12] which are then mapped to the pixels of an image. To distinguish the signal contributions, they are encoded with spatial information by the external application of a pulsed sequence of magnetic field gradients. This section begins by introducing basic imaging pulse sequences [18, 8, 73, 32], proceeds to describe the main MRI system components, and ends by describing some limitations to image resolution.

2.3.1 Frequency Encoding

The signal's frequency was historically the first [69], and is conceptually the simplest, parameter to encode with voxel position. Suppose we take two jugs of water, as shown in figure 2.9a, and place them in a strong B_z field of magnitude B_o to which the nuclear magnetization aligns. By using a 90° RF-pulse we flip the magnetization into the transverse plane where it precesses at the Larmor frequency $\omega_o = -\gamma B_o$. Then an x-directed spatial gradient G_x on the B_z field is imposed such that $B_z = B_o + xG_x$ and the total externally applied field strength is

$$|\mathbf{B}| = \sqrt{(B_o + xG_x)^2 + (\Delta B_x)^2 + \left(\Delta B_y\right)^2} = B_o \sqrt{1 + 2\frac{xG_x}{B_o} + \left(\frac{xG_x}{B_o}\right)^2 + \left(\frac{\Delta B_x}{B_o}\right)^2 + \left(\frac{\Delta B_y}{B_o}\right)^2}$$

where ΔB_x and ΔB_y are the spatially dependent x and y fields that accompany G_x according to Maxwell's equations (see section 2.1). Provided B_o is large compared to ΔB_x and ΔB_y, the Larmor frequency becomes a simple function $\omega \simeq -\gamma (B_o + xG_x)$ mapping precession frequency to position along the x-axis. Since B_o is usually several teslas while xG_x is on the order of milliteslas, the approximation holds. For this reason,

[12] A volume element as in section 2.2.5.

whenever field gradients are mentioned, at least in this section, we consider only the spatial variations in B_z and ignore the associated transverse fields since their influence on the Larmor frequency is small.

If, while the gradient is imposed, an echo signal is acquired over a time T_{Acq} as shown in figure 2.9b, the signal from a voxel can be found from equation 2.2.29 by setting $\theta(t) = \int_0^t \Delta\omega(\tau)d\tau + \psi = -\gamma G_x xt + \phi$ since the gradient is constant during signal acquisition. Ignoring relaxation ($T_E \ll T_2$) and measuring the time from T_E, this signal is

$$s = \alpha\Im(x, y, z)e^{i\left(-\gamma x G_x(t+T_{Acq}/2)+\phi\right)}.$$

Note that during the first half of the signal acquisition a magnetization phase $-\gamma G_x x T_{Acq}/2$ accumulates which is cancelled by the phase accumulated during the pre-phasing gradient lobe which sets $\phi = \gamma G_x x T_{Acq}/2$. For a gradient-echo image, the pre-phasing lobe must be negative and placed between the 90° pulse and signal acquisition; however, for a spin-echo image, the pre-phasing lobe may be positive and placed before the 180° pulse as shown in the figure – the 180° pulse changes the sign of the phase. In either case the result is an echo at time T_E and the signal is

$$s = \alpha\Im(x, y, z)e^{-i\gamma x G_x t}$$

where $\Im(x, y, z)$ is just the flipped equilibrium magnetization $M_o(x, y)$ which depends on the local density of hydrogen atoms. However, since more sophisticated pulse sequences can make $\Im(x, y)$ depend on other tissue properties, such as T_1, we do not replace it with $M_o(x, y)$ in the following calculations.

Now considering the whole material volume, the total acquired signal is

$$S(t) = \alpha \int_V \Im(x, y, z)e^{-i\gamma x G_x t}dV$$

and the inverse Fourier transform yields

$$I(x') = \frac{\alpha}{2\pi}\int_{-\infty}^{\infty}\left(\iiint \Im(x, y, z)e^{-i\gamma x G_x t}dxdydz\right)e^{i\gamma x' G_x t}dt$$
$$I(x) = \frac{\alpha\gamma G_x}{2\pi}\iint \Im(x, y, z)dydz$$
$$I(x) \propto \iint \Im(x, y, z)dydz.$$

Therefore $I(x)$ is a one-dimensional image of the function $\Im(x, y, z)$.

An important limitation of frequency encoding arises from the chemical shifts (slight differences in resonant frequency) between biological materials, particularly between fat and water. During the imaging sequence this difference shifts the image of fat with respect to the image of water. The actual image acquired will therefore be composed of the water image added to the shifted fat image.

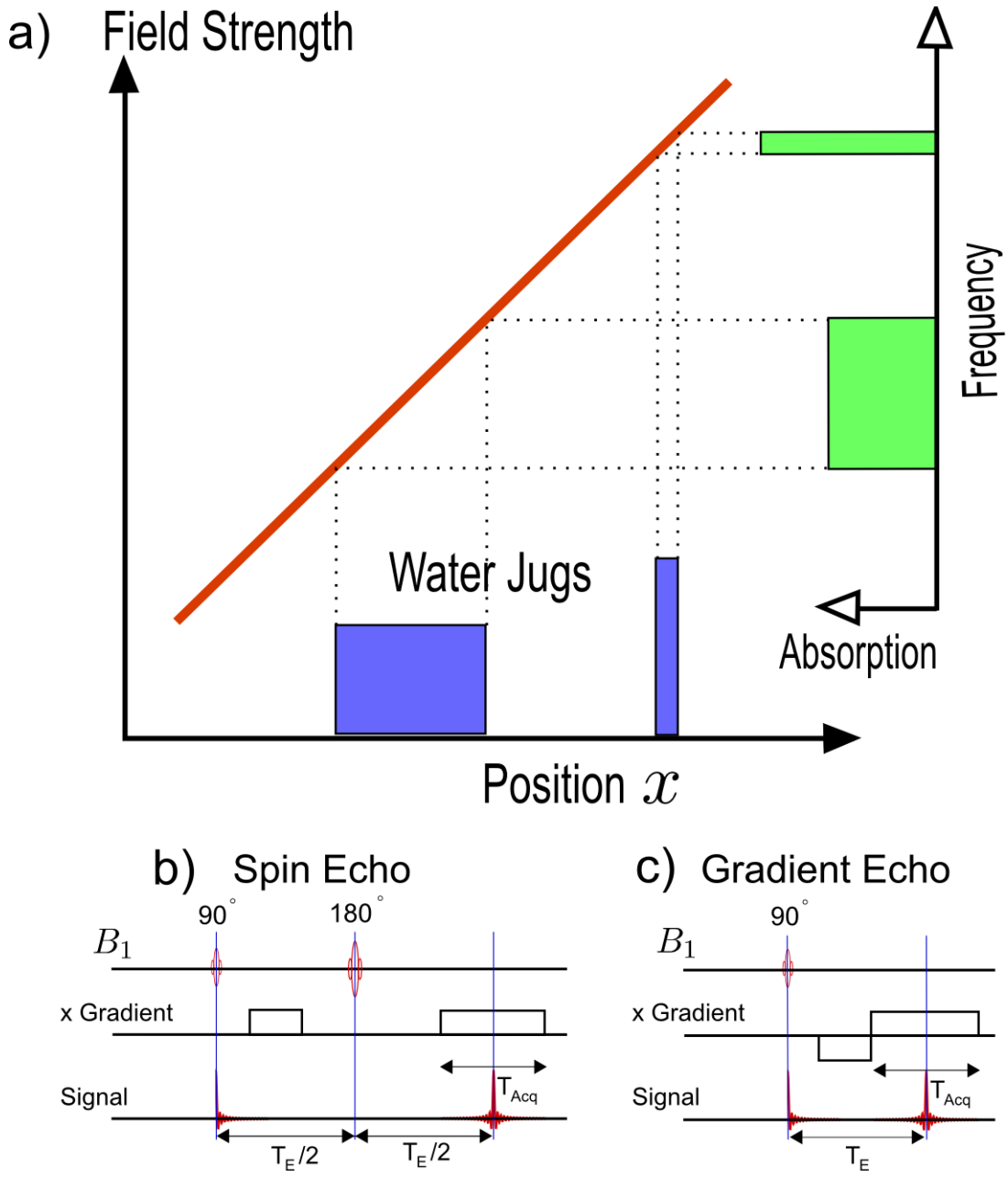

Figure 2.9: In a) two jugs of water are placed in a field gradient and the real, or absorption, part of the Fourier spectrum forms their one dimensional image. In b) and c) pulse sequences that may be used to produce this image are shown for the spin- and gradient-echo cases.

2.3.2 Slice Selection

Using a one dimensional projection at successive angles, a complete three dimensional image of the initially flipped magnetization distribution $\Im(x, y, z)$ could be re-constructed using the Radon transform for back-projection. However in practice this is rarely done; instead separate techniques are used to localize signal for each dimension. As shown in figure 2.10, one of these techniques is to confine the signal source to a certain slice of material by flipping only the magnetization in that slice. If a slice of thickness Δz in the z-direction is selected, the frequency encoding described in the last section produces a one dimensional image of only the selected slice and thus brings us one step closer to a three dimensional image.

Slice selection further exploits the linear relationship between resonant frequency and magnetic field strength by applying a field gradient during the 90° excitation pulse. This confines on-resonance magnetization to a certain plane and ensures that magnetization far from that plane is not appreciably influenced by the excitation pulse. By changing the centre frequency $\omega_r/(2\pi)$ (see equation 2.2.5) of the excitation pulse, the on-resonance plane can be placed anywhere along the applied field gradient. Once the slice has been selected, any further RF pulses (B_1 pulses are also referred to as "RF" due to the radio frequencies involved) also require a concurrent gradient to keep magnetization outside the slice from becoming excited; this includes the 180° inversion pulse used to create a spin echo. From section 2.2.1, off-resonance magnetization rotates about the vector sum of $\mathbf{B_1'}$ and $\mathbf{B_z'} = -\frac{1}{\gamma}\Delta\omega\hat{\mathbf{z}}$ where $\Delta\omega = \omega_0 - \gamma G_z z - \omega_r$ grows with distance from the on-resonance plane. Thus magnetization near the on-resonance plane is also flipped by the excitation pulse but not by the same rotation axis or angle. Thus although a slice with some finite thickness is excited, the magnitude and phase of transverse magnetization has a varying profile over that slice.

As shown in figure 2.11, the RF pulse waveform defines the slice profile. A desirable slice profile produces constant transverse magnetization with constant phase within the slice but produces no transverse magnetization outside. If we assume, inaccurately, that the Bloch equations provide a linear relationship between magnetization flip angle and the Fourier coefficients of the RF waveform, then an ideal RF pulse has a rectangular spectrum and thus a waveform shaped as $\text{sinc}(t) = \frac{\sin(t)}{t}$. The figure shows that if the flip angle remains small and only the magnitude of the transverse magentization is considered, a fairly rectangular slice profile is achieved. However, the phase profile, while representing merely a delay for small flip angles, becomes progressively non-linear as the flip angle increases. The reason for this complex behaviour is that the Bloch equations are inherently non-linear – notice that as the RF amplitude increases the flip profile does not grow linearly. The non-linearity is caused by magnetization with a particular resonant frequency responding to a narrow bandwidth of the RF-pulse rather than a single frequency component; thus to produce higher quality slice profiles, the non-linear nature of the Bloch equations must be taken into account. Much work has been done on this subject and has resulted in specialized techniques for the design of slice-selective pulses. An example is the Shinnar-Le Roux method [94, 51] where information about acceptable variations

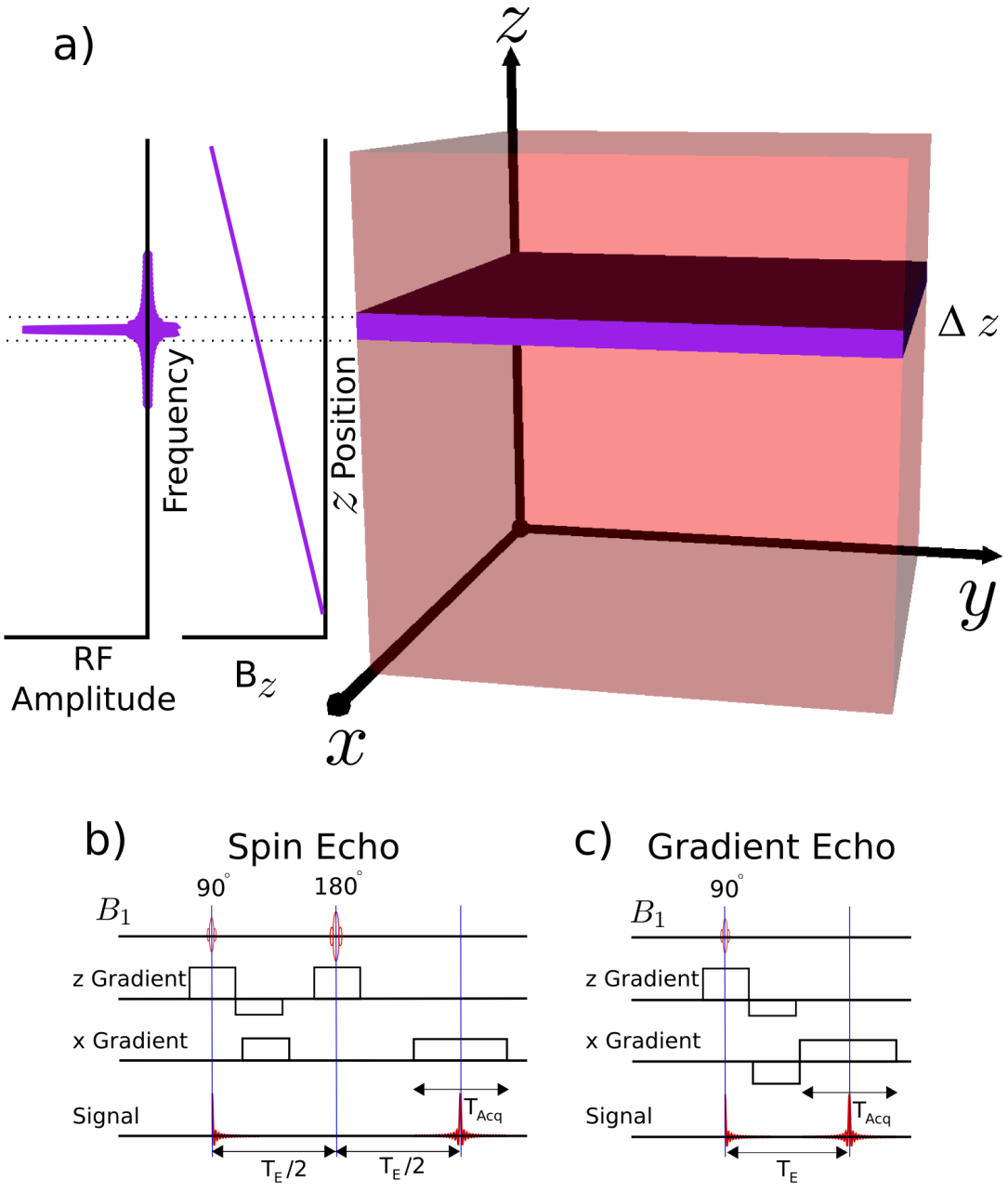

Figure 2.10: Part a) shows a slice of thickness Δz selected by the application of a 90° RF-pulse applied with a field gradient. Shifting the centre frequency of the pulse changes the z-position of the selected slice. Parts b) and c) show the required modifications to the pulse sequences in figure 2.9. As shown, the slice selective z-gradient needs a re-phasing lobe when used with a 90° pulse just as the x-gradient requires a pre-phasing lobe.

of magnetization over the slice can be specified and used to design the selective pulse.

2.3.3 Phase Encoding

With the signal isolated to a particular slice Δz and its frequency mapped to x-position with G_x, the signal's phase can also be encoded with spatial information in the y-direction [73, pg 224-227]. This extra information allows a two dimensional image of the slice to be reconstructed and a fully three dimensional image can be formed from successive slices.

Figure 2.12 shows a schematic of the pulse sequences already considered but now repeated N times and modified to include a y-gradient which has a different amplitude each time. During the time T_{pe} over which each y-gradient is applied, the y-gradient introduces a unique phase to the signal acquired in that repetition. Ignoring relaxation and measuring time from T_E, the signal acquired on repetition j is:

$$S_j(t) = \alpha \Delta z \iint_{slice} \Im(x,y) e^{-i\gamma y \int_0^{T_{pe}} p_j G_{ymax}(\tau)d\tau} e^{i\gamma G_x x T_{acq}/2} e^{-i\gamma x \int_{-T_{Acq}/2}^{t} G_x(\tau)d\tau} dxdy \tag{2.3.1}$$

where $p_j = 2\frac{j}{N-1} - 1$ runs from -1 to 1 as the repetition number increases from zero, G_{ymax} is the maximum y-gradient magnitude applied during the sequence, and $\gamma G_x x T_{acq}/2$ is the phase introduced by the pre-phasing lobe of the x-gradient. However, assuming perfectly square gradient pulses, the signal becomes

$$S_j(t) = \alpha \iint_{slice} \Im(x,y,z) e^{-i\gamma p_j G_{ymax} T_{pe} y} e^{-i\gamma G_x t x} dxdydz$$

which is immediately recognizable as the two-dimensional Fourier transform of the initially flipped magnetization distribution $\Im(x,y,z)$ over the slice. After all the signals have been acquired, a two-dimensional inverse Fourier transform may be used to reconstruct an image. Ignoring the discrete nature of the N repetitions and signal sampling with respect to time, we assume a continuous variable p so that the inverse Fourier transform yields

$$\begin{aligned} I(x,y) &= \tfrac{1}{4\pi^2} \iint [S(p,t)]\, e^{i\gamma p G_{ymax} T_{pe} y'} e^{i\gamma G_x t x'} dpdt \\ I(x,y) &= \tfrac{\alpha\gamma^2 G_x G_{ymax} T_{pe}}{4\pi^2} \int_{slice} \Im(x,y,z)dz \\ I(x,y) &\propto \int_{slice} \Im(x,y,z)dz \end{aligned} \tag{2.3.2}$$

which reconstructs the two dimensional initial magnetization distribution within the selected slice. The discrete nature of signal acquisition further complicates the situation but as the number of signal samples per phase encoding and the number of phase encodings both increase, the re-constructed image approximates the continuous result ever more closely.

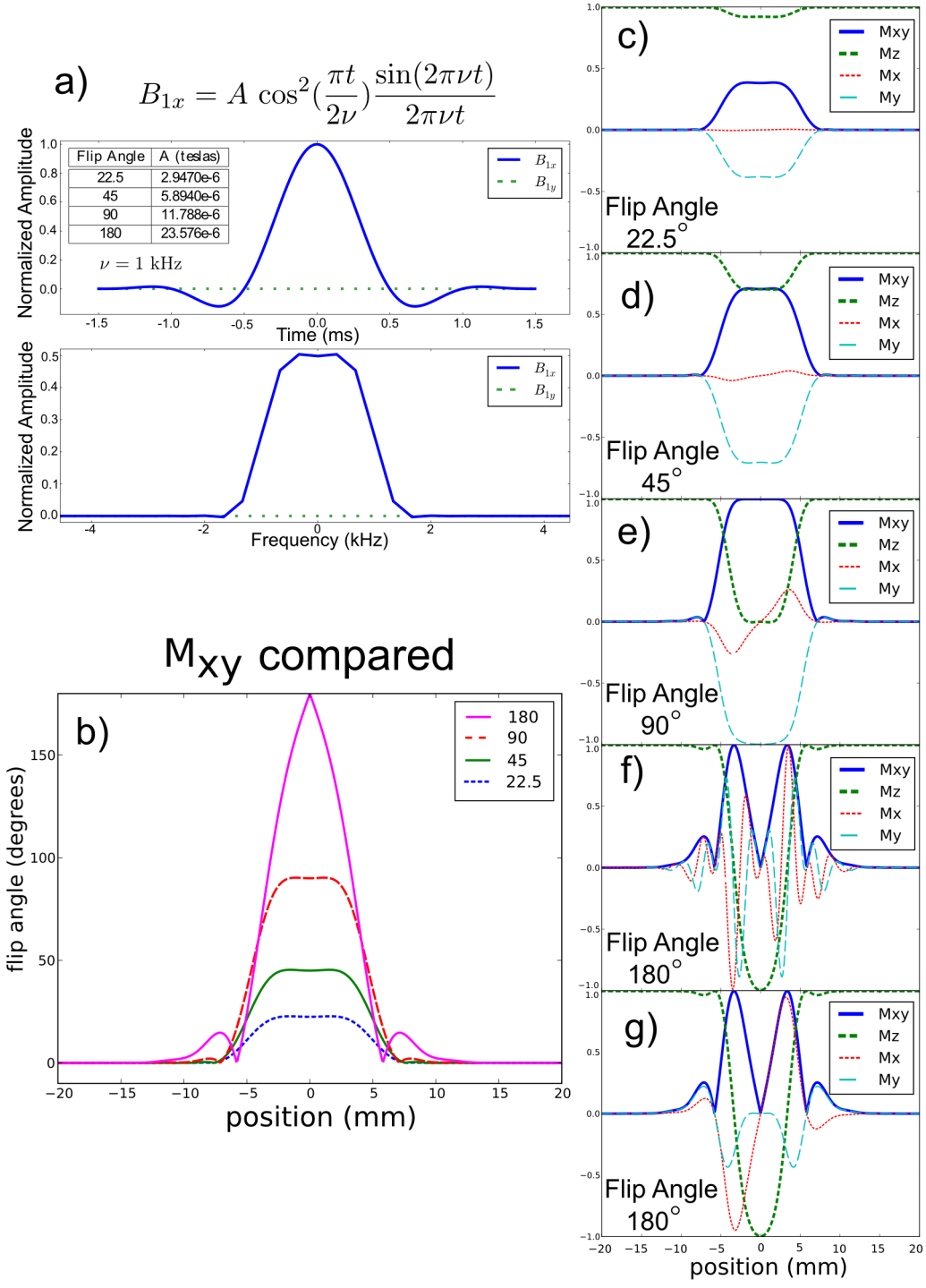

Figure 2.11: Isochromats in the presence of a gradient of magnitude $G_z = 4.697$ mT/m $\left(\frac{\gamma}{2\pi}G_z = 200\ \text{Hz/mm}\right)$ and the B_{1x} pulse shown in a) were simulated using equation 2.2.24 with different amplitudes for the B_{1x} pulse and the customary re-phasing gradient lobe shown in figure 2.10. The B_{1x} pulse was Hann filtered $\left(\cos^2(\frac{\pi t}{2\nu})\right)$ to reduce Gibbs ringing [117, pg 141] in the frequency domain. In b) we see that there is a non-linear relationship between flip angle and B_{1x} amplitude. Parts c-f) show the final states of the simulated isochromat components after the re-phasing gradient lobe and, since 180° pulses are not usually played with a re-phasing lobe, part g) shows the isochromat components after the pulse but without the re-phasing lobe. Clearly the linear approximation of the Bloch equations breaks down.

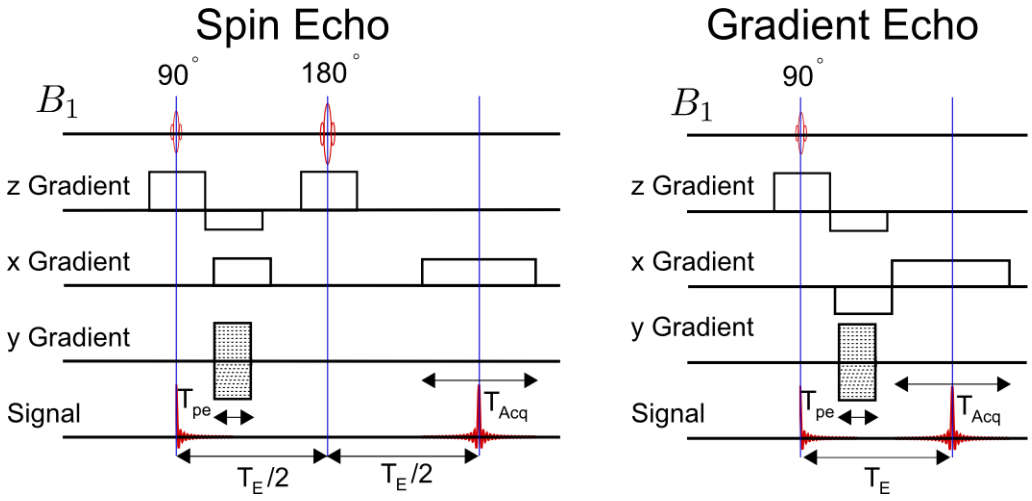

Figure 2.12: Two dimensional spin- and gradient-echo pulse sequences require multiple signal acquisitions where the y-gradient is applied with a different value each time. The dotted lines indicate successive y-gradient values for each signal acquisition.

2.3.4 MRI System Overview

From this description of imaging we see that an MRI machine needs a main magnetic field B_0, magnetic field gradients, and a rapidly oscillating pulsed B_1 field. In a clinical MRI system, shown schematically in figure 2.13, the main field is produced by a superconducting winding cooled in a metallic cryostat, the x, y, and z gradients are each produced by their own gradient coil and associated power supply, while the B_1 field is produced, as well as signal acquired, by RF-coils and their associated electronics. The gradient coils are supplemented with shim coils that produce spatial B_z field harmonics (section 2.1.4) used for fine adjustments to the B_0 field, and the whole system is enclosed within a Faraday cage to isolate it from external electromagnetic signals. Since the gradient and shim coils both produce spherical harmonics of B_z, the first four spherical harmonics being a homogeneous field and linear gradients along the x, y, and z directions, we shall often refer to all of them together as spherical harmonic production coils, or just harmonic production coils for short

The largest and most expensive MRI component is the main field magnet [87] which produces a field of one or more teslas to an accuracy greater than ten parts per million over a roughly spherical region around 50 cm in diameter. This marvel of precision engineering is made of super-conducting windings bathed in liquid helium. As the strength of the main field increases so does the equilibrium magnetization M_0 (equation 2.2.19) and thus the available signal for imaging is proportional to ω_0^2 (see section 2.2.4). However the noise increases linearly with field strength[13] and thus ω_0 so the signal to noise ratio increases linearly with B_0 [49]. Stated differently, stronger gradients can be used at higher B_0 field strengths for

[13]The effective RF-coil resistance R_m due to the patient's conductivity increases as ω_0^2 and thus the associated noise increases proportional to $\sqrt{R} \propto \omega_0$.

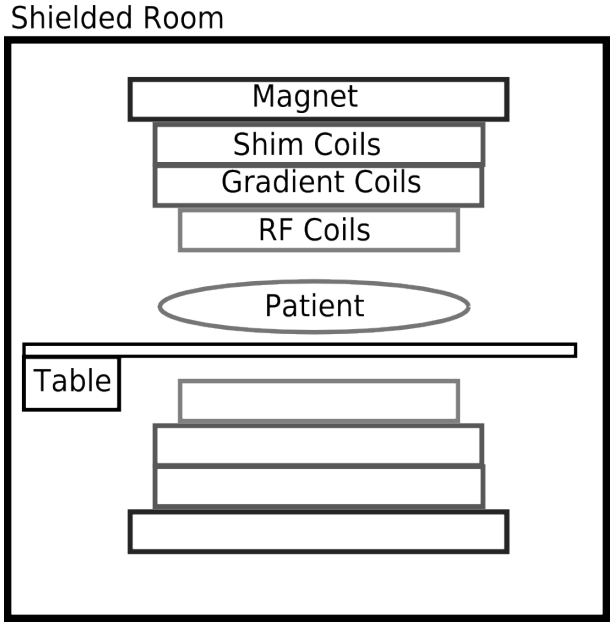

Figure 2.13: The bulk of an MRI system is its main B_o magnet. Within the bore of this magnet there are several layers of coils, both for the gradient and RF systems. At the centre is a table where the patient is placed.

increased resolution without a loss in SNR. This increase in signal is the reason for the steady increase in the field strength used for MRI designs with the most powerful field strengths now over 10 T. Higher field strength is not without problems, however, since the wavelength of the B_1 field becomes comparable to the size of the patient and a homogeneous B_1 field over the patient is no longer a solution to Maxwell's equations [45]. Moreover, the field shifts caused by magnetic susceptibility also increase with B_0 and can ruin field homogeneity over the region of interest.

Any increase in magnet bore space greatly increases the system cost due to engineering challenges in the main magnet design. For this reason, there is a desire to keep the bore space small while maximizing the space for the patient. As far as the gradient system is concerned, this is accomplished by placing the gradient/shim coils as close to the magnet cryostat as possible. However, strong currents switching through these coils induce eddy currents (section 2.1.3.2) in the nearby cryostat which produce their own fields that distort the desired gradient field. Reducing the effect of eddy currents is a major challenge in gradient system design, especially as gradient strength and switching rate increase, and is the main topic of this thesis.

2.3.5 Point Spread Function

As we have seen, magnetic resonance images are formed by encoding signal parameters with spatial information. In this section we briefly investigate the two imaging sequences from section 2.3.3 and show how image resolution is limited both by the MRI equipment and the properties of the material being

imaged. If an image $I(x,y)$ of some function of tissue-dependent initial magnetization $\Im(x,y)$ is desired, then image acquisition can be expressed with a point spread function PSF(x,y) such that the acquired image $I(x,y)$ is

$$I(x,y) = \iint \Im(x,y)\text{PSF}(x-x', y-y')dx'dy' = \Im(x,y) * PSF(x,y)$$

where $*$ denotes convolution [73, chapter 5]. Then for theoretically perfect imaging, the point spread function collapses into a Dirac delta function such that $I(x,y,z) = \Im(x,y,z)$.

Let us re-consider the pulse sequences in figure 2.12 now taking into account the limited acquisition time $-T_{Acq}/2 \leq t \leq T_{Acq}/2$ and signal relaxation therein as well as the limited phase encoding window $-1 \leq p \leq 1$. If we make the simplifying assumptions (section 2.2.3) that spin-spin relaxation takes the form of an exponential decay and re-phasing in a spin echo takes the form $e^{-|t|/T_2'}$ we can re-write equation 2.3.1 as

$$\begin{gathered} S(p,t) = \alpha\Delta z \text{rect}\left(\tfrac{t}{T_{acq}}\right)\text{rect}\left(\tfrac{p}{2}\right)\iint_{slice}\Im(x,y)e^{-(T_E+t)/\mathfrak{T}}e^{-|t|/\mathfrak{T}'}e^{-i\gamma y T_{pe}pG_{ymax}}e^{-i\gamma x G_x t}dxdy \\ \text{rect}(q) = \begin{cases} 1 & -1/2 < q < 1/2 \\ 0 & \text{otherwise} \end{cases} . \end{gathered} \tag{2.3.3}$$

In this equation we combine the signal formulae for gradient- and spin-echo imaging by introducing time constants $\mathfrak{T}$ and $\mathfrak{T}'$ which depend on the echo type. For a spin echo, de-phasing associated with B_o inhomogeneity re-phases so $\mathfrak{T} = T_2$ and $\mathfrak{T}' = T_2'$. For gradient echoes, however, that particular re-phasing does not occur so $\mathfrak{T} = T_2^*$ and $\mathfrak{T}' = \infty$. Note that we are still not taking into account the distorting effects of eddy currents or the finite nature of sampling in either the frequency or phase direction. The upshot is that any limitations found with this method are fundamental in that they still occur if eddy current effects are practically eliminated and if the signal sampling rate and the amount of time spent acquiring phase encoded signals become very large.

Limiting, for now, analysis to a region where $\mathfrak{T}$ and $\mathfrak{T}'$ are uniform, we recognize equation 2.3.3 as a two-dimensional Fourier transform

$$S(p,t) = \frac{\alpha\Delta z}{\gamma^2 G_x G_{ymax} T_{pe}} e^{-(T_E+t)/\mathfrak{T}}e^{-|t|/\mathfrak{T}'}\text{rect}\left(\frac{t}{T_{acq}}\right)\text{rect}\left(\frac{p}{2}\right)\mathfrak{F}_x[\mathfrak{F}_y[\Im(x,y)]] \tag{2.3.4}$$

where

$$\begin{gathered} \mathfrak{F}_x[f(x)] = \int_{-\infty}^{\infty} f(x)e^{-i\omega_x t}d\omega_x \qquad \mathfrak{F}_y[f(y)] = \int_{-\infty}^{\infty} f(y)e^{-i\omega_y p}d\omega_y \\ \mathfrak{F}_x^{-1}[f(t)] = \tfrac{1}{2\pi}\int_{-\infty}^{\infty} f(t)e^{i\omega_x t}dt \qquad \mathfrak{F}_y^{-1}[f(p)] = \tfrac{1}{2\pi}\int_{-\infty}^{\infty} f(p)e^{i\omega_y p}dp \\ \omega_x = \gamma G_x x \qquad \omega_y = \gamma G_{ymax} T_{pe} y \end{gathered} . \tag{2.3.5}$$

Applying the inverse transform in both dimensions produces a function $Q(x,y) = \mathfrak{F}_x^{-1}[\mathfrak{F}_y^{-1}[S(p,t)]]$:

$$Q(x,y) = \frac{\alpha\Delta z}{\gamma^2 G_x G_{ymax} T_{pe}} \mathfrak{F}_x^{-1}[u(t)e^{-(T_E+t)/\mathfrak{T}}] * \mathfrak{F}_x^{-1}[e^{-|t|/\mathfrak{T}'}] * \mathfrak{F}_x^{-1}[\mathrm{rect}\left(\frac{t}{T_{acq}}\right)] * \mathfrak{F}_y^{-1}[\mathrm{rect}\left(\frac{p}{2}\right)] * \Im(x,y)$$

$$Q(x,y) = \frac{\alpha\Delta z \mathfrak{T}\mathfrak{T}' T_{Acq}}{4\pi^4\gamma^2 G_x G_{ymax} T_{pe}} e^{-T_E/\mathfrak{T}} \left(\frac{1+i\mathfrak{T}\omega_x}{1+\mathfrak{T}^2\omega_x^2}\right) * \left(\frac{1}{1+\mathfrak{T}'^2\omega_x^2}\right) * \mathrm{sinc}\left(\frac{T_{Acq}}{2}\omega_x\right) * \mathrm{sinc}\left(\omega_y\right) * \Im(x,y).$$

where the unit step function $u(t)$ has been included to facilitate the use of Fourier transform tables [123]. The function $Q(x,y)$ is the desired image $\Im(x,y)$ convolved with something resembling a point spread function except that the first convolution term has an imaginary component that does not collapse into a delta function. To avoid this problem, the real part of $Q(x,y)$, also called the absorption part, is taken as the acquired image $I(x,y)$

$$\begin{aligned} I(x,y) &= \Im(x,y) * \mathrm{PSF}(x,y) \\ \mathrm{PSF}(x,y) &\propto e^{-T_E/\mathfrak{T}} \left(\tfrac{1}{1+\mathfrak{T}^2\omega_x^2}\right) * \left(\tfrac{1}{1+\mathfrak{T}'^2\omega_x^2}\right) * \mathrm{sinc}\left(\tfrac{T_{Acq}}{2}\omega_x\right) * \mathrm{sinc}\left(\omega_y\right). \end{aligned} \tag{2.3.6}$$

which is a version of the desired image $\Im(x,y)$ blurred by the point spread function $\mathrm{PSF}(x,y)$. The image resolution is limited by the width of the PSF at half its maximum value since two points placed that far apart would be blurred by the PSF into a single wide peak. Although this analysis was limited to regions where $\mathfrak{T}$ and $\mathfrak{T}'$ are constant, these parameters vary throughout the material making the image resolution dependent on position.

In figure 2.14, the point spread function's convolution factors are plotted along the frequency encoded direction (x) for a spin-echo image using typical parameters. In order to increase image resolution along x, the convolution terms must be narrowed by increasing any of the quantities $G_x T_{Acq}$, $G_x T_2$, and $G_x T_2'$. Now the spin-spin relaxation time T_2 is an intrinsic property of the material and thus beyond our control but T_2' is a function of B_o homogeneity and is partially under the control of the MRI system's designer and, through the shim coils, its operator. However, as shown in the figure, the quantity $G_x T_{Acq}$ is typically most important for image resolution [32] where the maximum value of G_x is set by the gradient system performance and the maximum acquisition time is set by the bandwidth of the NMR signal reception electronics through $T_{Acq} = 1/BW$.

Although this analysis shows that image resolution in the frequency-encoded direction is usually limited by the MRI equipment, image quality is not always improved by increasing the strength of G_x and the length of T_{Acq}. For example, since there is a limited equilibrium magnetization (equation 2.2.19) from which to extract signal; as the image resolution increases the signal to noise ratio steadily decreases until eventually a more powerful, and expensive, super-conducting magnet is needed. Moreover, concentrating solely on long T_{Acq} is counter-productive since the signal reception electronics must have a variable bandwidth, narrow for high resolution and wide for a broad field of view.

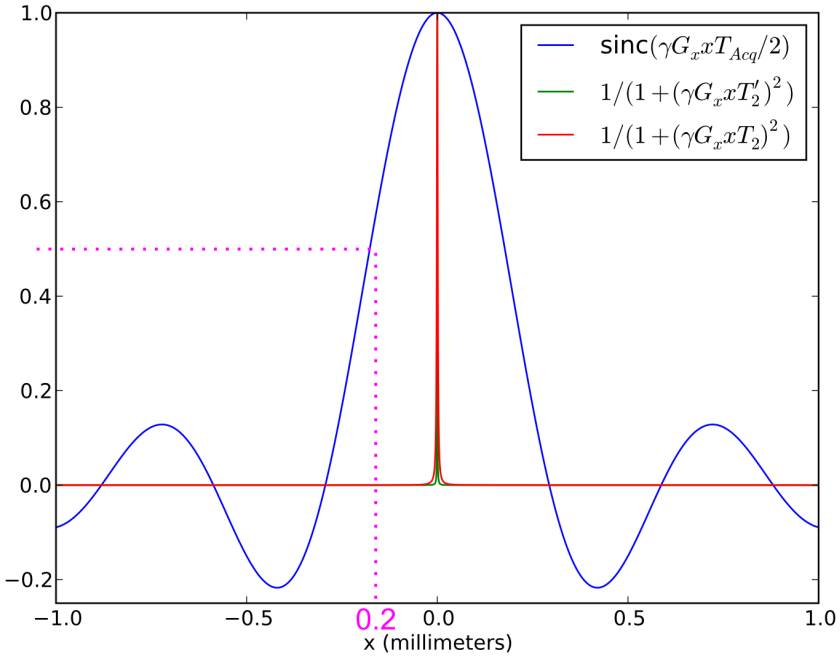

Figure 2.14: The point spread function components estimated using human white brain matter ($T_2 \approx 67$ ms [73, pg 229], $T_2^* \approx 53$ ms [95], $T_2' \approx 1/\left(\left(1/T_2^*\right) - (1/T_2)\right) = 253$ ms) in a Tim Trio 3 T MRI with maximum acquisition time 2 ms (computed from RF receiver bandwidth of 500 Hz [125, pg 586]), and $G_x = 40$ mT/m [125, pg 585]. The full width half max (FWHM) of this point spread function is 0.2 mm giving a theoretical resolution of 0.4 mm.

2.4 Summary

The physics included in this chapter started with electromagnetism and built to a description of image formation in MRI. With respect to electromagnetics, the spherical harmonics of fields and potentials in a quasi-static source-free region were described along with eddy currents and mutual- and self-inductance. As far as NMR and MRI are concerned, the Bloch equations (equation 2.2.22 or 2.2.24) and their special-case solutions (equations 2.2.8 and 2.2.23) were presented along with the point spread function.

Chapter 3

Required Engineering

As mentioned in the introduction, this thesis introduces a new method of controlling the effects of eddy currents produced by the gradient system. In order to understand this method it must be placed within the context of gradient system engineering and electronic control system design. Thus we now adjust our gaze to take a broad survey of the MRI's gradient system – emphasizing the design of gradient coils, the problem of eddy currents, as well as standard solutions to that problem – and present those parts of both control-system theory and practice which will be of use in subsequent chapters.

3.1 Practical Gradient System Considerations

3.1.1 Gradient System Engineering

As mentioned in section 2.3, the ability to produce switched magnetic field gradients is central to the formation of magnetic resonance images. An MRI's gradient subsystem includes x, y, and z gradient coils through which current waveforms with bandwidths up to 100 kHz flow. These currents, which may be as great as 600 A, are produced by gradient amplifiers that have peak output voltages as high as 1.2 kV [84] and often employ pulse width modulation (PWM) in their output stages to avoid over-heating [113] – since the output transistors are either fully on or fully off at any instant when using PWM, minimal energy is dissipated as heat in the amplifier. When the gradient coils and amplifiers are combined, they produce gradient fields over a spherical region roughly 50 cm in diameter that are as strong as 0.040 T/m and may slew at a rate of $180\,\mathrm{T{\cdot}m^{-1}\cdot s^{-1}}$ [125, pg 585]. The other field production coils, the shim coils used for fine adjustments, also require their own amplifiers, albeit with significantly lower power than the gradient amplifiers.

Fundamentally the gradient system is limited by peripheral nerve stimulation (PNS) [41, 119, 61] caused by the electric fields produced as a gradient field slews. The first sign of this effect is a slight tap-

ping/tingling sensation that may become painful as $\frac{dB}{dt}$ increases[1]. PNS puts an upper limit on the maximum patient volume over which a certain gradient slew rate can be used and thus strongly slewing gradients must be applied using small gradient coils placed around a specific part of the patient's anatomy. Also with respect to patient safety, it is important that the mechanical design of the gradient coils be such that the loud acoustic vibrations, produced by the Lorentz force[2] on the current in the coils, do not damage the patient's hearing.

Although PNS and acoustic noise impose fundamental safety limitations, most of the effort in gradient system design is directed towards producing strong gradient waveforms that are also accurate in both space and time, while maximizing the bore space available for the patient and keeping the power requirements, and thus gradient amplifier cost, down. Production of a spatially accurate gradient field, or an arbitrary spherical harmonic for shim adjustment, requires a design algorithm which takes a field profile as an input and produces a coil winding path. When current flows along this path it must produce the desired field profile while keeping inductance L low and the strength of the harmonic per unit current η high. If we use the root mean square deviation of the actual field B_{actual} from the desired field $B_{desired}$ over a region of interest V as a measure of how well the design achieves the desired field, these factors can be combined in a figure of merit [130]

$$\beta = \frac{\eta^2/L}{\sqrt{\frac{1}{V}\int\left(\frac{B_{actual}(x,y,z)}{B_{desired}(x,y,z)} - 1\right)^2 dV}} \tag{3.1.1}$$

providing a simple point of comparison between coils of the same radii produced by different algorithms.

Although spatial accuracy is a result of coil geometry, temporal accuracy is hindered by the eddy currents which are induced in nearby conductors, primarily the magnet cryostat, which produce their own distorting fields as the coil currents switch. Excluding gradient coils specialized for a specific anatomy, limitations on bore space require that the field production coils be placed as close to the cryostat as possible. For this reason, efforts are made to minimize flux linkage to the cryostat while keeping coil inductance, and thus peak power requirements, small. Eddy currents are also a problem for the main magnet designer as they deposit significant heat into the magnet cryostat which complicates magnet thermal design and contributes to the loss of cryogenic helium by boiling.

3.1.1.1 Gradient and Shim Coil Design

The coils that Golay [35] embroidered, just as pictures are embroidered with thread into cloth, are early examples of harmonic production coil design. He attached those coils to the pole faces of his NMR magnet and used them to correct magnetic inhomogeneity. Today, there are many mathematical and/or

[1] Although PNS must be kept below painful levels, it is imperceptible in most scans [33].

[2] For 600 A flowing through a wire in a 3 T magnetic field the Lorentz force is 180 N/cm. This current may be switching at several kHz.

computational techniques used to design gradient and shim coils[3] but since the design of these coils is not our primary aim, the methods will be described in broad overview rather than mathematical detail.

One plan for the design of harmonic production coils is to use lines, arcs, rings or other current elements in order to produce the desired spherical harmonic while cancelling undesired harmonics. A very simple example of this technique is the Maxwell pair z-gradient coil in which current runs in opposite directions through two circular rings that are placed on a common axis and spaced such that the third order zonal harmonic cancels. A general mathematical framework for this method is given by Roméo and Hoult [111] and can be used to build more complicated coils such as the x-gradient coil shown in figure 3.1a). Unfortunately, coils designed with this method are highly sensitive to wire placement errors and are not easily optimized for anything other than the desired magnetic field.

The second plan starts with a generalized current distribution, describes it mathematically, and then optimizes it to produce the desired magnetic field. This plan has a significant advantage over the first in that, in addition to producing a desired harmonic, the coil patterns can be optimized with respect to power consumption [50], self-inductance [130], acoustic noise [17], and other criteria. Turner's target field method [129], which forms the basis for much subsequent work, describes a continuous current distribution on a cylinder of infinite extent in terms of Fourier transforms along the axial and azimuthal directions and these transforms are used to write the associated B_z field as a Fourier-Bessel series. Then a desired magnetic field, called a target field, is specified – either analytically or numerically, point by point – and the coil's current distribution is found by inverting the Fourier-Bessel expression for the B_z field. Now the infinite extent of the cylinder is a notable weakness in the original target field method but subsequent work has removed this restriction [19, 34, 120]. To actually construct a coil, however, the current distribution is truncated to a finite length and discretized into individual wires by following the contours of its stream function [12] – since the current distribution is confined to a cylindrical surface, the vector potential associated with the current distribution (remember from equation 2.1.6 that $\nabla \cdot \mathbf{J} = 0$ when $\rho = 0$) has a single vector component in the cylindrically radial direction, the scalar value of which is the stream function. An important departure from the target field approach, although it still employs a stream function, is the power-minimization-matrix method of Hoult and Deslauriers [50] in which the magnetic field is expressed directly in terms of spherical harmonics. In that method a finite length cylinder is split into discrete rings with the current on each ring described with a Fourier series. The Fourier coefficients on each ring are related to the B_z harmonics and this results in a rectangular matrix which can be inverted using the Moore-Penrose inverse [6] to find the current coefficients given a desired B_z harmonic while minimizing power.

Although methods discussed so far employ orthogonal functions in the description of the magnetic field, coils have been designed with a combination of the Biot-Savart law and varying degrees of computational brute force, such as simulated annealing [20] and conjugate gradient descent [138]. These

[3] Many of those developed before 1993 are summarized by Turner [131].

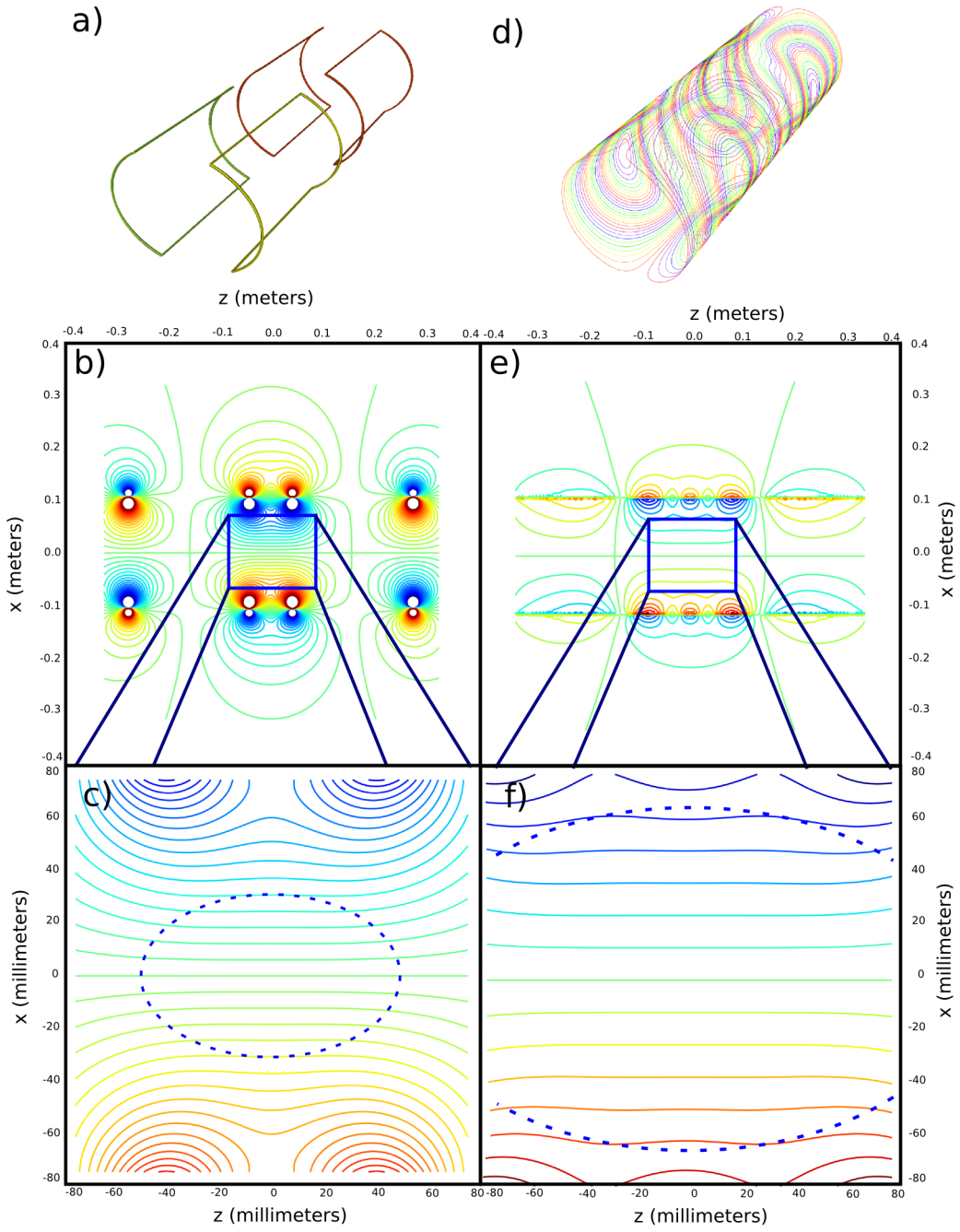

Figure 3.1: In a) a simple saddle-shaped x-gradient coil is made from discrete current elements arranged such that spherical harmonic $T_{3,1}$ is nulled [111, fig 8b]. Below the coil diagram, a contour plot of the coil's B_z field in the xz-plane is shown over the whole coil b). In c) the contour plot only covers a small region near the centre of the coil – the dotted ellipse encloses a region in which the spatial field variation is primarily a x-gradient ($G_x = dB_z/dx$). In d) the x-gradient coil has been designed using a generalized wire distribution such that unwanted harmonics up to and including $T_{9,1}$ have been nulled. As can be seen from the B_z contour plots e) and f), this second coil produces a much larger region of constant G_x.

techniques allow gradient and shim coils to be wound on geometries including discs [97], planes [2], and domes [70, 115] to accommodate special considerations. Indeed, there are now computational techniques that allow the winding of gradient coils on any arbitrary surface [98, 100][4]. Yet other techniques, in an attempt to provide more degrees of freedom during coil optimization, allow the wire to have a fully three dimensional structure rather than constraining it to a surface [116, 134].

With respect to eddy currents, an important requirement for gradient coils is that they produce minimal flux linkage to surrounding conductors, especially the cryostat. A passive shield can be made from a thick conducting sheet or mesh but then eddy currents flow in the shield rather than the cryostat. However for a coil surrounded by a passive shield, the magnetic fields, including those produced by eddy currents, can be computed and the coil design altered to restore homogeneity [132] – albeit for a limited time period. More conventionally, the flux interacting with the cryostat may be minimized as part of the gradient coil design [13, 78, 79, 120] and this usually involves building the coil in layers, with current through the outer layers actively cancelling the field outside the coil; coils of this kind are called "actively shielded". Since the cryostat is the most important host for eddy currents, there have also been efforts to integrate the design of the cryostat and gradient coils [42]. Essentially all MRI systems are equipped with actively shielded gradient coils made of multiple layers but these coils require more space than their unshielded counterparts; moreover they still allow a small amount of flux to escape which induces residual deleterious eddy currents. These are of greatest concern in localized spectroscopy and echo planar imaging.

3.1.1.2 Residual Eddy Currents

Including the eddy currents following a gradient pulse, B_z can be written [66, 54] as

$$B_z(t) = \sum_{m=0}^{\infty}\sum_{n=m}^{\infty} B_{z,n,m}(t) = \sum_{m=0}^{\infty}\sum_{n=m}^{\infty} B_{za,n,m}(t)T_{n,m} + B_{zb,n,m}(t)T'_{n,m}$$

where $T_{n,m}$ and $T'_{n,m}$ are the spherical harmonics from section 2.1.4. The subscript 'z' on the magnetic field coefficients $B_{za,n,m}$(t) and $B_{zb,n,m}$(t) denotes their association with B_z (rather than B_x or B_y) and the coefficients have been written as explicit functions of time. Now the magnetic field $B_z(t)$ arises from both the coil currents and the eddy currents such that $B_z(t) = B_z^{\text{coil}}(t) - B_z^{\text{eddy}}(t)$ which means that each of the terms $B_{zab,n,m}(t)$ may be expressed as

$$B_{zab,n,m}(t) = B^{\text{coil}}_{zab,n,m}(t) - B^{\text{eddy}}_{zab,n,m}(t) \tag{3.1.2}$$

where the subscript $'ab'$ is used rather than writing the equation first for $B_{za,n,m}(t)$ and again for $B_{zb,n,m}(t)$. If we naively ignore oscillatory eddy currents due to mechanical vibration, $B^{\text{eddy}}_{zab,n,m}(t)$ may be approximated

[4]Gradient coil patterns have even been produced to be wrapped over coffee mugs and tea pots, not for practical reasons but to demonstrate the generality of the approach. [99]

with a sum of decaying exponentials

$$B^{\text{eddy}}_{zab,n,m}(t) = \sum_j E_{jab,n,m} e^{-t/\tau_{jab,n,m}} \tag{3.1.3}$$

each with its own magnitude $E_{jab,n,m}$ and time constant $\tau_{jab,n,m}$.

Now B_1 pulse sequences can be designed to minimize the effect that eddy currents have on an image [108] and the field distortions may be mapped, possibly with an array of NMR probes [80, 5, 139] but more likely with a specialized MRI image acquisition, allowing the image distortion to be removed after acquisition [21, 44, 53]. However, the most common solution to this problem is called pre-emphasis [27, 55, 92] where the combined field from the gradient/shim coils and associated eddy currents is used to produce the desired field harmonics. This requires that the field distortions be carefully mapped and then that the current waveforms driven in the coils be shaped such that

$$B^{\text{coil}}_{zab,n,m}(t) = B^{\text{desired}}_{zab,n,m}(t) + \sum_j E_{jab,n,m} e^{-t/\tau_{jab,n,m}}.$$

This ensures that $B_{zab,n,m}(t) = B^{\text{desired}}_{zab,n,m}(t)$ where the functions of time $B^{\text{desired}}_{zab,n,m}(t)$ are the desired field harmonics.

Although pre-emphasis is widely used, it makes two assumptions that are not strictly correct, the first being that the required pre-emphasis current stays the same from scan to scan. Subtle hardware changes alter the eddy currents so that pre-emphasis currents require frequent re-calibration; so frequently in fact, that methods have been developed for its simplification [118]. Another common assumption is that the transient field caused by eddy currents can be corrected by altering the current through the active field production coil. In other words, it is assumed that the eddy current field has the same spatial profile as the harmonic which excited it, although with a reduced and opposite amplitude. This is not strictly true since the eddy current field can be shown to have a spatial profile which includes spherical harmonic components other than those present in an applied gradient [126]; further, the temporal behaviour of each harmonic may be unique and difficult to describe with decaying exponentials as in equation 3.1.3. A well-known example in this regard is the transitory oscillation of the B_0 field following a gradient pulse [112], an effect usually associated with cryostat acoustic resonances. Correcting all such components by the use of pre-emphasis requires measuring [27] the exponential terms in equation 3.1.3, computing the appropriate currents [68, 103, 58], and then feeding them through the shim coils. However, the shim coils also produce further eddy currents, greatly complicating the situation.

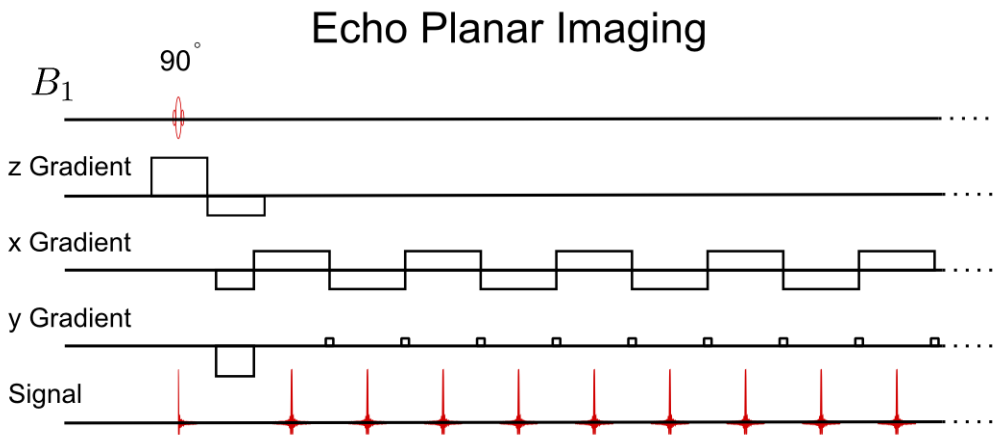

Figure 3.2: A simple echo planar imaging sequence. Signal is acquired with every echo caused by the alternating lobes of the x-gradient but the tiny 'blips' on the y-gradient phase encode each echo. If maximum resolution is desired in a 128×128 pixel image acquired in a time $T_{image} \approx 2T_2^* \approx 100$ ms then the x-gradient is switched at approximately $128/100$ ms $= 1.28$ kHz.

3.1.2 Eddy Currents as a Limitation of the Gradient System

3.1.2.1 Echo Planar Imaging

The problem of eddy currents becomes particularly important whenever the gradient or shim currents are large and rapidly switched. This occurs in echo planar imaging [77, 73, pg 303] (EPI) where the gradient field is continuously switched at or near the limits of the gradient system's performance (figure 3.2). Since EPI can generate a 128x128 pixel image in under 100 ms [8, pg 702], it is useful for imaging dynamic biological processes such as heart motion and brain function [8, pg 702]. The basic EPI sequence, which can be modified for specific applications, extends the gradient-echo sequence by producing multiple gradient echoes from a single excitation pulse. Since each of these echoes is individually phase-encoded, a complete 2D-image can be acquired before the available signal fades as T_2^*. However, fast imaging has a price [8, pg 726]: the eddy currents, and associated distortions shown in figure 3.3, are at their maximum since the gradients are switching at peak power.

3.1.2.2 Magnetic Susceptibility and Dynamic Shimming

Because it is based on gradient echoes, EPI is also particularly sensitive to B_0 inhomogeneity [56, 107], particularly that caused by variations in magnetic susceptibility [72, 71]. Essentially EPI reconstruction assumes a certain mapping of phase to position along the phase encoding gradient but this mapping, and thus the image, is distorted by the additional phase that is accumulated due to spatial variations in the B_0 field. Fine adjustment of the shim coil currents can produce a homogeneous B_0 field in a small region, but outside that region these adjustments tend to *reduce* field homogeneity. Fortunately, to produce an undistor-

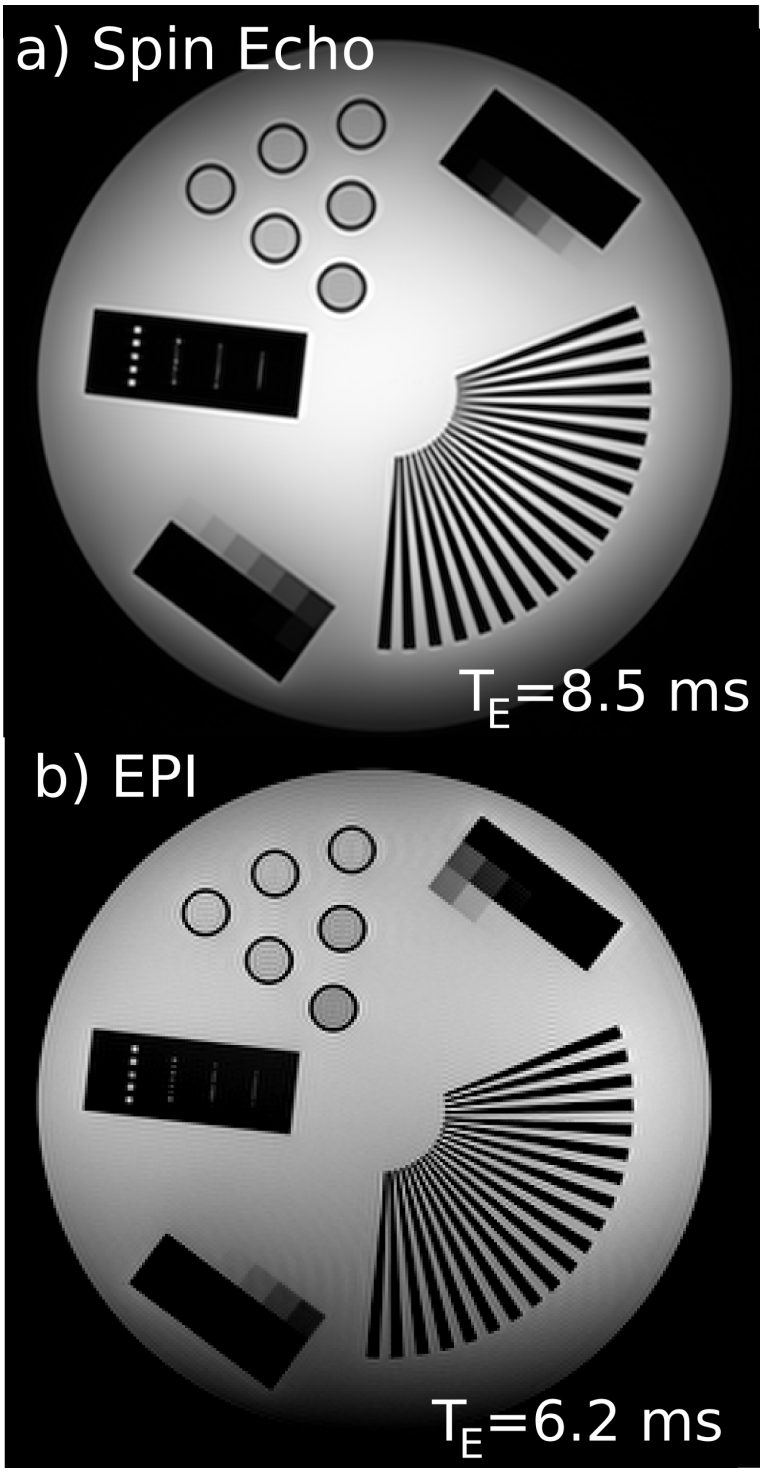

Figure 3.3: Both parts a) and b) are 256×256 pixel images of a phantom taken with a 3T Siemens Tim Trio MRI; the vertical direction with respect to the page is phase encoded. The difference is that in a) a spin-echo imaging sequence was used (201 Hz/pixel) while in b) an EPI sequence was used (752 Hz/pixel). The EPI image has a reduced image quality compared to the spin-echo image and is characterized by image artifacts in the phase-encoded direction. These residual artifacts – caused in part by field inhomogeneity and eddy currents – are especially prevalent around the six circular vials in the top left quadrant of the phantom.

ted three-dimensional image from a series of two dimensional slices, the field need only be homogeneous over the slice being scanned at a given moment. Therefore the whole image volume can be dynamically shimmed [109, 3, 86] by changing the shim coil currents between slices.

Today, dynamic shimming is not yet a standard option on clinical scanners and is usually only attempted for imaging sequences that are particularly sensitive to magnetic susceptibility effects, including but not limited to EPI, or at high field strengths where those effects are pronounced. However, as B_0 field strengths continue to increase so will the demand for dynamic shimming and the hardware required for driving precise current waveforms, rather than static current levels, through the shim coils. Now, unlike the gradient coils, shim coils are generally not actively shielded – doing so would further tax bore space – so switching multiple shim coils during dynamic shimming produces complex eddy current fields. Although these eddy current fields could be mapped and pre-emphasis applied [109] to the complete set of gradient and shim coils, the task is *significantly* complicated by the fact that the ideal shim current pulses depend on all the harmonics of the field and are unique for every image slice, every image sequence, and, due to anatomical variations, every patient.

3.1.3 Proposed Dynamic Pre-emphasis

With the advent of dynamic shimming, especially when used in conjunction with EPI, the complexity of eddy current fields will increase. It follows that an alternative method of pre-emphasis, which does not require re-calibration and is easily expandable to a number of harmonics, is desirable. This thesis proposes *dynamic* pre-emphasis as an alternative to the previously described *static* pre-emphasis. In static pre-emphasis the fields are mapped *before* image acquisition, even if it is only minutes before in a quick calibration scan, whereas the goal of dynamic pre-emphasis is to continuously sense the fields and correct them *concurrently* with the waveforms that are driven through the gradient and shim coils. Of course such a scheme requires a sensor that responds very quickly to the field, a mechanism to determine what correction to apply, and a way to apply that correction.

Fortunately, a harmonic correction can be easily applied by altering the current through the appropriate gradient or shim coil and negative feedback, the topic of the next section, can be used to determine that correction. However, the formidable problem remains of designing a sensor for each B_z harmonic and then using the sensors in feedback loops to control the current through their respective harmonic production coils. Since a changing magnetic field induces a voltage in a wire nearly instantly, and previous work shows how to wrap coils to produce a single harmonic, it is natural to attempt a coil design where the voltage induced is proportional to only the change in a single B_z spherical harmonic. These spherical harmonic inductive detection coils could be wound on the surface of a cylinder to fit existing MRI geometry and avoid interference with the patient. Using gradient coil design and negative feedback as a starting point, this thesis therefore lays the foundation for dynamic pre-emphasis using spherical harmonic inductive detection coils

as sensors.

3.2 Electronic Control System Design

Negative feedback control systems [25], which we shall use to control the spherical harmonics of B_z, have been part of engineering practice since James Watt's 1769 introduction of the fly-ball governor for controlling the speed of steam engines [82, 25]. Although J. C. Maxwell, of electrodynamic fame, analyzed feedback systems mathematically [81], it was the work of Bode, Nyquist, and Black [25, pg 5] – on amplifiers for telephone systems – which made feedback analysis widely known. This section introduces feedback theory for both single and coupled systems with a view to the design of a field harmonic control system.

3.2.1 Single Loop Analysis

The central problem solved by negative feedback is that, for a given process and input, the time course of the process output is undesirable. In our situation, the process is the combination of a harmonic production coil, amplifier, and eddy currents while the output is the associated magnetic field harmonic as a function of time. The solution shown in figure 3.4 is to use an accurate sensor to determine the process output, compare it with the desired output, and compensate the process input appropriately. The system behaviour will then depend primarily on the properties of the sensor (B) and compensator (C) rather than the process (A). However, system designers must neither under-compensate, producing sub-optimal performance, nor over-compensate such that the correction exceeds the initial error enough to cause oscillation or excessive ringing.

For our purposes, we assume that all parts of the system are linear and time independent. That is, a single frequency input to any system component at any time produces a single frequency output with amplitude and phase modified according to the value of the component's transfer function at that frequency. A transfer function, found either by Fourier or Laplace [123, ch 32] analysis, has a complex number with magnitude and phase associated with every frequency. Referring back to figure 3.4, we note that the input to the compensator must be Diff = Input $- B$ (Output) and thus the total system output is Output = (Diff) CA which simplifies to:

$$\text{Output} = \left(\frac{CA}{1+CAB}\right)\text{Input} = \left(\frac{1}{B}\frac{1}{\left(1+\frac{1}{CAB}\right)}\right)\text{Input} = (T)\ \text{Input} \tag{3.2.1}$$

where T is the feedback system transfer function. The product CAB is called the open loop transfer function since it describes the system as if the sensor output were not connected to the difference block, but rather used as the system output. Note that if the absolute magnitude (gain) of the compensator's transfer function

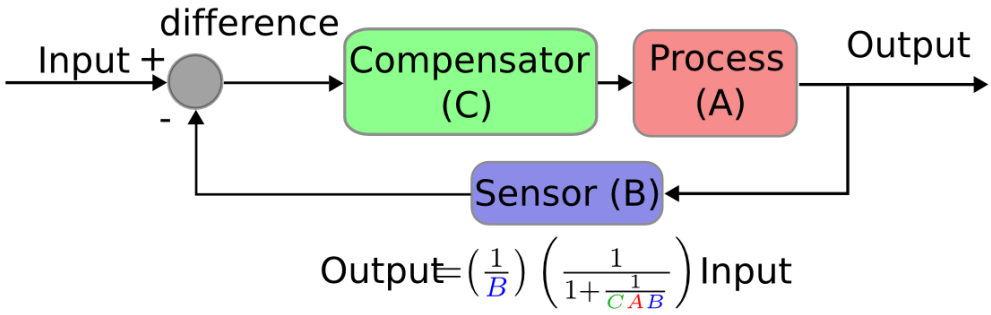

Figure 3.4: The canonical negative feedback example. The output of a process (A) is sensed by (B) and the difference between the sensor's output and the system's input is used to determine the input to the process. Provided that the gain of (CA) is high, the characteristics of the total feedback system depend primarily on the sensor.

is sufficiently high then the total system transfer function depends primarily on the properties of the sensor $\left(\frac{1}{B}\right)$. However, all system components cause attenuation and phase lag at sufficiently high frequencies. Thus if the open loop transfer function's phase lag becomes 180° below the critical angular frequency ω_c where the transfer function's magnitude drops to unity, the system will oscillate. This is because the $-180°$ phase shift causes the difference block to become an addition block which successively adds to the process input with each pass through the loop. Therefore if the system is to remain stable, there must be a phase margin ($\phi_m = \phi_u + 180°$) between the phase of the open loop transfer function when its magnitude drops to unity ϕ_u and a phase of $-180°$; this is the Bode stability criterion.

Many feedback systems can be approximated by assuming that the sensor transfer function is a real constant over a wide bandwidth and that the process and compensator transfer functions have the form $1/(\alpha s + 1)$ where s is the Laplace variable and α is some constant. In this case, using equation 3.2.1, the total transfer function can be written in the form:

$$T = \frac{K}{\left(s^2/\omega_n^2 + 2\zeta s/\omega_n\right) + 1} \tag{3.2.2}$$

where K is a constant gain, $\zeta < 1$ is called the damping ratio, and ω_n is called the natural frequency. By inspection of equations 3.2.1 and 3.2.2 the open loop transfer function is

$$\Lambda = \frac{\omega_n^2}{s\,(s + 2\zeta\omega_n)} \tag{3.2.3}$$

and the sensor gain is $\frac{1}{K}$. Moreover, if the system input is a unit step, then the Laplace transform of the

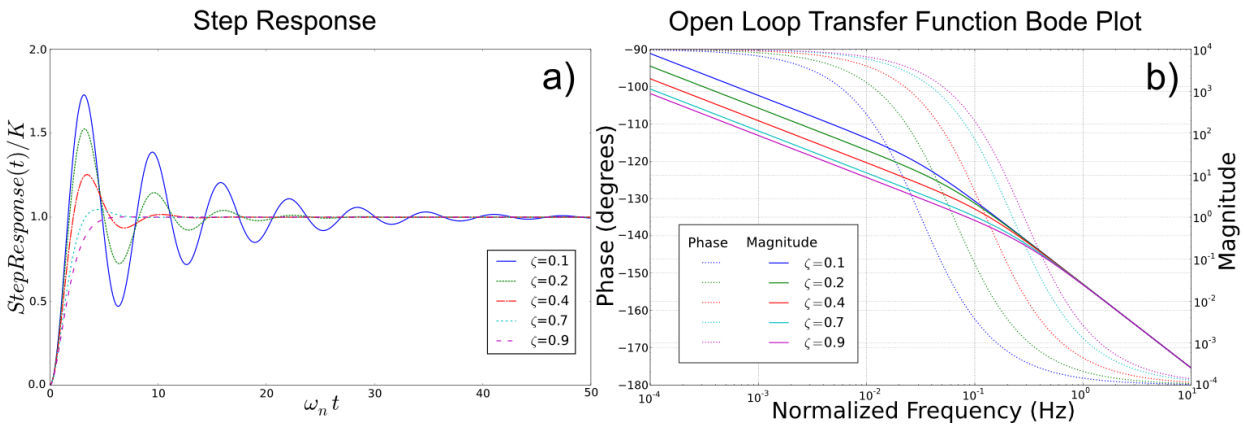

Figure 3.5: A simple example showing the characteristic overshoot and slight ringing typical of feedback systems for various values of damping ratio ζ. Part a) shows the system response to a step input and b) is a Bode plot of the open loop transfer function. The phase margin can be read from b) as the phase difference from $-180°$ of a transfer function when its magnitude reaches 1. Note that time and frequency are both normalised to ω_n.

system output is T/s which has the following time domain representation:

$$StepResponse(t) = K\left(1 - \frac{e^{-\zeta\omega_n t}\sin\left(\sqrt{1-\zeta^2}\omega_n t + \arccos\zeta\right)}{\sqrt{1-\zeta^2}}\right) \tag{3.2.4}$$

as can be verified from a table of Laplace transforms [101]. In figure 3.5 the step response and open loop transfer function are plotted for various values of ζ and we see that adjusting the phase margin provides control over the overshoot and settling time in the step response. Although a phase margin of 45° ($\zeta = 0.42$) is often used since it produces a rapid rise with minimal ringing, the correct choice ultimately depends on the system under consideration.

Real world control systems are more complicated than the model shown in figure 3.4. For such systems the reduction rules of figure 3.6 can be used to simplify the block diagrams until they resemble the canonical system shown in figure 3.4. Once the block diagram is simplified, desired values for overshoot, rise time, and settling time can be specified and used to choose an appropriate compensator. Often the compensator has the form $\frac{\kappa}{s/\alpha+1}$ where α is chosen so that the open loop transfer function satisfies the Bode stability criterion and κ is a gain used to increase the magnitude of the open loop transfer function. In some cases, however, the resulting feedback system is not satisfactory and the compensator must be given the form $\sum_i \kappa\,(s/\alpha_i + 1) \,/\, \sum_j \left(s/\alpha_j + 1\right)$ where the additional terms are intended to cancel similar terms in the process transfer function. In any event, the use of negative feedback allows an undesirable transfer function A to be replaced with $T = 1/\left(B\left(1 + \frac{1}{CAB}\right)\right) \simeq 1/B$ where B and C are specified by the system designer.

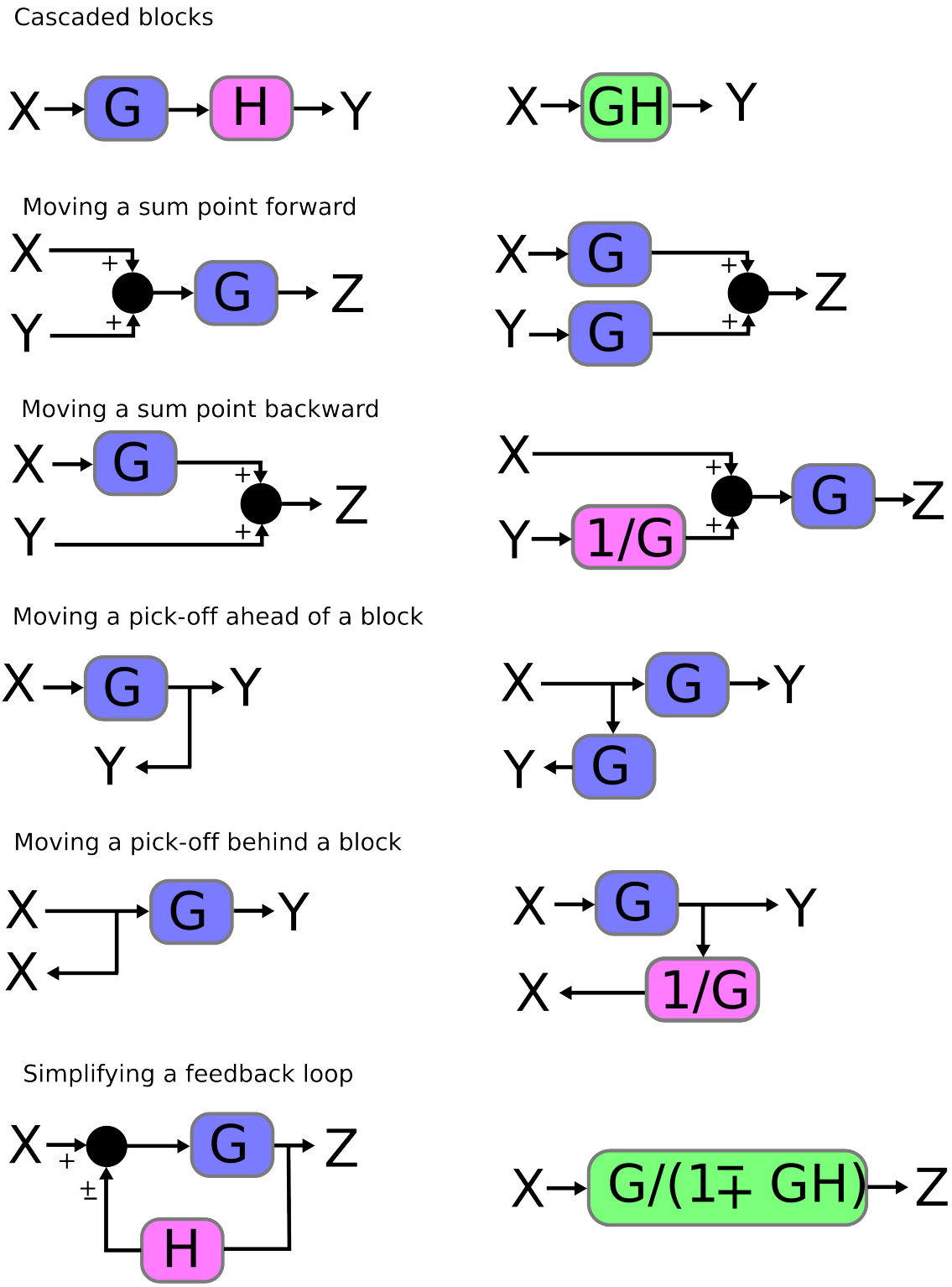

Figure 3.6: These rules [25] are determined from simple algebraic considerations.

3.2.2 Electronic Control System Implementation and Op-amps.

One way to implement the difference and compensation blocks of a feedback system is to use operational amplifiers [76, 16, 59, 60] (shown in figure 3.7a). These devices, usually called 'op-amps.', multiply the difference between two high impedance ($10^5 - 10^{12}\Omega$) [60, pg 1.62] electrical inputs, usually voltage inputs rather than current, by a large amplification factor $\left(> 10^5\right)$ [60, pg 1.10] and produce the result as a voltage at their output. If we assume, as shown in figure 3.7a, that an op-amp. has a transfer function of the form $T_{op} = \frac{A_v}{1+s/\omega_o}$ as well as an input error $V_{err} = V_{offset} + V_{noise}$ composed of a constant offset and random electronic noise [14, 43, 75], then the output with response to V_+ and V_- at the input terminals is:

$$V_o = (V_+ - V_- + V_{err})\, T_{op}.$$

Normally there are manufacturing variabilities with respect to A_v and ω_0 so these devices are used within local feedback blocks which make the transfer function of the block independent of the specific device parameters. An important ramification of this approach is that the feedback elements define the operation of the block, earning the operational amplifier its name. These operational blocks, rather than the op-amps. themselves, are used as building blocks in control systems.

An important op-amp. configuration is shown in figure 3.7b. Analyzing this circuit, we see that the voltage at the inverting input, marked with a '-' sign, has contributions from V_{in} and V_o

$$V_- = \frac{Z_f}{Z_i + Z_f} V_{in} + \frac{Z_i}{Z_i + Z_f} V_o$$

while the voltage at the non-inverting input, marked with a '+' sign, has only a contribution from V_{ip}

$$V_+ = \frac{Z_{pG}}{Z_{ip} + Z_{pG}} V_{ip}$$

where the components labelled Z can be composed of resistors, inductors, and capacitors yielding a complex and frequency dependent impedance. Remembering the op-amp. error, this information is used to translate the circuit diagram of figure 3.7b into the feedback diagram of figure 3.7c; and the block diagram simplification rules of figure 3.6 are used to reveal the individual transfer functions from V_{err} (figure 3.7d), V_{in} (figure 3.7e), and V_{ip} (figure 3.7f) to the output. Combining them gives the total output voltage

$$V_o = \left(\frac{Z_{pG}}{Z_{in}} \frac{Z_{in} + Z_f}{Z_{ip} + Z_{pG}} V_p - \frac{Z_f}{Z_i} V_n + \left(1 + \frac{Z_f}{Z_i}\right) V_{err} \right) \left(\frac{1}{1 + \left(1 + \frac{Z_f}{Z_i}\right)/T_{op}} \right) \tag{3.2.5}$$

which is largely independent of T_{op} provided A_v is large.

3.2.2.1 Electronic Integrator

The first important operational block can be found from the configuration in figure 3.7b by connecting the positive op-amp. terminal directly to ground $\left(V_p = Z_{ip} = Z_{pG} = 0\right)$, choosing the feedback im-

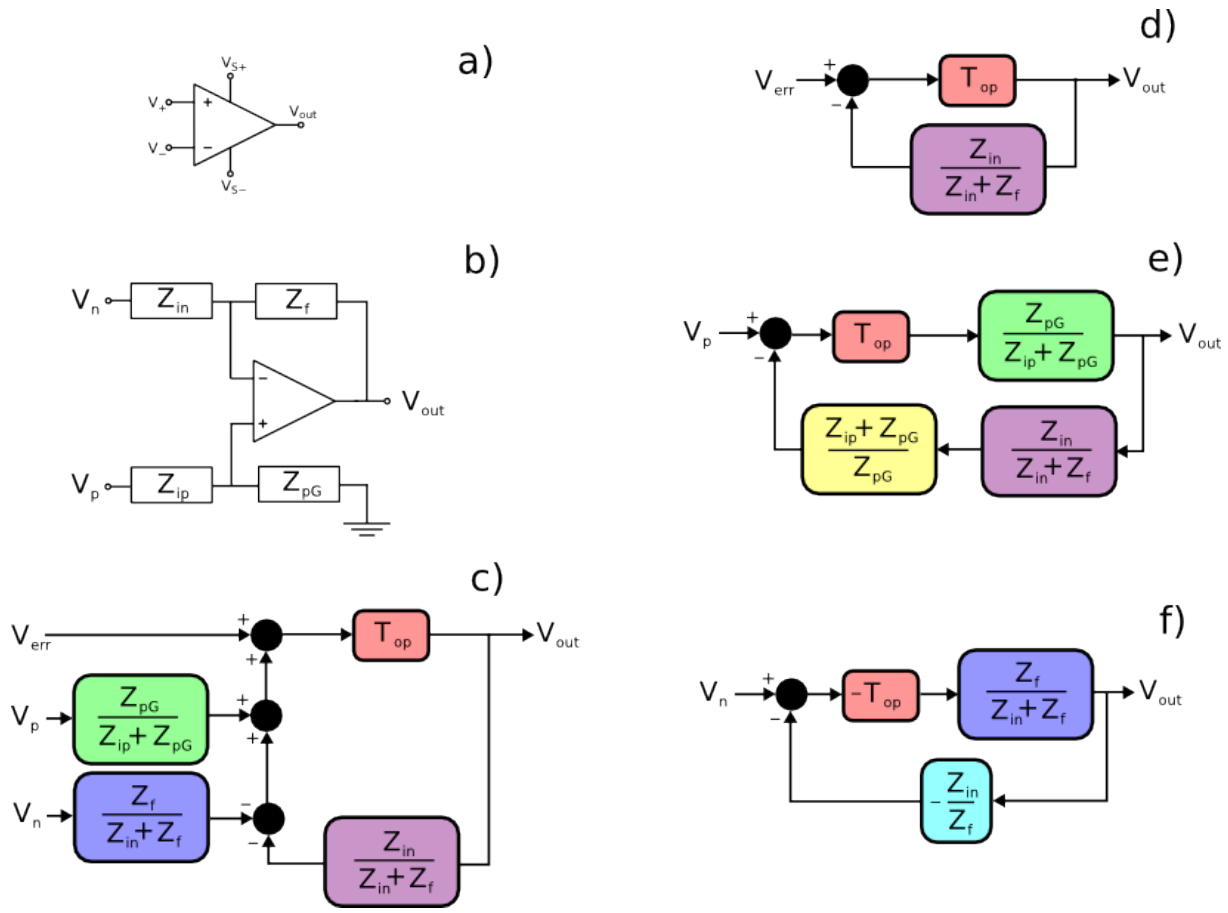

Figure 3.7: In a) an op-amp. is shown and in b) it is placed in a common configuration with the power rails hidden for simplicity. In c) the electrical circuit is converted to a feedback diagram and in d,e,f) this feedback diagram is simplified by assuming that only one of the inputs (V_{err}, V_p, V_n) is active.

pedance to be a capacitor $\left(Z_f = \frac{1}{j\omega C_f}\right)$, and the input impedance to be a resistor $Z_i = R_i$ – note that we are now following electrical engineering convention with $j = \sqrt{-1}$. This causes equation 3.2.5 to simplify to

$$V_o = \left(-\frac{1}{j\omega R_i C_f} V_n + \left(1 + \frac{1}{j\omega R_i C_f}\right) V_{err}\right)\left(\frac{1}{1 + \left(1 + \frac{1}{j\omega R_i C_f}\right)/T_{op}}\right) \tag{3.2.6}$$

which is just $V_o = -\frac{1}{j\omega R_i C_f} V_{in}$ if we ignore V_{err} and T_{op}. Now the transformation $j\omega \rightarrow s$ shows this transfer function to be the Laplace integration operator $\frac{1}{s}$ multiplied by a constant and thus this circuit performs mathematical integration with respect to time on the input signal and produces the result at its output.

Unfortunately this is not a practical circuit because V_{err} includes a constant offset which, when integrated, causes the output to rise until it hits the maximum output voltage. To solve this problem, we choose the feedback impedance to be a resistor and capacitor in parallel $Z_f = \frac{R_f}{1+j\omega R_f C_f}$ rather than a capacitor alone so that the output is

$$V_o = -\frac{R_f}{R_i}\left(\frac{1}{1 + j\omega R_f C_f}\right) V_n + \left(1 + \frac{R_f}{R_i}\left(\frac{1}{1 + j\omega R_f C_f}\right)\right) V_{\text{err}} \tag{3.2.7}$$

and the zero frequency contribution of V_{err} to the output is now only $\left(1 + \frac{R_f}{R_i}\right) V_{\text{offset}}$; this output offset can be designed to fall within acceptable values for the op-amp. output voltage V_0. Since we have changed the circuit transfer function, this practical integrator now only works on signals with angular frequencies much larger than $\omega_c = \frac{1}{R_f C_f}$.

In the context of feedback systems, the practical integrator may be used as a simple compensator since it has a transfer function of the form $\frac{1}{1+s/\omega_0}$. If Z_i is also replaced by a capacitor in parallel with a resistor, rather than using a resistor alone, then the transfer function becomes $T = -\frac{R_f}{R_i}\frac{1+j\omega R_i C_i}{1+j\omega R_j C_j}$ and a chain of these blocks may be used for compensators of the form $\frac{\sum_i(1+s/\alpha_i)}{\sum_j(1+s/\alpha_j)}$.

3.2.2.2 Difference and Instrumentation Amplifiers

Another important operational block sets $Z_{ip} = Z_{in} = R_i$ and $Z_f = Z_{pG} = R_f$ such that the transfer function in equation 3.2.5 becomes

$$V_o = \left(\frac{R_f}{R_i}\left(V_p - V_n\right) + \left(1 + \frac{R_f}{R_i}\right) V_{err}\right)\left(\frac{1}{1 + \left(1 + \frac{R_f}{R_i}\right)/T_{op}}\right). \tag{3.2.8}$$

This block can be used to implement the difference depicted as a circle in figure 3.4 by setting $R_f = R_i$ and ignoring the error terms such that $V_o = V_p - V_n$. However when using this difference block, also called a difference amplifier, care must be taken to drive the V_p and V_n inputs with low impedance sources, such as op-amp. outputs, since the inputs to this block have relatively low impedance unlike the inputs to the op-amp. itself.

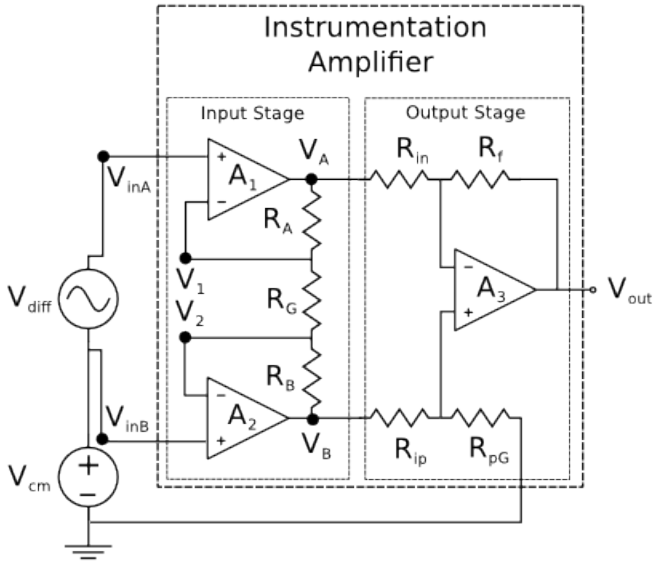

Figure 3.8: The instrumentation amplifier is a configuration of three op-amps. which amplifies the difference between V_{inA} and V_{inB} without amplifying V_{cm}. Both V_{inA} and V_{inB} are high impedance op-amp. inputs.

When amplifying a sensor signal one often needs the difference of the voltage at the sensor's terminals but the low input impedance of the difference amplifier above would unacceptably modify the sensor signal. The op-amp. configuration shown in figure 3.8, called an instrumentation amplifier [62], still uses a difference amplifier but buffers each difference amplifier input with an op-amp. With reference to figure 3.7a, the input op-amps. are configured such that $Z_{\text{ip}} = 0$ and $Z_{\text{pG}} = \infty$ and, for the input block involving A_1, $V_n = V_2$, $Z_{\text{in}} = R_G$, and $Z_f = R_A$ such that $V_A \simeq -\frac{R_A}{R_G} V_2 + \left(1 + \frac{R_A}{R_G}\right) V_{\text{inA}}$. Now $V_{\text{inA}} = V_{\text{cm}} + V_{\text{diff}}$ and the high gain of A_2 ensures $V_2 = V_{\text{inB}} = V_{\text{cm}}$ so that applying the same analysis to the block involving A_2 while assuming that $R_B = R_A$ and that the op-amps. all have the same transfer function T_{op} we have:

$$\begin{aligned} V_A &= \left(\left(1 + \tfrac{R_A}{R_G}\right) V_{\text{diff}} + V_{\text{cm}} + \left(1 + \tfrac{R_A}{R_G}\right) V_{\text{err1}}\right) Q \\ V_B &= \left(-\tfrac{R_A}{R_G} V_{\text{diff}} + V_{\text{cm}} + \left(1 + \tfrac{R_A}{R_G}\right) V_{\text{err2}}\right) Q \end{aligned} \tag{3.2.9}$$

where

$$Q = 1/\left(1 + (1 + R_A/R_G)/T_{\text{op}}\right). \tag{3.2.10}$$

An important property of this input stage is that there is no gain for V_{cm}. Assuming that the V_{err} term in the second stage is insignificant, we can use equation 3.2.8 to find the instrumentation amplifier output:

$$\begin{aligned} V_o &= \tfrac{R_f}{R_i} (V_B - V_A) Q \\ V_o &= -\tfrac{R_f}{R_i} \left(\left(1 + \tfrac{2R_A}{R_G}\right) V_{\text{diff}} + \left(1 + \tfrac{R_A}{R_G}\right)\left(V_{\text{err2}} - V_{\text{err1}}\right)\right) Q^2. \end{aligned} \tag{3.2.11}$$

The instrumentation amplifier has very high input impedances equal to those of the input op-amps., rejects common mode signals, and allows the voltage difference between its input terminals to be amplified. Moreover, setting the input stage amplification factor does not require careful matching of gains for each input but can be done by adjusting a single resistor R_G.

As we have seen, various op-amp. configurations form operational blocks that are useful in control system implementation. The difference of two signals is found using the difference amplifier described by equation 3.2.8; a simple compensator may be formed using the practical integrator of equation 3.2.7; and the instrumentation amplifier shown in figure 3.8 may be used as a sensor pre-amplifier.

3.2.3 Coupled Feedback Loop Analysis

In engineering practice, feedback systems are designed to be un-coupled such that each system is responsible for its own output variable. However, there are circumstances – which will manifest themselves in our field harmonic control system – where each feedback system influences not only its own output variable but also those of other systems. To quantify this effect, the single loop analysis of section 3.2.1 can be extended to multiple coupled feedback systems. First consider n independent feedback systems each with its own input, transfer function, and output. Trivially, the inputs may be placed in an input vector and multiplied by a diagonal transfer function matrix $\mathbf{T}$ such that $\mathbf{Output} = \mathbf{T}\,\mathbf{Input}$.

Now if the systems are coupled at the process output, with each process influencing many output variables, and also at the sensor inputs, with each sensor responding to many output variables, we write $\mathbf{DIFF} = \mathbf{Input} - \mathbf{B}\,\mathbf{Output}$ where $\mathbf{B}$ is not diagonal and $\mathbf{DIFF}$ is a vector of difference functions. The output is then $\mathbf{Output} = \mathbf{C}\,\mathbf{A}\,\mathbf{DIFF}$, where $\mathbf{C}$ is a diagonal matrix but $\mathbf{A}$ is not, and a little matrix algebra yields

$$\mathbf{Output} = (\mathbf{I} + \mathbf{C}\,\mathbf{A}\,\mathbf{B})^{-1}\,\mathbf{C}\,\mathbf{A}\,(\mathbf{Input}) = \mathbf{T}\,\mathbf{Input} \tag{3.2.12}$$

where $\mathbf{I}$ is the identity matrix. Remembering that every element of the matrices in equation 3.2.12 is a function of the Laplace variable s, the transfer function from input a to output b is the matrix element $T_{a,b}$, not to be confused with the spherical harmonic, determined by matrix algebra. We can either find $T_{a,b}$ as an explicit function of s by using a computer algebra system such as *Mathematica* or numerically for every frequency of interest using the discrete Fourier transform. By putting test inputs into the input vector, such as a step function $1/s$, the resulting output variables can be simulated to reveal any undesirable cross-coupling interactions. Even though the form of equation 3.2.12 is very similar to that of equation 3.2.1, which suggests that the rules of figure 3.6 can be directly applied to coupled feedback systems, this is not actually the case since matrix multiplication does not commute. Therefore when analyzing coupled feedback systems we restrict ourselves to symbolic manipulations.

3.3 Summary

An MRI machine's gradient system is an impressive piece of engineering which aims to produce a spatially and temporally accurate magnetic field over a region of interest within the patient. This system's accuracy is limited, in part, by the effects of eddy currents induced in nearby conductors. Established techniques to reduce these effects become difficult as the number of switched gradient and/or shim coils increases. With the inexorable rise in B_0 field strengths, there is an associated desire to counter the effects of magnetic susceptibility by dynamically switching the currents through the shim coils. Therefore, we have proposed dynamic rather than static pre-emphasis to mitigate the influence of eddy currents without the need for complex *a priori* calibrations.

Since dynamic pre-emphasis uses negative feedback – a standard technique in electronic design – we briefly introduced the subject, including its implementation with op-amps. Dynamic pre-emphasis requires the operation of coupled feedback loops, so a theory was developed in section 3.2.3 allowing us to determine whether the coupling between feedback loops causes the system's behaviour to depart significantly[5] from that of uncoupled loops. Although this theory of coupled feedback loops flows naturally from that of single loops, and has most probably been investigated by others, I was unable to find it in the literature.

For dynamic pre-emphasis to be actually employed, sensors must be developed that are able to continuously detect the harmonics of the field during the rise time of the gradients without obstructing the patient's access to the magnet bore.

[5] A theory allowing the actual *synthesis* of coupled feedback systems is beyond the scope of this thesis.

Part II

The Theory

Prologue

Section 3.1.3 introduced a central goal of this thesis: to produce a wire pattern such that the voltage induced in it is proportional to the rate of change of a single harmonic of B_z. The first step in achieving this goal is to compute the voltage induced in a wire pattern by the change in a single harmonic through equation 2.1.12. Now we know from section 2.1.3 that in a source-free region small enough to be quasi-static for frequencies of interest, the Cartesian components of the magnetic field, vector potential, and magnetic scalar potential may be expressed in spherical harmonics. Although these functions have interrelated harmonic coefficients, we do not yet know how to identify which harmonics of the vector potential are associated with a particular harmonic of B_z. Therefore in chapter 4, section 4.1 outlines how to find these relationships and section 4.2 uses them to develop a design method for harmonic detection coils.

Since the harmonic detection coils cannot control eddy currents on their own, the theory required for a whole spherical harmonic feedback system is developed in chapter 5 where section 5.2 gives an overview of the design of such systems and insight into important trade-offs. Since image quality is of the utmost importance, section 5.3 closes the chapter with a technique for optimizing the feedback systems with respect to minimal image degradation arising from field noise and eddy current distortion.

Chapter 4

Designing a Spherical Harmonic Inductive Detection Coil

4.1 Fields and Potentials in Spherical Harmonics

As already mentioned, the goal of this section is to determine what transverse field, vector potential and scalar potential correspond to a given magnetic field in a quasi-static source-free region (section 2.1.4) so that they can be used to design a detection coil's wire distribution. From Gauss's Law for magnetic field (section 2.1) we know that magnetic field exists in closed loops. Therefore if a magnetic field has spatial variations in a region of interest, they are accompanied by relationships between the field's Cartesian components. Although the derivations are difficult, the result (section 4.1.3) is worth the effort since it provides a succinct description of the fields and potentials with a single set of coefficients and is quite easy to apply (see section 4.1.4). Much of the analysis in this section and section 4.2 is adapted and expanded from a paper by Edler and Hoult [28].

4.1.1 The Magnetic Scalar Potential

Our first step is to focus on the magnetic scalar potential since it is simpler than the vector potential. Starting with the total B_z field in spherical harmonics:

$$B_z = \sum_{m=0}^{\infty}\sum_{n=m}^{\infty} B_{z,n,m} = \sum_{m=0}^{\infty}\sum_{n=m}^{\infty} B_{za,n,m}T_{n,m} + B_{zb,n,m}T'_{n,m} \tag{4.1.1}$$

and integrating term by term with respect to z gives magnetic scalar potentials of the form

$$\Psi^0_{n,m} = \int B_{z,n,m}dz = \frac{1}{n+m+1}\left(B_{za,n,m}T_{n+1,m} + B_{zb,n,m}T'_{n+1,m}\right) + Q_{n,m}(x,y)$$

where each scalar function $Q_{n,m}(x,y)$ is independent of z and acts as an integration constant.

4.1.1.1 Finding B_x and B_y from the Magnetic Scalar Potential

The harmonics of the scalar potential may be differentiated, using the rules in table 2.3, to determine the harmonics of B_x and B_y associated with the harmonics of B_z (section 2.1):

$$B_{x,n,m} = \frac{\partial \Psi^0_{n,m}}{\partial x}, \quad B_{y,n,m} = \frac{\partial \Psi^0_{n,m}}{\partial y}$$

$$\begin{aligned} B_{x,n,m} = & \frac{1}{2(n+m+1)}\Big(-(1+\delta_{m,0})\left\{B_{za,n,m}T_{n,m+1} + B_{zb,n,m}T'_{n,m+1}\right\} + \\ & (1-\delta_{m,0})(n+m)(n+m+1)\left\{B_{za,n,m}T_{n,m-1} + B_{zb,n,m}T'_{n,m-1}\right\}\Big) + \frac{\partial Q_{n,m}}{\partial x} \\ B_{y,n,m} = & \frac{1}{2(n+m+1)}\Big((1+\delta_{m,0})\left\{B_{zb,n,m}T_{n,m+1} - B_{za,n,m}T'_{n,m+1}\right\} + \\ & (1-\delta_{m,0})(n+m)(n+m+1)\left\{B_{zb,n,m}T_{n,m-1} - B_{za,n,m}T'_{n,m-1}\right\}\Big) + \frac{\partial Q_{n,m}}{\partial y} \end{aligned} \tag{4.1.2}$$

4.1.1.2 Integration Constants and Super-Sectoral Harmonics

In equation 4.1.2, the derivatives of the scalar functions $Q_{n,m}(x,y)$ are unknown and thus the exact form of the transverse field harmonics is uncertain. To identify these integration constants, we start by considering the complete scalar potential Ψ

$$\Psi = \sum_{m=0}^{\infty}\sum_{n=m}^{\infty}\left[\frac{1}{n+m+1}\left(B_{za,n,m}T_{n+1,m} + B_{zb,n,m}T'_{n+1,m}\right) + Q_{n,m}(x,y)\right]$$

where if we define

$$\Psi_{n,m} = \frac{1}{n+m+1}\left(B_{za,n,m}T_{n+1,m} + B_{zb,n,m}T'_{n+1,m}\right)$$

and collect the integration terms together we have $\Psi = Q(x,y) + \sum_{n=0}^{\infty}\sum_{m=0}^{n}\Psi_{n,m}$. Now the sectoral harmonics do not depend on z, so we can consider the function $Q(x,y)$ to be a sum of sectoral harmonics

$$Q(x,y) = \sum_{p=0}^{\infty} q_{a,p}T_{p,p} + q_{b,p}T'_{p,p}, \tag{4.1.3}$$

so that

$$\Psi = \left(\sum_{p=0}^{\infty} q_{a,p}T_{p,p} + q_{b,p}T'_{p,p}\right) + \left(\sum_{m=0}^{\infty}\sum_{n=m}^{\infty}\frac{1}{n+m+1}\left(B_{za,n,m}T_{n+1,m} + B_{zb,n,m}T'_{n+1,m}\right)\right).$$

Since the first sum is entirely sectoral while the second sum has no sectoral terms ($n+1 \neq m$), the sums may be unified by making the definition

$$q_{a,n} \equiv \frac{B_{za,n-1,n}}{2n}, \; q_{b,n} \equiv \frac{B_{zb,n-1,n}}{2n} \tag{4.1.4}$$

such that

$$Q_{n-1,m} = \frac{\delta_{n,m}}{2n}\left(B_{za,n-1,n}T_{n,n} + B_{zb,n-1,n}T'_{n,n}\right) \tag{4.1.5}$$

and the magnetic scalar potential becomes

$$\Psi = \sum_{m=0}^{\infty}\sum_{n=m-1}^{\infty}\frac{1}{n+m+1}\left(B_{za,n,m}T_{n+1,m} + B_{zb,n,m}T'_{n+1,m}\right). \tag{4.1.6}$$

Although equation 4.1.6 seems to be written in B_z harmonics, the physical meaning of the coefficients $B_{zab,m-1,m}$, where $n = m-1$, remains unclear since they do not contribute to the B_z field in equation 4.1.1. As a first step in clarifying their meaning we examine the functions $T_{m-1,m},\ T'_{m-1,n}$ through the Legendre polynomials $P_{m-1,m}$ defined in equation 2.1.32. That equation shows that when $n = m-1$, as it does for the coefficients $B_{zab,m-1,m}$, the polynomial $(1-x^2)^{m-1}$ has terms of maximum exponent $2(m-1)$, and after differentiating $m-1$ times the maximum exponent is reduced to $m-1$ such that the final m differentiations leave

$$P_{m-1,m}(x) = 0. \tag{4.1.7}$$

Therefore, the functions $T_{m-1,m}, T'_{m-1,m}$ are trivial in that they are identically zero everywhere. However since these functions are zero, their *coefficients* $B_{zab,m-1,m}$ need not be. In fact the coefficients play an important role in the following theory, and thus we give the name 'super-sectoral' to any spherical harmonic where $n = m-1$.

Let us now turn our attention to the contribution that these coefficients make to the transverse fields B_x and B_y. By setting $n = m-1$ in equation 4.1.2 we find

$$\begin{aligned} B_{x,m-1,m} &= \tfrac{1}{2}(1-\delta_{m,0})(2m-1)\left\{B_{za,m-1,m}T_{m-1,m-1} + B_{zb,m-1,m}T'_{m-1,m-1}\right\} + \frac{\partial Q_{m-1,m}}{\partial x} \\ B_{y,m-1,m} &= \tfrac{1}{2}(1-\delta_{m,0})(2m-1)\left\{B_{zb,m-1,m}T_{m-1,m-1} - B_{za,m-1,m}T'_{m-1,m-1}\right\} + \frac{\partial Q_{m-1,m}}{\partial y} \end{aligned} \tag{4.1.8}$$

and differentiation of equation 4.1.5 gives

$$\begin{aligned} \frac{\partial Q_{m-1,m}}{\partial x} &= \tfrac{1}{2}(1-\delta_{m,0})(2m-1)\left(B_{za,m-1,m}T_{m-1,m-1} + B_{zb,m-1,m}T'_{m-1,m-1}\right) \\ \frac{\partial Q_{m-1,m}}{\partial y} &= \tfrac{1}{2}(1-\delta_{m,0})(2m-1)\left(B_{zb,m-1,m}T_{m-1,m-1} - B_{za,m-1,m}T'_{m-1,m-1}\right) \end{aligned} \tag{4.1.9}$$

such that combining equations 4.1.8 and 4.1.9 produces

$$B_{x,m-1,m} = (1-\delta_{m,0})(2m-1)\left\{B_{za,m-1,m}T_{m-1,m-1} + B_{zb,m-1,m}T'_{m-1,m-1}\right\} \tag{4.1.10}$$

$$B_{y,m-1,m} = (1-\delta_{m,0})(2m-1)\left\{B_{zb,m-1,m}T_{m-1,m-1} - B_{za,m-1,m}T'_{m-1,m-1}\right\}. \tag{4.1.11}$$

Therefore the super-sectoral coefficients of B_z have physical meaning in that they are related to the sectoral harmonics of the transverse field. Moreover, by adding and subtracting equations 4.1.10 and 4.1.11 we find

$$\begin{aligned} B_{za,m-1,m} &= \tfrac{(1+\delta_{m-1,0})}{(2m-1)}\left(B_{xa,m-1,m-1} - B_{yb,m-1,m-1}\right) \\ B_{zb,m-1,m} &= \tfrac{(1+\delta_{m-1,0})}{(2m-1)}\left(B_{xb,m-1,m-1} + B_{ya,m-1,m-1}\right) \end{aligned} \tag{4.1.12}$$

where $B_{xab,m-1,m-1}$ and $B_{yab,m-1,m-1}$ are sectoral coefficients of the transverse fields from the sums

$$\begin{aligned} B_x &= \textstyle\sum_{m=0}^{\infty}\sum_{n=m}^{\infty} B_{xa,n,m}T_{n,m} + B_{xb,n,m}T'_{n,m} \\ B_y &= \textstyle\sum_{m=0}^{\infty}\sum_{n=m}^{\infty} B_{ya,n,m}T_{n,m} + B_{yb,n,m}T'_{n,m}. \end{aligned}$$

Thus the super-sectoral harmonic coefficients $B_{zab,m-1,m}$ may be computed directly from the harmonics of the transverse field ~ unlike the vague $Q(x, y)$ functions which they replace.

Now the B_z sum in equation 4.1.1 can be safely extended to super-sectoral harmonics due to equation 4.1.7 and thus we adjust all the magnetic field sums to absorb the integration constants of the magnetic scalar potential (super-sectoral harmonics of B_z) so that equations 4.1.1 and 4.1.2 become:

$$B_z = \sum_{m=0}^{\infty}\sum_{n=m-1}^{\infty} B_{z,n,m}, \quad B_x = \sum_{m=0}^{\infty}\sum_{n=m-1}^{\infty} B_{x,n,m}, \quad B_y = \sum_{m=0}^{\infty}\sum_{n=m-1}^{\infty} B_{y,n,m}$$

$$B_{z,n,m} = B_{za,n,m}T_{n,m} + B_{zb,n,m}T'_{n,m}$$

$$\begin{aligned} B_{x,n,m} = \quad & \tfrac{1}{2}\Big[-\tfrac{(1+\delta_{m,0})}{(n+m+1)}\left(B_{za,n,m}T_{n,m+1} + B_{zb,n,m}T'_{n,m+1}\right) + \\ & (1-\delta_{m,0})(n+m)\left(B_{za,n,m}T_{n,m-1} + B_{zb,n,m}T'_{n,m-1}\right)\Big] \end{aligned} \tag{4.1.13}$$

$$\begin{aligned} B_{y,n,m} = \quad & \tfrac{1}{2}\Big[\tfrac{(1+\delta_{m,0})}{(n+m+1)}\left(B_{zb,n,m}T_{n,m+1} - B_{za,n,m}T'_{n,m+1}\right) + \\ & (1-\delta_{m,0})(n+m)\left(B_{zb,n,m}T_{n,m-1} - B_{za,n,m}T'_{n,m-1}\right)\Big]. \end{aligned} \tag{4.1.14}$$

Although changing the summation indices has no influence on B_z, the transverse fields now depend on only two B_z harmonics rather than showing a vague dependence on $Q(x, y)$. Investigating the transverse fields when $n = m-1$ reveals that the harmonics $T_{m-1,m+1}$, $T_{m-1,m+1}$ are zero[1] but the harmonics $T_{m-1,m-1}$, $T'_{m-1,m-1}$ are the sectoral harmonics of the transverse field which arise partly from the integration constants in equation 4.1.2. The coefficients $B_{zab,m-1,m}$ provide a way to represent the part of the transverse field that is completely independent of B_z, which arises from currents flowing in the z-direction, within the summation for B_z. Note that the coefficient $B_{za,-1,0}$, which influences the $T_{0,0}$ component of the magnetic scalar potential, cannot be defined in this way since the transverse field harmonics $T_{-1,-1}, T'_{-1,-1}$ do not exist. Therefore, this coefficient remains undefined and is the arbitrary offset which may be added to any scalar potential. The coefficients $B_{zb,n,0}$ also remain undefined since $T'_{n,0} = 0$ and so, as far as the field is concerned, they can take any value. Later, in section 4.1.2.4 we set these coefficients to zero.

[1] The same logic used to develop equation 4.1.7 applies.

4.1.1.3 Summary

In summary, by assuming a B_z magnetic field of the form

$$\begin{aligned} B_z &= \textstyle\sum_{m=0}^{\infty} \sum_{n=m-1}^{\infty} B_{z,n,m} \\ B_{z,n,m} &= B_{za,n,m} T_{n,m} + B_{zb,n,m} T'_{n,m} \end{aligned} \tag{4.1.15}$$

a magnetic scalar potential

$$\begin{aligned} \Psi &= \textstyle\sum_{m=0}^{\infty} \sum_{n=m-1}^{\infty} \Psi_{n,m} \\ \Psi_{n,m} &= \frac{1}{n+m+1} \left(B_{za,n,m} T_{n+1,m} + B_{zb,n,m} T'_{n+1,m} \right) \end{aligned} \tag{4.1.16}$$

has been found along with the associated transverse magnetic fields

$$B_x = \sum_{m=0}^{\infty} \sum_{n=m-1}^{\infty} B_{x,n,m}, \quad B_y = \sum_{m=0}^{\infty} \sum_{n=m-1}^{\infty} B_{y,n,m}$$

$$\begin{aligned} B_{x,n,m} = \; & \tfrac{1}{2} \Big[-\tfrac{(1+\delta_{m,0})}{(n+m+1)} \left(B_{za,n,m} T_{n,m+1} + B_{zb,n,m} T'_{n,m+1} \right) + \\ & (1-\delta_{m,0})(n+m) \left(B_{za,n,m} T_{n,m-1} + B_{zb,n,m} T'_{n,m-1} \right) \Big] \end{aligned} \tag{4.1.17}$$

$$\begin{aligned} B_{y,n,m} = \; & \tfrac{1}{2} \Big[\tfrac{(1+\delta_{m,0})}{(n+m+1)} \left(B_{zb,n,m} T_{n,m+1} - B_{za,n,m} T'_{n,m+1} \right) + \\ & (1-\delta_{m,0})(n+m) \left(B_{zb,n,m} T_{n,m-1} - B_{za,n,m} T'_{n,m-1} \right) \Big]. \end{aligned} \tag{4.1.18}$$

where the coefficients of the super-sectoral harmonics of B_z are defined using equation 4.1.12. These super-sectoral harmonics have no physical significance for B_z but are the sectoral coefficients of the magnetic scalar potential which describe the part of the transverse fields unrelated to B_z – that is the sectoral harmonics of the transverse field. Only the coefficient $B_{za,-1,0}$ is devoid of physical significance since it is just an arbitrary offset of the magnetic scalar potential.

4.1.2 Vector Potential

Determining the vector potential from the magnetic field amounts to finding the inverse curl

$$\mathbf{A} = \nabla^{-1} \times \mathbf{B}. \tag{4.1.19}$$

This difficult task is made easier by working in a quasi-static source-free region (section 2.1.4) where both field and potential may be expressed in spherical harmonics such that the analysis may proceed term by term. Moreover, working in the Coulomb gauge (section 2.1.2) provides the vector potential with a freedom which may be exploited to simplify the mathematics.

4.1.2.1 Differentiating the Vector Potential

We start by computing the field from the harmonics of the vector potential using the relationships:

$$\begin{aligned} A_{x,n,m} &= A_{xa,n,m}T_{n,m} + A_{xb,n,m}T'_{n,m} \\ A_{y,n,m} &= A_{ya,n,m}T_{n,m} + A_{yb,n,m}T'_{n,m} \\ A_{z,n,m} &= A_{za,n,m}T_{n,m} + A_{zb,n,m}T'_{n,m} \end{aligned} \tag{4.1.20}$$

$$B_x = \frac{\partial A_z}{\partial y} - \frac{\partial A_y}{\partial z},\ B_y = \frac{\partial A_x}{\partial z} - \frac{\partial A_z}{\partial x},\ B_z = \frac{\partial A_y}{\partial x} - \frac{\partial A_x}{\partial y} \tag{4.1.21}$$

and the derivatives from table 2.3. We find

$$\begin{aligned} B_{x,n,m} = & -\frac{(1+\delta_{m,0})}{2}\left\{-A_{zb,n,m}T_{n-1,m+1} + A_{za,n,m}T'_{n-1,m+1}\right\} + \\ & -\frac{(1-\delta_{m,0})(n+m)(n+m-1)}{2}\left\{-A_{zb,n,m}T_{n-1,m-1} + A_{za,n,m}T'_{n-1,m-1}\right\} + \\ & -(n+m)\left(A_{ya,n,m}T_{n-1,m} + A_{yb,n,m}T'_{n-1,m}\right) \\ B_{y,n,m} = & \frac{(1+\delta_{m,0})}{2}\left\{A_{za,n,m}T_{n-1,m+1} + A_{zb,n,m}T'_{n-1,m+1}\right\} + \\ & -\frac{(1-\delta_{m,0})(n+m)(n+m-1)}{2}\left\{A_{za,n,m}T_{n-1,m-1} + A_{zb,n,m}T'_{n-1,m-1}\right\} + \\ & (n+m)\left(A_{xa,n,m}T_{n-1,m} + A_{xb,n,m}T'_{n-1,m}\right) \\ B_{z,n,m} = & \frac{-(1+\delta_{m,0})}{2}\left\{\left(A_{ya,n,m} + A_{xb,n,m}\right)T_{n-1,m+1} + \left(A_{yb,n,m} - A_{xa,n,m}\right)T'_{n-1,m+1}\right\} + \\ & \frac{(1-\delta_{m,0})(n+m)(n+m-1)}{2}\left\{\left(A_{ya,n,m} - A_{xb,n,m}\right)T_{n-1,m-1} + \left(A_{xa,n,m} + A_{yb,n,m}\right)T'_{n-1,m-1}\right\} \end{aligned} \tag{4.1.22}$$

where the indices are for the harmonics of the vector potential and not the field. In these equations one harmonic n, m of A_x or A_y influences two harmonics of B_z and a single harmonic of each transverse field. In contrast, a single harmonic n, m of A_z influences two harmonics of each transverse field but has no influence on B_z.

Although the harmonics of the vector potential are related to those of the field, it is not immediately obvious how to invert the relationship. Our first step is to change indices from those of the vector potential to those of the field and collect terms:

$$\begin{aligned} B_{x,n,m} = & \left(\frac{1}{2}(1+\delta_{m-1,0})A_{zb,n+1,m-1} + \frac{(1-\delta_{m+1,0})(n+m+1)(n+m+2)}{2}A_{zb,n+1,m+1} + \right. \\ & \left. -(n+m+1)A_{ya,n+1,m}\right)T_{n,m} + \\ & \left(-\frac{1}{2}(1+\delta_{m-1,0})A_{za,n+1,m-1} - \frac{(1-\delta_{m+1,0})(n+m+1)(n+m+2)}{2}A_{za,n+1,m+1} + \right. \\ & \left. -(n+m+1)A_{yb,n+1,m}\right)T'_{n,m} \end{aligned} \tag{4.1.23}$$

$$\begin{aligned} B_{y,n,m} = & \left(\frac{1}{2}(1+\delta_{m-1,0})A_{za,n+1,m-1} - \frac{(1-\delta_{m+1,0})(n+m+1)(n+m+2)}{2}A_{za,n+1,m+1} + \right. \\ & \left. (n+m+1)A_{xa,n+1,m}\right)T_{n,m} + \\ & \left(\frac{1}{2}(1+\delta_{m-1,0})A_{zb,n+1,m-1} - \frac{(1-\delta_{m+1,0})(n+m+1)(n+m+2)}{2}A_{zb,n+1,m+1} + \right. \\ & \left. (n+m+1)A_{xb,n+1,m}\right)T'_{n,m} \end{aligned} \tag{4.1.24}$$

$$B_{z,n,m} = \begin{array}{c} \frac{1}{2}\left\{-(1+\delta_{m-1,0})\left(A_{ya,n+1,m-1}+A_{xb,n+1,m-1}\right)+ \\ (1-\delta_{m+1,0})(n+m+1)(n+m+2)\left(A_{ya,n+1,m+1}-A_{xb,n+1,m+1}\right)\right\}T_{n,m}+ \\ \frac{1}{2}\left\{-(1+\delta_{m-1,0})\left(A_{yb,n+1,m-1}-A_{xa,n+1,m-1}\right)+ \\ (1-\delta_{m+1,0})(n+m+1)(n+m+2)\left(A_{xa,n+1,m+1}+A_{yb,n+1,m+1}\right)\right\}T'_{n,m} \end{array} \tag{4.1.25}$$

Which, considering only B_z (equation 4.1.25) gives

$$\begin{aligned} B_{za,n,m} = & \frac{-(1+\delta_{m-1,0})}{2}\left(A_{ya,n+1,m-1}+A_{xb,n+1,m-1}\right)+ \\ & \frac{(1-\delta_{m+1,0})(n+m+1)(n+m+2)}{2}\left(A_{ya,n+1,m+1}-A_{xb,n+1,m+1}\right) \\ B_{zb,n,m} = & \frac{-(1+\delta_{m-1,0})}{2}\left(A_{yb,n+1,m-1}-A_{xa,n+1,m-1}\right)+ \\ & \frac{(1-\delta_{m+1,0})(n+m+1)(n+m+2)}{2}\left(A_{xa,n+1,m+1}+A_{yb,n+1,m+1}\right) \end{aligned} \tag{4.1.26}$$

but this relationship is a ladder where each harmonic of B_z is influenced by two harmonics of transverse vector potential. To invert this relationship it seems one would need to know all the harmonics of B_z and then adjust all the harmonics of the vector potential correctly; a difficult task to say the least.

4.1.2.2 Determining A_x and A_y: A Question of Symmetry

Undaunted, we remember from section 2.1.2 that the vector potential is not unique and any gradient of a spherical harmonic[2] may be added without violating the Coulomb gauge criterion $\nabla \cdot \mathbf{A} = 0$. This allows a specific vector potential to be selected to simplify equation 4.1.26 and make the inverse curl (equation 4.1.19) possible. Again, table 2.3 provides us with a means of determining the gradient of symmetric and anti-symmetric spherical harmonics:

$$\begin{aligned} \nabla T_{n,m} = & \frac{1}{2}\left\{-(1+\delta_{m,0})T_{n-1,m+1}+(1-\delta_{m,0})(n+m)(n+m-1)T_{n-1,m-1}\right\} & \hat{x} \\ & \frac{1}{2}\left\{-(1+\delta_{m,0})T'_{n-1,m+1}-(1-\delta_{m,0})(n+m)(n+m-1)T'_{n-1,m-1}\right\} & \hat{y} \\ & (n+m)T_{n-1,m} & \hat{z} \\ \nabla T'_{n,m} = & \frac{1}{2}\left\{-(1+\delta_{m,0})T'_{n-1,m+1}+(1-\delta_{m,0})(n+m)(n+m-1)T'_{n-1,m-1}\right\} & \hat{x} \\ & \frac{1}{2}\left\{(1+\delta_{m,0})T_{n-1,m+1}+(1-\delta_{m,0})(n+m)(n+m-1)T_{n-1,m-1}\right\} & \hat{y} \\ & (n+m)T'_{n-1,m} & \hat{z} \end{aligned} \tag{4.1.27}$$

Careful consideration of this gradient reveals that by adding $a\nabla T_{n,m}$ to equation 4.1.20, any number a may be added to $A_{xa,n,m}$ provided it is also subtracted from $A_{yb,n,m}$; similarly adding $b\nabla T'_{n,m}$ allows any number b to be added to $A_{xb,n,m}$ provided it is also added to $A_{ya,n,m}$. Of course adding such terms has an influence on terms $(n-1, m+1)$ in transverse $\mathbf{A}$ and $(n-1, m)$ in A_z but the transverse influence can be

[2] Actually the gradient of any solution to Laplace's equation.

controlled by adding gradient terms of successively higher degree. In this way we may constrain the vector potential such that

$$A_{xb,n,m} = -A_{ya,n,m}, \;\; A_{xa,n,m} = A_{yb,n,m} \tag{4.1.28}$$

causing equation 4.1.25 to become

$$B_{z,n,m} = (1 - \delta_{m+1,0})(n + m + 1)(n + m + 2)\left\{A_{ya,n+1,m+1}T_{n,m} + A_{yb,n+1,m+1}T'_{n,m}\right\} \tag{4.1.29}$$

and we pick out the coefficients

$$\begin{aligned} A_{ya,n+1,m+1} &= \tfrac{B_{za,n,m}}{(n+m+1)(n+m+2)} \\ A_{xa,n+1,m+1} &= \tfrac{B_{zb,n,m}}{(n+m+1)(n+m+2)} \end{aligned} \tag{4.1.30}$$

where we have noted that $m \neq -1$ under any circumstance. Using these coefficients with equations 4.1.20 and 4.1.28 reveals a relation between the transverse components of the vector potential and B_z:

$$\begin{aligned} A_{x,n,m} &= \tfrac{B_{zb,n,m}T_{n+1,m+1} - B_{za,n,m}T'_{n+1,m+1}}{(n+m+1)(n+m+2)} \\ A_{y,n,m} &= \tfrac{B_{za,n,m}T_{n+1,m+1} + B_{zb,n,m}T'_{n+1,m+1}}{(n+m+1)(n+m+2)} \end{aligned} \tag{4.1.31}$$

leaving only $A_{z,n,m}$ out of reach.

Therefore freedom in the Coulomb gauge has been used to make a harmonic of the transverse vector potential influence only one B_z harmonic, rather than two as in equation 4.1.22. Instead, this freedom could have been used to form simple relationships between the harmonics of B_x or B_y and the vector potential, but we have chosen to focus our attention on B_z. Stated differently, an infinite set of vector potentials satisfies the Coulomb gauge criterion $\nabla \cdot \mathbf{A} = 0$ but only a subset allows a simple mapping from harmonics of B_z to those of transverse vector potential; we have found and chosen that subset.

4.1.2.3 Determining A_z: Constraining the Vector Potential

Now in order to find the harmonics of A_z we re-arrange equation 4.1.21 as

$$\frac{\partial A_z}{\partial y} = B_x + \frac{\partial A_y}{\partial z}. \tag{4.1.32}$$

but any harmonics of B_x and $\frac{\partial A_y}{\partial z}$ or ladder combination thereof could be tried in attempt to find a harmonic representation of $\frac{\partial A_z}{\partial y}$ which reveals $A_{z,n,m}$. However, if we remember that the harmonics of B_x can be found from equation 4.1.17 via the scalar potential while those of $\frac{\partial A_y}{\partial z}$ are found by differentiating equation 4.1.31 such that

$$\frac{\partial A_{y,n,m}}{\partial z} = \frac{B_{za,n,m}T_{n,m+1} + B_{zb,n,m}T'_{n,m+1}}{(n+m+1)}$$

then we can write equation 4.1.32 using harmonics that are all derived from the same B_z coefficients:

$$\frac{\partial A_{z,n,m}}{\partial y} = B_{x,n,m} + \frac{B_{za,n,m}T_{n,m+1} + B_{zb,n,m}T'_{n,m+1}}{(n+m+1)} \tag{4.1.33}$$

$$\frac{\partial A_{z,n,m}}{\partial y} = \begin{array}{c} \frac{1}{2}\left[-\frac{(1+\delta_{m,0})}{(n+m+1)}\left(B_{za,n,m}T_{n,m+1} + B_{zb,n,m}T'_{n,m+1}\right) + \right. \\ \left.(1-\delta_{m,0})(n+m)\left(B_{za,n,m}T_{n,m-1} + B_{zb,n,m}T'_{n,m-1}\right)\right] + \frac{B_{za,n,m}T_{n,m+1}+B_{zb,n,m}T'_{n,m+1}}{(n+m+1)} \end{array}.$$

Fortunately, the right side of this equation is an anti-derivative as seen from combining lines 2 and 5 in table 2.3 so that

$$A_{z,n,m} = \frac{(1-\delta_{m,0})\left(-B_{zb,n,m}T_{n+1,m} + B_{za,n,m}T'_{n+1,m}\right)}{(n+m+1)} + C(x,z) \tag{4.1.34}$$

where $C(x,z)$ is a function acting as a constant of integration.

Now applying these same logical steps starting from $\frac{\partial A_z}{\partial x} = \frac{\partial A_x}{\partial z} - B_y$ rather than equation 4.1.32 we also find

$$A_{z,n,m} = \frac{(1-\delta_{m,0})\left(-B_{zb,n,m}T_{n+1,m} + B_{za,n,m}T'_{n+1,m}\right)}{(n+m+1)} + D(y,z) \tag{4.1.35}$$

and if both equations 4.1.34 and 4.1.35 are true, the integration constants must obey $C(x,z) = D(y,z) = E(z)$. Note that $E(z)$ has no effect on the magnetic field since $\mathbf{B} = \nabla \times \mathbf{A}$ (equation 4.1.21) guarantees that only x and y derivatives are ever applied to A_z; this means that $E(z)$ is a manifestation of freedom still remaining in the vector potential. Although the function $E(z)$ could be broken into zonal harmonics, we arbitrarily constrain the vector potential such that $E(z) = 0$ yielding

$$A_{z,n,m} = \frac{(1-\delta_{m,0})\left(-B_{zb,n,m}T_{n+1,m} + B_{za,n,m}T'_{n+1,m}\right)}{(n+m+1)}. \tag{4.1.36}$$

Having found a form for $A_{z,n,m}$ we now ask if there is any alternative to our proposal in equation 4.1.33. We know that the vector potential can be written in spherical harmonics and that equation 4.1.32 is true; therefore by differentiating a single harmonic of A_z we see the same pattern of harmonics as in equation 4.1.33 which is the only pattern possible. Therefore we have stumbled across the correct set of field harmonics to associate with $A_{z,n,m}$ plus or minus an arbitrary function $E(z)$ which has no influence on the magnetic field and which we have therefore set to zero. One can also approach this problem starting with coefficients of A_z rather than coefficients of the field but this makes the pattern of harmonics *much* more difficult to recognize; in that case, however, the function $E(z)$ arises from zonal harmonics of A_z rather than as an arbitrary integration constant.

4.1.2.4 Verifying the Vector Potential

The analysis used to determine the vector potential from the field, leading to equations 4.1.31 and 4.1.36, is not a mechanical derivation using straightforward rules like those used to find the scalar potential. Therefore it is natural to question whether the correct vector potential has actually been found. Fortunately we have two simple checks that can be used to verify our result, namely $\nabla \times \mathbf{A} = \mathbf{B}$ and $\nabla \cdot \mathbf{A} = 0$. Certainly the magnetic field as determined from the vector potential should match equations 4.1.15, 4.1.17, and 4.1.18 determined from the scalar potential and the vector potential should still satisfy the Coulomb criterion.

Magnetic field from the vector potential using table 2.3: To find B_z from the vector potential we employ

$$B_{z,n,m} = \frac{\partial A_{y,n,m}}{\partial x} - \frac{\partial A_{x,n,m}}{\partial y}$$

such that

$$B_{z,n,m} = \frac{1}{(n+m+1)(n+m+2)(1-\delta_{m+1,0})} \left\{ \begin{array}{c} \left[B_{za,n,m} \frac{1}{2} \{ -(1+\delta_{m+1,0}) T_{n,m+2} + \\ (1-\delta_{m+1,0})(n+m+1)(n+m+2) T_{n,m} \} + \\ B_{zb,n,m} \frac{1}{2} \left\{ -(1+\delta_{m+1,0}) T'_{n,m+2} + \\ (1-\delta_{m+1,0})(n+m+1)(n+m+2) T'_{n,m} \right\} \right] - \\ \left[B_{zb,n,m} \frac{1}{2} \left\{ -(1+\delta_{m+1,0}) T'_{n,m+2} - \\ (1-\delta_{m+1,0})(n+m+1)(n+m+2) T'_{n,m} \right\} - \\ B_{za,n,m} \frac{1}{2} \{ (1+\delta_{m+1,0}) T_{n,m+2} + \\ (1-\delta_{m+1,0})(n+m+1)(n+m+2) \} \right] \end{array} \right\}$$

which simplifies to $B_{z,n,m} = B_{za,n,m} T_{n,m} + B_{zb,n,m} T'_{n,m}$ as it should. For B_x we have

$$B_{x,n,m} = \frac{\partial A_{z,n,m}}{\partial y} - \frac{\partial A_{y,n,m}}{\partial z}$$

$$B_{x,n,m} = \begin{array}{c} \frac{(1-\delta_{m,0})}{(n+m+1)} \left[-B_{zb,n,m} \frac{1}{2} \left\{ -(1+\delta_{m,0}) T'_{n,m+1} - (1-\delta_{m,0})(n+m)(n+m+1) T'_{n,m-1} \right\} \right. \\ \left. + B_{za,n,m} \frac{1}{2} \{ (1+\delta_{m,0}) T_{n,m+1} + (1-\delta_{m,0})(n+m)(n+m+1) T_{n,m-1} \} \right] - \\ \frac{1}{(n+m+1)(n+m+2)(1-\delta_{m+1,0})} \left[B_{za,n,m}(n+m+2) T_{n,m+1} + \right. \\ \left. B_{zb,n,m}(n+m+2) T'_{n,m+1} \right] \end{array}$$

which becomes

$$B_{x,n,m} = \begin{array}{c} \frac{(1-\delta_{m,0})}{(n+m+1)}\left[B_{zb,n,m}\frac{1}{2}\left\{T'_{n,m+1} + (n+m)(n+m+1)T'_{n,m-1}\right\}\right. \\ \left. +B_{za,n,m}\frac{1}{2}\left\{T_{n,m+1} + (n+m)(n+m+1)T_{n,m-1}\right\}\right] - \\ \frac{1}{(n+m+1)}\left[B_{za,n,m}T_{n,m+1} + \right. \\ \left. B_{zb,n,m}T'_{n,m+1}\right] \end{array}$$

and then

$$B_{x,n,m} = \begin{array}{c} \frac{\left(\frac{(1-\delta_{m,0})}{2}-1\right)}{(n+m+1)}\left[B_{za,n,m}T_{n,m+1} + B_{zb,n,m}T'_{n,m+1}\right] + \\ \frac{1}{2}(1-\delta_{m,0})(n+m)\left[B_{za,n,m}T_{n,m-1} + B_{zb,n,m}T'_{n,m-1}\right]. \end{array}$$

This simplifies to

$$B_{x,n,m} = \begin{array}{c} \frac{1}{2}\left[-\frac{(1+\delta_{m,0})}{(n+m+1)}\left(B_{za,n,m}T_{n,m+1} + B_{zb,n,m}T'_{n,m+1}\right) + \right. \\ \left. (1-\delta_{m,0})(n+m)\left(B_{za,n,m}T_{n,m-1} + B_{zb,n,m}T'_{n,m-1}\right)\right] \end{array}$$

which is identical to equation 4.1.17 and verification of $B_{y,n,m}$ is so similar that it need not be shown. Thus algebraic brute force verifies that the vector potential gives rise to the correct magnetic field.

Testing that $\nabla \cdot \mathbf{A} = 0$: Again this is merely a matter of algebraic manipulation using derivatives from table 2.3. The divergence is $\nabla \cdot \mathbf{A}_{n,m} = \frac{\partial A_{x,n,m}}{\partial x} + \frac{\partial A_{y,n,m}}{\partial y} + \frac{\partial A_{z,n,m}}{\partial z}$ where

$$\frac{\partial A_{x,n,m}}{\partial x} = \frac{\begin{array}{c}\left[B_{zb,n,m}\frac{1}{2}\left\{-(1+\delta_{m+1,0})T_{n,m+2} + (1-\delta_{m+1,0})(n+m+1)(n+m+2)T_{n,m}\right\} - \right. \\ \left. B_{za,n,m}\frac{1}{2}\left\{-(1+\delta_{m+1,0})T'_{n,m+2} + (1-\delta_{m+1,0})(n+m+1)(n+m+2)T'_{n,m}\right\}\right]\end{array}}{(n+m+1)(n+m+2)(1-\delta_{m+1,0})}$$

$$\frac{\partial A_{y,n,m}}{\partial y} = \frac{\begin{array}{c}\left[B_{za,n,m}\frac{1}{2}\left\{-(1+\delta_{m+1,0})T'_{n,m+2} - (1-\delta_{m+1,0})(n+m+1)(n+m+2)T'_{n,m}\right\} + \right. \\ \left. B_{zb,n,m}\frac{1}{2}\left\{(1+\delta_{m+1,0})T_{n,m+2} + (1-\delta_{m+1,0})(n+m+1)(n+m+2)T_{n,m}\right\}\right]\end{array}}{(n+m+1)(n+m+2)(1-\delta_{m+1,0})}$$

$$\frac{\partial A_{z,n,m}}{\partial z} = (1-\delta_{m,0})\left[-B_{zb,n,m}T_{n,m} + B_{za,n,m}T'_{n,m}\right].$$

Collecting the coefficients for various harmonics

$$\begin{array}{rl} T_{n,m}: & B_{zb,n,m} - (1-\delta_{m,0})B_{zb,n,m} = 0 \quad \text{where } m \neq 0 \\ T'_{n,m}: & -B_{za,n,m} + (1-\delta_{m,0})B_{za,n,m} = 0 \quad \text{where } m \neq 0 \end{array}$$

$$\begin{array}{rl} T_{n,m+2}: & \frac{(1+\delta_{m+1,0})\left(-B_{zb,n,m}+B_{zb,n,m}\right)}{2(n+m+1)(n+m+2)(1-\delta_{m+1,0})} = 0 \\ T'_{n,m+2}: & \frac{(1+\delta_{m+1,0})\left(B_{za,n,m}-B_{za,n,m}\right)}{2(n+m+1)(n+m+2)(1-\delta_{m+1,0})} = 0 \end{array}$$

gives an obvious zero for every case except $m = 0$. In that case, however, $T'_{n,0} = 0$ so the coefficient of $T_{n,0}$ is $B_{zb,n,0} - (1 - \delta_{0,0})B_{zb,n,0} = B_{zb,n,0}$ and thus we require that $B_{zb,n,0} = 0$ to satisfy the Coulomb criterion. Note that until now the coefficients $B_{zb,n,0}$ have not had any definition with regard to the field since $T'_{n,0}$ is everywhere zero but these coefficients do influence the vector potential so we must set $B_{zb,n,0} = 0$ for the vector potential to remain a member of the Coulomb gauge.

4.1.3 Relationships between Fields and Potentials

In a quasi-static source-free region the mathematics above allows one set of coefficients to be used to describe the complete vector magnetic field, vector potential, and scalar potential. These coefficients can either be thought of as the spherical harmonic coefficients of the magnetic scalar potential or those of B_z plus some terms for sectoral B_{xy}. Each coefficient represents a complete and independent solution to Maxwell's equations, albeit in a quasi-static source-free region, and these solutions can be built up to describe any physically realizable solution therein. To make the results of this analysis clear, table 4.1 presents all the important relationships between the fields and potentials with their respective equation numbers. In that table, Ψ_0 is an arbitrary number, E is an arbitrary sum of zonal harmonics and the coefficients $B_{za,n,m}$ and $B_{zb,n,m}$ are usually the spherical harmonic coefficients of the B_z field. However when $m = 0$ we set $B_{zb,n,0} = 0$ since it would otherwise remain undefined; and when $n = m - 1$, the super-sectoral case, the coefficients are derived using the equations in table 4.2.

4.1.4 Examples

Despite their difficult derivation, the relationships in table 4.1 are easily applied. As a first example, consider a uniform z-directed magnetic field produced within an infinitely long solenoid. Here only the coefficient $B_{za,0,0} = 1$ is non-zero and the equations from table 4.1 give

$$\begin{aligned} B_x &= 0 & A_x &= -\tfrac{1}{2}T'_{1,1} = -y \\ B_y &= 0 & A_y &= \tfrac{1}{2}T_{1,1} = x \\ B_z &= 1 & A_z &= 0 \end{aligned}$$
$$\Psi = T_{1,0} = z$$

since $T'_{0,0} = T_{0,1} = T'_{0,1} = 0$. Note that there are no transverse fields, as is expected within a solenoid, and that the potentials do indeed produce $B_z = 1$. All the information about the potentials and transverse fields can be immediately found from knowledge of B_z.

Increasing the field complexity slightly, let us now consider a magnetic field where only the coefficient $B_{za,1,0} = 1$ differs from zero; this is a z-gradient which may be produced by passing current through a Maxwell coil as seen in figure 4.1a. In this case the equations from table 4.1 give

Equation	Equation Number
$B_x = \sum_{m=0}^{\infty} \sum_{n=m-1}^{\infty} B_{x,n,m}$ $B_y = \sum_{m=0}^{\infty} \sum_{n=m-1}^{\infty} B_{y,n,m}$ $B_z = \sum_{m=0}^{\infty} \sum_{n=m-1}^{\infty} B_{z,n,m}$	
$\Psi = \Psi_0 + \sum_{m=0}^{\infty} \sum_{n=m-1}^{\infty} \Psi_{n,m}$ $A_x = \sum_{m=0}^{\infty} \sum_{n=m-1}^{\infty} A_{x,n,m}$ $A_y = \sum_{m=0}^{\infty} \sum_{n=m-1}^{\infty} A_{y,n,m}$ $A_z = E + \sum_{m=0}^{\infty} \sum_{n=m-1}^{\infty} A_{z,n,m}$	
$B_{x,n,m} = \frac{1}{2(n+m+1)} \left\{ -(1+\delta_{m,0}) \left\{ B_{za,n,m} T_{n,m+1} + B_{zb,n,m} T'_{n,m+1} \right\} + (1-\delta_{m,0})(n+m)(n+m+1) \left\{ B_{za,n,m} T_{n,m-1} + B_{zb,n,m} T'_{n,m-1} \right\} \right\}$	4.1.17
$B_{y,n,m} = \frac{1}{2(n+m+1)} \left\{ (1+\delta_{m,0}) \left\{ B_{zb,n,m} T_{n,m+1} - B_{za,n,m} T'_{n,m+1} \right\} + (1-\delta_{m,0})(n+m)(n+m+1) \left\{ B_{zb,n,m} T_{n,m-1} - B_{za,n,m} T'_{n,m-1} \right\} \right\}$	4.1.18
$B_{z,n,m} = B_{za,n,m} T_{n,m} + B_{zb,n,m} T'_{n,m}$	4.1.15
$A_{x,n,m} = \frac{B_{zb,n,m} T_{n+1,m+1} - B_{za,n,m} T'_{n+1,m+1}}{(n+m+1)(n+m+2)}$	4.1.31
$A_{y,n,m} = \frac{B_{za,n,m} T_{n+1,m+1} + B_{zb,n,m} T'_{n+1,m+1}}{(n+m+1)(n+m+2)}$	4.1.31
$A_{z,n,m} = \frac{(1-\delta_{m,0})}{(n+m+1)} \left(-B_{zb,n,m} T_{n+1,m} + B_{za,n,m} T'_{n+1,m} \right)$	4.1.36
$\Psi_{n,m} = \frac{1}{n+m+1} \left(B_{za,n,m} T_{n+1,m} + B_{zb,n,m} T'_{n+1,m} \right)$	4.1.16

Table 4.1: The equations above are written with indices for the spherical harmonics of B_z and are copied from the equation numbers listed.

Equation	Equation Number
$B_{za,m-1,m} = \frac{(1+\delta_{m-1,0})}{(2m-1)} \left(B_{xa,m-1,m-1} - B_{yb,m-1,m-1} \right)$	4.1.12
$B_{zb,m-1,m} = \frac{(1+\delta_{m-1,0})}{(2m-1)} \left(B_{xb,m-1,m-1} + B_{ya,m-1,m-1} \right)$	4.1.12

Table 4.2: The super-sectoral coefficients are derived from the sectoral components of the transverse fields and have no physical significance for the B_z field.

$$\begin{aligned} B_x &= -\tfrac{1}{2}T_{1,1} = -\tfrac{1}{2}x & A_x &= -\tfrac{1}{6}T'_{2,1} = -\tfrac{1}{2}yz \\ B_y &= -\tfrac{1}{2}T'_{1,1} = -\tfrac{1}{2}y & A_y &= \tfrac{1}{6}T_{2,1} = \tfrac{1}{2}xz \\ B_z &= z & A_z &= 0 \\ \Psi &= \tfrac{1}{2}T_{2,0} = \tfrac{1}{4}\left(2z^2 - y^2 - x^2\right) \end{aligned} \tag{4.1.37}$$

where the transverse fields match those produced about the centre of a Maxwell coil (see figure 4.1c-d) and the transverse fields exist to support the field $B_z = z$. Again, the transverse fields and potentials are found with ease from the knowledge that $B_z = z$. However, as the region of interest within the Maxwell coil increases, a single coefficient $B_{za,1,0} = 1$ is no longer sufficient to describe the field within that region – more coefficients are required.

Thus far we have considered examples where $B_z \neq 0$; however, when the current is entirely in the z-direction the B_z field vanishes and only super-sectoral coefficients are required. The field associated with the first of these coefficients $B_{za,0,1} = 1$ is

$$\begin{aligned} B_x &= \tfrac{1}{2}T_{0,0} = \tfrac{1}{2} & A_x &= 0 \\ B_y &= 0 & A_y &= 0 \\ B_z &= 0 & A_z &= \tfrac{1}{2}T'_{1,1} = \tfrac{1}{2}y \\ \Psi &= \tfrac{1}{2}T_{1,1} = \tfrac{1}{2}x \end{aligned} \tag{4.1.38}$$

and exists in the half-space where $y < 0$ provided that a uniform current flows in the z-direction over the entire zx-plane. Although this is merely a uniform B_x field, note how table 4.2 can be used to determine that $B_{za,0,1} = 2B_{xa,0,0}$ since $B_x = \frac{1}{2}T_{0,0}$.

A slightly more interesting super-sectoral example is $B_{za,1,2} = 1$. Yet again tables 4.1 and 4.2 can be used to determine the associated fields and potentials:

$$\begin{aligned} B_x &= \tfrac{3}{2}T_{1,1} = \tfrac{3}{2}x & A_x &= 0 \\ B_y &= -\tfrac{3}{2}T'_{1,1} = -\tfrac{3}{2}y & A_y &= 0 \\ B_z &= 0 & A_z &= \tfrac{1}{4}T'_{2,2} = \tfrac{3}{2}xy \\ \Psi &= \tfrac{1}{4}T_{2,2} = \tfrac{3}{4}\left(x^2 - y^2\right). \end{aligned} \tag{4.1.39}$$

which may be physically realized, as shown in figure 4.1e-f, using a cylindrical array of current filaments. Just as within the Maxwell coil, the field produced within this array can be accurately described with a single harmonic coefficient ($B_{za,1,2}$) provided that the region of interest is not too large.

These examples demonstrate that each harmonic coefficient represents a physically realizable field configuration, at least within a quasi-static region of interest. Moreover, the super-sectoral harmonics introduced in section 4.1.1.2 have a simple interpretation: they correspond to allowable field configurations

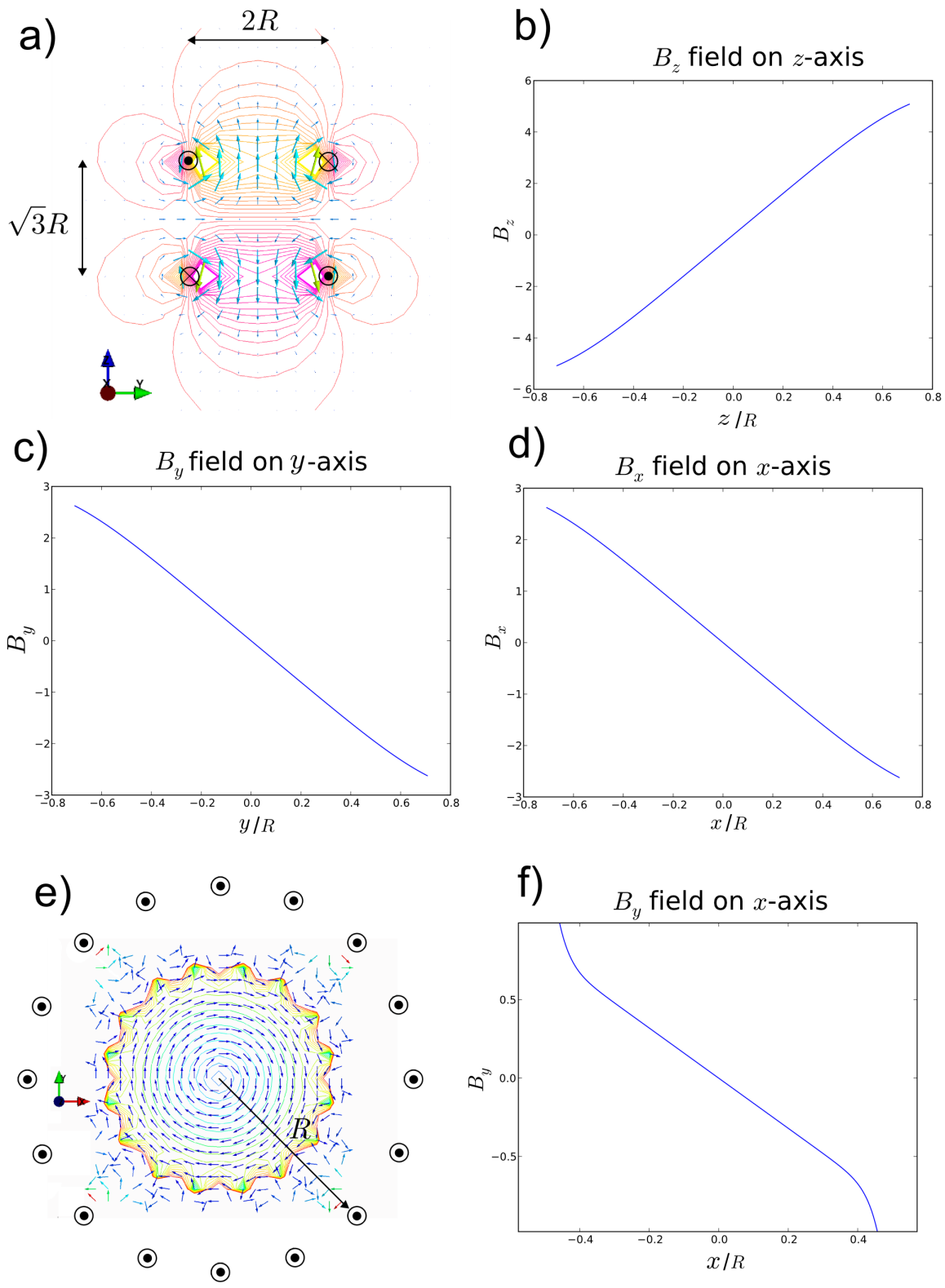

Figure 4.1: In a) we see the field produced by a Maxwell coil in the zy-plane. The arrows point in the direction of the field while the contours correspond to the values of B_z. Parts b-d) each plot a single component of the magnetic field produced by the Maxwell coil along an axis. In e), sixteen infinitely long filaments carry current in the z-direction. The contours correspond to values of B_ϕ while the arrows point in the direction of the field as before. In f) the field B_y arising from the current filaments is plotted along the x-axis; the plot of B_ϕ along any axis in the zy-plane passing through the origin has the same shape.

where $B_z = 0$. Given a series of harmonic coefficients, the equations of table 4.1 provide simple[3] and direct access to a polynomial representation of the fields and potentials in terms of the coordinates x, y, z. The relationships developed in this section may be useful for a broad range of problems.

4.2 Determining the Coil Pattern

Using the relationships developed in the last section, our goal is now to produce a wire pattern where the sum of the voltages induced by a changing magnetic field cancel for every B_z harmonic except one. Then the voltage measured at the coil leads is proportional to the time derivative of that unique harmonic.

The design processes for harmonic detection and harmonic production (gradient/shim) coils (chapter 3.1) are similar in that both seek an optimum wire pattern on the surface of a cylinder. However, upon investigation of target field methods (section 3.1.1.1), we see that there are no target field points readily available in the detection problem. Therefore, a method is used which describes the field in terms of an orthogonal basis set and since shim coils have been designed along these lines by Hoult and Deslauriers [50], it is their general mathematical pathway which we follow.

4.2.1 Voltage induced in a Wire Distribution

From equation 2.1.12, the voltage induced in an elementary length of wire $d\mathbf{l}$ at some point P on the surface of a cylindrical coil former is $dV = -(\nabla\Theta) \cdot d\mathbf{l} - \frac{\partial}{\partial t}\mathbf{A} \cdot d\mathbf{l}$ where Θ is the electric scalar potential from equation 2.1.8. Now as a point of clarification, the mathematics of this section uses two kinds of points: as shown in figure 4.2, we use spherical coordinates (r, θ, ϕ) for the field points and spherical (f, α, ψ) or cylindrical (z, R, ψ) coordinates for the location of elementary wires. Now if we have at P several such elementary wire lengths in parallel covering a width ds, with each length being ultimately in series as part of a single distributed winding, then the induced voltage at P is $dV = -(Wds)\frac{\partial}{\partial t}\mathbf{A} \cdot d\mathbf{l}$ where W is the wire winding density in wires per meter and the contribution from $\mathbf{\Theta}$ is dropped because the path eventually forms a closed loop. If da is the elementary area $dsdl$, then for the entire winding

$$V = -\frac{d}{dt}\int \mathbf{A} \cdot \mathbf{W} da \equiv -\frac{d}{dt}\int \Phi da \equiv -\frac{d}{dt}\Phi_T \tag{4.2.1}$$

where $\mathbf{W}$ is the *vector* winding density which lies on the cylinder's surface, Φ is magnetic flux linkage at point P, and Φ_T is the total flux linkage (equation 2.1.13). We must now deduce $\mathbf{W}$ over the surface of the cylinder such that $V = 0$ for all potentials $\mathbf{A}$ but that desired. If, inside a sphere that encompasses the coil former, we now write the vector potential $\mathbf{A}$ as a sum of spherical harmonics arising from the magnetic field $\mathbf{B}$ according to the equations of section 4.1, we may compute the integral $\Phi_T = \int \mathbf{A} \cdot \mathbf{W} da$ over a cylindrical surface with radius R.

[3] Converting the spherical harmonics $T_{n,m}$ and $T'_{n,m}$ into polynomials can be time consuming by hand but is easy to automate with a computer algebra system.

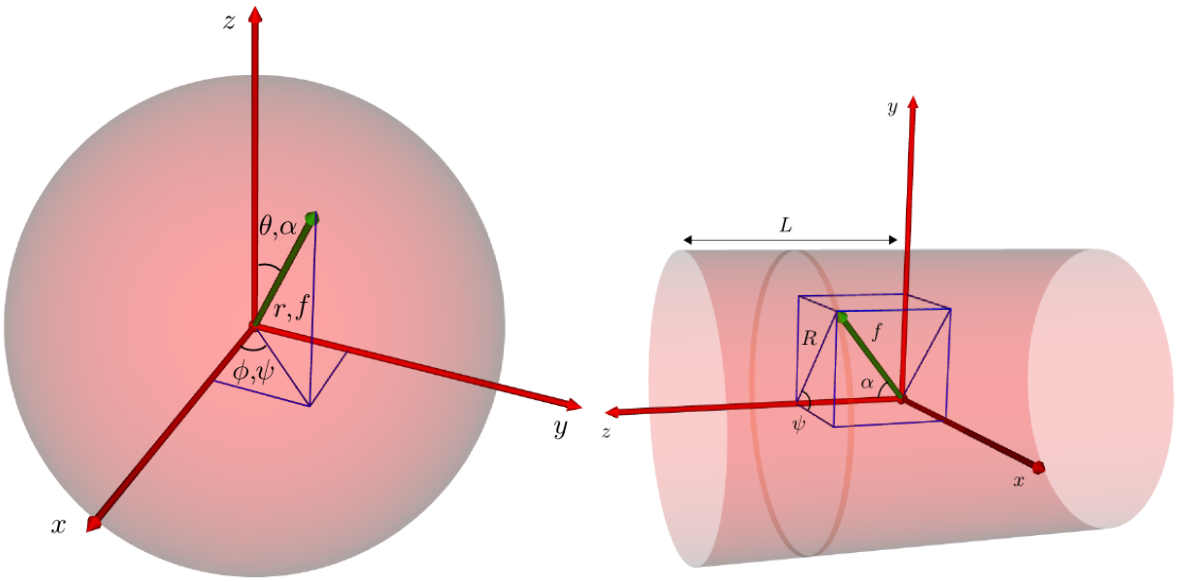

Figure 4.2: In a) a field or potential point has spherical coordinates (r, θ, ϕ) but source points, actually voltage induction points in this case, have coordinates (f, α, ψ). In b) the cylindrical coil former coordinates (z, R, ψ) of a wire density element are shown with equivalent spherical coordinates (f, α, ψ). The coil former dimensions R and L are fixed.

We express the wire density on the surface of the coil former $\mathbf{W}$ as a Fourier series:

$$\begin{aligned} W_z(z, \psi) &= F_j(z) \sin(j\psi) \\ W_\psi(z, \psi) &= G_j(z) \cos(j\psi) \end{aligned} \tag{4.2.2}$$

where j is an integer and the relation

$$F_j(z) = \frac{j}{R} \int G_j(z) dz \tag{4.2.3}$$

ensures the condition $\nabla \cdot \mathbf{W} = 0$[4] is met. Choosing W_ψ to depend on $\cos(j\psi)$ rather than $\sin(j\psi)$ restricts our calculation to the detection of $B_{z,n,m} = B_{za,n,m} T_{n,m}$ but we can easily extend the result to $T'_{n,m}$ by rotating the wire density. Using this wire density, the contribution to the total flux linkage at point $P(R, \psi, z)$ (or $P(f, \alpha, \psi)$ in spherical coordinates) is

$$\Phi da = \mathbf{A} \cdot \mathbf{W} da = \left((-A_x \sin\psi + A_y \cos\psi) W_\psi + A_z W_z \right) dz R d\psi \tag{4.2.4}$$

and the flux linkage to a complete cylindrical wire density can be found by integrating this equation over ψ and z with R kept fixed.

[4]This is just the continuity equation 2.1.6 adapted for the winding density.

4.2.2 Integrating the Vector Potential

We start the vector potential integral by employing equations 4.1.31 and 4.1.36 so that the integral of a single harmonic term in equation 4.2.4 becomes

$$\Phi_{n,m} = R\int_{-L}^{L}\int_{-\pi}^{\pi}\begin{pmatrix} -\frac{B_{zb,n,m}T_{n+1,m+1}-B_{za,n,m}T'_{n+1,m+1}}{(n+m+1)(n+m+2)}\sin(\psi)G_j(z)\cos(j\psi)+ \\ \frac{B_{za,n,m}T_{n+1,m+1}+B_{zb,n,m}T'_{n+1,m+1}}{(n+m+1)(n+m+2)}\cos(\psi)G_j(z)\cos(j\psi)+ \\ \frac{(1-\delta_{m,0})}{(n+m+1)}\left(-B_{zb,n,m}T_{n+1,m}+B_{za,n,m}T'_{n+1,m}\right)F_j(z)\sin(j\psi)\end{pmatrix}d\psi dz.$$

Collecting terms we have

$$\Phi_{n,m} = R\int_{-L}^{L}\int_{-\pi}^{\pi}\Big((C_1+C_2)\,G_j(z)+(C_3+C_4)\,F_j(z)\Big)\,d\psi dz$$

where

$$C_1 = \frac{B_{za,n,m}\cos(\psi)-B_{zb,n,m}\sin(\psi)}{(n+m+1)(n+m+2)}\cos(j\psi)T_{n+1,m+1}(f,\alpha,\psi)$$

$$C_2 = \frac{B_{zb,n,m}\cos(\psi)+B_{za,n,m}\sin(\psi)}{(n+m+1)(n+m+2)}\cos(j\psi)T'_{n+1,m+1}(f,\alpha,\psi)$$

$$C_3 = -\frac{(1-\delta_{m,0})\,B_{zb,n,m}}{(n+m+1)}\sin(j\psi)T_{n+1,m}(f,\alpha,\psi)$$

$$C_4 = \frac{(1-\delta_{m,0})\,B_{za,n,m}}{(n+m+1)}\sin(j\psi)T'_{n+1,m}(f,\alpha,\psi).$$

This leaves four separate integrals which may be added to find the total flux linkage due to a single B_z harmonic

$$\Phi_{n,m} = \Delta z R\Big[(I_1+I_2)\,G_j(z)+(I_3+I_4)\,F_j(z)\Big],\quad I_k = \int_{-L}^{L}\int_{-\pi}^{\pi}C_k\,d\psi dz. \tag{4.2.5}$$

4.2.2.1 I_1

Starting with I_1 we have

$$I_1 = \int_{-L}^{L}\int_{-\pi}^{\pi}\frac{f^{n+1}P_{n+1,m+1}(\cos\alpha)\left(B_{za,n,m}\cos(\psi)-B_{zb,n,m}\sin(\psi)\right)}{(n+m+1)(n+m+2)}\cos(j\psi)\cos((m+1)\psi)d\psi dz$$

where we remember that the integral of an odd function over an even interval such as $-\pi$ to π is zero such that the contribution of $B_{zb,n,m}\sin(\psi)\cos(j\psi)\cos((m+1)\psi)$ to this integral is equal to zero. Therefore we are left with

$$I_1 = \int_{-L}^{L} \frac{f^{n+1} P_{n+1,m+1}(\cos\alpha) B_{za,n,m}}{(n+m+1)(n+m+2)} dz \int_{-\pi}^{\pi} \cos(\psi)\cos(j\psi)\cos((m+1)\psi) d\psi$$

and a little trigonometric manipulation gives

$$\begin{aligned}\int_{-\pi}^{\pi} \cos(\psi)\cos(j\psi)\cos((m+1)\psi) d\psi &= \tfrac{1}{2}\int_{-\pi}^{\pi} \cos((m+1)\phi)\left(\cos((j+1)\phi) + \cos((j-1)\phi)\right) d\psi \\ &= \tfrac{\pi}{2}\left(\delta_{m+1,j+1} + \delta_{m+1,-j-1} + \delta_{m+1,j-1} + \delta_{m+1,1-j}\right)\end{aligned}$$

so that the integral becomes

$$I_1 = \frac{\pi}{2} \int_{-L}^{L} \frac{f^{n+1} P_{n+1,m+1}(\cos\alpha) B_{za,n,m}}{(n+m+1)(n+m+2)} dz \left(\delta_{m,j} + \delta_{m,-j} + \delta_{m,-j-2} + \delta_{m,j-2}\right)$$

where $\delta_{a,b}$ is the Kronecker delta function.

4.2.2.2 I_2

In a similar fashion to I_1, the contribution to

$$I_2 = \int_{-L}^{L}\int_{-\pi}^{\pi} \frac{f^{n+1} P_{n+1,m+1}(\cos\alpha)\left(B_{zb,n,m}\cos(\psi) + B_{za,n,m}\sin(\psi)\right)}{(n+m+1)(n+m+2)} \cos(j\psi)\sin((m+1)\psi) d\psi dz$$

by $B_{zb,n,m}$ drops to zero because it is multiplied by the even integral of an odd function. This leaves

$$I_2 = \int_{-L}^{L} \frac{f^{n+1} P_{n+1,m+1}(\cos\alpha) B_{za,n,m}}{(n+m+1)(n+m+2)} dz \int_{-\pi}^{\pi} \sin(\psi)\cos(j\psi)\sin((m+1)\psi) d\psi$$

and again some trigonometric manipulation yields

$$\begin{aligned}\int_{-\pi}^{\pi} \sin(\psi)\cos(j\psi)\sin((m+1)\psi) d\psi &= \tfrac{1}{2}\int_{-\pi}^{\pi} \cos(j\psi)\left(\cos(m\psi) - \cos((m+2)\psi)\right) d\psi \\ &= \tfrac{\pi}{2}\left(\delta_{m,j} + \delta_{m,-j} - \delta_{m,-j-2} - \delta_{m,j-2}\right)\end{aligned}$$

such that

$$I_2 = \frac{\pi}{2} \int_{-L}^{L} \frac{f^{n+1} P_{n+1,m+1}(\cos\alpha) B_{za,n,m}}{(n+m+1)(n+m+2)} dz \left(\delta_{m,j} + \delta_{m,-j} - \delta_{m,-j-2} - \delta_{m,j-2}\right).$$

4.2.2.3 I_3

The contribution from I_3 is zero since

$$I_3 = -\int_{-L}^{L} \frac{(1-\delta_{m,0})\, f^{n+1} P_{n+1,m}(\cos\alpha) B_{zb,n,m}}{(n+m+1)} dz \int_{-\pi}^{\pi} \sin(j\psi)\cos(m\psi) d\psi = 0$$

for any value of j or m.

4.2.2.4 I_4

Finally

$$I_4 = \int_{-L}^{L} \frac{(1-\delta_{m,0})\, f^{n+1} P_{n+1,m}(\cos\alpha) B_{za,n,m}}{(n+m+1)} dz \int_{-\pi}^{\pi} \sin(j\psi)\sin(m\psi) d\psi$$

has the simple solution

$$I_4 = \pi \int_{-L}^{L} \frac{(1-\delta_{m,0})\, f^{n+1} P_{n+1,m}(\cos\alpha) B_{za,n,m}}{(n+m+1)} dz \left(\delta_{m,j} + \delta_{m,-j}\right).$$

4.2.2.5 Completing the Integration

Adding the four integrals in equation 4.2.5 yields

$$\Phi_{n,m} = \int_{-L}^{L} \frac{R\pi\left(\delta_{m,j} + \delta_{m,-j}\right) B_{za,n,m}}{(n+m+1)(n+m+2)} \left[\begin{array}{c} \left(f^{n+1} P_{n+1,m+1}(\cos\alpha)\right) G_j(z) + \\ (1-\delta_{m,0})\,(n+m+2) f^{n+1} P_{n+1,m}(\cos\alpha) F_j(z) \end{array} \right] dz.$$

Note that $m \geq 0$ so that $\delta_{m,j} + \delta_{m,-j} = \delta_{m,j}$ except when $m = 0$ in which case it equals two. This means that only when the degree of the field is the same as that of the wire density ($j = m$) is there any contribution to the flux and, for a field $B_{z,n,m}$ oscillating at angular frequency ω, the induced voltage is $V_{n,m} = -\omega\Phi_{n,m}$ where

$$\Phi_{n,m} = \begin{array}{c} \frac{\pi R B_{za,n,m}(1+\delta_{m,0})}{(n+m+1)(n+m+2)} \int_{-L}^{L} f^{n+1} \left[P_{n+1,m+1}(\cos\alpha) G_m(z) + \right. \\ \left. (1-\delta_{m,0})(n+m+2) P_{n+1,m}(\cos\alpha) F_m(z) \right] dz \end{array} \tag{4.2.6}$$

is the flux response to $B_{z,n,m}$. Therefore, the total voltage generated in the winding by an arbitrary magnetic field is

$$V_T = -\omega\Phi_T = -\omega \sum_{n=m-1}^{\infty} \Phi_{n,m} \tag{4.2.7}$$

where each term $\Phi_{n,m}$ is due to the B_z field harmonic $B_{za,n,m}$. The coefficients $B_{za,n,m}$ set the magnitude of the flux response $\Phi_{n,m}$ and the $B_{zb,n,m}$ coefficients drop out due to our choice of azimuthal wire density variation in equation 4.2.2. In contrast to shim coil design, where only azimuthally directed current influences the B_z field, the induced voltage depends on both axial $F_m(z)$ and azimuthal $G_m(z)$ wire densities (equation 4.2.6).

4.2.3 Harmonic Flux Linkage: Matrix Representation

To design a harmonic detection coil we use matrix algebra and sample the wire density functions at a finite interval Δz. The integral then becomes a summation and equation 4.2.6 may be written in the form:

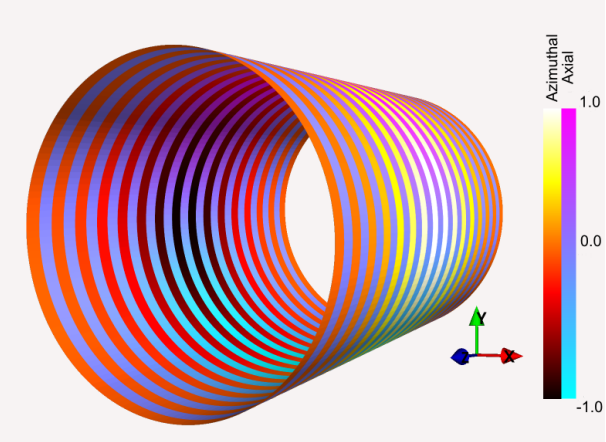

Figure 4.3: Equation 4.2.9 causes the axial wire density to be staggered by $\Delta z/2$ with respect to the the azimuthal wire density. As exaggerated in the figure, this produces alternating bands of axial and azimuthal wire density where each band has its own Fourier coefficient. For this figure the coefficients were chosen arbitrarily.

$$\mathbf{\Phi_d} = \mathbf{S}\,\mathbf{D} \tag{4.2.8}$$

where the sum over the elements of $\mathbf{\Phi_d}$ is the total flux $\Phi_T = V_T/\omega$. The vector $\mathbf{D}$ includes both the axial and azimuthal wire density coefficients from the discrete rings and $\mathbf{S}$ is a matrix generated from the integrand of equation 4.2.6 with rows corresponding to harmonic order and columns to axial position on the coil former. The matrix $\mathbf{S}$ includes the $B_{za,n,m}$ weights which represent a typical field for which we must find an optimum coil. To avoid confusion between actual harmonic coefficients of a field and coefficients chosen by the coil designer, we shall use the notation $\kappa_{ab,n,m}$ to refer to $B_{zab,n,m}$ coefficients chosen by a coil designer and $\alpha_{ab,n,m}$ to refer to a desired flux response rather than an actual flux response $\Phi_{ab,n,m}$[5]. Following the logic of Hoult and Deslauriers [50], we include equation 4.2.3 in the matrix $\mathbf{S}$ by extending the latter with equations of the form

$$0 = -\frac{m\Delta z}{R}G_m(q\,\Delta z) + F_m((q+\frac{1}{2})\Delta z) - F_m((q-\frac{1}{2})\Delta z) \tag{4.2.9}$$

where q is the index of axial position. Note that for computational accuracy the axial and azimuthal sampling points are staggered by $\Delta z/2$ (figure 4.3). Finally, we add two more rows which set the axial wire density to zero at the ends of the coil former.

Truncating the number of orders in $\mathbf{\Phi_d}$ to some value n_{max}, causes equation 4.2.8 to become a rectangular matrix of finite size and since the matrix is rectangular, there is a family of solutions rather than a single unique solution. We desire a solution that keeps the total wire length small while being fairly

[5]As usual, the presence of a subscripts a and b denote association with the harmonics $T_{n,m}$ and $T'_{n,m}$ respectively while the presence of both is a short hand for writing something like '$\alpha_{a,n,m}$ and $\alpha_{b,n,m}$'.

simple to fabricate. The Moore-Penrose inverse [6] solves problems of this kind by imposing the additional constraint that the sum of the squares of the result vector is minimal; in our case the result vector is composed of the wire density coefficients and this additional constraint is a reasonable approximation to minimum wire length. So if we apply the Moore-Penrose inverse to equation 4.2.8 we obtain

$$\mathbf{D} = \mathbf{S}^{\dagger}\mathbf{\Phi_d} \tag{4.2.10}$$

which is a prescription for the windings needed to detect a distribution of flux densities or, if all terms but one in $\mathbf{\Phi_d}$ are zero, to detect a sole spherical harmonic.

4.2.4 Discretization and the Stream Function

Once the wire density coefficients have been found they are used to determine a stream function Γ [12] on the surface of the coil former where $W_\psi = \frac{\partial\Gamma}{\partial z}$ and $RW_z = \frac{\partial\Gamma}{\partial\psi}$. As shown in figure 4.4, a small increment in this function

$$d\Gamma = \frac{\partial\Gamma}{\partial z}dz - \frac{\partial\Gamma}{\partial\psi}d\psi = W_\psi dz - W_z R d\psi \tag{4.2.11}$$

is the constant amount of wire density "flowing" between contours Γ_i and $\Gamma_{i+1} = \Gamma_i + d\Gamma$ over any helical segment $(Rd\psi, dz)$ separating them. Thus the stream function contours may be used to place discrete wires which, if there are a great number of them, approximate the continuous wire distribution.

Following Hoult and Deslauriers [50] once more, the stream function can be found by arbitrarily setting $\Gamma = 0$ at $z = \psi = 0$ and then integrating

$$\Gamma = \int d\Gamma = \int W_\psi dz - R\int W_z d\psi$$

first along z at $\psi = 0$ and then about the ψ direction with z held constant. Thus at the point (z, ψ) the stream function is:

$$\begin{aligned}\Gamma_m &= \textstyle\int_0^z G_m(z)\cos(0)dz - R\int_0^\psi F_m(z)\sin(m\psi)d\psi \\ &= \tfrac{R}{m}\cos(m\psi)F_m(z)\end{aligned} \tag{4.2.12}$$

where we have made use of equation 4.2.3. From this function, given the coefficients $F_m((q-\frac{1}{2})\Delta z)$ from above, the stream function contours can be found and split into discrete lengths of wire.

4.2.5 An Example of Spherical Harmonic Detection Coil Design

Having developed a theory for designing a detection coil's continuous wire distribution, we now use that theory to produce a wire distribution that detects the spherical harmonic $T_{2,1}$ – chosen arbitrarily – and none other up to and including $n = 7$. Since this is an example we start by arbitrarily choosing a coil

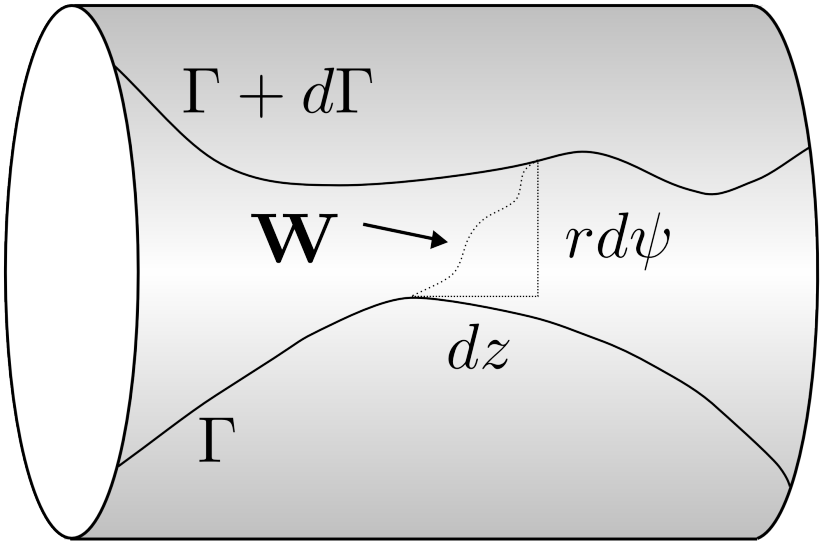

Figure 4.4: The stream function on the surface of a cylindrical coil former.

former geometry with radius $R = 0.6$ m and total length $2L = 3.2$ m and consider it as 401 strips of axially directed wire density separated by 400 strips of azimuthal wire density as shown in figure 4.3. Given this geometry it is a simple matter to generate the vector $\mathbf{\Phi_d}$ and the matrix $\mathbf{S}$ from equation 4.2.8. The vector $\mathbf{\Phi_d}$ is merely

$$\mathbf{\Phi_d} = \begin{pmatrix} 0 \\ 0 \\ 1 \\ 0 \\ 0 \\ 0 \\ 0 \\ 0 \\ \vdots \\ 0 \\ 0 \end{pmatrix} \tag{4.2.13}$$

where the ellipsis stands for the 400 zeros required to implement equation 4.2.9 and the final two zeros are used to null the values of F_m on either end of the coil former. Note that since the summation in equation 4.2.7 is from $n = m - 1$, the desired response to $T_{2,1}$ is the third element in $\mathbf{\Phi_d}$.

To generate the matrix $\mathbf{S}$ we replace the integral in equation 4.2.6 with a sum of the form:

$$\Phi_{n,m} = \pi R \Delta z \kappa_{a,n,m} \left[\sum_{q=0}^{399} K_1(q) + \sum_{q=0}^{400} K_2(q) \right] \tag{4.2.14}$$

where

$$\begin{aligned} K_1(q) &= \tfrac{(1+\delta_{m,0})}{(n+m+1)(n+m+2)} f(q)^{n+1} P_{n+1,m+1}(\cos\alpha(q)) G_m(q\Delta z - L/2) \\ K_2(q) &= \tfrac{(1-\delta_{m,0})}{(n+m+1)} f(q)^{n+1} P_{n+1,m}(\cos\alpha(q)) F_m((q-\tfrac{1}{2})\Delta z - L/2) \end{aligned} \tag{4.2.15}$$

and we choose $\kappa_{a,n,m} = \left(\left(\frac{L}{2}\right)^2 + R^2 \right)^{-n}$ such that high order harmonics are not excessively weighted (see section 6.2.2.1). Then equation 4.2.6 takes the schematic form

$$\mathbf{\Phi_d} = \mathbf{S}\,\mathbf{D} = \begin{pmatrix} K_1 & K_2 \\ \nabla \cdot \mathbf{W} = 0 & \\ \text{end constraints} & \end{pmatrix} \begin{pmatrix} F_m(-(L+\Delta z)/2) \\ \vdots \\ F_m((L+\Delta z)/2) \\ G_m(-L/2) \\ \vdots \\ G_m(L/2) \end{pmatrix} \tag{4.2.16}$$

where K_1 and K_2 stand for arrays of matrix elements produced using equation 4.2.15, $\Delta \cdot \mathbf{W} = 0$ stands for matrix elements generated using equation 4.2.9, and the end constraints are merely two lines stating that $F_m(-(L+\Delta z)/2) = F_m((L+\Delta z)/2) = 0$. After producing the matrix $\mathbf{S}$ and taking its Moore-Penrose inverse, we use equation 4.2.10 to compute the vector $\mathbf{D}$. The first four hundred and one elements of $\mathbf{D}$ are the F_m wire density coefficients shown in figure 4.5a and using equation 4.2.12 it is a trivial matter to compute the stream function Γ shown in figure 4.5b. Finally, a simple test of this procedure is to take the vector $\mathbf{D}$ and multiply it by the matrix $\mathbf{S}$ to see the wire density's response to various harmonics. Performing this test for the example above yields

$$\mathbf{\Phi'_d} = \begin{pmatrix} -3.46e-14 \\ -3.76e-14 \\ 1.00 \\ 4.86e-14 \\ 1.98e-15 \\ 8.46e-15 \\ -8.40e-15 \\ 2.40e-14 \\ \vdots \end{pmatrix} \tag{4.2.17}$$

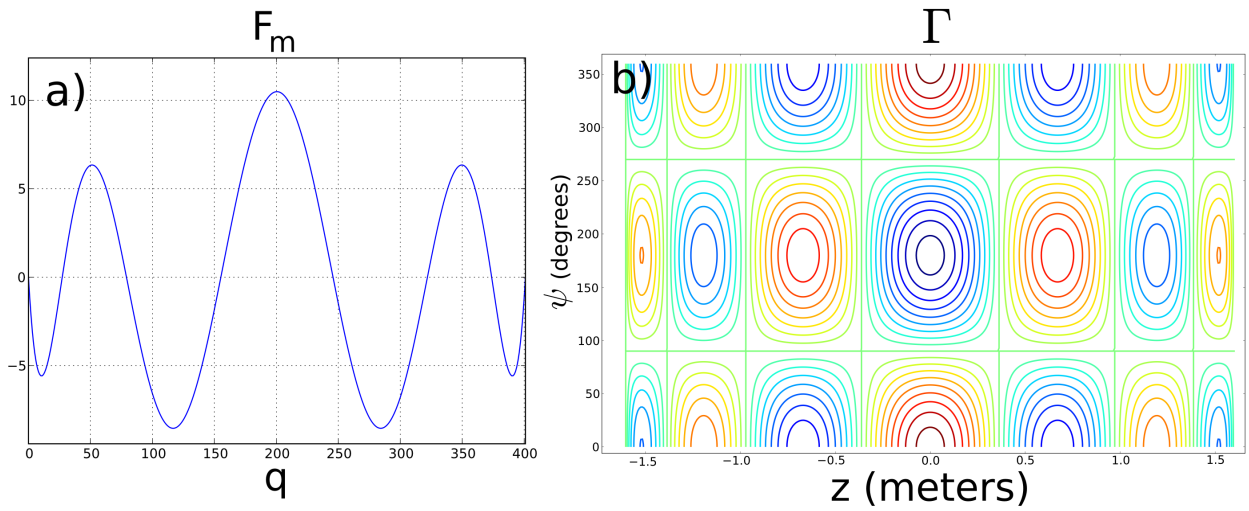

Figure 4.5: Part a) shows the four hundred and one F_m wire winding coefficients computed in section 4.2.5 for a coil designed to detect $T_{2,1}$ while part b) shows selected contours of the associated stream function Γ. These contours could be followed with wire to approximate the continuous distribution and produce a spherical harmonic detection coil.

which is nearly identical to $\mathbf{\Phi_d}$ specified in equation 4.2.13; the differences are caused by numerical rounding error.

4.3 Summary

The goal of this chapter has been to develop a method to produce a wire path that produces a voltage across its leads proportional to the rate of change of a single spherical harmonic of the magnetic field. Since it seemed easiest to determine the voltage induced in a wire density – as described by equation 4.2.2 – from the vector potential (equation 2.1.12) rather than the electric[6] or magnetic fields, section 4.1 determined what vector potential is associated with each harmonic of B_z; the related transverse fields B_x and B_y are also found along the way. An important result – although unsurprising in retrospect – is that knowledge of the rate of change of B_z through its spherical harmonics is insufficient to determine the voltage induced in a wire since there are transverse magnetic fields that are independent of B_z which may nonetheless induce a voltage. The mathematical trickery of "super-sectoral" harmonics was developed to incorporate the coefficients of these independent transverse fields, composed solely of sectoral harmonics of B_x and B_y, into a summation over the coefficients of B_z.

Section 4.2 borrowed the idea of a continuous current distribution from gradient/shim coil design and adapted it to the essentially identical concept of a continuous *wire* distribution. The vector potential was used to compute the flux linkage due to each field harmonic. Then this relationship was inverted allowing

[6]The electric field's spherical harmonics can be found using equation 2.1.8 and the results in table 4.1.

wire densities to be designed given a desired flux linkage or voltage. To produce a physically realizable wire path, the continuous wire distribution was discretized using the contours of a stream function and these contours were interconnected.

At the time of writing, the method developed in this chapter is the only known way to produce spherical harmonic detection coils. However just as many methods exist for designing gradient and shim coils, we expect that other design techniques may also be developed for detection coils.

Chapter 5

Designing the Feedback System

5.1 System Layout and Model

Having developed a method for designing spherical harmonic inductive detection coils, we now consider the incorporation of one such coil into a negative feedback system designed to control a single detected harmonic.

5.1.1 Layout of a Single Harmonic Feedback Loop

Our first problem in designing such a system is that the voltage signal produced at the leads of a harmonic detection coil is not proportional to the harmonic, as required for negative feedback, but rather the harmonic's time derivative. Therefore the detection coil's signal must be integrated with respect to time as shown in figure 5.1a; however the electronic circuit used to perform the integration introduces finite offsets and, when integrated, these offsets accumulate until the integrator output saturates at its physical limit. For this reason, just as in section 3.2.2.1, exact integration of the form $1/s$ must be replaced with practical integration of the form $1/(s + \omega_I)$ where ω_I is the angular frequency where integration starts.

Although practical integration keeps the offsets finite, for frequencies below ω_I another problem arises: the integrator output remains proportional to the harmonic's time derivative rather than the harmonic itself. Thus a feedback system relying solely on a detection coil followed by a practical integrator cannot control any frequency below ω_I, including a static offset. Thus solving the integrator's offset problem has produced a new offset problem, this time for the entire feedback system.

Fortunately, at low enough frequencies the eddy currents and their associated fields are essentially zero (section 2.1.3.2) so each harmonic magnitude is simply proportional to the current through the associated gradient/shim coil, which can be measured by the voltage drop across a series resistor. Therefore, as depicted in figure 5.1b, at low frequencies the feedback signal can be produced by coil current flowing through a resistor and at high frequencies, where eddy currents are important, the feedback signal can be

taken from the integrator output. Merging the two branches of this split feedback path into a single feedback path requires that the sensing resistor be followed by an active low-pass filter set for a smooth cross-over between the two paths.

In order to determine the filter settings we describe the split feedback path mathematically. We represent the harmonic under control with H, the sensing resistance with R, and the harmonic production coil current with i_c where $K_c = H/i_c$ is a constant describing the production coil's ability to produce the desired field harmonic. Then if D, F_I, and F_L are the transfer functions of the detection coil, electronic integrator, and low-pass filter where

$$D = sK_D \quad F_I = \frac{K_I}{\omega_I + s} \quad F_L = \frac{K_L}{1 + s/\omega_L}, \tag{5.1.1}$$

and $K_D, K_I, K_L, \omega_I, \omega_L$ are constants, then the transfer function B of the combined feedback path is

$$\begin{aligned} B &= \tfrac{RK_L/K_c}{1+s/\omega_L} + \tfrac{sK_DK_I/\omega_I}{1+s/\omega_I} \\ B &= \tfrac{RK_L}{K_C}\left(\tfrac{1}{1+s/\omega_L} + \tfrac{s/\omega_Q}{1+s/\omega_I}\right) \end{aligned} \tag{5.1.2}$$

where

$$\omega_Q = \frac{RK_L}{K_cK_DK_I}\omega_I. \tag{5.1.3}$$

Therefore, as shown in figure 5.1c, we set

$$\omega_I = \omega_L = \omega_Q \tag{5.1.4}$$

for a smooth cross-over between the paths and $B = RK_L/K_c = K_DK_I$ becomes a constant of proportionality relating, over a wide bandwidth, the harmonic magnitude H to the voltage signal used for negative feedback.

The block diagram in figure 5.1b could be largely implemented with digital electronics. In such an implementation the preamplified detection coil signal, resistor voltage, and input voltage would first be sampled and then operated on by a computer algorithm acting as a compensator. The algorithm's output would then be used as a digital input to a pulse-width-modulated current source. However, only analog components were used in the actual experimental method (part III) and thus we proceed with continuous mathematics and the Laplace transform, deferring analysis of a discretely sampled system to some later date.

5.1.2 Harmonic Production Coil and Eddy Currents

Despite the complex geometry of harmonic production coils and eddy currents, their interaction can be modelled quite simply by considering the eddy currents as a superposition of current distributions each of which produces only a single harmonic of the B_z field. Therefore a harmonic production coil is inductively coupled to a large number of these distributions but primarily to the one which produces the

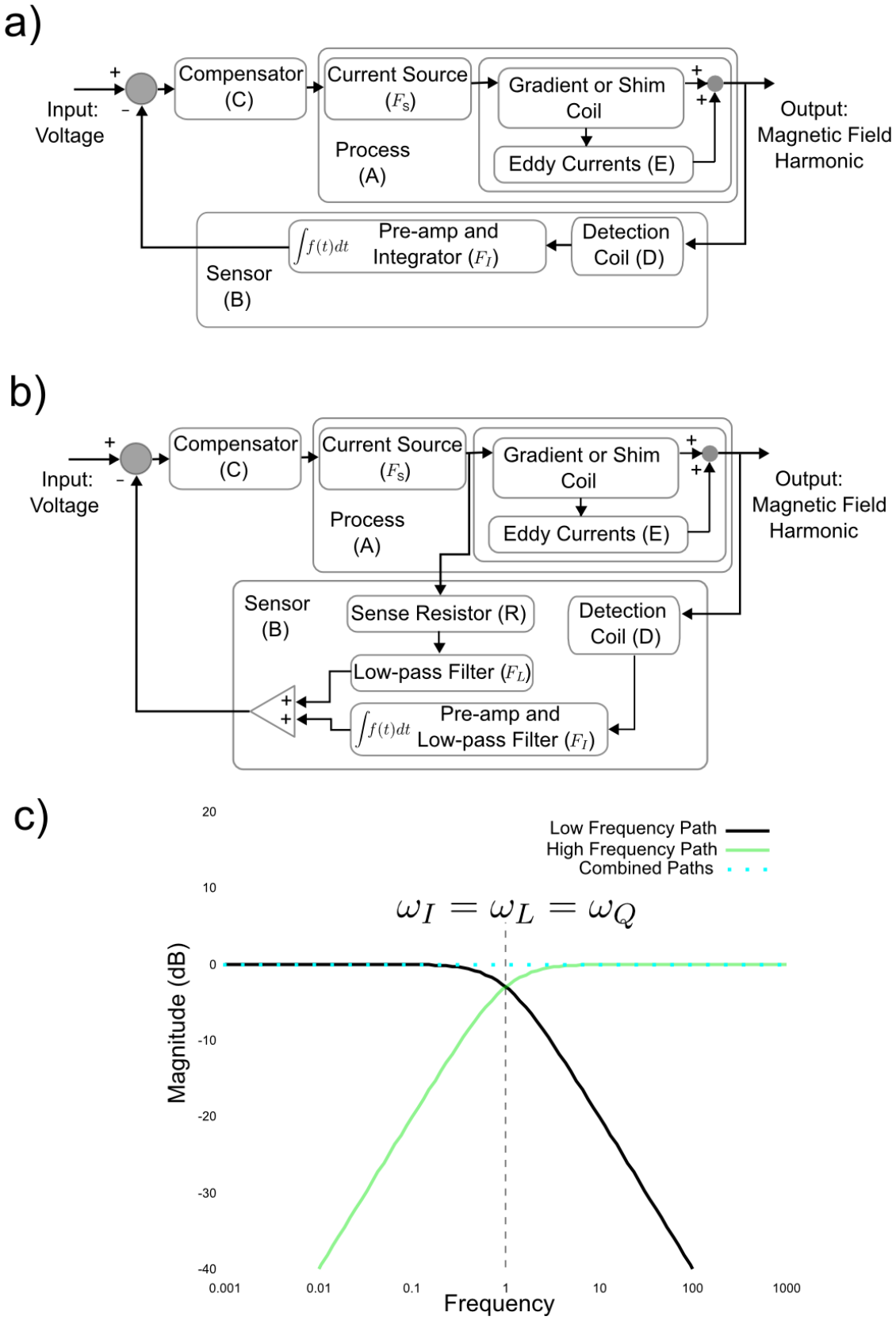

Figure 5.1: The feedback diagram in a) assumes an ideal integrator circuit with absolutely zero offset. However to be practical, the feedback path is split as shown in b) and part c) shows the desired cross-over between the two paths. The feedback diagrams are grouped into compensator, process, and sensor for comparison with the canonical feedback system in figure 3.4.

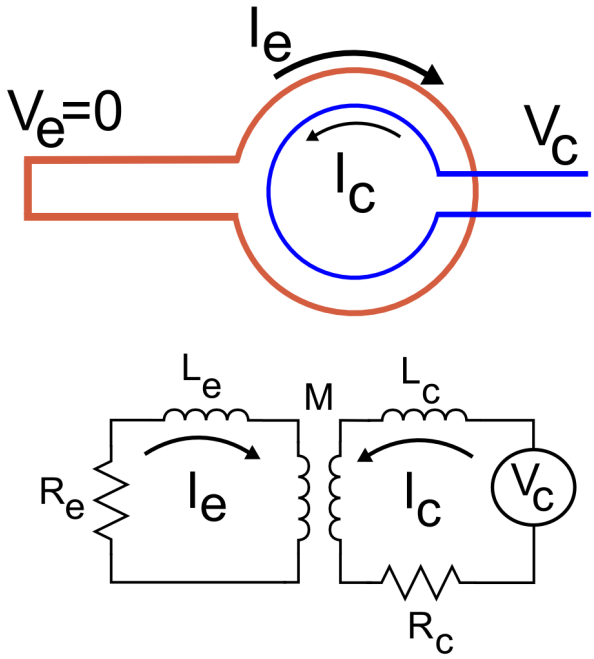

Figure 5.2: A model of the interplay between a harmonic production coil and that part of the eddy currents which produce the same harmonic.

same harmonic as the coil. As shown in figure 5.2, we model this primary eddy current distribution i_e as a closed circuit inductively coupled to a field production coil in which a current i_c is driven by an externally applied voltage V_c.

Elementary circuit analysis reveals that

$$V_c = i_c R_c + s i_c L_c - s i_e M$$

$$0 = i_e R_e + s i_e L_e - s i_c M$$

where M is the mutual inductance between the circuits while R_e, R_c, L_e and L_c are the respective resistances and self-inductances of the eddy-current distribution and harmonic production coil; some manipulation yields

$$i_e = \left(\frac{Ms}{R_e + L_e s} \right) i_c. \tag{5.1.5}$$

Now the strength of the magnetic field harmonic H has contributions from both the coil and eddy-current distribution such that $H = K_c i_c - K_e i_e$ where K_c and K_e are the respective coupling constants and K_c has already been defined in section 5.1.1. By employing equation 5.1.5 we can write $H = G i_c$ where

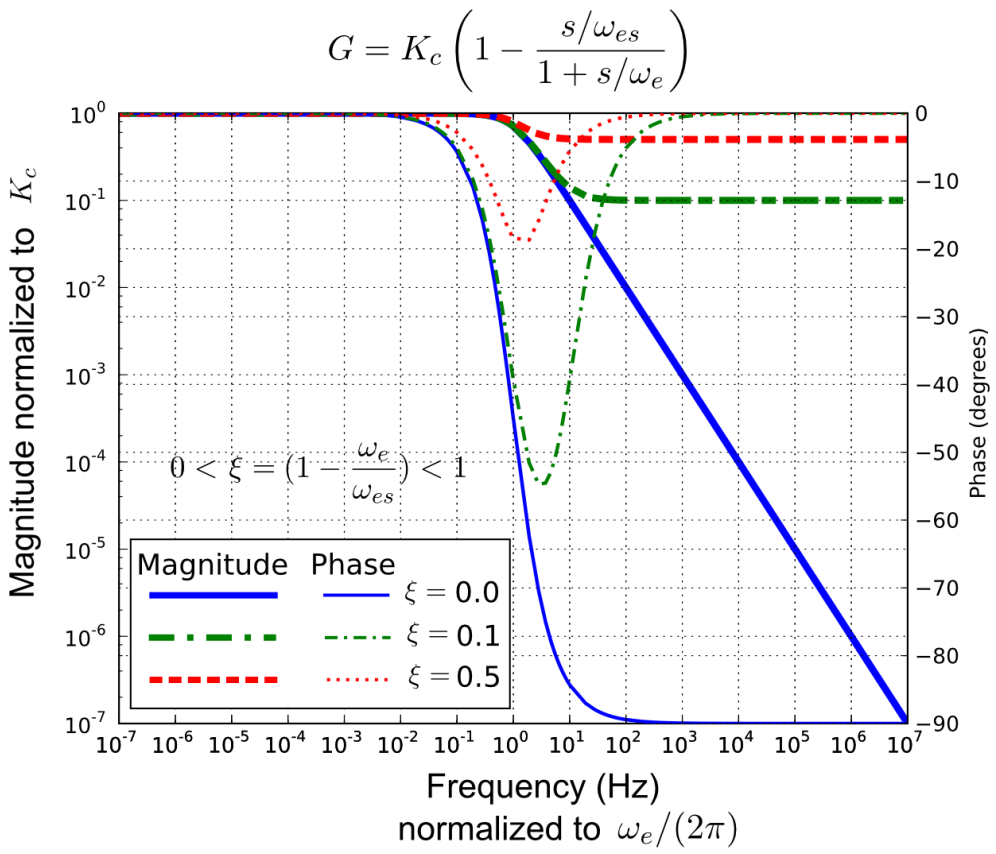

Figure 5.3: The magnitude and phase of the combined model given in equation 5.1.6.

$$G = K_c - \frac{K_e M s}{R_e + L_e s}.$$

However the parameters R_e and L_e are not easily measured so we substitute $\omega_e = \frac{R_e}{L_e}$, and $\omega_{es} = \frac{R_e K_c}{K_e M} \geq \omega_e$ which yields

$$\begin{aligned} G &= K_c\left(1 - \tfrac{s/\omega_{es}}{1+s/\omega_e}\right) \\ &= K_c\left(\tfrac{1+\xi s/\omega_e}{1+s/\omega_e}\right). \end{aligned} \tag{5.1.6}$$

We note that even for frequencies much greater than ω_{es} the secondary contribution from the eddy currents cannot exceed the primary contribution from the coil and thus $\omega_{es} \geq \omega_e$. The characteristics of this transfer function are depicted in figure 5.3 where the dimensionless parameter

$$\xi = (1 - \frac{\omega_e}{\omega_{es}}) \tag{5.1.7}$$

lying between 0 and 1 has been defined such that as ξ approaches 0 the eddy-current effect becomes ever more severe.

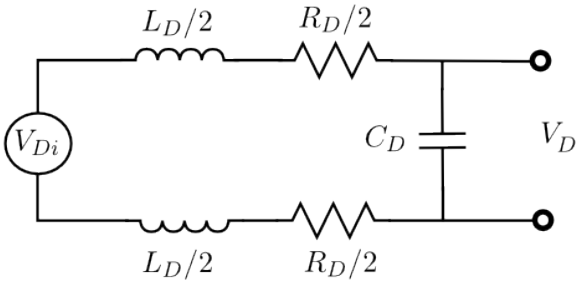

Figure 5.4: Detection coil circuit model

5.1.3 Improved Detection Coil Model

Moving beyond the simplistic detection coil model $D = sK_D$ used in equation 5.1.1 we now make an effort to include the detection coil's resistance R_D, inductance L_D, and inter-winding capacitance C_D as shown in figure 5.4. According to this model the voltage induced in the detection coil remains $V_{Di} = sK_DH$ as before but now the wire of the coil itself filters the signal. Considering the circuit model as a simple voltage divider, the voltage across the capacitance, and thus the output coil terminals, is

$$V_D = \left(\frac{1}{1 + R_DC_Ds + L_DC_Ds^2}\right)V_{Di} = \left(\frac{sK_D}{1 + R_DC_Ds + L_DC_Ds^2}\right)H$$

where we identify the detection coil's transfer function as

$$D = \frac{sK_D}{1 + R_DC_Ds + L_DC_Ds^2}. \tag{5.1.8}$$

Thus above some frequency determined by either R_DC_D or L_DC_D, the detection coil's transfer function is no longer sK_D but rolls off. Clearly R_D, C_D, and L_D can all be reduced – and thus the bandwidth expanded – by using less wire on fewer contours in the approximation of the wire density function (section 4.2.3). However this also decreases the detection coil's sensitivity K_D and the accuracy to which the continuous wire distribution is approximated: a trade-off exists between sensitivity and bandwidth.

5.1.4 The Whole Feedback System Model

Having investigated the eddy currents, production coil, and detection coil, the only blocks in figure 5.1b that have not yet been modelled are the current source (F) and feedback compensator (C). The current source, probably a commercial gradient amplifier as described in section 3.1.1, has a flat transfer function below some critical frequency after which it begins to roll off due to its own internal feedback circuitry. Although this transfer function can be measured experimentally or acquired from the manufacturer, the model

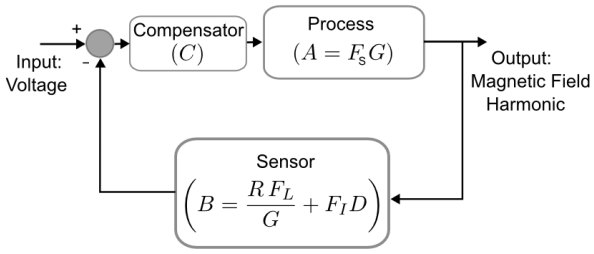

Figure 5.5: Simplified block diagram

$$F_S = \frac{K_S}{1 + s/\omega_S} \tag{5.1.9}$$

encompasses its gain K_S and limited bandwidth.

The feedback compensator, on the other hand, is entirely under the system designer's control. It should have sufficient gain such that the system output depends only on the input and the feedback path and its transfer function should be chosen such that the system has sufficient bandwidth but does not oscillate. Although the final form of this compensator depends on the actual transfer function of the current source and the constraints on the total system's overshoot and settling time (figure 3.5), for now we assume that it is

$$C = \frac{K_{Cmp}}{1 + s/\omega_{Cmp}}. \tag{5.1.10}$$

Now that each part of the feedback system in figure 5.1b has a model, the block diagram may be simplified to figure 5.5 using the rules in figure 3.6. The total transfer function T of the harmonic feedback system is then

$$T = \frac{1}{B}\left(\frac{1}{1 + \frac{1}{\Lambda}}\right) \tag{5.1.11}$$

where

$$\begin{aligned} A &= F_S\, G \\ B &= \tfrac{R F_L}{G} + F_I D \\ \Lambda &= A\, B\, C. \end{aligned} \tag{5.1.12}$$

Applying the various models – F_I and F_L from equation 5.1.1, D from equation 5.1.8, G from equation 5.1.6, and F_S from equation 5.1.9 – we write

$$A = K_c\left(\frac{K_S}{1 + s/\omega_S}\right)\left(1 - \frac{s/\omega_{es}}{1 + s/\omega_e}\right) \tag{5.1.13}$$

and

$$B = \frac{RK_L}{K_c}\left(\frac{1}{(1+s/\omega_L)\left(1-\frac{s/\omega_{es}}{s/\omega_e+1}\right)} + \frac{s/\omega_Q}{(1+s/\omega_I)\left(1+R_DC_Ds+L_DC_Ds^2\right)}\right) \tag{5.1.14}$$

where ω_Q is defined in equation 5.1.3. Note that despite the complexity of these functions, provided that $\omega_I = \omega_L = \omega_Q$, the complete system's transfer function simplifies to $T \simeq \frac{1}{B} \simeq \frac{K_c}{RK_L} = \frac{1}{K_DK_I}$ over its operational bandwidth.

Armed with a complete system model, our task is now to choose the various system parameters, and possibly a different form for the compensator, such that the total system has the desired flat frequency response, greatly reduced eddy current effects, and neither oscillates nor drifts. Independence from system characteristics, in this case eddy currents, is a hallmark of negative feedback and is provided by a high open loop gain which may be increased as necessary with K_{Cmp} and/or K_S provided that the gain of Λ falls below unity well before its phase reaches $-180°$ (see chapter 3.2).

5.2 General System Considerations

Many of the choices made in the design of a harmonic feedback system inevitably depend on factors specific to a given situation such as which harmonics are of interest, the time constants of the eddy currents, the desired system performance, and the available funds and technology. However, there are a few fundamental considerations that transcend the details of any particular system and it is to these that we now turn.

5.2.1 Integrator Design

Any feedback system using a spherical harmonic inductive detection coil requires a preamplifier incorporated into its integrator (F_I in figure 5.1) to boost the small signals induced by low frequency changes in the spherical harmonic. When designing the integrator one must consider common mode sensor voltage, maximum harmonic slew rate, and the total system's gain. The system's gain is set by choosing K_I since the transfer function of the whole system is $T \simeq 1/B \simeq 1/(K_DK_I)$ (equation 5.1.11) where K_D is already fixed (section 5.1.3). Therefore K_I should be set such that a maximal swing of the input voltage, whatever that may be for a given system, results in the desired maximal swing of the output harmonic.

Although the desired signal from the detection coil is the voltage difference between its leads, there may also be signals common to both leads, possibly as a result of capacitive coupling to the gradient coil. Therefore it is important that the combined integrator and preamplifier circuit reject these common-mode signals. Instrumentation amplifiers (section 3.2.2.2) are specially designed for this purpose and, as in figure 5.6a, the block F_I can be implemented by the cascade of an instrumentation amplifier and practical

op-amp. integrator from section 3.2.2.1. However, connecting a preamplifier directly to the detection coil unnecessarily limits harmonic slew rate due to excessive signal at the mesh point p_M – that is the dynamic range of the block F_I is limited which, because it is an integrator, limits the system's harmonic slew rate.

To see this problem, consider both low frequency changes in the harmonic near ω_I and high frequency changes near the limit of the system's bandwidth. Since the detection coil's output signal is proportional to frequency, the high frequency harmonic changes – caused by rapid gradient or harmonic switching – induce large voltages in the detection coil that may damage the instrumentation amplifier while the low frequency changes induce small voltages near the preamplifier's noise floor. Because of these small voltages, the instrumentation amplifier must be operated at high gain but this gain also amplifies the already large high frequency signals. Since there is a limit to the preamplifier's maximum output voltage at p_M there is also a limit on how large these high frequency signals can be and thus on the maximum rate of change (slew rate) of the harmonic under control. However, for the configuration in figure 5.6a, the slew rate is limited unnecessarily since the high frequency signals with large amplitude at p_M are subsequently greatly attenuated by the following integrator circuit. By moving the attenuation of high frequencies before the preamplifier, the artificial limit on slew rate is relaxed without degrading the signal to noise ratio for the small low frequency signals.

This is accomplished by dividing the electronic integrator into two stages. The first, as shown in figure 5.6b, is a passive low-pass filter which connects directly to the coil, protects subsequent stages from large transient voltages, and is balanced so that any common mode voltage is rejected by the preamplifier. After amplification, the single ended signal has its low frequency components integrated by an active filter which meshes with the low pass filter at ω_M such that, as shown in figure 5.6c, the two stages comprise a single low-pass filter with cut-off frequency ω_I. Ideally ω_M is set to the largest value compatible with not overloading the preamplifier's output at p_M in order to maximize the signal to noise ratio of low frequency signals for a given maximum harmonic slew rate.

If distortion or clipping occurs at p_M, or any other point in the feedback path, incorrect information about the controlled harmonic is fed back which leads to undesirable, and possibly unsafe, system behaviour. Therefore some mechanism should shut the system down if the voltage at point p_M nears the limit of the preamplifier's output swing.

5.2.2 Feedback Cross-over Point Revisited

The location of the cross-over point between the two branches of the split feedback path is of critical importance to system design because even if it is set much lower than ω_e, the characteristic frequency of the eddy currents, the eddy currents still slightly distort the feedback path's operation. Although our original model of the feedback path (equation 5.1.2) does not show this distortion, it does show that the feedback path transfer function can be simplified to the constant $B = RK_L/K_c = K_D K_I$ by choosing the

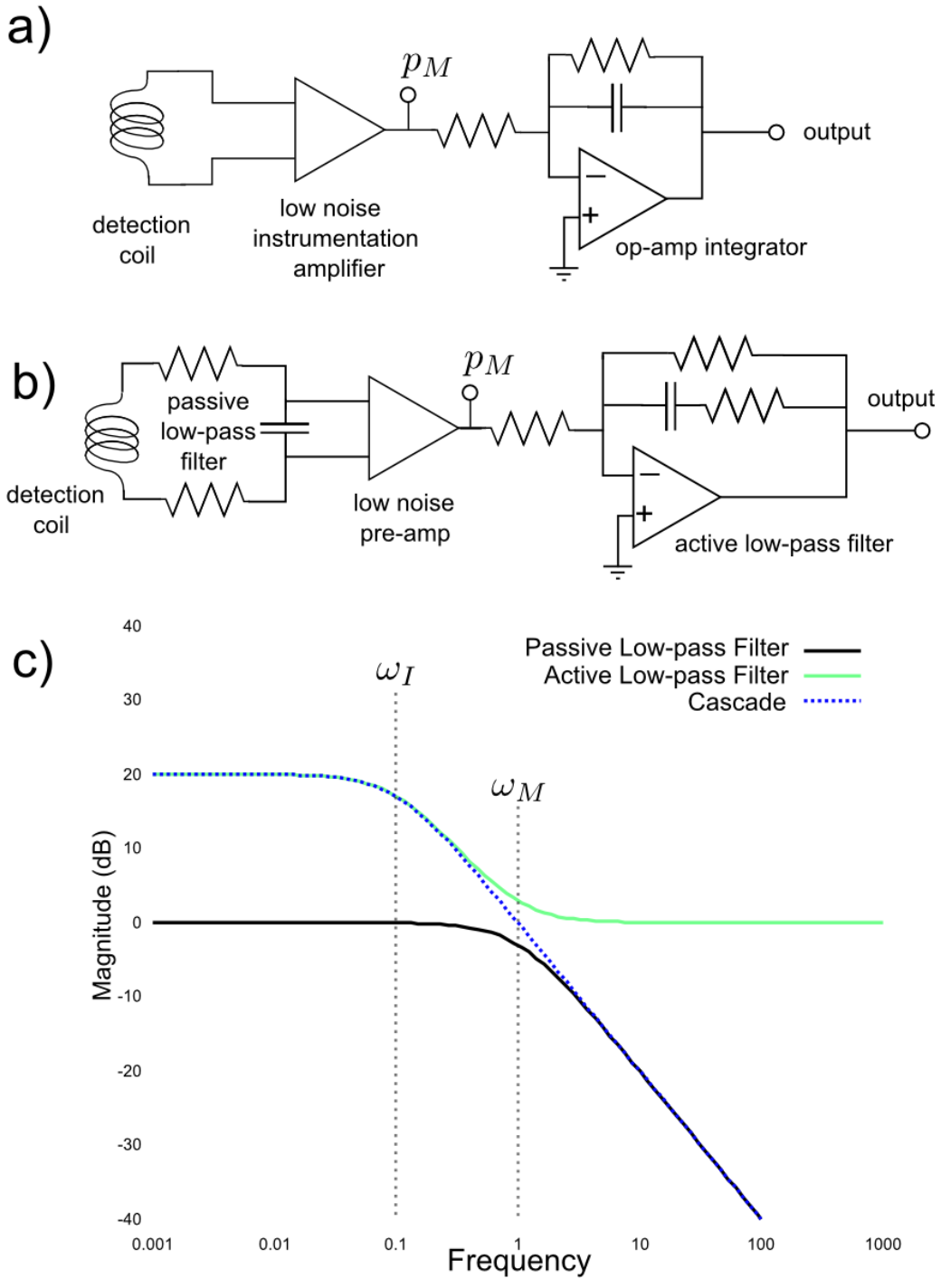

Figure 5.6: In a) the preamplifier and integrator are cascaded naively. In b) high frequency signals are attenuated before the preamplifier and the two filters are meshed as shown in c) so that together they integrate the signal.

integrator's start frequency ω_I, the low-pass filter's cross-over frequency ω_L, and the relationship between the gains of the two paths (ω_Q in equation 5.1.3) such that $\omega_I = \omega_L = \omega_Q$. However equation 5.1.14 is a more complete model where setting $\omega_I = \omega_L = \omega_Q$ yields

$$B = \frac{K_D K_I}{(1 + s/\omega_I)} \left(\frac{1}{\left(1 - \frac{s/\omega_{es}}{s/\omega_e + 1}\right)} + \frac{s/\omega_I}{(1 + R_D C_D s + L_D C_D s^2)} \right). \tag{5.2.1}$$

Now at frequencies either far below ω_I or far above ω_{es} and ω_I, but within the detection coil's bandwidth, this model of the split feedback path again simplifies to $B \simeq K_D K_I = RK_L/K_c$ but, as shown in figure 5.7, the eddy currents cause a slight deviation near ω_I which diminishes as the ratio

$$\zeta = \frac{\omega_e}{\omega_I} \tag{5.2.2}$$

is increased. The result of this deviation is that the feedback path does not perfectly sense the harmonic and thus the system does not exactly reproduce the harmonic's desired temporal evolution.

Now from equation 5.2.1 it is clear that to keep the deviation small we must have $\omega_I \ll \omega_e$ but, since the eddy currents become more significant as $\xi = (1 - \frac{\omega_e}{\omega_{es}})$ (equation 5.1.7) goes to zero, precisely how much below ω_e we should set ω_I depends on ξ. Thus a better, although still approximate, statement is $\omega_I \ll \omega_e \xi$ or $\xi\zeta \gg 1$; the actual relationship between ξ, ζ, and feedback deviation is plotted in figure 5.7d. However, since ξ is entirely determined by the eddy currents, the product $\zeta\xi$ may only be increased by decreasing ω_I but this amplifies errors associated with the preamplifier and integrator circuit (sections 3.2.2.1 and 5.2.1).

5.2.3 Preamplifier Noise and Offset

In order to analyze the errors associated with the integrator without precise knowledge of its implementation we refer these errors to the integrator's input, as shown in figure 5.8, realizing that the power spectrum of this error signal depends on the system's details. Although the detection coil's intrinsic resistance generates white noise which can also be referred to the integrator's input, that noise is expected to be much less than the low-frequency flicker noise produced by the preamplifier. In any case, just as we used figure 5.1 to determine the transfer function from system input to system output (equation 5.1.11) we now use figure 5.8 to find the transfer function between the error signal and the system output. Therefore the harmonic output due to the error signal is $H_{err} = T_{err} E_{rror}$ where

$$T_{err} = \frac{-CF_S F_I G}{1 + CF_s F_L R + CF_s F_I G D} \tag{5.2.3}$$

and manipulation using equations 5.1.11 and 5.1.12 yields

$$T_{err} = -F_I T. \tag{5.2.4}$$

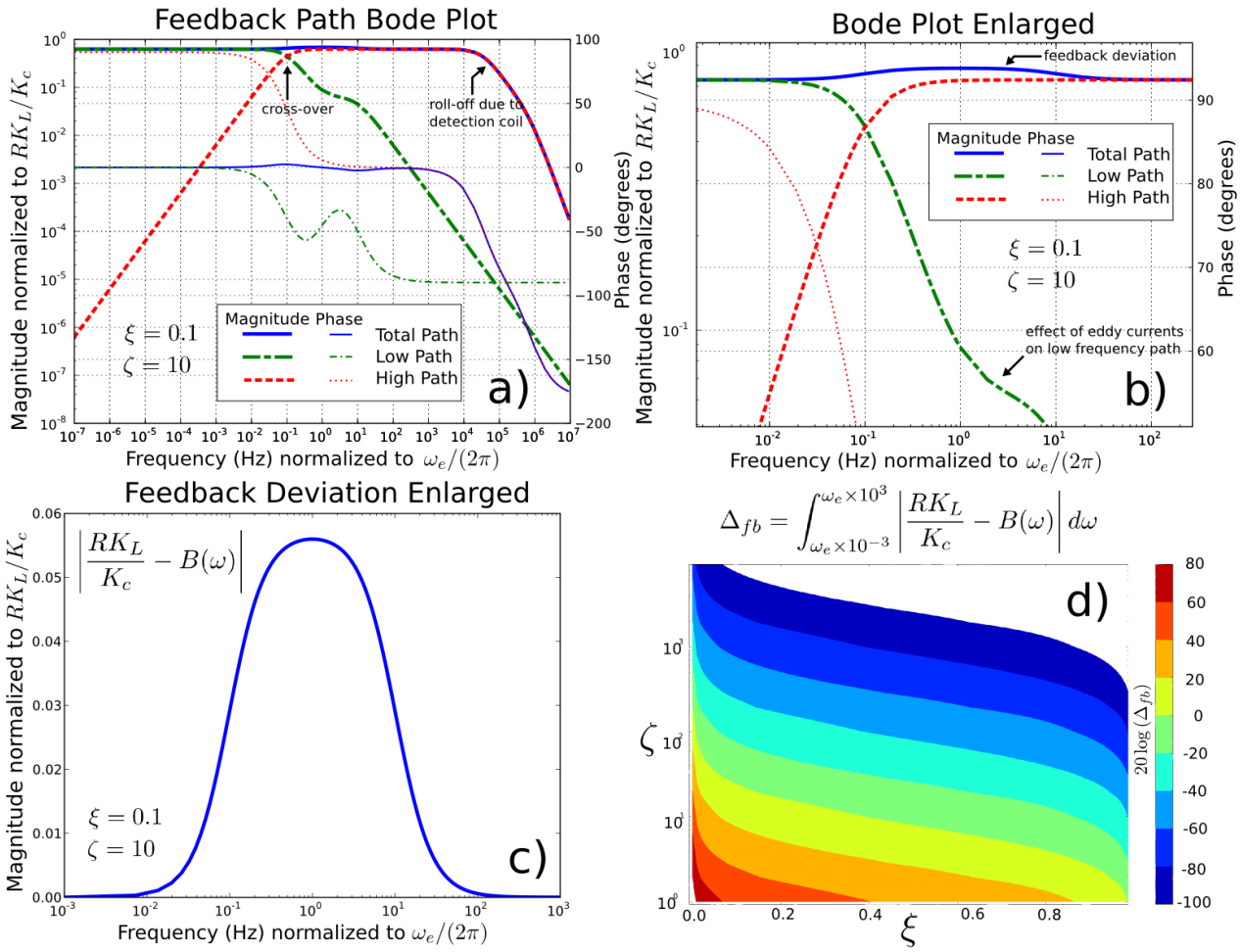

Figure 5.7: In a) the feedback path's transfer function as modelled by equation 5.2.1 is plotted along with its high and low frequency branches. Ideally the cross-over point would look like figure 5.1c but there is a deviation as seen in the detailed view of the cross-over point in b); the absolute value of this deviation is shown in c). This deviation can be assigned a numeric value with the integral $\Delta_{fb} = \int_{\omega_e \times 10^{-3}}^{\omega_e \times 10^{3}} \left|\frac{RK_L}{K_c} - B(\omega)\right| d\omega$ used to produce the plot in d).

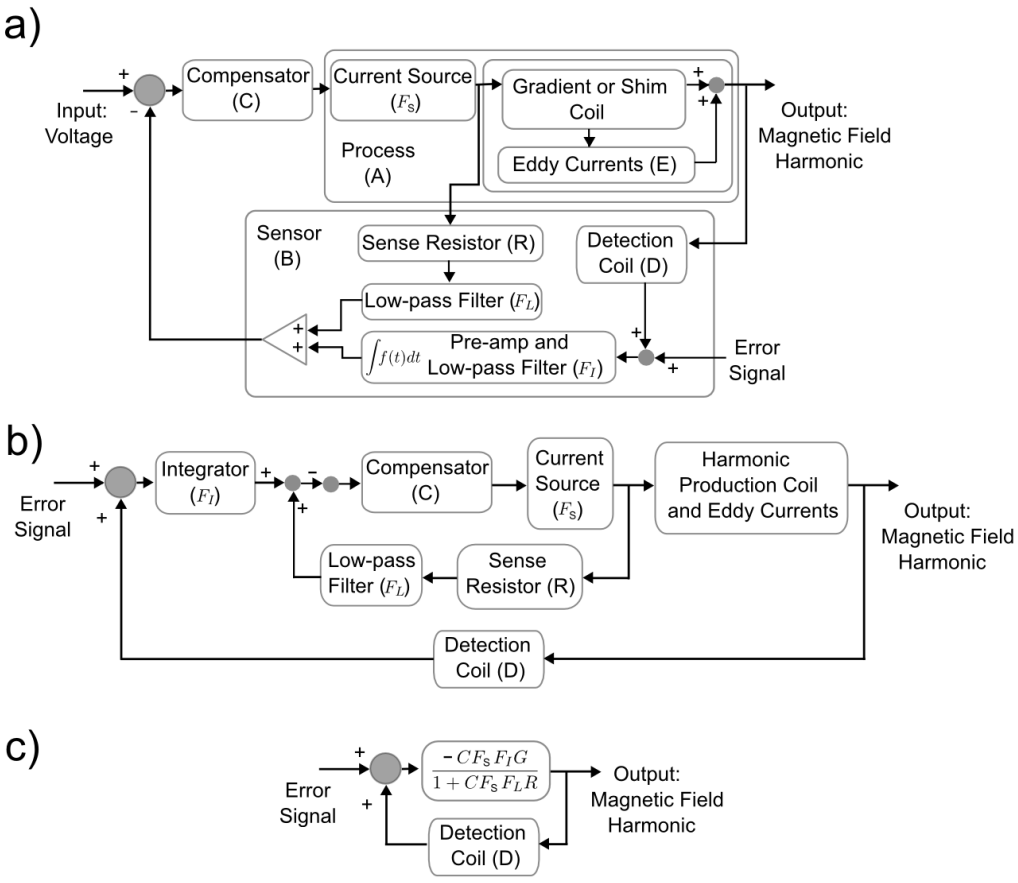

Figure 5.8: In a) the feedback system is shown with an error signal referred to the input of the integrator F_I. In b) the system is re-arranged to show its form with respect to the error signal and harmonic output. The diagram in b) is simplified to produce the diagram in c).

The total output harmonic is merely the superposition of the contributions from the input signal and the error signal

$$H = T\, I_{nput} - F_I\, T\, E_{rror} = T\left(I_{nput} - F_I\, E_{rror}\right). \tag{5.2.5}$$

Since $F_I = \frac{K_I}{\omega_I + s}$ (equation 5.2.8), the low frequency noise and static offsets on the output field harmonic are proportional to the term K_I/ω_I which increases as the integration start frequency ω_I is reduced. So we have two conflicting requirements: ω_I must be kept as low as possible to reduce feedback path deviation near the cross-over frequency (section 5.2.2) but must also be as high as possible to minimize the influence of the error signal introduced by the preamplifier and integrator. Clearly a trade-off must be made between spherical harmonic distortion and noise, the distortion arising from residual eddy current effects and the noise originating in the integrator circuit.

5.2.4 Feedback Loop Interaction

Another important consideration is the interaction of multiple feedback loops (section 3.2.3) used to simultaneously control several harmonics of the magnetic field. These feedback loops inevitably interact due to the imperfection of the production and detection coils as well as the production of multiple eddy current harmonics. In order to determine if this interaction degrades system performance, we may express the blocks of figure 5.1b in matrices modelling all the feedback loops at once. The production coil and eddy current model from equation 5.2.6 can be placed into a matrix $\mathbf{G}$ with one row for every production coil and elements

$$G_{\alpha,\beta} = K_{c,\alpha,\beta}\left(1 - \frac{\xi_\alpha s/\omega_{e,\alpha}}{1 + s/\omega_{e,\alpha}}\right) \tag{5.2.6}$$

where $K_{c,\alpha,\beta}$ is the coupling of harmonic production coil α to harmonic β. In a similar fashion the detection coils have a slight response to harmonics they were not designed to detect so the array of detection coils can be represented with a matrix $\mathbf{D}$ with elements

$$D_{\alpha,\beta} = \frac{sK_{D,\alpha,\beta}}{1 + R_{D,\alpha}C_{D,\alpha}s + L_{D,\alpha}C_{D,\alpha}s^2}. \tag{5.2.7}$$

Now the compensator, current source, integrator, resistor, and low-pass filter blocks from the various systems can also be placed in matrices $\mathbf{C}$, $\mathbf{F_S}$, $\mathbf{F_I}$, $\mathbf{R}$, and $\mathbf{F_L}$ with elements

$$C_\alpha, \quad F_{S,\alpha} = \frac{K_{S,\alpha}}{1 + s/\omega_{S,\alpha}}, \quad F_{I,\alpha} = \frac{K_{I,\alpha}}{\omega_{I,\alpha} + s}, \quad R_\alpha, \quad F_{L,\alpha} = \frac{K_{L,\alpha}}{1 + s/\omega_{L,\alpha}} \tag{5.2.8}$$

but since there is no interaction between the systems at these stages the matrices are diagonal.

Referring to figure 5.1b, if $\mathbf{I_c}$ is a vector containing the Laplace transforms of the currents through the various harmonic production coils then $\mathcal{H} = \mathbf{G}\mathbf{I_c}$ is a vector of the Laplace transforms of the harmonic coefficients. Arranging the Laplace transform of the system input into another vector $\mathcal{V}$ we write

$$\mathbf{I_c} = \mathbf{F_S}\mathbf{C}\left[\mathcal{V} - (\mathbf{F_L}\mathbf{R} + \mathbf{F_I}.\mathbf{D}\mathbf{G})\,\mathbf{I_c}\right]$$

and remembering that matrix multiplication does not commute we can solve for $\mathcal{H}$ as

$$\mathcal{H} = \mathbf{T}\mathcal{V} \tag{5.2.9}$$

where

$$\mathbf{T} = \mathbf{G}\left[\mathbf{1} + \mathbf{F_S}\mathbf{C}\,(\mathbf{F_L}\mathbf{R} + \mathbf{F_I}\mathbf{D}\mathbf{G})\right]^{-1}\mathbf{F_S}\mathbf{C} \tag{5.2.10}$$

is the matrix of transfer functions relating the harmonics to the system inputs. Provided that the system inputs and circuit parameters are known, then the time evolution of the harmonics under feedback control can be computed by taking the inverse Laplace transforms of the elements of $\mathcal{H}$.

5.3 The Image Quality Effects of Field Noise and Distortion: Choosing ω_I and Fine Tuning the Compensator

In section 5.2.3 it became clear that regardless of the exact properties of a harmonic feedback system, a method is required to choose ω_I for an optimal trade-off between harmonic noise and distortion; that is the combined influence of these effects must be minimized. Moreover, the choice of a feedback compensator also affects harmonic distortion through the control system's overshoot and settling time (see figure 3.4). Since the ultimate goal is to produce quality magnetic resonance images by reducing the distorting effect of eddy currents, we shall use "image degradation" as our minimization criterion and thus maximize "image quality" with respect to ω_I and the feedback compensator as well.

5.3.1 Quantitative Image Quality

In order to cast image quality as an objective quantity to be maximized, rather than leaving it in the eye of the beholder, we return to the point spread function (PSF) presented in section 2.3.5. In MRI, the PSF is fundamentally limited by factors including the imaging pulse sequence, the acquisition time T_{acq}, the material being imaged, and the gradient magnitude. If $\mathrm{PSF}_{\mathrm{ideal}}$ is the best possible PSF given the limitations outside the control of the gradient system designer and $\mathrm{PSF}_{\mathrm{degraded}}$ has been degraded further by field noise and distortion from any aspect of the gradient system, then we may define the image quality with respect to the ideal as

$$\begin{gathered}\text{Quality} = 1 - \text{Degradation} \\ \text{Degradation} = \frac{\Delta\mathrm{PSF}}{\mathrm{PSF}} = \int_{\text{image}} \left(\frac{\mathrm{PSF}_{\mathrm{ideal}} - \mathrm{PSF}_{\mathrm{degraded}}}{\mathrm{PSF}_{\mathrm{ideal}}} \right)^2 dI.\end{gathered} \tag{5.3.1}$$

Determining $\mathrm{PSF}_{\mathrm{ideal}}$ and $\mathrm{PSF}_{\mathrm{degraded}}$ from first principles is a daunting task. First of all, they depend on the details of a particular imaging sequence and its digital image reconstruction. So the gradient system designer must start with a particular imaging sequence against which to optimize – probably a gradient-echo sequence which operates the system near its limit – and then test that the image quality is near maximum for other sequences as well. But even with a particular sequence in mind, the analytical techniques of section 2.3.5 are difficult to apply since they must be expanded to incorporate the statistical nature of noise and the effect of higher order spherical harmonics, neither of which may have been considered by the sequence's designer.

Fortunately, image reconstruction in MRI always starts with a digital representation of the acquired NMR signal and the subsequent algorithms are readily available, either in the literature or as functional software. Therefore by simulating the NMR signal produced in response to a particular imaging sequence, an image can be formed by passing the simulated signal through the appropriate algorithm. Moreover, if the simulated volume is homogeneous save for one point, then the resulting image is a point spread function which may be used to numerically compute image quality as defined in equation 5.3.1. Therefore our task is to simulate the NMR signal both with and without noise and distortion on the harmonics of the gradient field and repeat the simulation for different values of ω_I and with various feedback compensators until an optimum is found.

5.3.2 Simulating the Harmonic Control System and NMR Signal

Numerical simulation of the output harmonic for a given input is rather straightforward given the system model in equations 5.1.11 and 5.1.12: merely take the discrete Fourier transform of the input signal, multiply each frequency component by the complex number found by evaluating the model at that frequency, and use the discrete inverse Fourier transform to find the result. The only complication comes when simulating the effect of noise. However we note that electronic noise is a stationary random process: the noise voltage changes with time but not the probability associated with each a particular voltage value. Thus, like the thermally fluctuating magnetic field in section 2.2.2.1, the noise voltage has a Fourier transform $F(\omega)$ with a specific magnitude at every frequency but randomly changing phases and thus its power spectrum $J(\omega) = F(\omega)F^*(\omega)$ does not change with time. Provided we know this noise power spectrum – the necessary information is usually found on the preamplifier's data sheet – it may be used in conjunction with numerically generated random phases from a uniform distribution to produce a simulated input error signal. The effect that this error has on the output harmonic can be determined by using the error transfer function from equation 5.2.3 just as equations 5.1.11 and 5.1.12 were used to determine the effect of the input on the output. The total output harmonic is just the superposition of the output due to the error signal and that due to the input signal.

Starting with the noisy and distorted harmonic magnitudes from simulated feedback loops, the next step is to simulate the NMR signal. Numerical simulation of NMR and MRI is well established [133, 7, 124] and can be based on equation 2.2.24, a known solution to the Bloch equations such as equation 2.2.23, or computational quantum mechanics. There are two main considerations when choosing a simulator for the optimization of a harmonic control system: it must be able to accept arbitrary waveforms for many harmonics of the gradient field as produced from circuit simulation and it must execute quickly enough that an optimization can be performed in a reasonable amount of time. Most MRI simulation software does not model the harmonics of the gradient field beyond the x, y, and z gradients and does not accept arbitrary noisy waveforms even for those three. Moreover, simulation that is based directly on the Bloch equations is

quite computationally demanding and is best performed using a cluster of parallel computers. Therefore as a first attempt at optimizing a spherical harmonic control system, we develop the theory for a simple MRI simulator based on the solution to Bloch's equations when $B_1 = 0$ that can accept arbitrary waveforms of high order spherical harmonics.

Starting from equation 2.2.23, the transverse magnetization in the rotating frame when $B_1 = 0$ evolves as

$$M'_{x,y}(\mathbf{r},t) = M_0(\mathbf{r})\sin(\alpha(\mathbf{r}))e^{-t/T_2(\mathbf{r})}e^{i\theta(\mathbf{r},t)}$$
$$\theta(\mathbf{r},t) = \int_0^t \Delta\omega(\mathbf{r},\tau)d\tau$$

where the initial transverse magnetization M_0, relaxation T_2, and flip angle α all depend on position $\mathbf{r}$. Remembering from section 2.2.1 that $\Delta\omega = -\gamma\Delta B_z(t)$ where $B_z = \Delta B_z(\mathbf{r},t) + B_o$, we can write the phase evolution $\theta(\mathbf{r},t)$ in terms of the time integrals of the spherical harmonics coefficients

$$\theta(\mathbf{r},t) = -\gamma\sum_{n,m}\left[A_{i,n,m}(t)T_{n,m} + B_{i,n,m}(t)T'_{n,m}\right] \tag{5.3.2}$$

where

$$A_{i,n,m}(t) = \int_0^t A_{n,m}(\tau)d\tau \qquad B_{i,n,m}(t) = \int_0^t B_{n,m}(\tau)d\tau.$$

Then $A_{i,n,m}(t)$ and $B_{i,n,m}(t)$ can be found by numerically integrating the noisy and distorted waveforms of the coefficients $A_{n,m}(t)$ and $B_{n,m}(t)$ generated by circuit simulation. Since this gives the transverse magnetization $M'_{x,y}(\mathbf{r},t)$ of a point-like isochromat, the signal $s_v(t)$ from a rectangular voxel with volume $\Delta x\Delta y\Delta z$ can be found by integrating

$$s_v(t) = \alpha\int_{x-\frac{\Delta x}{2}}^{x+\frac{\Delta x}{2}}\int_{y-\frac{\Delta y}{2}}^{y+\frac{\Delta y}{2}}\int_{z-\frac{\Delta z}{2}}^{z+\frac{\Delta z}{2}} M'_{x,y}(\mathbf{r},t)dxdydz.$$

Assuming that the material properties do not change appreciably within a voxel we have

$$s_v(t) = M_{0,v}\sin(\alpha_v)e^{-t/T_{2,v}}V_{int}(\mathbf{r},t) \tag{5.3.3}$$

where

$$\begin{aligned} V_{int,v}(t) &= \iiint_{\text{voxel}} e^{-i\gamma\sum_{n,m}\left[A_{i,n,m}(t)T_{n,m}+B_{i,n,m}(t)T'_{n,m}\right]}dV \\ &= \iiint_{\text{voxel}} \prod_{n,m}\left[e^{-i\gamma A_{i,n,m}(t)T_{n,m}}e^{-i\gamma B_{i,n,m}(t)T'_{n,m}}\right]dV \end{aligned} \tag{5.3.4}$$

and $dV = dxdydz$. Thus, provided we choose a finite number of harmonics, simulation is reduced to finding $A_{i,n,m}(t)$, $B_{i,n,m}(t)$ through circuit simulation, evaluating the integral $V_{int,v}(t)$ to find $s_v(t)$ for every voxel, and feeding the total digital signal $S(t) = \sum_v s_v(t)$ through the appropriate image reconstruction algorithm.

5.3.2.1 Linear Gradients Only

To see how $V_{int,v}(t)$ can be evaluated let us consider only the coefficients $A_{1,1}(t)$, $B_{1,1}(t)$, and $A_{1,0}(t)$,that is x,y, and z gradients which could also be written as $G_x(t)$, $G_y(t)$, and $G_z(t)$. Denoting time integration with a subscript 'i', $V_{int,v}(t)$ is now

$$\begin{aligned} V_{int,v}(t) &= \iiint_{\text{voxel}} \left[e^{-i\gamma G_{i,x}(t)x} e^{-i\gamma G_{i,y}(t)y} e^{-i\gamma G_{i,z}(t)z} \right] dxdydz \\ &= \int_{x_1}^{x_2} e^{-i\gamma G_{i,x}(t)x} dx \int_{y_1}^{y_2} e^{-i\gamma G_{i,y}(t)y} dy \int_{z_1}^{z_2} e^{-i\gamma G_{i,z}(t)z} dz \\ &= \left[\frac{e^{-i\gamma G_{i,x}(t)x_2} - e^{-i\gamma G_{i,x}(t)x_1}}{-i\gamma G_{i,x}(t)} \right] \left[\frac{e^{-i\gamma G_{i,y}(t)y_2} - e^{-i\gamma G_{i,y}(t)y_1}}{-i\gamma G_{i,y}(t)} \right] \left[\frac{e^{-i\gamma G_{i,z}(t)z_2} - e^{-i\gamma G_{i,z}(t)z_1}}{-i\gamma G_{i,z}(t)} \right] \end{aligned} \tag{5.3.5}$$

where the rectangular voxel is defined by diagonally opposite vertices (x_1, y_1, z_1) and (x_2, y_2, z_2). Note that the functions $G_{i,x}(t)$, $G_{i,y}(t)$, and $G_{i,z}(t)$ need only be determined once and do not vary between voxels but that $V_{int,v}(t)$, although trivial, must be recomputed for every voxel and at every time.

5.3.2.2 Higher Order Harmonics

Unfortunately evaluating $V_{int,v}(t)$ for higher order harmonics becomes considerably more difficult. In general the spherical harmonics $T_{n,m}$ and $T'_{n,m}$ can be represented as polynomials in x, y, z by converting from spherical to Cartesian coordinates and thus $V_{int,v}(t)$ involves the integral of an exponential with a large polynomial in its argument. A closed form solution to this problem is not readily available and thus we express $V_{int,v}(t)$ as

$$V_{int,v}(t) = \iiint_{\text{voxel}} \cos(\theta(\mathbf{r}, t))dV + i \iiint_{\text{voxel}} \sin(\theta(\mathbf{r}, t))dV,$$

where $\theta(\mathbf{r}, t)$ is from equation 5.3.2, and evaluate both integrals numerically for every time point. Fortunately the integrands share the function $\theta(\mathbf{r}, t)$ which varies only slightly over a voxel and this knowledge may be used to speed up the computation but since our experimental method only involved the gradients G_x, G_y, and G_z we defer the simulation of higher order harmonics to a later date.

5.4 Summary

In summary, figure 5.1b gives a general layout of a harmonic control system. When designing such a system the desired bandwidth and slew rate must be specified for each harmonic and these can be found from the most demanding imaging sequence – at least as far as the gradient system is concerned – that is expected to be used. Given these constraints and a coil former geometry for the harmonic detection coils, each detection coil should be designed with as many contours as the system bandwidth will allow. Perhaps the most important design decision is the placement of ω_I. Section 5.3 outlines a method for optimizing this

parameter with respect to field noise and distortion but this method may also be used to optimize the choice of feedback compensator. With ω_I finally set, the integrator's internal mesh point ω_M is determined by the specified harmonic slew rate.

Part III

Methods and Results

Chapter 6

Experiment Design and Results

Having developed a theory for the design of spherical harmonic detections coils and their associated feedback systems, we now describe a set of experiments used to test that theory. Incorporating spherical harmonic control systems into an operational MRI machine requires accurately positioning a set of harmonic detection coils within the bore of the magnet and re-routing the input of each harmonic production coil's current drive amplifier. Since this requires either a dedicated MRI or a large setup and tear down time, I was unable to obtain access to a working instrument and experiments were therefore devised which do not rely on the presence of a static B_0 field. To further contain the cost of these experiments, I personally designed and fabricated both the mechanical and electrical apparatus.

The goal of these experiments was to produce eddy current fields analogous to those in an MRI and control those fields using dynamic pre-emphasis. The time evolution of a magnetic field's harmonics up to $n = 5, m = 5$ was determined by measuring the evolving B_z field following a gradient pulse at points on the surface of a sphere and later computing the spherical harmonics at every time point. Since the experiments were performed without an MRI machine and its associated B_0 field, the design and fabrication of harmonic production coils was greatly simplified as there was no significant Lorentz force. For simplicity, we chose to implement feedback loops only for the B_z gradients G_x, G_y, and G_z.

6.1 Basic Setup and Mechanical Design

As shown in figure 6.1, the experimental setup includes a field probe (sniffer coil) to directly measure the magnetic field, a computer to log the results, and the coils and electronics for the three feedback loops. All the gradient coils are mounted together on a fixed coil former (figure 6.2a) while the detection coils are mounted on a separate movable former (figure 6.2b) allowing the mutual inductance between the two sets of coils to be plotted with respect to their relative position. An aluminium tube surrounding the coils simulates an MRI machine's cryostat and acts as a host for eddy currents. Adjusting the field plotting

Declination θ (degrees)	Azimuth ϕ (degrees)
7.5	0
22.5	30
37.5	60
52.5	90
67.5	120
82.5	150
97.5	180
112.5	210
127.5	240
142.5	270
157.5	300
172.5	330

Table 6.1: Probe positions used to compute spherical harmonics up to and including order and degree five. Since every azimuthal position must be mapped for each declination, there are 144 points in all.

apparatus (figure 6.2c-f) allows the field probe to be positioned at points on the surface of a sphere (radius 4.1 cm) and the axial position of this sphere can be changed by moving the probe up or down within its tube (figure 6.2d). After measuring the field at the positions shown in table 6.1 and storing the results in a computer, the fast spherical harmonic transform [110, 65, 57, 64] was used to compute the spherical harmonics of the magnetic field with respect to time.

The mechanical design consists of a stationary support structure shown in figure 6.2a on which the gradient coils were wound and the other mechanical components rest. The cylindrical gradient coil former was cut from a length of green plastic sewer pipe (outer diameter 21.3 cm) while the rest of the support structure was machined from annealed high density polyethylene (white plastic). The detection coil former (figure 6.2b was cut from a smaller green plastic sewer pipe (outer diameter 15.9 cm) and was attached to a large acrylic tube which fit snugly ($\sim$ 0.1 mm clearance) into several circular holes along the top of the support structure. Moving the acrylic tube allows the detection coils to be repositioned and, as shown in figure 6.3a-b, their position can be read from the markings on a wooden dowel as well as a paper protractor affixed to the top of the support structure. The acrylic tube is held in place by two opposing grips.

Inside this support tube, and separated from it by plastic spacers, rests a field plotting apparatus [80] (figure 6.2c-f) which consists of two wheels at fixed axial positions within a tubular acrylic chassis. Two rods of equal length were connected to the wheels at positions 90° apart, one to hold the probe and the other for support, such that the wheels turn together while both tubes remain axially orientated. As the wheels turn, the field probe's position (figure 6.3c) traces an arc in the θ direction which, when rotated azimuthally by turning the whole acrylic chassis, sweeps out a sphere. The declination θ can be read from a protractor on the top wheel and the azimuthal position ϕ can be read from the same protractor used to read the azimuthal position of the detection coil. A large circular hole was cut in the bottom of the field plotter's

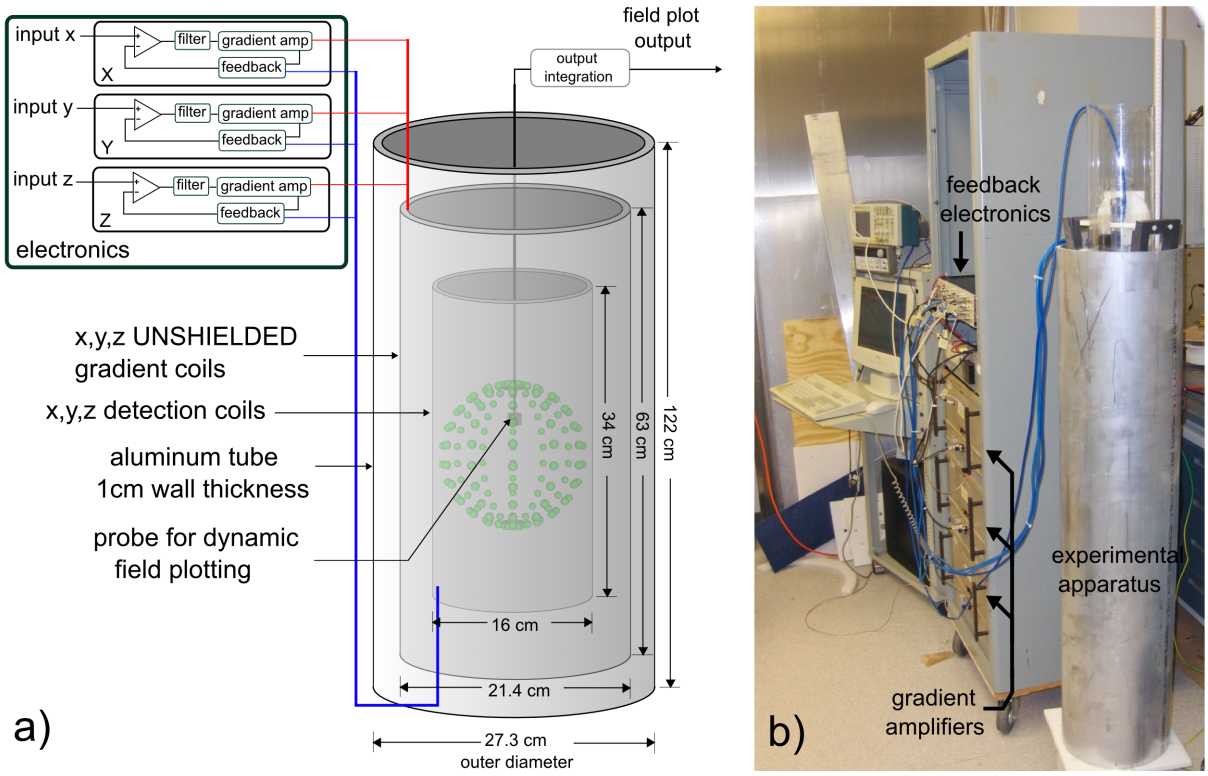

Figure 6.1: Part a) is a schematic of the complete experimental setup and b) is a photograph of its implementation.

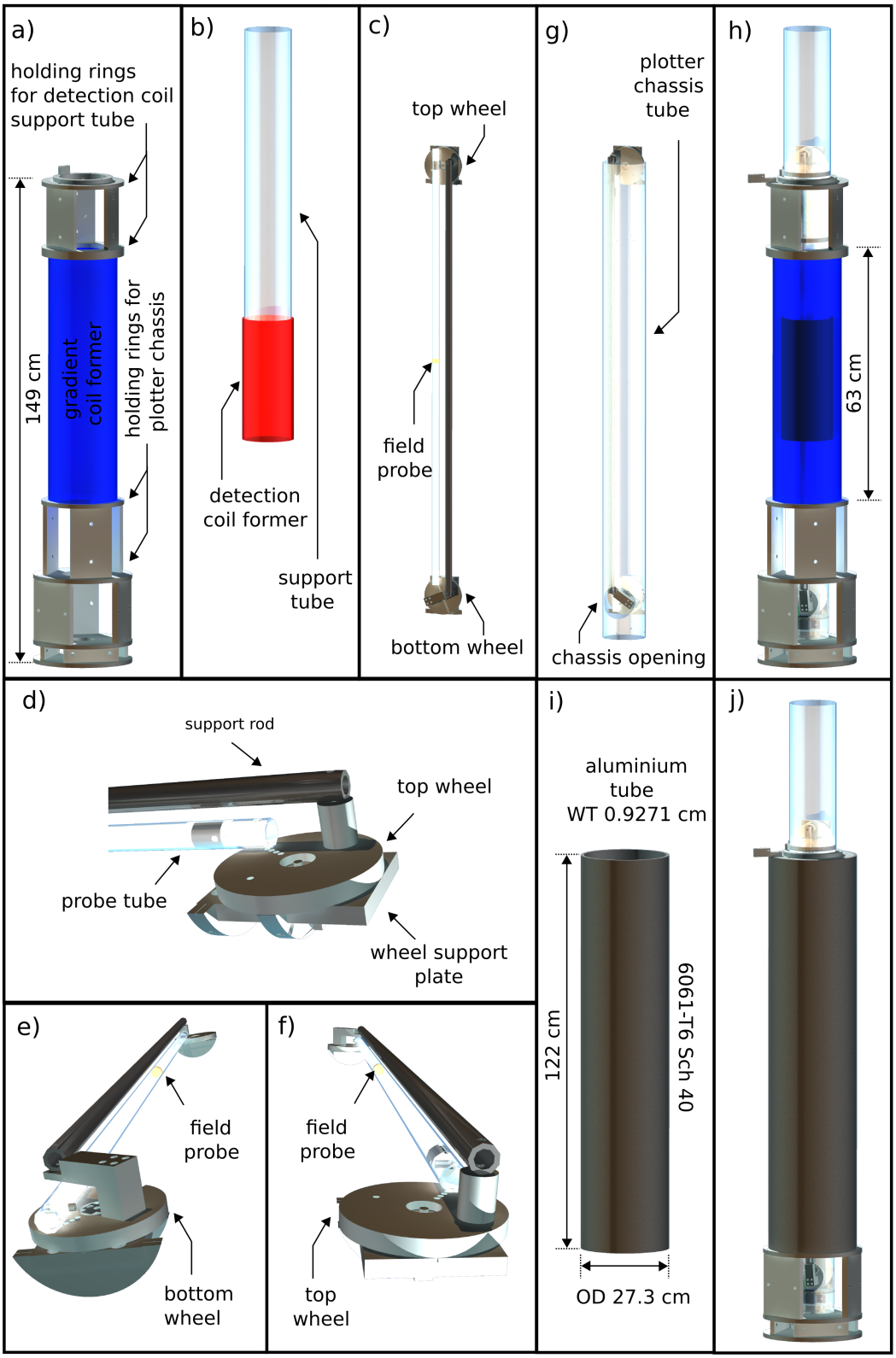

Figure 6.2: Part a) shows the basic support structure and the fixed gradient coil former into which the movable detection coil former in b) was fit. The rings at the top of the structure hold the detection coil support tube shown in b) while the rings at the bottom hold the plotter chassis tube shown in g). Parts c-g) show the apparatus used to position the field probe and in h) the two coil formers and field plotting apparatus are shown assembled. Part i) shows the removable aluminium tube and j) shows the complete assembly.

acrylic chassis (figure 6.3d) thus providing access to the bottom wheel such that the probe tube and support rod can be connected.

6.2 Practical Coil Considerations

6.2.1 Gradient Coils

The gradient coils were wound in consecutive layers on the former shown in figure 6.2a. Since this former has an outer radius of 10.6 cm, its outer surface is only 2.1 cm from the inner surface of the aluminium tube and thus the gradient coils were wound in this space. Due to this close proximity, gradient coils would usually be designed with substantial active shielding (section 3.1.1.1). However, our goal is not to minimize eddy-current fields – as is done when designing an actual MRI machine – but rather to verify dynamic pre-emphasis. Therefore gradient coils were designed using the *unshielded* shim-coil design method of Hoult and Deslauriers [50]. Although this method is not ideal for gradient coils, it does produce single layer coils which can fit into the 2.1 cm space and, due to commonality with the detection coil design method in section 4.2, a single set of software tools can be applied to the design of either type of coil. The result is that rapidly switched currents through the unshielded gradient coils strongly couple to the aluminium tube and induce large, and easily detected, eddy currents.

The first of the software tools was written in *Mathematica* and used to determine the Fourier wire density coefficients F_j and G_j (equation 4.2.2). For detection coils this software generated a rectangular matrix from equation 4.2.8 which was then inverted using *Mathematica's* 'PseudoInverse' function. However for gradient coils, the matrix was generated using the relationship between the azimuthal wire density coefficients $G_j(z)$ and the produced field harmonic coefficients $B_{za,n,m}$ [50], that is

$$B_{za,n,m} = \int_{-L}^{L} \frac{-G_m(z)\mu_o}{4} \sum_{n=m}^{\infty} \frac{\sin(\alpha)(n-m)!}{f^{n+1}(n+m)!} \left[P_{n+1,m+1}(\cos\alpha) - (n-m+2)(n-m+1)P_{n+1,m-1}(\cos\alpha)\right] dz. \tag{6.2.1}$$

The three gradient coils were each designed to produce only a single harmonic while other harmonics of order less than or equal to $n = 5$ were explicitly nulled.

The resulting wire density coefficients were then passed from *Mathematica* to a set of software tools written in the computer languages C and Python. When given a desired number of contours with which to approximate the stream function (section 4.2.4), one of these tools output a list of wire line segments following those contours and another software tool then connected the contours with additional segments so that the list formed a single closed wire path. With the segment endpoints saved to a file, yet more software tools displayed the segments (figure 6.4a) and predicted the magnetic field using the Biot-Savart law (equation 2.1.23). As shown in figure 6.4b, another software tool was able to produce a two dimensional projection of a wire path, including arrows to mark wire direction, which could then be printed full size on

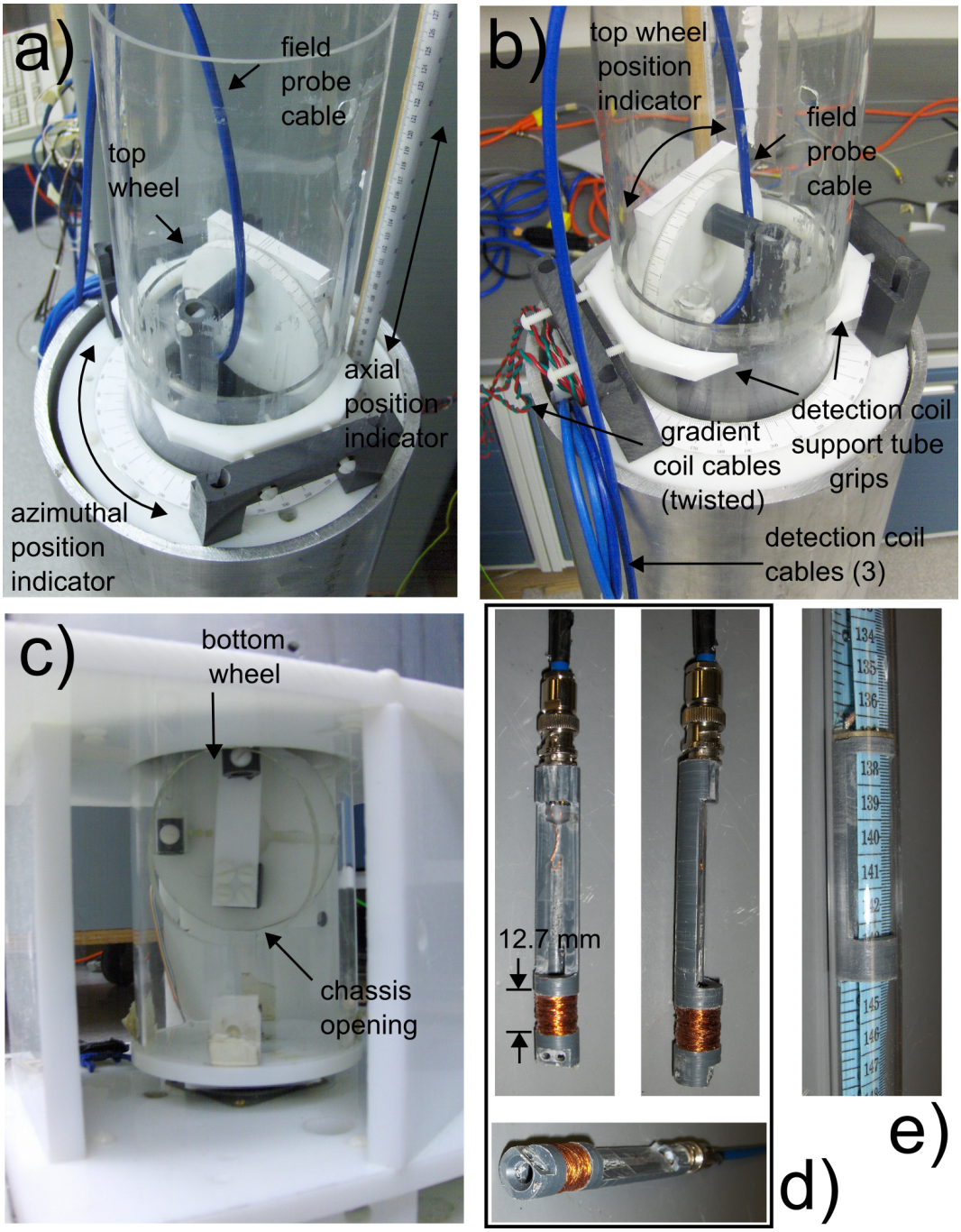

Figure 6.3: Photos a) and b) show the top of the experimental assembly from two different angles. In both photos the grips holding the detection coils in place, the top of the field plotting apparatus, and the paper markings used for measurement can be seen. Photo c) shows the bottom of the assembly below the aluminium tube. Here the bottom wheel of the field apparatus can be clearly seen as well as the large hole cut to access it. The three photos in d) show the sniffer coil used as a field probe; the length of its former provided stability when placed within the the probe tube. The photo in e) shows a close up of a hall effect sensor placed within the probe tube which is on a tiny printed circuit board affixed to the top of a plastic component used for mechanical stability. Turning a dial at the top of the probe tube moved a length of tailor's tape and since either probe could be connected to the tape, the probe could be placed precisely. Although the Hall probe was useful for secondary verification, the results presented in this thesis were produced by using the sniffer coil followed by an electronic integrator.

a sheet of paper. This sheet could then be wrapped around the coil former and used as a winding template. However before fabrication, software was used to verify that the contours were few enough that there would be physical space for the wires.

Once the G_z wire path had been generated, the paper winding template was affixed to the gradient coil former with spray-on artist's glue. The coil was then hand-wound by following the arrows on the template with 0.813 mm diameter copper magnet wire[1] which was painstakingly fixed in place with clear cellophane tape. After the gradient coil was wrapped, it was covered in a cellulose filler compound called "Polyfilla" and, after waiting for the compound to become firm but not completely dry, the coil was centred on an axial spindle and placed on the table of a milling machine. The milling machine's bit was set to cut into the polyfilla at a fixed depth so that as the gradient coil was turned on the spindle, and the table shifted in the axial direction, a smooth cylindrical surface was formed just above the G_z coil. This cylindrical surface was then used as the foundation for the G_x coil which was similarly wrapped, covered in "Polyfilla", and machined to provide a foundation for the G_y coil. Once complete, the three-layered gradient coils were connected to their current sources using banana plugs and standard hook-up wire.

6.2.2 Detection Coils

The detection coil wire density coefficients and discrete wire segments were found using the same software used for the gradient coils above, the differences being that the rectangular matrix was generated directly from equation 4.2.8 and the matrix size was chosen to reject unwanted harmonics up to and including $n = 7$. In both types of coil, the connections between contours take the form of short, axially directed wire segments as can be clearly seen in figure 6.5. For a field production coil, axially directed wire segments produce no B_z field and thus do not degrade coil performance. However for a harmonic detection coil, the voltage induced in every wire segment contributes to the total voltage. Therefore the flux linkage to the contour interconnects was cancelled by running a return wire directly over them.

6.2.2.1 Calculating the Flux Response

To simulate the performance of a detection coil design, the flux linkage of an arbitrary wire pattern to the individual field harmonics can be found since the total flux linkage Φ_T to a wire segment with endpoints $\mathbf{a}$ and $\mathbf{b}$ is $\Phi_T = -\int_{\mathbf{a}}^{\mathbf{b}} \mathbf{A} \cdot d\mathbf{l}$ (equation 2.1.13) where $\mathbf{A}$ is the vector potential expressed in terms of the field harmonics. Using tables 4.1 and 4.2 the vector potential can be determined numerically at any spatial location and thus by numerical integration[2] of $\mathbf{A} \cdot d\mathbf{l}$ along the entire wire path – one segment at a time – the coil pattern's flux response can be computed.

[1] Belden 8076 magnet wire AWG 20 (www.belden.com)

[2] We used the Gauss-Kronrod 61 point algorithm implemented in the GNU scientific library [30].

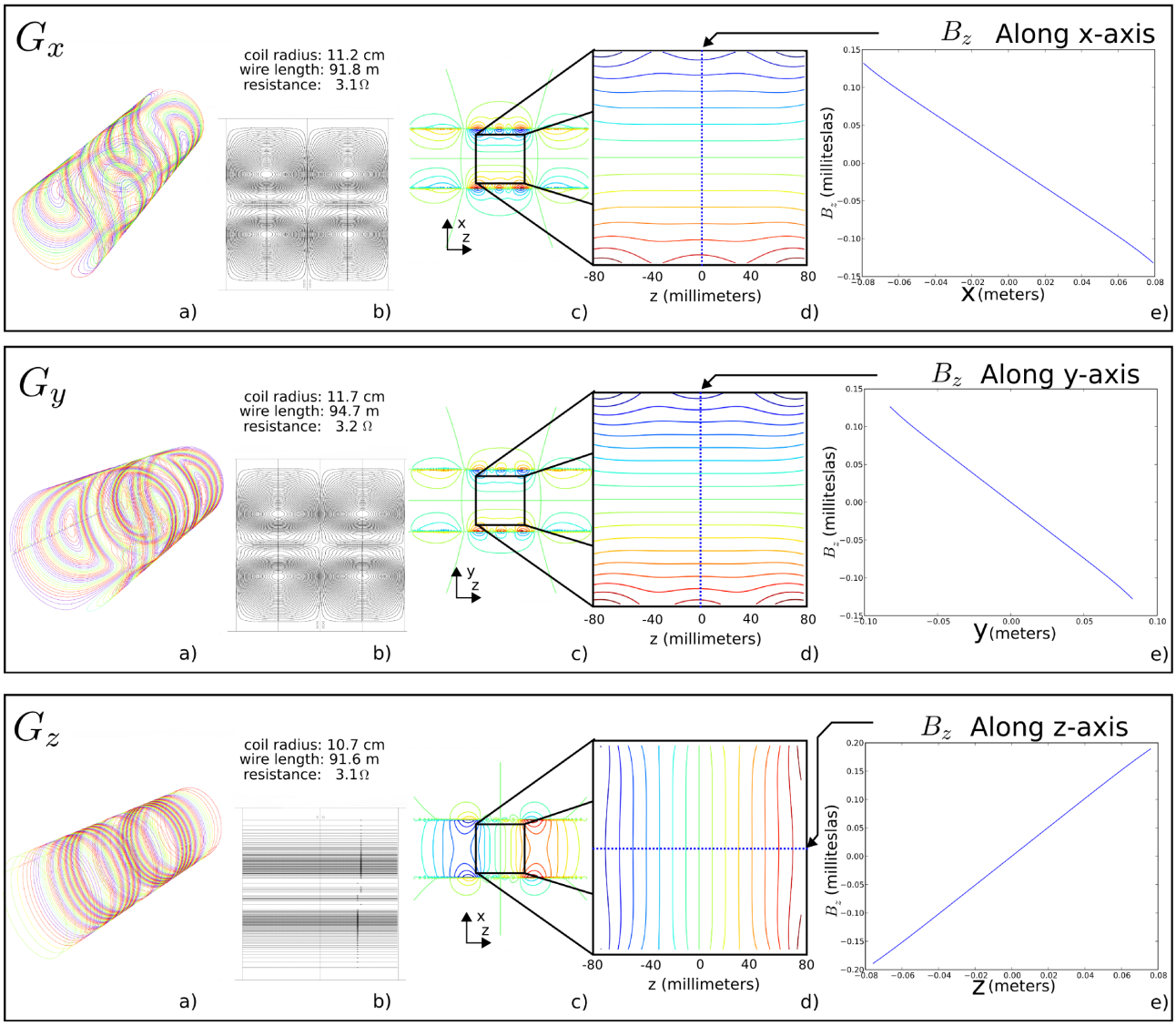

Figure 6.4: For each gradient coil, a) shows the wire path in three dimensions and b) shows a scaled version of the wrapping template. Parts c) and d) are contour plots of the simulated B_z field at two levels of detail, and part e) is a simulated field plot along an axis of interest assuming a current of 1 A flows in the coil. The plots in e) begin to deviate slightly from a straight line as the distance from the centre increases.

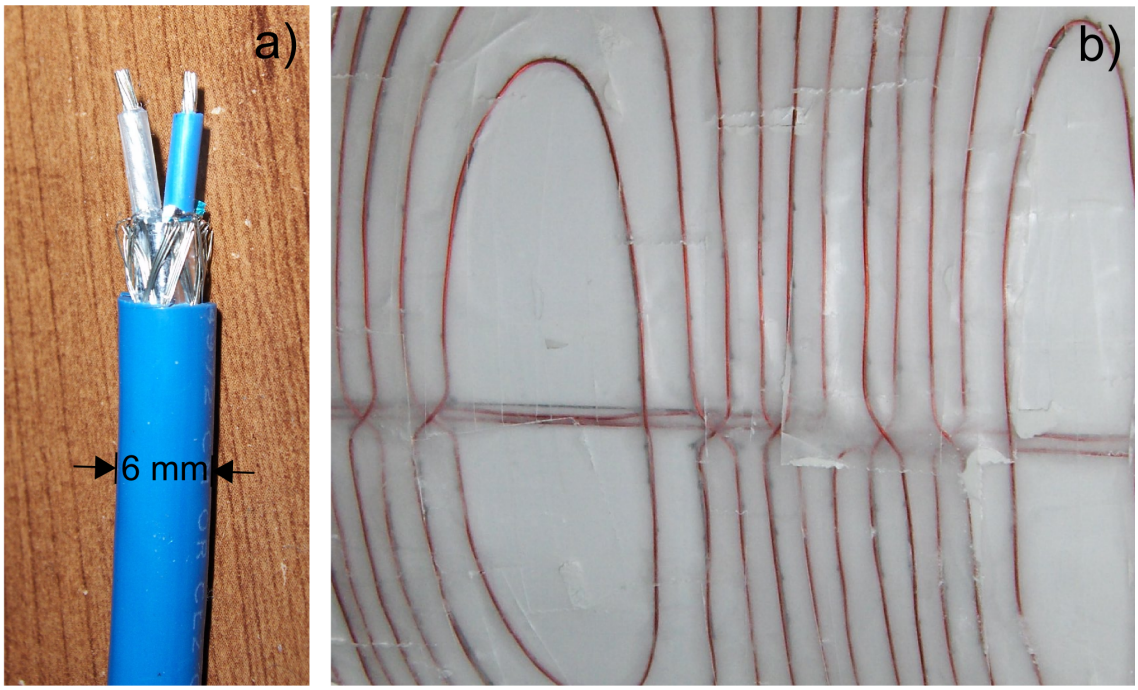

Figure 6.5: Photo a) is of twin-axial cable and photo b) is a close-up of the D_x coil before it was covered in polyfilla; the wire is held by clear plastic tape to the winding template which can be occasionally seen, with its arrows, beneath the wire. Note the connections between contours and the return wires down the centre. There are two return wires on the top half of the coil because winding was started at the coil's axial centre but the twin-axial connection was placed on the coil's top edge.

However, when computing the flux response we must select arbitrary harmonic coefficients $\kappa_{ab,n,m}$ for the field rather than using physical coefficients $B_{zab,n,m}$ and the arbitrary coefficients should be selected such that comparing flux responses is meaningful. To appreciate the problem, consider computing a detection coil's harmonic flux response with coefficients chosen such that $\kappa_{ab,n,m} = 1/R_{ref}^n$ where R_{ref} is chosen to cancel the factors r^n in the spherical harmonics $T_{n,m}, T'_{n,m}$ first on a sphere much larger than the detection coil and then a second time on a sphere much smaller than the coil. Obviously, due to the r^n dependence of the spherical harmonics, the high order flux responses computed when R_{ref} is the radius of the large sphere will be much smaller than when R_{ref} is the radius of the small sphere. Thus, for a reasonably fair comparison between harmonics – and between coils of different geometry – we compute flux responses using $\kappa_{ab,n,m} = 1/R_{ref}^n$ such that $R_{ref} = \sqrt{(L/2)^2 + R^2}$ where R and L and are the detection coil's radius and length; flux responses computed in this way are shown in figure 6.6.

6.2.2.2 The Voltage Induced in a Discretized Coil

Although the voltage induced in a discrete wire path can be computed directly from the flux linkage to various field harmonics, it is useful to have a direct link between the desired flux coefficient $\alpha_{n,m}$ used in equation 4.2.8 and the simulated flux response computed from the wire path as above. From equation 4.2.7, the total voltage generated in a continuous wire distribution is $V_T = -\omega\Phi_T = -\omega\sum_{n=m-1}^{\infty}\Phi_{n,m}$ where each function $\Phi_{n,m}$ found in equation 4.2.6 depends on the wire density coefficients and the harmonic coefficient $B_{za,n,m}$. Now when a detection coil's wire pattern is designed, a desired flux response $\alpha_{i,j}$ (usually $\alpha_{i,j} = 1$) is specified for a given design harmonic ($n = i, m = j$) with arbitrary coefficient $\kappa_{i,j}$ where all other desired flux responses are specified as zero and thus all other harmonic coefficients $\kappa_{n,m}$ are basically irrelevant. Thus, imagining it were possible to produce the continuous wire distribution, the voltage induced in it would be $V = -\omega\alpha_{i,j}$ when it is placed in a field where the harmonic of interest has amplitude $\kappa_{i,j}$ and oscillates at angular frequency ω. Therefore the voltage induced in this continuous distribution when exposed to a physical harmonic magnitude $B_{za,i,j}$ would be $V = -\omega\frac{\alpha_{i,j}B_{za,i,j}}{\kappa_{i,j}}$. However discretization of the continuous wire distribution into wire segments causes stream function contours to be chosen such that each contour is separated by an amount $\Delta\Gamma$ corresponding to a single wire in the physical coil (see section 4.2.4). Thus the voltage induced in the actual wire path should be

$$V = -\omega\frac{\alpha_{i,j}B_{za,i,j}}{\Delta\Gamma\kappa_{i,j}} \tag{6.2.2}$$

and deviations from this value are caused by errors introduced either by discretization or by manufacturing.

Another important consideration when determining the voltage induced in a detection coil is its mutual inductance to a nearby field production coil (gradient coil in our case). Since a field production coil only produces a single harmonic within a limited region and a detection coil may not fit entirely within this

region, the flux response to individual harmonics is not always sufficient to determine the mutual inductance between coils. Instead we use the Neumann equation (equation 2.1.25) to directly compute the mutual inductance between the sets of wire segments making up each coil and these results are given in figure 6.6.

With the simulations complete, the detection coils were fabricated on a coil former of radius 7.9 cm using 0.455 mm[3] diameter copper magnet wire. This smaller wire could be used because, unlike the gradient coils, the current flowing in a detection coil is limited by the high input impedance of the integrator circuit. Twin-axial cable (see figure 6.5) was used to connect each coil to its preamplifier. In this cable the conductors are very close together to minimize inductive coupling, and are surrounded by a conductive sheath to minimize capacitive coupling. Just as with the gradient coils, the detection coils were wrapped in successive layers separated by machined "Polyfilla".

6.2.2.3 Detection Coil Aspect Ratio and n_{max}

Practically, the radius R and length L of the former on which the detection coils are wound is limited by the dimensions of the magnet bore. Here, the length is not limited by the aluminium tube but by the requirement that the detection coil former be free to move by 10 cm in the axial direction and not interfere with other mechanical components.

In general, within a sphere of radius $R_{ref} = \sqrt{(L/2)^2 + R^2} < \infty$ that encompasses the coil former[4], the magnetic field can always be described as a sum of spherical harmonics, and the larger the radius, the more orders are needed to attain a given descriptive accuracy – certainly more than the maximum number n_{vol} needed to accurately describe the field in the volume of interest for magnetic resonance. For a fixed radius R, longer coils require more orders to be rejected in the detection coil design – that is an increased n_{max}. At first sight, this implies that the length L should be a *minimum*. However, as L decreases, it is found that there is a limit to the number of orders that may be rejected, and an undesirable point may come where that limit is less than n_{vol}.

It follows that there is an optimal coil former aspect ratio R/L but that the determination of that ratio is difficult. Compounding the difficulty is the accuracy to which a wire pattern approximates its continuous distribution. Then, increasing the maximum rejected order n_{max} may actually reduce a detection coil's accuracy. Further, the optimal length may be different for the detection of different harmonics. Figure 6.6 shows the wire pattern and flux response for first order detection coils with rejection up to and including seventh order. The winding length required for the D_z coil is considerably less than that for the D_x or D_y coils. However, attempts to reduce the length of the two tesseral detection coils resulted in an impractically compressed wire density and eventually, the failure to find a solution.

All the above factors are reflected in the graphs of flux response. Because the windings of the zonal

[3]Rea 25.0 AWG HNSR magnet wire (www.reawire.com).

[4]The field at a point with radial coordinate $f > R_{ref}$ can be described using harmonics that vary as $f^{-(n+1)}$.

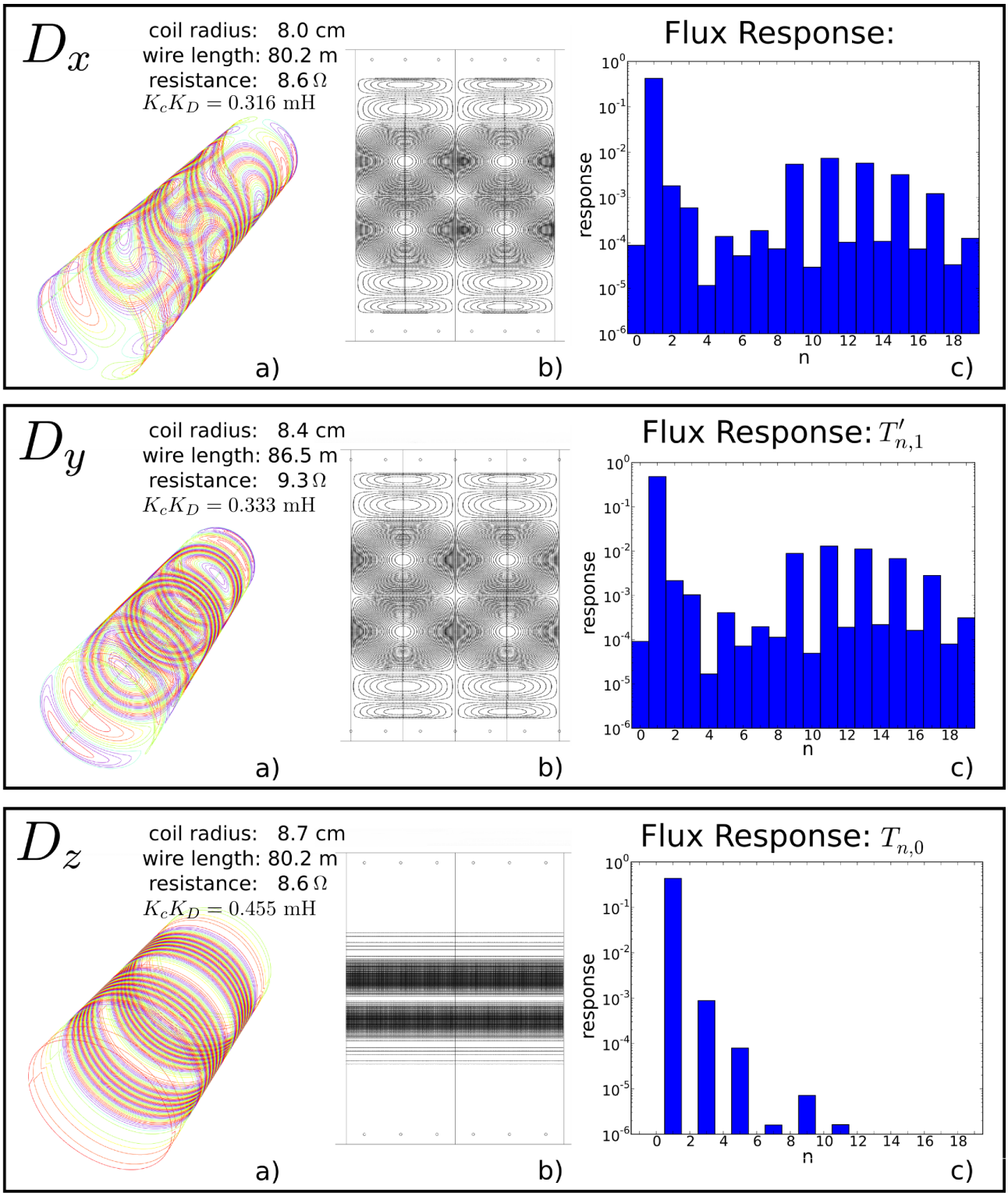

Figure 6.6: For each coil: a) and b) are the wire pattern and wrapping template while c) is the harmonic flux response computed using $R_{ref} = \sqrt{(L/2)^2 + R^2}$. The coil former length is $L = 34$ cm and for each coil the mutual inductance $M = K_cK_D$ between it and the corresponding gradient coil is given as computed using the Neumann formula.

D_z coil occupy a length considerably shorter than R_{ref}, the response to higher orders decreases rapidly even when the design maximum of seven is exceeded. However, this is not the case for the longer D_x and D_y coils and the response starts to rise by the point at which the fifth order is reached, implying that discretization errors are present. A relatively large response is also seen for higher odd orders when comparing with the response for the D_z coil, and this may be attributed to the longer winding. Clearly more orders should be rejected for this winding length, but given that discretization errors are already evident by the fifth order, there seemed to be little point in attempting this correction.

6.2.2.4 A Detection Coil's Resonant Frequency and Bandwidth

Once the detection coils were constructed a simple experiment was performed to determine their bandwidth and verify the model in figure 5.4 and equation 5.1.8. Each detection coil was placed in a circuit as shown in figure 6.7a and the voltage amplitude across R_o measured as a function of the frequency of the sinusoidal wave produced by the function generator. Theoretically the transfer function of the circuit should be

$$\frac{V_o}{V_i} = \frac{R_o}{R_o + Z_D + R_i} \tag{6.2.3}$$

where

$$Z_D = \frac{R_D + sL_D}{1 + sR_DC_D + s^2L_DC_D} \tag{6.2.4}$$

is the impedance of the detection coil.

Each detection coil's resistance R_D was easily found using a digital multimeter but the values for C_D and L_D were merely adjusted numerically until the theoretical parts of figure 6.7b-d approximately fit the experimental results. Once these rough values for C_D and L_D were determined, they were used to plot (see figure 6.7e) the transfer function from a voltage induced in the detection coil by nearby magnetic fields to the resulting voltage between the coil's leads (equation 5.1.8). From these results we see that our detection coil model works reasonably well provided the coil is operated well below its self-resonant frequency. We also note that these particular coils have operational bandwidths of approximately 100 kHz.

6.3 Electrical Design

6.3.1 Electronics Overview

Each feedback channel was designed as shown in figure 6.8 to include a feedback compensator, gradient current amplifier (Techron 7570), gradient and detection coils, and a split feedback path consisting

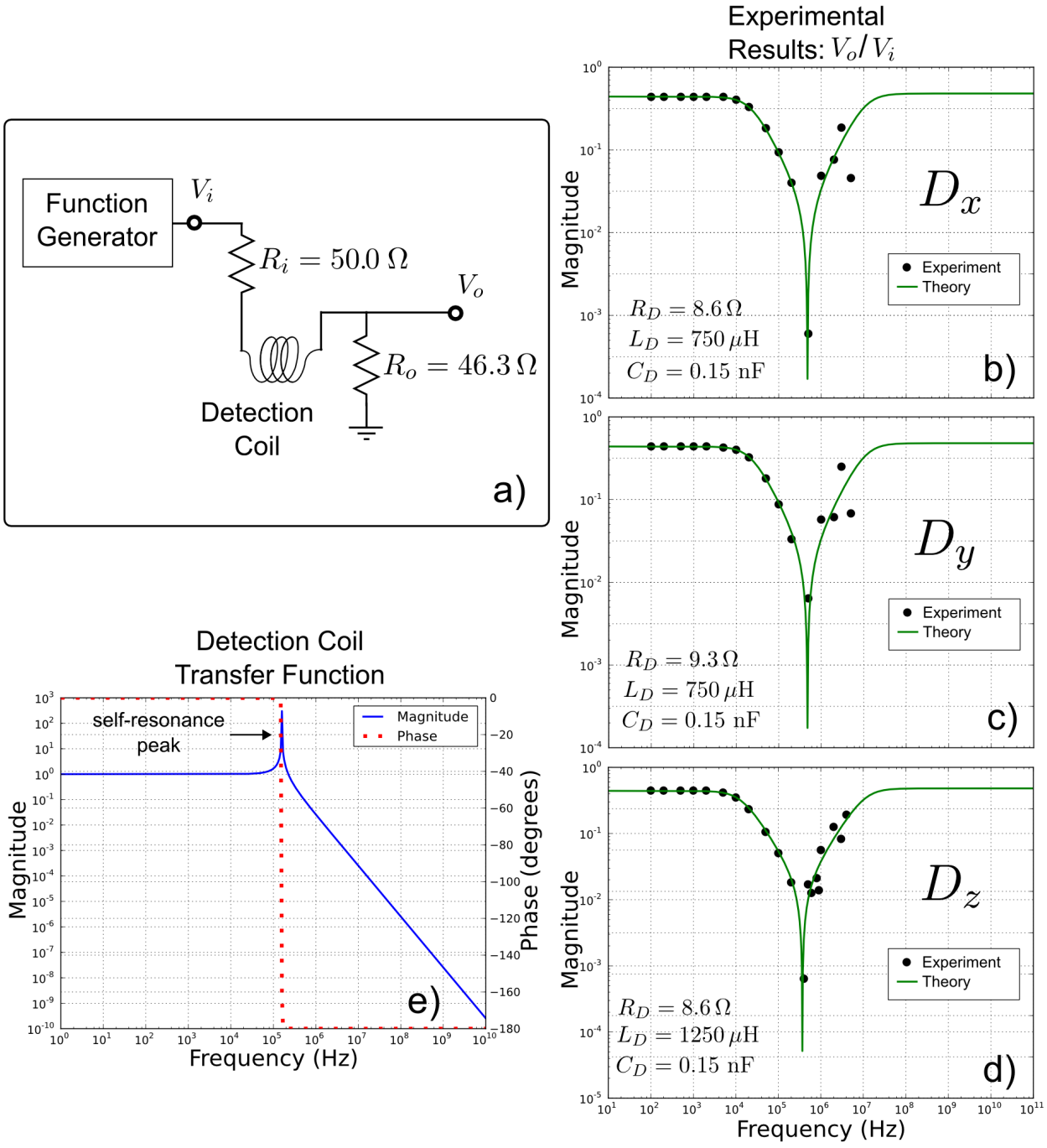

Figure 6.7: Part a) shows the experimental setup used to characterize the detection coils and parts b-d) plot the ratio V_o/V_i found both from experiment and from equation 6.2.3 using the R_D, L_D, and C_D values listed. Finally in e), equation 5.1.8 is plotted using the values R_D, L_D, and C_D values determined from the D_x coil's experimental results; the transfer functions for all three detection coils are nearly identical and so only one is plotted.

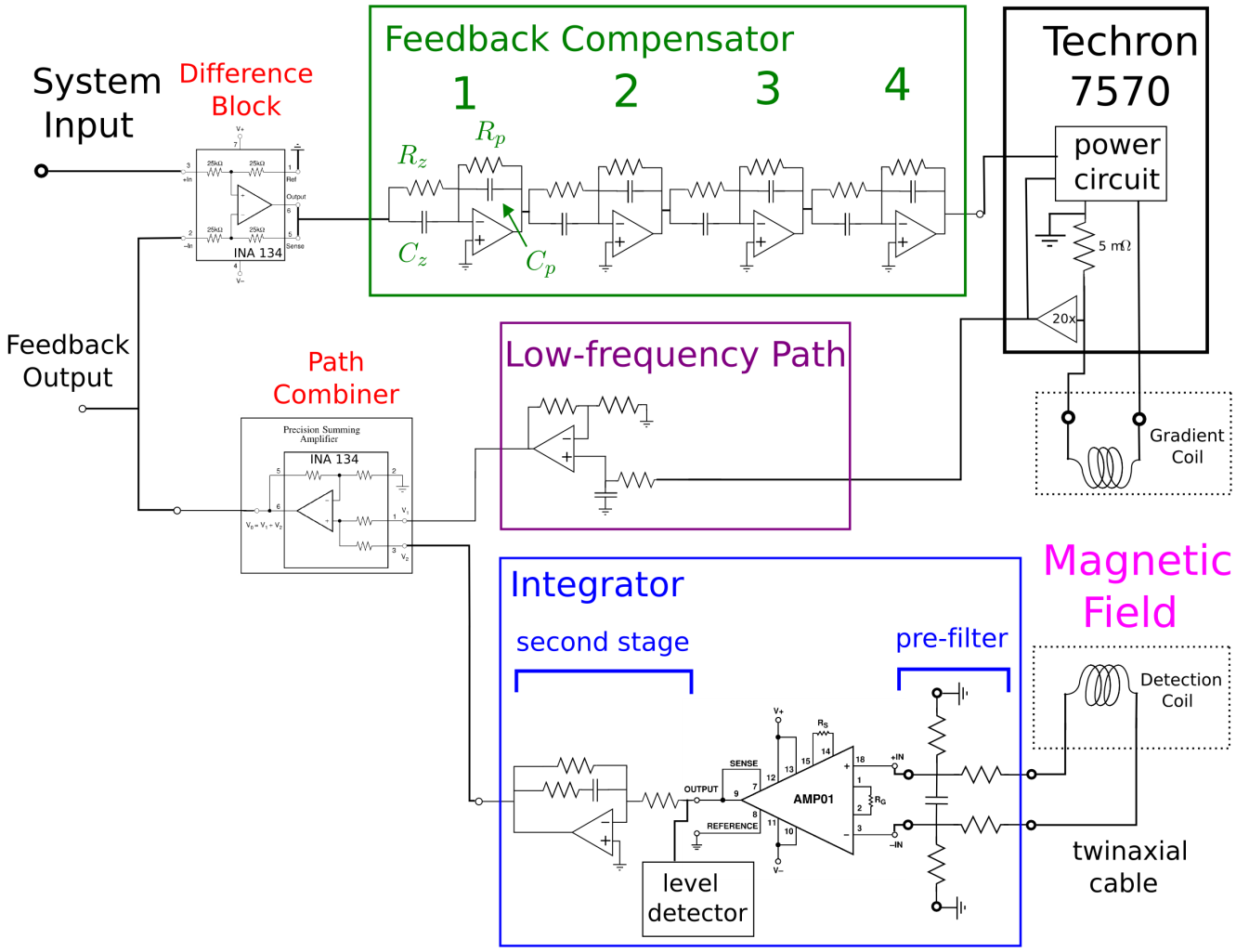

Figure 6.8: Single harmonic control system

of an integrator, low-pass filter, and summing circuitry. Since MRI images could not be acquired, the cross-over frequency ω_I between the two paths was not optimized as described in section 5.3 but was chosen to be $\omega_I/(2\pi) = 0.5\,\text{Hz}$.

6.3.2 Current Amplifiers: Techron 7570

The Techron 7570 power supply amplifiers, which are mounted in the rack shown in figure 6.1, can each drive up to 2 kW of power (limited to 20 A and 100 V) into their respective gradient coils with a maximum slew rate of $32\,\text{V}/\mu\text{s}$. These outdated (circa 1988) amplifiers do not employ digital pulse width modulation and produce trivial output power compared to those normally used in MRI (see section 3.1.1) but they were readily available, being castoffs from previous projects, and can draw power from standard 115 V electrical sockets. Each Techron 7570 ensures that its output current is proportional to its single-ended input

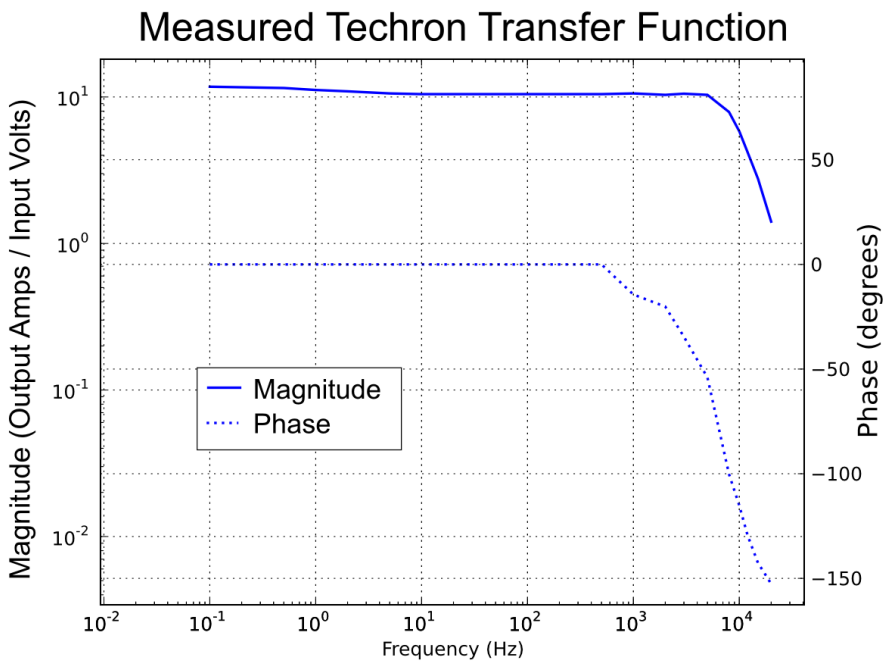

Figure 6.9: The transfer function from the the Techron 7570's input voltage to its output current driven through the G_x coil. The transfer function is essentially the same for the amplifiers driving the G_y and G_z coils and the gain is $K_S = 10$ A/V. Note that the transfer function's magnitude is not level between 0.1 Hz and 10 Hz.

voltage [127, pg 4-5] by using the voltage across an internal 5 mΩ current sensing resistor as a feedback signal; this signal is amplified 20x and provided as an output on the amplifier's front panel. Each amplifier's transfer function was measured by connecting a gradient coil to its output, a frequency generator and an oscilloscope probe to its input, and another oscilloscope probe to its current sense output. By comparing the oscilloscope waveforms to one another at successive frequencies, the result shown in figure 6.9 was acquired.

6.3.3 Parameterizing the Eddy Currents and Selecting ω_I

Before the feedback system could be designed, the parameters ω_e and ξ in the eddy current model $G = K_c\left(\frac{1+\xi s/\omega_e}{1+s/\omega_e}\right)$ (equation 5.1.6) needed to be determined. This was accomplished separately for each of the three gradients by driving a sinusoidal waveform through the gradient coil and measuring the output of an electronic integrator ($f_I = \omega_I/(2\pi) = 0.5$ Hz) connected to the corresponding detection coil; the results are shown in figure 6.10. The parameters ω_e and ξ shown in the figure were found merely by adjusting them until the model approximately fit the experimental results.

As can be seen, below ~ 2 Hz the eddy currents are not appreciable and beyond ~ 80 Hz their effect remains constant with frequency. Now from equation 2.1.29 we know that the skin depth equals the tube's

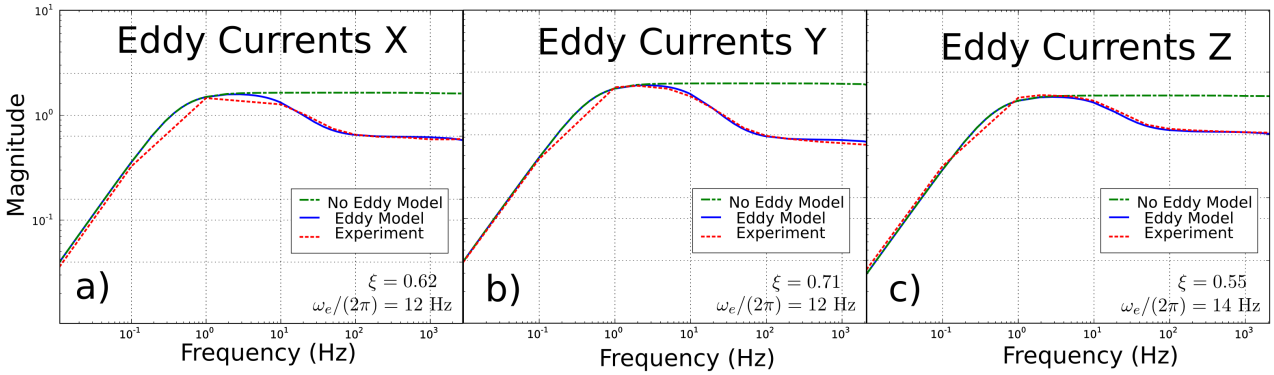

Figure 6.10: Parts a), b) and c) graph the transfer function of the channels x, y, and z from the input of the Techron 7570 through the gradient coil, detection coil, and an integrator with $\omega_I/(2\pi) = 0.5$ Hz. The experimental results fit the simple eddy current model presented in figure 5.3 and for each channel ω_e and ξ were adjusted by hand to fit the experimental results. Below 0.5 Hz the integrator no longer functions but rather produces a roll-off.

thickness[5] at a frequency $f = 1/(\mu_o \pi \sigma \delta^2) = 78.1$ Hz. For frequencies above this value, the eddy currents do not flow appreciably in the whole thickness of the tube and thus the eddy current effect no longer increases with frequency. However as the frequency drops below $\sim$ 2 Hz the tube becomes increasingly transparent to magnetic fields.

Although the integrator used to characterize the eddy currents had $\omega_I/(2\pi) = 0.5$ Hz and below this frequency the eddy current effects are small, it is not immediately obvious that 0.5 Hz is an acceptable cross-over frequency between the two feedback paths (see figure 6.8) since small eddy current effects persist albeit with vanishingly small amplitude (section 5.2.2). However, since we are not planning to acquire an image and the mathematics of section 5.3 was developed after the experiment was designed, an alternative method to that of section 5.3 was required for choosing ω_I.

Fortunately, the equations of section 5.1.4 allow the entire feedback system to be modelled for any value of ω_I. Ignoring the limited bandwidth of the detection coils and using the compensator model to be developed in section 6.3.5, the transfer function T of the entire feedback system was found. Multiplying T by the Laplace transform of a unit step input $(1/s)$ and using the 'InverseLaplaceTransform' function from *Mathematica* produces a closed form equation, albeit many pages long, for the system's step response; this equation is plotted for various values of ω_I in figure 6.11. As can be seen in the figure, there is a characteristic 'droop' in the step response caused by eddy current distortion of the feedback path (section 5.2.2) which has nothing to do with the overshoot and ringing common to feedback systems (figure 3.5). Having no specific engineering requirements to satisfy, we accept $\omega_I/(2\pi) = 0.5$ Hz as the cross-over frequency between the two feedback paths because the associated step-response differs from the ideal by only a few percent.

[5] Aluminium has a resistivity of $\rho = \frac{1}{\sigma} = 2.65 \times 10^{-8}\,\Omega$m [74, ch 12] and the aluminium tube has a wall thickness of $\delta = 9.271 \times 10^{-3}$ m (figure 6.2i).

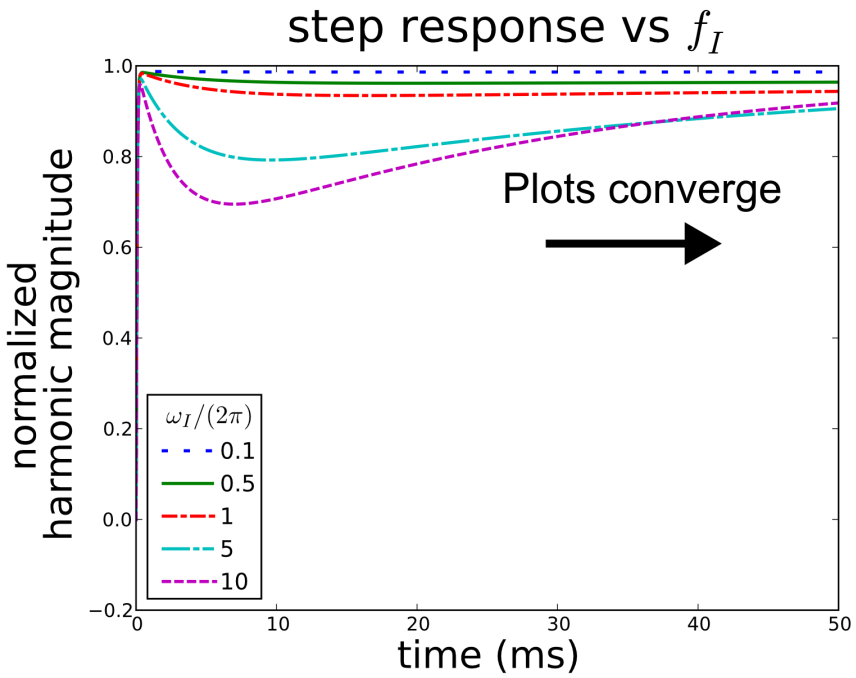

Figure 6.11: The feedback system's step response is simulated for various choices of ω_I. The high-frequency feedback path causes the harmonic output to rise quickly and the low-frequency path ensures that the result eventually converges to the correct value. However the 'droop' during intermediate times is caused by deviation in the feedback path due to eddy currents (see figure 5.7).

With ω_I set, the integrator's internal mesh frequency ω_M was chosen to maximize signal to noise ratio for a certain maximum harmonic slew rate (section 5.2.1). Although this value can be determined by simulation, it was set by trial and error at approximately $\omega_M \simeq 10\,\omega_I = 2\pi \times 4.5$ Hz. The mesh between the two integrator stages was achieved by carefully measuring component values and was verified by measuring the integrator response to a sine wave at frequencies above and below the mesh point to ensure that both points fit on a single-pole filter response.

6.3.4 The Integrator and Split Feedback Path

The transfer function of the feedback path, especially that of the integrator (section 5.2.1), is of the utmost importance in determining the transfer function of the complete feedback system. In addition to producing an excellent transfer function, the feedback path must not introduce excessive noise or offset into the system and this is accomplished primarily by selecting an appropriate preamplifier.

6.3.4.1 The AMP01 and other Integrated Circuits

The AMP01, shown in figure 6.12, was selected as a preamplifier because of its low flicker noise ($0.12\,\mu V_{pp}$ between 0.1 Hz and 10 Hz), its fairly low offset voltage (50μV maximum), and its high linearity.

Figure 6.12: Part a) shows the AMP01's schematic; note that the gain can be altered by adjusting R_s. In b) the AMP01's frequency response is shown for various gain settings and c) is a plot of the amplifier's input noise voltage which is dominated by flicker noise below 10 Hz and by white noise with a magnitude of approximately $5\,\mathrm{nV}/\sqrt{\mathrm{Hz}}$ above 10 Hz. The AMP01 is an instrumentation amplifier (section 3.2.2.2) produced by Analog Devices (www.analog.com) and these three images were taken from the manufacturer's datasheet.

It has a bandwidth of over 10 kHz and by adjusting the resistor R_s while keeping R_G fixed, the AMP01's gain can be adjusted between 0.1 and 10^4. A small bias current (4 nA) flows from each of the AMP01's inputs and must be given a path to ground and, depending on the path, the difference between these offset currents (typically 0.2 nA) may introduce an erroneous input voltage in addition to the amplifier's intrinsic $50\,\mu$V input offset voltage. Since the AMP01's properties are specified for $\pm 15V$ power supplies, these supply voltages were used for all analog components in the feedback system.

In addition to the AMP01, several other integrated circuits should be mentioned. As shown in figure 6.8, the INA134 is an op-amp. with four integrated resistors which have been laser trimmed to precisely 25 kΩ. This precision makes implementing both the difference amplifier of equation 3.2.8 and the signal summing block between the two feedback paths fairly straightforward. Another important integrated circuit is the OP177, a high quality op-amp. with a gain-bandwidth product of over 500 kHz; it was used wherever a simple op-amp. is shown in figure 6.8.

The clip detector shown in figure 6.8 is a simple circuit which turns on a warning light if the AMP01's output departs from the range ±13 V. This was accomplished by monitoring the AMP01's output with two comparators, each with its output connected to a separate digital flip-flop. Therefore if the AMP01's output ever departed from the range ±13 V a warning light would turn on and stay on until explicitly reset by cycling the feedback system's power.

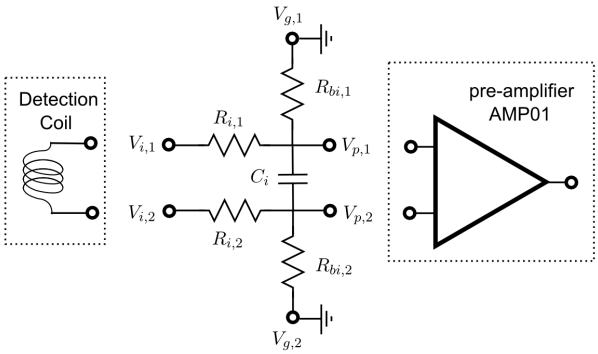

Figure 6.13: Pre-filter schematic

6.3.4.2 The Pre-filter

To provide a path for the AMP01's bias currents, two resistors were added to the pre-filter circuit in figure 5.6b resulting in the circuit in figure 6.13. However, the new resistors must not appreciably alter the pre-filter's transfer function or introduce excessive noise. Fortunately, provided that the value of the additional resistors R_{bi} is much larger than that of the input resistors R_i, the circuit is simply a low-pass filter as before. Moreover, when the resistors are matched such that $R_{i,1} = R_{i,2} = R_i$ and $R_{bi,1} = R_{bi,2} = R_{bi}$, symmetry ensures both that differential signals detected by the AMP01 arise solely from the difference $V_{i,1} - V_{i,2}$ and that common mode signals rejected by the AMP01 arise solely from signals common to $V_{i,1}$ and $V_{i,2}$. However, to design the pre-filter properly we must know precisely how unmatched resistors degrade common mode rejection and what influence the ratio R_{bi}/R_i has on the circuit's transfer function. We must also determine the noise generated by the resistors and how it compares to the noise of the AMP01.

Assuming that the AMP01's input impedance ($\sim 1\ \mathrm{G}\Omega$) is much higher than that of any component in the pre-filter, the voltage at $V_{p,1}$ is merely a super-position of the voltages produced at $V_{p,1}$ due to each of the inputs $V_{i,1}$, $V_{i,2}$, $V_{g,1}$, and $V_{g,2}$ – we are considering the points $V_{g,1}$ and $V_{g,2}$ as inputs to analyze the noise arising from $R_{bi,1}$ and $R_{bi,2}$. Therefore the voltage at $V_{p,1}$ due to $V_{i,1}$ is found by the voltage divider $V_{p,2} = \frac{R_{bi,2}\|Z_Q}{R_{i,2}+R_{bi,2}\|Z_Q} V_{i,2}$ where $a \parallel b = \frac{ab}{a+b}$ stands for the parallel combination of impedances and Z_Q is formed from the capacitor's impedance $Z_{ci} = \frac{1}{j\omega C_i}$ in series with the parallel combination of $R_{i,1}$ and $R_{bi,1}$. From similar considerations, the total voltages at $V_{p,1}$ and $V_{p,2}$ are

$$\begin{aligned} V_{p,1} &= D'_L V_{i,1} + D'_N V_{g,1} + D_L D'_M V_{i,2} + D_N D_M V_{g,2} \\ V_{p,2} &= D_L V_{i,2} + D_N V_{g,2} + D'_L D_M V_{i,1} + D'_N D'_M V_{g,1} \end{aligned} \tag{6.3.1}$$

where

$\delta = V_{i,1} - V_{i,2}$	input differential
$q = \frac{1}{2}\left(V_{i,1} + V_{i,2}\right)$	input common mode
$\Delta = V_{p,1} - V_{p,2}$	output differential
$\Xi = \frac{1}{2}\left(V_{p,1} + V_{p,2}\right)$	output common mode

Table 6.2: Pre-filter differential and common mode signal definitions

$$\begin{aligned} D_L &= \tfrac{R_{bi,2}\|Z_Q}{R_{i,2}+R_{bi,2}\|Z_Q} & D'_L &= \tfrac{R_{bi,1}\|Z'_Q}{R_{i,1}+R_{bi,1}\|Z'_Q} \\ D_M &= \tfrac{R_{i,1}\|R_{bi,1}}{Z_Q} & D'_M &= \tfrac{R_{i,2}\|R_{bi,2}}{Z'_Q} \\ D_N &= \tfrac{R_{i,2}\|Z_Q}{R_{bi,2}+R_{i,2}\|Z_Q} & D'_N &= \tfrac{R_{i,1}\|Z'_Q}{R_{bi,1}+R_{i,1}\|Z'_Q} \end{aligned}$$

$$Z_Q = Z_{ci} + R_{i,1} \parallel R_{bi,1} \quad Z'_Q = Z_{ci} + R_{i,2} \parallel R_{bi,2}.$$

Since we are primarily interested in the differential and common mode voltages at the filter's input and output ports (summarized in table 6.2) we re-arrange equation 6.3.1 to read

$$\begin{aligned} \Delta &= D'_L\left(1 - D_M\right)V_{i,1} - D_L\left(1 - D'_M\right)V_{i,2} + D'_N\left(1 - D'_M\right)V_{g,1} - D_N\left(1 - D_M\right)V_{g,2} \\ \Xi &= \tfrac{1}{2}D'_L\left(1 + D_M\right)V_{i,1} + \tfrac{1}{2}D_L\left(1 + D'_M\right)V_{i,2} + \tfrac{1}{2}D'_N\left(1 + D'_M\right)V_{g,1} + \tfrac{1}{2}D_N\left(1 + D_M\right)V_{g,2.} \end{aligned} \tag{6.3.2}$$

and replacing the input voltages with the input differential and common mode signals we have

$$\begin{aligned} \Delta &= \tfrac{1}{2}\left[D'_L\left(1 - D_M\right) + D_L\left(1 - D'_M\right)\right]\delta + \left[D'_L\left(1 - D_M\right) - D_L\left(1 - D'_M\right)\right]q \\ \Xi &= \tfrac{1}{2}\left[D'_L\left(1 + D_M\right) + D_L\left(1 + D'_M\right)\right]q + \tfrac{1}{4}\left[D'_L\left(1 + D_M\right) - D_L\left(1 + D'_M\right)\right]\delta. \end{aligned} \tag{6.3.3}$$

where we have assumed $V_{g,1} = V_{g,2} = 0$. The general effect of the additional resistors can be teased out of these opaque equations by assuming that the resistors are perfectly matched and thus all primed terms precisely equal their un-primed counterparts. Then after a little algebra we find that

$$\Delta = \left(\frac{1}{1 + R_i/R_{bi}}\right)\frac{1}{1 + j\omega 2\left(R_i \parallel R_{bi}\right)C_i}\delta \tag{6.3.4}$$

where, compared to a circuit where $R_{bi} = \infty$, the signal is attenuated by a factor $1/(1 + R_i/R_{bi})$ and the effective resistance for determining the cut-off frequency is $2\left(R_i \parallel R_{bi}\right)$ rather than $2R_i$. However, for realistic resistor matching, equation 6.3.3 still permits numerical simulation of the degraded circuit performance.

The values $R_{bi} = 1\,\mathrm{M\Omega}$, $R_i = 1.8\,\mathrm{k\Omega}$, and $C_i = 10\,\mu\mathrm{F}$ were selected for the pre-filter and the resistors were matched to better than 1%. Using these values ensures that 99.8% of the DC signal passes through the filter (equation 6.3.4) and in figure 6.14a we see that matching the resistors to better than 1% ensures that common mode rejection is always greater than 40 dB. However, the AMP01's 4 nA input bias current flowing through R_{bi} generates a tremendous 4 mV offset voltage common to each input. Fortunately

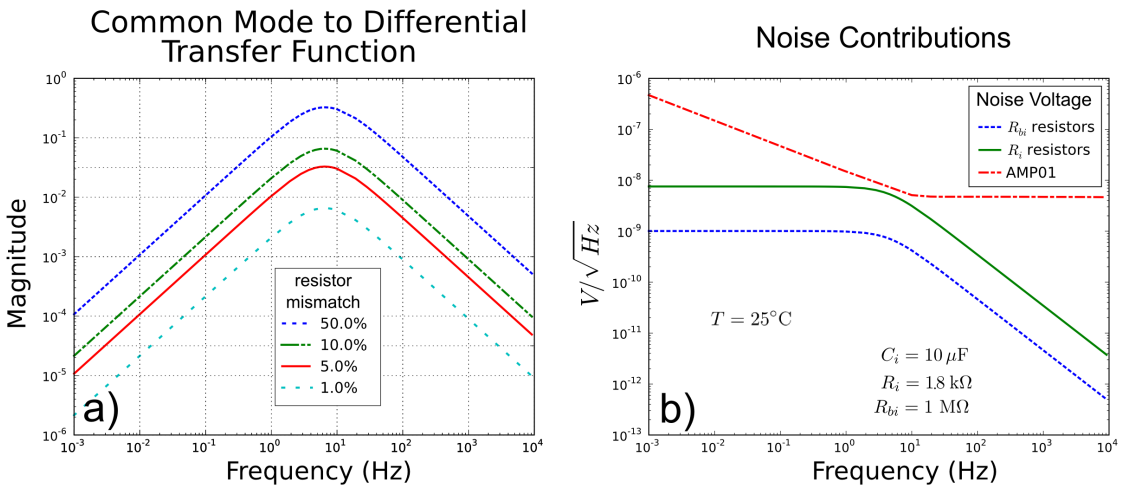

Figure 6.14: Equation 6.3.3 gives the transfer function from input common mode to output differential as $\Delta/q = \left[D'_L\,(1 - D_M) - D_L\left(1 - D'_M\right)\right]$ which is plotted in a) for various values of resistor mismatch. In b) the noise contributions from resistors R_{bi} and R_i (equations 6.3.5 and 6.3.6) are compared to the intrinsic noise of the AMP01 referred to its input.

only voltage differences are amplified and thus we are primarily interested in the input offset current [60, pg 1.59], the difference between the the two input bias currents (typically 0.2 nA at 25°C for the AMP01). To find the differential voltage resulting from this bias current imbalance, we note that approximately half of this current flows from one AMP01 input to ground through each of the two resistors R_{bi}. Therefore the voltage difference generated by the input offset current is due to 0.1 nA flowing through $2R_i$ and the detection coil to reach the second input. This produces an offset of only $3.6\,\mu$V which does not appreciably alter the AMP01's intrinsic offset voltage of $50\,\mu$V.

Ideally noise in a feedback system arises from the intrinsic properties of the sensor, in this case the detection coil's resistance. However, the realities of electronic amplification at low frequencies often cause the preamplifier to be the prime noise source and from figure 6.12c we see that, after 10 Hz, the AMP01 has a flat noise power spectrum (section 2.2.2.1) $J_{\mathrm{AMP01}}(\omega) = (5\,\mathrm{nV}/\sqrt{\mathrm{Hz}})^2$ which is the same as that generated by thermal noise in an object with resistance $R = 1.5\,\mathrm{k}\Omega$ at 25°C[6]. Since, the presence of C_i significantly attenuates the noise before it reaches the inputs of the AMP01, we expect that resistance values larger than 1.5 kΩ may be used in the pre-filter without degrading noise performance but further analysis is required.

Starting this noise analysis from equation 6.2, and assuming perfectly matched resistors, the combined noise power generated from the resistors with value R_{bi} is

[6]The noise power spectrum generated by a resistor is is $J_R(\omega) = 4kTR$ where T is the absolute temperature in kelvin, k is Boltzmann's constant, and R is the resistance in ohms.

$$\begin{aligned}\Delta_{nbi}^2 &= 2D_N^2\left(1-D_M\right)^2 V_g^2 \\ &= 8\left(\tfrac{1}{1+R_{bi}/R_i}\right)^2\left(\tfrac{1}{1+j\omega 2(R_i\|R_{bi})C_i}\right)^2 kTR_{bi}\end{aligned} \tag{6.3.5}$$

where the noise power generated by one resistor is $4kTR_{bi}$ and we have assumed that the noise is uncorrelated. Moreover, due to the symmetry of the circuit, we also see that the noise power due to the resistors with value R_i is

$$\Delta_{ni}^2 = 8\left(\frac{1}{1+R_i/R_{bi}}\right)^2\left(\frac{1}{1+j\omega 2\left(R_i \parallel R_{bi}\right)C_i}\right)^2 kTR_i. \tag{6.3.6}$$

These functions are plotted in figure 6.14b where we note that the noise contribution from the AMP01 always dominates that from the resistors, at least for the resistor values we chose, and thus explicitly adding the resistors to any subsequent noise analysis will have little effect on the result.

6.3.4.3 The Total Feedback Path

Now that the pre-filter's additional resistors have been considered, and both the feedback crossover frequency ($\omega_I/(2\pi) = 0.5$ Hz) and the integrator's internal mesh frequency ($\omega_M/(2\pi) = 4.5$ Hz) have been set, the remainder of the feedback path must be designed starting with the feedback path's gain K_DK_I. As mentioned in section 5.1.4, the system's transfer function is approximately $T \simeq \frac{1}{B} \simeq \frac{K_c}{RK_L} = \frac{1}{K_DK_I}$ over its operational bandwidth (equations 5.1.4, 5.1.11, and 5.1.14) and thus the product K_DK_I sets the system's gain from input voltage to output harmonic magnitude. Another important transfer function is that from the system's input voltage to the current driven in the gradient coil and it can be found using the rules from table 3.6 to be T/G where $G = K_c\left(\frac{1+\xi s/\omega_e}{1+s/\omega_e}\right)$ is the combined model of the gradient coil and eddy currents. Therefore the correspondence between a DC input voltage and the gradient coil current is the low frequency approximation $T/G \simeq T/K_c \simeq \frac{1}{K_DK_cK_I}$ where K_DK_c is the mutual inductance between the gradient and detection coils and K_I/ω_I is the DC gain of the integrator (equation 5.1.1).

Due to the limited dynamic range of the 12-bit digital-to-analog converter used as an input to the feedback system, the product $K_DK_cK_I$ was chosen such that a 4 V DC input corresponds to the maximum current that the Techron 7570 can drive into the G_x coil, that is 20 A. Since K_DK_c is set by coil geometry (for the x-channel $K_DK_c = 0.316$ mH from figure 6.6), the DC gain of the x-channel's integrator was set to $K_I/\omega_I \simeq 200$ by setting the AMP01's gain to 100 and the integrator's second stage gain to 2. With the feedback path's gain set, the low-frequency path's gain and cut-off frequency were set to match. Note that due to the 20× amplification of the Techron's internal feedback signal, the value used for R in equation 5.1.12 is $R = 20 \times 5\ \text{m}\Omega = 0.1\ \Omega$ rather than 5 mΩ. The result of these settings is that the transfer function from the input of the Techron 7570 to the feedback output (see figure 6.8) takes the form shown in figure 6.15 which has been verified by experiment. Since the product K_DK_c varies so little between the three feedback systems, nearly identical settings were used for the y- and z-channels.

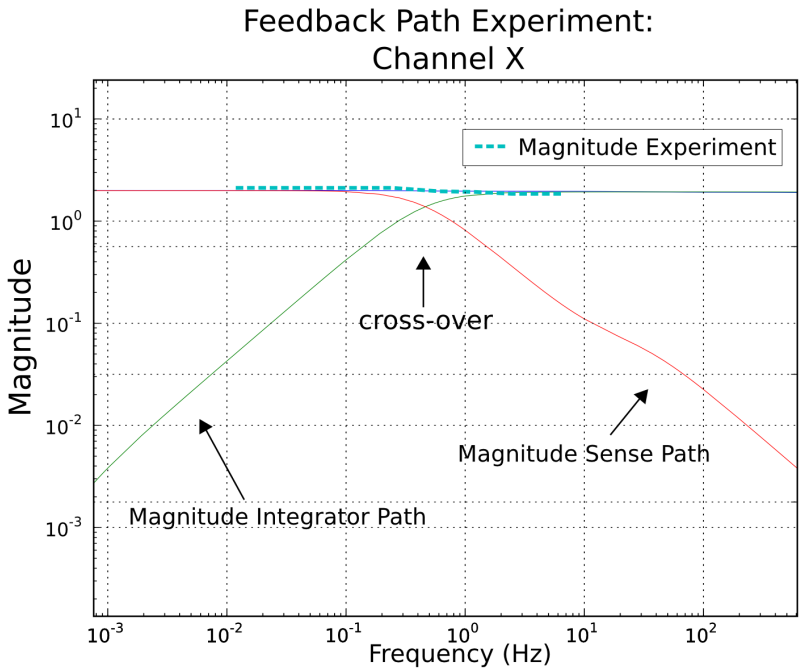

Figure 6.15: This plot compares the experimental and theoretical transfer functions from the Techron 7570's input to the output of the feedback path. The magnitude of this plot is $K_D K_I K_C K_S \simeq 2$ and the small deflection in the experimental results about the cross-over frequency is primarily due to the low frequency deflection in the Techron's frequency response as shown in figure 6.9.

6.3.5 The Feedback Compensator and the Whole Feedback Loop

With the feedback path's transfer function set, the final design step is to choose a compensator such that the system's step response and bandwidth are acceptable. From section 3.2.1 we see that the frequency at which the gain of the open loop transfer function descends to unity sets the bandwidth of the closed loop system and at this frequency the phase difference from -180° is related to the the overshoot and settling time of the step response. Using our model of the feedback path – including a Techron 7570 model fit to the experimental results in figure 6.9 – we simulated the open loop transfer functions resulting from various compensators and also investigated the closed loop transfer function and step response. Using this technique, the compensator transfer function

$$C_s = K_{Cmp} \frac{(1 + s/\omega_{z1})}{(1 + s/\omega_{p1})} \frac{(1 + s/\omega_{z2})}{(1 + s/\omega_{p2})} \tag{6.3.7}$$

was chosen with $K_{Cmp} = 375$, $\omega_{z1}/(2\pi) = 10$ kHz, $\omega_{p1}/(2\pi) = 50$ Hz, $\omega_{z2}/(2\pi) = 9.94$ kHz and $\omega_{p2}/(2\pi) = 99.9$ kHz. The factors $(1 + s/\omega_z)$ in the compensator's numerator were chosen to counter-act two of the many poles of the Techron's transfer function and thus increase the total system's bandwidth. Equation 6.3.7 is plotted in figure 6.16 along with its simulated ramifications for the complete feedback system. As can be seen, this choice of feedback compensator yields a phase margin of 30° which is associated with

Op-amp. #	R_p	C_p	R_z	C_z
1	3.38 kΩ	942 nF	2.37 kΩ	6.69 nF
2	15.9 kΩ	100 pF	2.43 kΩ	6.59 nF
3	10.0 kΩ	None	1.00 kΩ	None
4	7.98 kΩ	None	1.99 kΩ	None

Table 6.3: Each of the four op-amps. in figure 6.8 is connected to four passive components R_p, C_p, R_z, and C_z. The actual measured component values used for the compensator in the x-channel's feedback system are given above. Essentially the same values were used for the other channels with the variability between component values in different channels being less than 5%.

significant overshoot and a brief ringing. However the overshoot seems acceptable since it lasts less much than a millisecond. The compensator's passive components, shown in figure 6.8, were selected according to table 6.3.

6.3.6 The Field Probe

In addition to the feedback circuitry, the sniffer coil shown in figure 6.3d was followed by an electronic integrator and used as a field probe. The coil was made of AWG 36 magnet wire wound to a radial thickness of 3 mm on a cylindrical former of radius 4.7 mm and length 12.7 mm placed within the probe tube. The coil's output fed into a length of twin-axial cable connecting it to a two stage integrator using a design similar to that described above except it had $\omega_I/(2\pi) = 0.02$ Hz, $\omega_M/(2\pi) = 0.2$ Hz, and a DC gain $K_I/\omega_I = 21000$. This high gain was required due to the sniffer coil's small size but resulted in an output offset of approximately 1 V which was removed numerically after digital acquisition.

6.4 Results

Having described the coil designs and both the mechanical and electronic aspects of the experimental apparatus in detail, we now turn our attention to how this apparatus was used to verify dynamic pre-emphasis. Essentially each of the three channels was operated both with and without feedback while the field was plotted with respect to time on points over the surface of a sphere. However before that could be done, initial tests were performed verifying the operation of the apparatus.

6.4.1 Mutual Inductance Experiments

As shown in figure 6.17, the first of these tests was to remove the aluminium tube and measure the mutual inductance M between the gradient coils and their corresponding detection coils. The relative coil orientations were changed by moving the acrylic tube attached to the detection coil former and the mutual inductance was found by driving a 10 Hz sinusoidal current with amplitude $|i_c| = 5$ A into the gradient

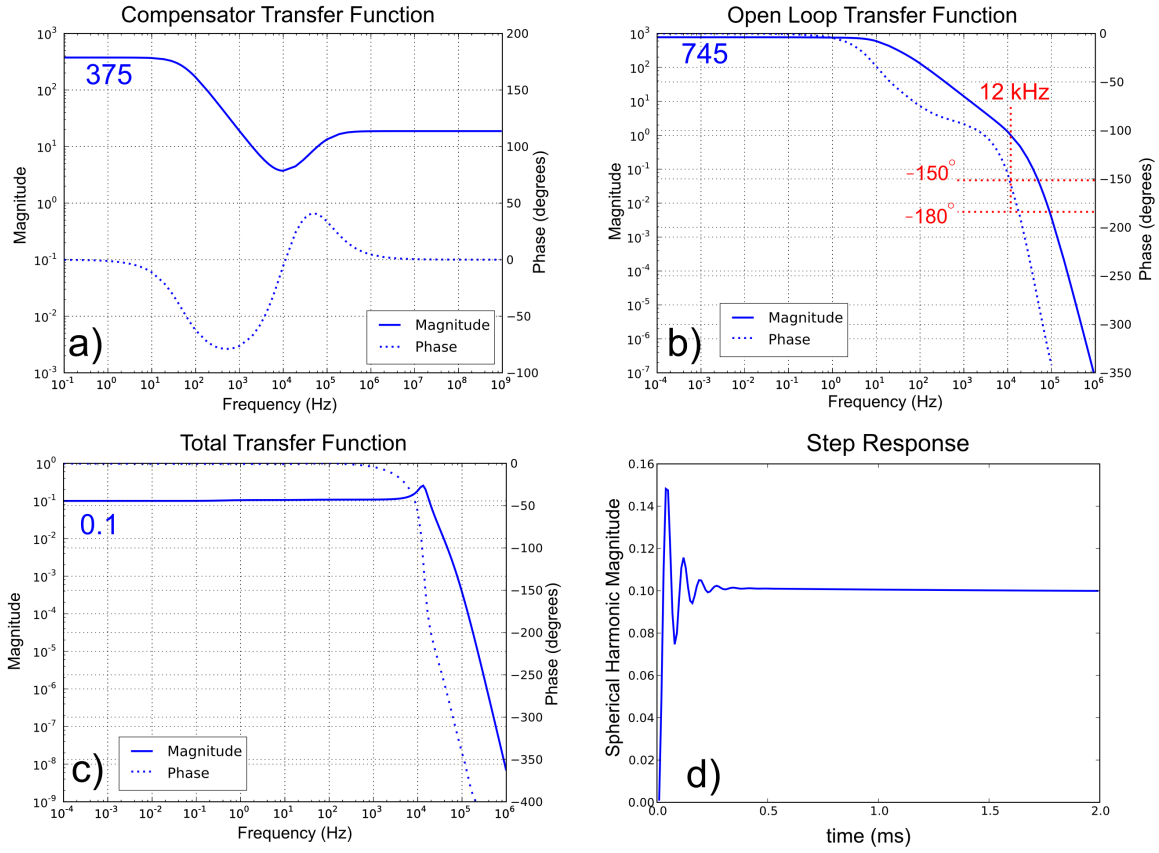

Figure 6.16: These four plots show the properties of the x-channel feedback system given the compensator in equation 6.3.7. Part a) shows the compensator's transfer function and its low frequency gain of 375. Part b) shows the open loop transfer function and the phase margin of 30°. The complete system's transfer function in part c) has a peak near 12 kHz characteristic of systems with significant overshoot and in d) the system's expected step response is simulated. Although precisely the same simulation was performed to produce the part of figure 6.11 where $\omega_I/(2\pi) = 0.5$ Hz, the overshoot and ringing is not visible in that figure because it ceases before 0.5 ms.

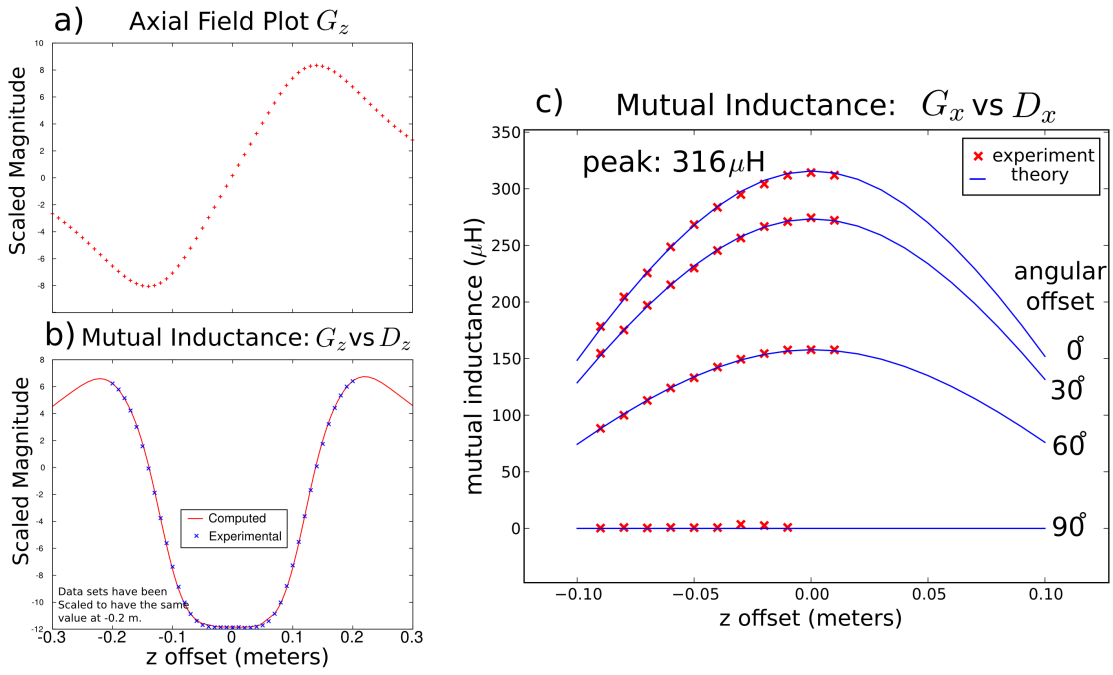

Figure 6.17: In part a) the gradient coil's field profile was plotted by measuring the mutual inductance between the G_z coil and a sniffer coil moved along its axis. Outside the gradient coil's central region the field is no longer dominated by $T_{1,0}$ and in part b) we see that the mutual inductance between the G_z and D_z coils continues to match the computed values even far from the central region. Finally in part c) we see that the mutual inductance between the G_x and D_x coils also matches the predicted value, this time as a function of both axial and azimuthal offset. Since the mutual inductance between G_y and D_y is very similar to that between G_x and D_x, it is not shown. (Parts a) and b) were published previously [28].)

coil and measuring the output amplitude $|V_o|$ of an integrator with gain K_I (equation 5.1.1) connected to the detection coil. The experimentally determined mutual inductance $M = |V_o| / (K_I |i_c|)$ was found to match the value computed numerically using the Neumann formula[7] (equation 2.1.25) and thus we can be confident that the apparatus orients the coils correctly and that no significant errors occurred during coil manufacturing.

6.4.2 Field Plots

The next step was to verify the operation of the field plotting apparatus shown in figure 6.2c-g. The sniffer coil described in section 6.3.6 was moved over the surface of a sphere with radius 4.1 cm and the field strengths due to each of the three gradient coils were measured at the points listed in table 6.1. As shown in figure 6.18, the results generally agree with the B_z field values computed numerically using the Biot-Savart Law (equation 2.1.23).

[7]For the zonal case, the mutual inductance between rings can also computed using a well known formula recorded by Grover [38].

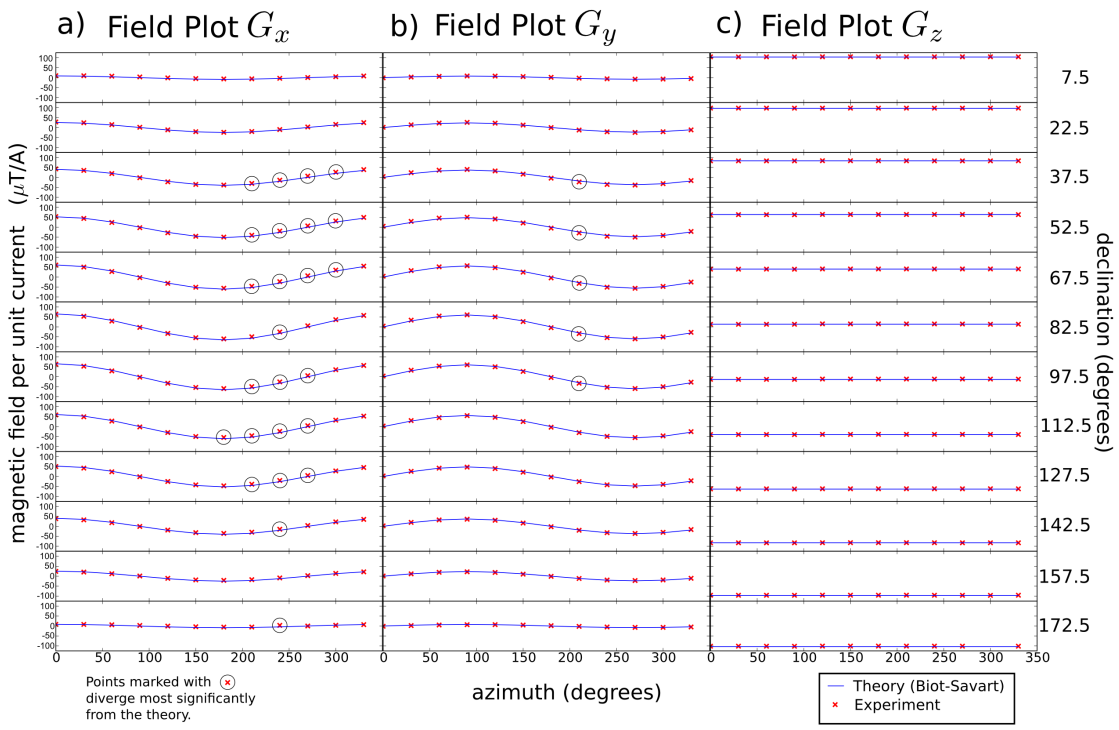

Figure 6.18: With the aluminium tube removed, these field plots were obtained from each of the three gradient coils using the sniffer coil followed by an integrator. The field plotting apparatus was used to place the sniffer coil at positions over the surface of a sphere with radius 4.1 cm and the theoretical values were computed using the Biot-Savart Law (equation 2.1.23).

Unfortunately the agreement between theory and experiment was initially very poor – approximately an order of magnitude worse than shown in figure 6.18 – mostly because the wheels at either end of the field plotting assembly would wobble slightly. This wobble was greatly reduced by replacing the original narrow supports under each wheel with large plates (visible in figure 6.2d) such that each wheel was supported under its entire bottom surface. Another important, and unresolved, problem is the static friction between the field plotter's tubular chassis and the plastic rings (shown in figure 6.2a) into which it fits. Although this snug fit ($\sim$ 0.1 mm) keeps the field plotting apparatus centred and allows for easy rotation, the static friction is much greater than kinetic friction so the apparatus jumps at the start of any rotation. Thus placing the sniffer coil at any azimuthal position takes multiple attempts. After being delayed for months by these and other mechanical problems, the fairly accurate, albeit far from perfect, results shown in figure 6.18 were obtained. These results demonstrate that the gradient coils do in fact produce field gradients and that the field plotting apparatus can be used to measure the field.

6.4.3 Dynamic Pre-emphasis Verified

With the experimental apparatus operational, dynamic pre-emphasis could be attempted. After the aluminium tube was put in place, a square pulse was fed repeatedly into the Techron 7570 responsible for driving the G_x coil. Over the course of each pulse two signals were recorded by the computer: the output of the sniffer coil's integrator and the coil current as measured by the Techron 7570's internal resister. Due to the small size of the sniffer coil there was significant noise on the integrator's output and thus for each of the 144 probe positions in table 6.1 the results from ten pulses were averaged. Then the open-source code SpharmonicKit [110] was used on the averaged data to calculate the spherical harmonic transform as a function of time. The resulting harmonic magnitude for $B_{za,1,1}$ is shown in figure 6.19a along with the G_x coil's current; other harmonic magnitudes were much smaller. As can be seen, it took about 60 ms for the eddy currents to die down and a constant harmonic magnitude to be established.

The experiment was then repeated with the feedback system engaged and square pulses fed into the system's input rather than directly into the Techron 7570. Again the sniffer coil was placed at a different locations over the surface of a sphere and the results from ten pulses averaged for each location. After computing the spherical harmonics as a function of time, the results shown in figure 6.19b were obtained. Note that the feedback system automatically produced the exponentially decaying current pulse in order to rapidly establish a constant harmonic magnitude. The results in this figure represent the successful completion of a central goal of this thesis: to experimentally demonstrate dynamic pre-emphasis.

Notice the small bump in the harmonic magnitude directly after its rapid rise. Since the system's overshoot and ringing settles in less than 0.5 ms, this bump is due to the small deviation in the feedback path caused by eddy currents (see figure 5.7) and is correctly predicted in figure 6.11 for a feedback system with $\omega_I/(2\pi) = 0.5$ Hz. Further reduction of ω_I would decrease this small deviation from a perfectly square pulse.

With dynamic pre-emphasis demonstrated on a single channel, the obvious next step was to operate all three channels simultaneously. The primary goal was to determine whether coupling between the channels degrades system performance; the first experimental results are shown in the left column of figure 6.20. In those results, a z-gradient ($B_{za,1,0}$) was generated under three separate circumstances: without feedback control, with feedback control of the z-gradient, and with feedback control operating simultaneously on x, y, and z channels. As can be seen by comparing parts b) and c) of figure 6.20, not only did simultaneous operation of all three channels not cause oscillation, there was no perceptible change in system performance. We have therefore experimentally demonstrated that multiple feedback loops can be used simultaneously to control multiple harmonics of the magnetic field. Although this satisfied the primary aim of the experiment, the limited accuracy of the field plotting apparatus meant that the beneficial effect of operating the two additional channels was difficult to distinguish. In order to increase the magnitude of the spurious harmonics,

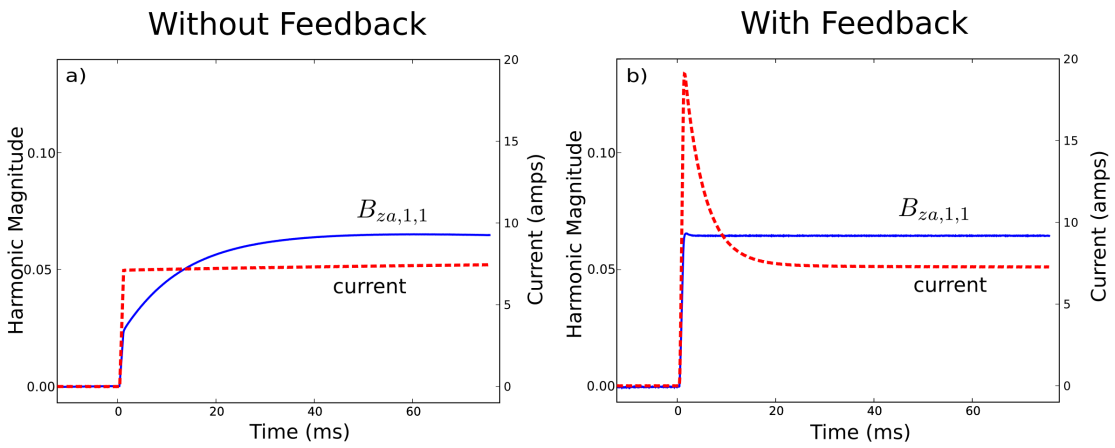

Figure 6.19: These results [29] demonstrate dynamic pre-emphasis applied to an x-gradient of B_z. The exponentially decaying pre-emphasis current in part b) was dynamically generated by analog circuits during the gradient's rise time without *a priori* knowledge of the gradient waveform or associated eddy currents.

and thus ease the detection of their cancellation, the symmetry of the aluminium tube about the central axis was broken.

To break this symmetry, the experimental apparatus was modified by using an electric grinder to remove approximately 0.5 cm from the plastic surface snugly fitting with the aluminium tube – there was not space to remove more. The aluminium tube was then offset laterally from the central axis, tilted slightly, and held in place with plastic spacers. With this new geometry the feedback experiments were repeated and as can be seen by comparing parts d-e) of figure 6.20 to parts a-b), the magnitude of spurious harmonics was increased as intended. Concentrating our attention on the spurious harmonic $B_{za,1,1}$ in part e), we found that when all the feedback channels were operated simultaneously $B_{za,1,1}$ was suppressed – as can be seen in part f) – because the x-channel feedback loop produced a small pre-emphasis current. This result indicates that operating multiple feedback loops simultaneously is beneficial in that it can suppress the production of spurious harmonics. However, much stronger evidence for suppression of unwanted harmonics could have been found if feedback control loops – including field production and detection coils – had been produced for the harmonics $B_{za,3,0}$ and $B_{za,0,0}$ (note the large spikes in these harmonics in parts e) of figure 6.20 which would have been suppressed in part f) if there had been control loops for those harmonics).

6.5 Summary

Dynamic pre-emphasis using spherical harmonic inductive detection coils has been successfully tested on three harmonics – the gradients G_x, G_y, and G_z – using three negative feedback loops each with its own gradient coil and detection coil. For the first time, eddy current effects have been successfully compensated by continuously generated – rather than previously calculated – pre-emphasis currents. This

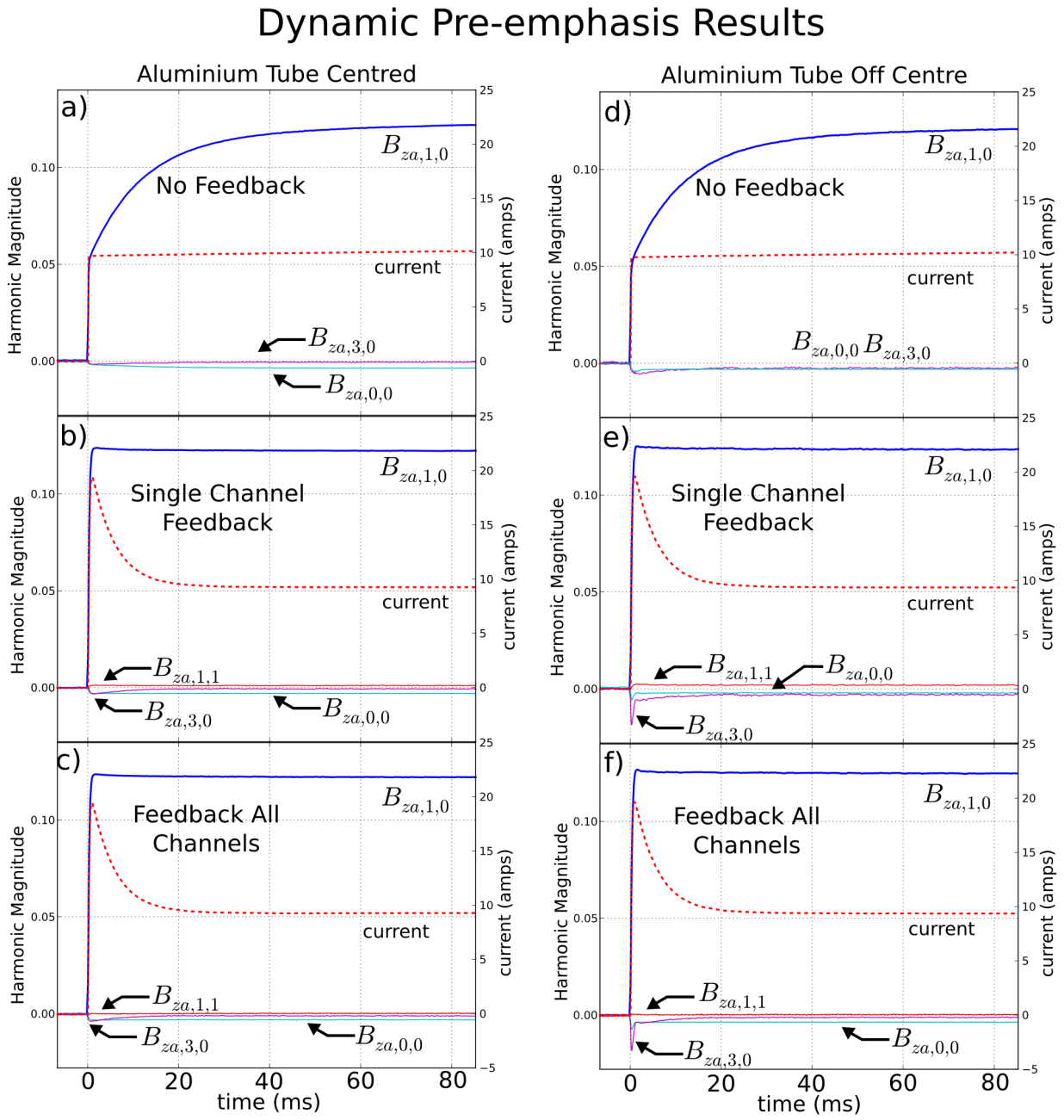

Figure 6.20: Dynamic pre-emphasis results

technique not only functioned on a single channel but also with all three channels operating simultaneously; thereby demonstrating that coupling need not cause oscillation. In fact, there was no observable degradation in performance with all three channels operating together.

To prepare for this final set of experiments, I designed and built three detection coils, three gradient coils, a mechanical support system on which to mount them, and a field plotting rig to independently measure the magnetic field harmonics. The coils and plotting rig were verified using mutual inductance and field plotting experiments. The eddy currents, the control system's electronics, and the bandwidth of the detection coils (approximately 10 kHz) were also characterized. The analysis of noise and mismatched components in the pre-amplifier/integrator was done with particular care since imperfections there have a large influence on the total system's quality. In addition, the cross-over between the two feedback paths was investigated both with simulation and experiment.

Despite an artificially severe eddy current problem, dynamic pre-emphasis has produced essentially the same currents that would have been generated using static pre-emphasis but without the system having *a priori* knowledge of the eddy currents. The cost of this convenience, however, is a set of specially designed detection coils and a feedback system for each one.

Part IV

Discussion and Conclusion

Chapter 7

Feedback Loop Considerations

Having demonstrated experimentally that dynamic pre-emphasis can be achieved using spherical harmonic detection coils in negative feedback loops, we now turn our attention to topics that may be of use in this technique's further development such that it might ultimately replace static pre-emphasis.

7.1 Optimum Cross-over Frequency and Image Simulation

When considering dynamic pre-emphasis for use in an actual imaging system, the optimal cross-over frequency ω_I between low- and high-frequency feedback paths must be found with respect to noise and distortion as described in section 5.3. We now determine what value should have been chosen for ω_I in our experimental setup.

Given an arbitrary gradient waveform, such as one with noise and distortion, equations 5.3.3, 5.3.4, and 5.3.5 provide a straightforward method for simulating both a point spread function and an MRI image. Moreover, the models developed for the feedback system along with knowledge of the preamplifier's noise signal allow us to determine what gradient waveform would actually be produced in response to a signal at the system's input – provided the gradient amplifier can generate the required current.

Ignoring the preamplifier's input offset voltage, we begin by simulating a gradient-echo used to produce a one-dimensional projection image of three 125 cm^3 cubes filled with human brain tissue which have been placed in a magnetic field $B_0 = 3\,\text{T}$. Two of these cubes contain white matter ($N = 0.61\,N_{\text{H}_2\text{O}}$, $T_1 = 510$ ms, $T_2 = 67$ ms)[1] and are stacked in the z-direction with their faces aligned along the coordinate axes and their centres located at $x = -5$ cm, $y = 0$ cm. The third cube also has its faces aligned along the coordinate axes but is filled with human grey matter ($N = 0.69\,N_{\text{H}_2\text{O}}$, $T_1 = 760$ ms, $T_2 = 77$ ms) and has its centre at $x = 5\,\text{cm}$, $y = 0\,\text{cm}$. After subjecting the cubes to a 90° RF pulse at $t = 0$ ms followed by the perfect gradient waveform shown in figure 7.1b, the Fourier transform of the 256 signal

[1] N can be used to find M_0 from equation 2.2.19 and $N_{\text{H}_2\text{O}}$ is the number of proton spins per unit volume in water.

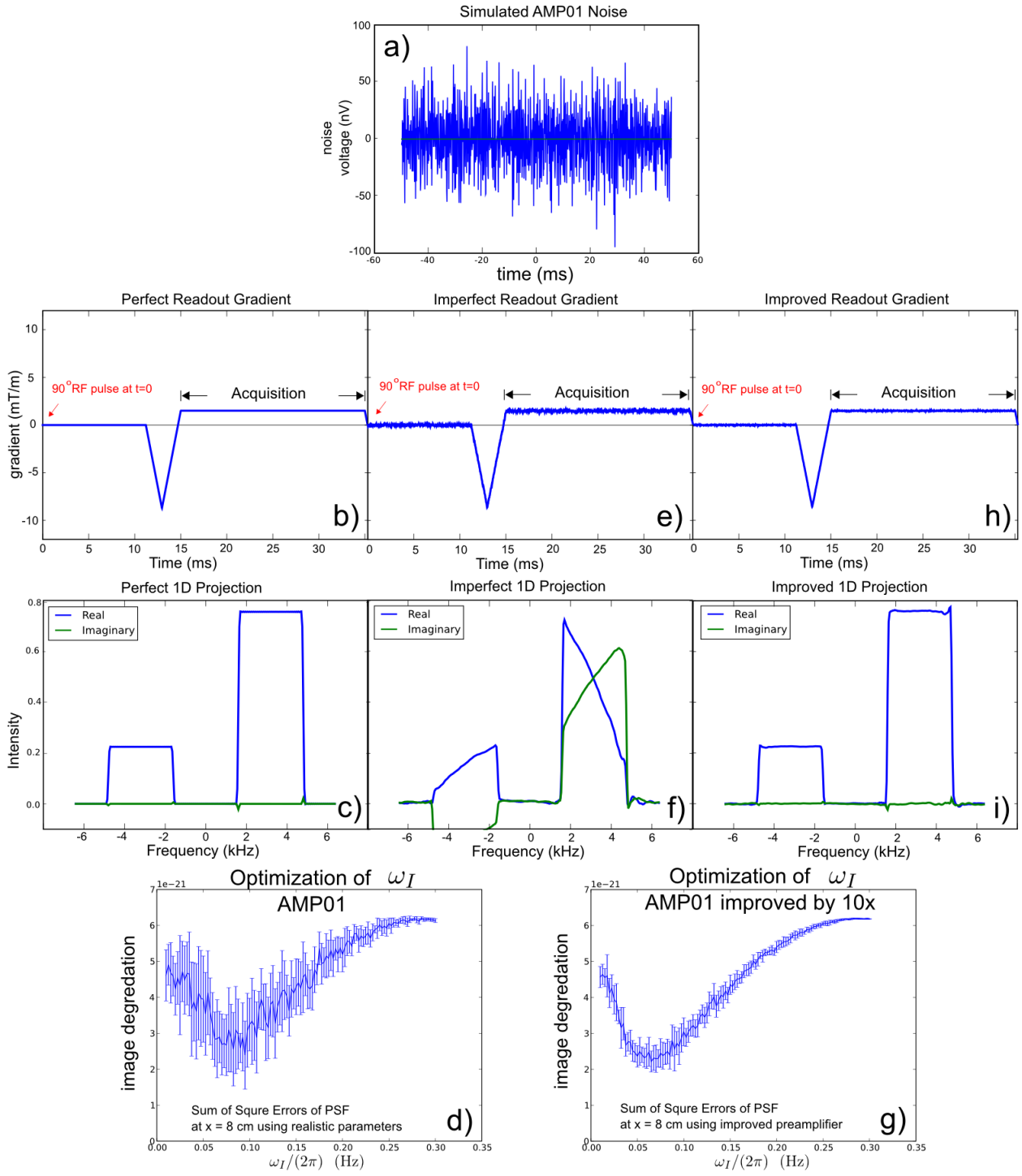

Figure 7.1: Part a) shows a simulated noise signal congruent with the information about the AMP01 given in figure 6.12c. Part b) shows a perfect gradient waveform which was used to generate the perfect 1D projection in part c). Part d) shows an attempt at optimizing ω_I using the parameters of our experimental apparatus and parts e) and f) show the resulting gradient waveform and 1D projection that such an optimum would produce. Assuming an improved preamplifier, the ω_I optimization is shown in part g) and the resulting gradient waveform and image are shown in parts h) and i). All 1D projections were formed using 256 simulated signal samples during a 20 ms acquisition time starting 15 ms after a 90° RF pulse.

samples collected during the 20 ms that the gradient remains steady at 1.5 mT/m produces the perfect one-dimensional image shown in figure 7.1c; to reduce Gibbs ringing, the signal was weighted with a Hamming window before Fourier transformation. The 90° RF pulse was simulated simply by starting all the simulated magnetization in the transverse plane at $t = 0$.

However we want to determine the point spread function arising from a noisy and distorted gradient and then compare it to a perfect point spread function by computing the image degradation (equation 5.3.1). Now the $\mathbf{r}$ dependence of the spherical harmonics, including our gradient, causes their field values to increase with distance from the origin and thus the influence of gradient noise and distortion on the point spread function are greatest at the field of view's outer edge. Therefore we repeat the simulation above but now using a single small cube of white matter (1 cm^3) placed at the field of view's edge ($x = 8$ cm) in order to simulate the image of a point – that is the point spread function.

Before proceeding, we must still specify a preamplifier noise signal to use in equation 5.2.5. Fortunately figure 6.12c provides us with the square root of the AMP01's noise power spectrum from which we can generate a noise signal as described in section 5.3.2. One such signal is shown in figure 7.1a but since it is not unique[2] we expect the computed image degradation to be slightly different every time the same power spectrum is used to generate a new noise signal. By repeating the computations several times for every value of ω_I, the average image degradation can be found as a function of ω_I and the maximum deviation from this value used as a measure of uncertainty.

In figure 7.1d this is done by computing the image degradation ten times for each value of ω_I where the AMP01's noise power spectrum was used to generate a new noise signal each time. Since image degradation seems to be minimized when $\omega_I/(2\pi) = 0.1$ Hz, this value was used in a simulated feedback system to produce the gradient waveform shown in figure 7.1e which was then used to simulate the one-dimensional image of the 125 cm^3 cubes shown in figure 7.1f. Qualitatively this one-dimensional projection is quite poor and thus for our experimental setup, where the eddy current effects are exceptionally large due to the use of unshielded gradient coils, the AMP01's intrinsic noise causes even the optimum choice of ω_I to produce an unacceptable result.

However, the results are greatly improved if we arbitrarily assume a preamplifier is used that has the same noise power spectrum as the AMP01 but divided by 10. In this case the image degradation vs. cross-over frequency is shown in figure 7.1g and has an optimum near $\omega_I/(2\pi) = 75$ mHz. Now using this value, the simulated system produces the gradient waveform in figure 7.1h and, returning once more to the 125 cm^3 cubes, the resulting one-dimensional image is fairly good (see figure 7.1i).

The surprising result of this analysis is that for significantly large eddy currents ($\xi \simeq 0.5$) and a preamplifier with a noise performance ten times that of the AMP01, the optimum cross-over frequency is

[2]Since a random number generator is used to choose the phases, using a different seed in that generator results in a slightly different signal.

approximately an order of magnitude below where eddy current effects first begin to distort the field and approximately two orders of magnitude below[3] ω_e. It is expected that the optimum cross-over frequency may be increased by reducing the strength of the eddy currents, reducing the preamplifier's noise level or the frequency at which this noise becomes dominated by flicker noise, or by changing the system geometry such that the characteristic frequency ω_e of the eddy currents is increased.

7.1.1 Selecting a Preamplifier

From the analysis above it is clear that selecting the correct preamplifier is critically important. Obviously the preamplifier must not distort the signal and its bandwidth must be at least as wide as that desired for the entire system, but specifying the preamplifier's noise and offset are more difficult. A possible approach is to specify an acceptable level of output harmonic offset and, for a certain imaging sequence, an acceptable level of image degradation (equation 5.3.1) due to imperfections in the gradient system. Then starting with models for the eddy currents – that is ξ and ω_e from equation 5.1.6 – and the electronic system components including an initial preamplifier choice, the optimum cross-over frequency should be computed. If both the image quality and the system's output harmonic outset are both within the design specifications at the optimum cross-over frequency, then the design is acceptable. If not, it is possible to trade image quality for reduced output harmonic offset by slightly increasing the cross-over frequency.

To see how this works, remember that $\frac{1}{B} = \frac{1}{K_D K_I}$ is the gain of the complete feedback system (equation 5.1.4) and that K_I/ω_I is the DC gain of the integrator (equation 5.1.1). Therefore from equation 5.2.3, the harmonic offset H_{offset} due to the preamplifier's input offset voltage V_{offset} is

$$H_{\text{offset}} = \frac{1}{B}\frac{K_I}{\omega_I} V_{\text{offset}} = \frac{1}{K_D \omega_I} V_{offset} \tag{7.1.1}$$

such that increasing ω_I reduces H_{offset}. Now if ω_I starts at its optimum value, any increase trades image quality for a reduced harmonic offset. However if this trade-off does not produce acceptable results, either select or construct another preamplifier which does produce acceptable results or change the design specifications.

7.2 Coupling between Feedback Loops and Oscillation

Another important topic is the possible degradation of system performance caused by simultaneous operation of multiple coupled feedback loops. Although this degradation was not apparent in the experimental results presented in section 6.4, the coupling between x- and y-channels could be made sufficient for oscillation by rotating the detection coil former with feedback engaged. In order to have confidence

[3] $\omega_e/2\pi \sim 10$ Hz for our system (see figure 6.3.3).

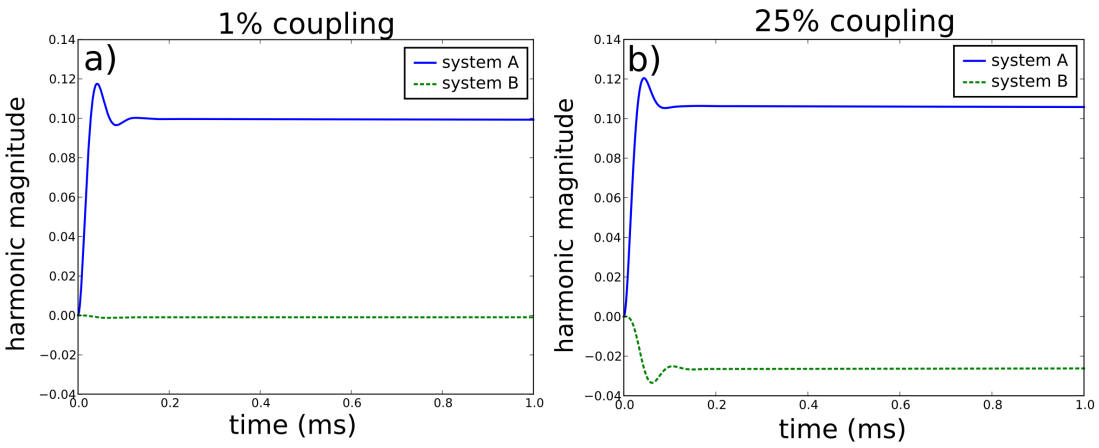

Figure 7.2: Multiple system feedback control in the presence of coupling

that a set of feedback loops will behave correctly, the models from section 5.1.4 can be used with the theory of section 5.2.4 to simulate the coupled systems.

Figure 7.2 shows the simulated step response of two coupled harmonic feedback systems where system A receives the step input while system B receives an input of zero. The two systems were generally modelled after the experimental setup described in section 6.3 but three key simplifications were made to reduce the computational expense: the compensator, Techron 7570, and integrator were all modelled using single-pole filter responses. From the figure we see that when the inter-system couplings, that is the products $K_{c,\alpha,\beta}K_{D,\alpha',\beta'} | \ \alpha \neq \alpha', \ \beta \neq \beta'$ from section 5.2.4, are approximately 1% of the on-diagonal values $K_{c,\alpha,\beta}K_{D,\alpha,\beta}$ then the step-response seems quite reasonable. However, when the couplings reach 25% the system performance is terribly degraded and, although it is not shown, when the couplings reach 30% the systems oscillate wildly. Control despite coupling is possible since the coupling is non-existent at low frequencies and therefore is only an issue during the gradient's rise time where it slightly alters the shape of the initial overshoot.

7.3 Designing a Whole System

When deciding whether or not to employ dynamic pre-emphasis rather than static pre-emphasis, one must determine whether dynamic pre-emphasis affords some benefit to image quality and under what circumstances this may be the case. Since this decision depends on the application, the eddy-current severity, and the available preamplifier technology, we merely outline a possible decision-making procedure.

Start by identifying an imaging sequence to be improved, probably some variant of gradient-echo imaging, and which harmonics may warrant a control system – likely those for which static pre-emphasis is currently applied or being considered including B_0. With respect to this imaging sequence, the designer

must specify a percent improvement in image quality (see equation 5.3.1) as caused by the switch from static to dynamic pre-emphasis. Moreover, each harmonic's bandwidth, slew rate, and offset requirements must be determined from the imaging sequence. With this done, the field production coils and amplifiers should be produced using normal techniques or the existing gradient hardware accepted. The gradient system should then be characterized so that static pre-emphasis can be applied; thus establishing a basis point for improvement and also eddy current models for use in feedback simulations.

With the starting point defined, the location and geometry of the detection coil former must also be chosen and an initial set of detection coils designed to fit on it. At this stage the most important aspects of the detection coil design are that they reject unwanted harmonics and that their bandwidths are sufficient to meet the specified requirements. Although we determined coil bandwidth experimentally in section 6.2.2.4, it should be possible to determine the bandwidth using electromagnetic simulation and thus iteratively increase the number of contours until the coil's bandwidth just meets design specifications.

Having produced computer models of detection coils, the next step would be to perform a series of simulations as in section 7.1 to find the optimum ω_I for the given imaging sequence using initial choices for the preamplifier and feedback compensator. As discussed in section 7.1.1, these simulations can be used in an iterative process with different preamplifier models until the design specifications are met. When this process is complete, the specified harmonic slew rates can each be used to finalize the internal mesh point ω_M of each integrator. Although further simulation may be performed to optimize the choice of feedback compensator, provided the system does not oscillate and the rise time is fast, the choice of preamplifier and ω_I are expected to be far more important. To ensure that this final design works for many imaging sequences, additional simulations should be performed using those sequences. However, the optimum value of ω_I is not expected to change significantly between imaging sequences.

As a side note, we expect that analog electronics are not the ideal choice due to the difficulties associated with building low frequency integrators and the availability of digital alternatives. In a digital system the detection coil's signal would be digitized after the pre-amplifier, the sense resistor's voltage would be digitized directly, and the input could be a pure stream of digital information. Since pulse width modulation is often used in modern current amplifiers, the input to such an amplifier could be digital as well. Replacing physical filters with digital alternatives is quite reasonable at audio frequencies and should have advantages with respect to manufacturing, miniturization, and the implementation of feedback compensators. However dgitization does nothing to solve the problem of offset at the output of the preamplifier.

Chapter 8

Coil Design Considerations

Narrowing our focus from the whole feedback system back to the detection coils, there are a number of important issues to discuss beyond simply designing a working detection coil using the techniques of section 4.2.

8.1 Discretization and Manufacturing Errors

Most notably, the performance of a theoretically perfect detection coil made from an unrealizable continuous wire distribution is degraded first when it is discretized into the contours of a stream function, then again when those contours are interconnected, and one final time when the pattern is manufactured using actual wire. As an example, the first step in designing the D_x coil in figure 6.6a was to generate a set of wire density coefficients by inverting a matrix generated from equation 4.2.6. By using equation 4.2.6 to test the flux response of the continuous wire distribution described by these coefficients, we find that the response to harmonics other than $T_{1,1}$ is supposedly less than 10^{-12} times the response to $T_{1,1}$. Unfortunately this continuous wire distribution could never actually be manufactured.

However the flux response of discrete contours approximating a continuous wire distribution (see section 6.2.2.1) can be computed numerically for individual harmonics. Defining the minimum harmonic rejection ratio as

$$\mathrm{HRR}_{\mathrm{min}} = \Phi_{\mathrm{least}}/\Phi_{\mathrm{interest}} \tag{8.1.1}$$

where Φ_{least} is a discrete coil's flux response to the least rejected harmonic and Φ_{interest} is that coil's response to the harmonic of interest, the results in figure 8.1a show that the contours generated for the D_x coil have $20\log(\mathrm{HRR}_{\mathrm{min}}) = -47$ dB. Now separate closed contours only form a coil when linked together and although this further degrades the flux response, as can be seen in figure 8.1b, it seems to do so primarily for harmonics which do not limit $\mathrm{HRR}_{\mathrm{min}}$. Finally, when the wire pattern is actually manufactured there are

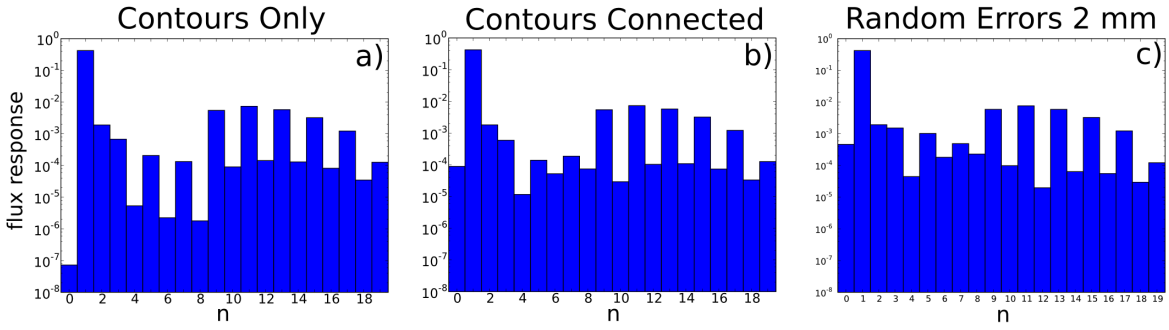

Figure 8.1: Each of the plots shows the flux response of the D_x coil at a different stage in its development using $R_{ref} = \sqrt{(L/2)^2 + R^2}$ as in section 6.2.2.1. In a) the flux response is computed before the contours are connected and in b) after they are connected. To simulate manufacturing errors, in c) each of the wire segments of the connected D_x coil are randomly moved by a distance between ±2 mm – not physically but within a computer – and the flux response simulated once more.

inevitably wire placement errors. In figure 8.1c we see the simulated flux response of the same detection coil where each wire segment has been randomly moved by a distance -2 mm $< R\psi < 2$ mm in the azimuthal direction. Again there is little effect on the minimum harmonic rejection ratio.

8.2 Incremental Flux Response

It is also interesting to investigate precisely how harmonics are either detected or rejected by a detection coil's wire distribution. Obviously there is a flux linkage, and thus the possibility of induced voltage, wherever vector potential aligns with a wire. Therefore over the entire coil flux linkages must cancel for rejected harmonics but add for the single detected harmonic. To see how the pseudo-inverse solves this problem, we can use a detection coil's wire density coefficients and equation 4.2.6 to determine the flux response contributed by each of a coil's discrete rings of axial or azimuthal wire density (see figure 4.3). As shown in figure 8.2, the contribution to flux response as a function of axial position along the D_x coil reveals that the flux linkages do cancel out for every harmonic except $T_{1,1}$. This is accomplished for even ordered harmonics by the flux linkage at one end of the wire distribution cancelling that from the other end. But for odd ordered harmonics the flux linkage near the centre cancels with that from both ends. Moreover it seems that as the harmonic order increases so does the importance of the extreme ends of the wire distribution. An understanding of why these patterns occur may be a useful starting point in developing alternative design techniques for harmonic detection coils.

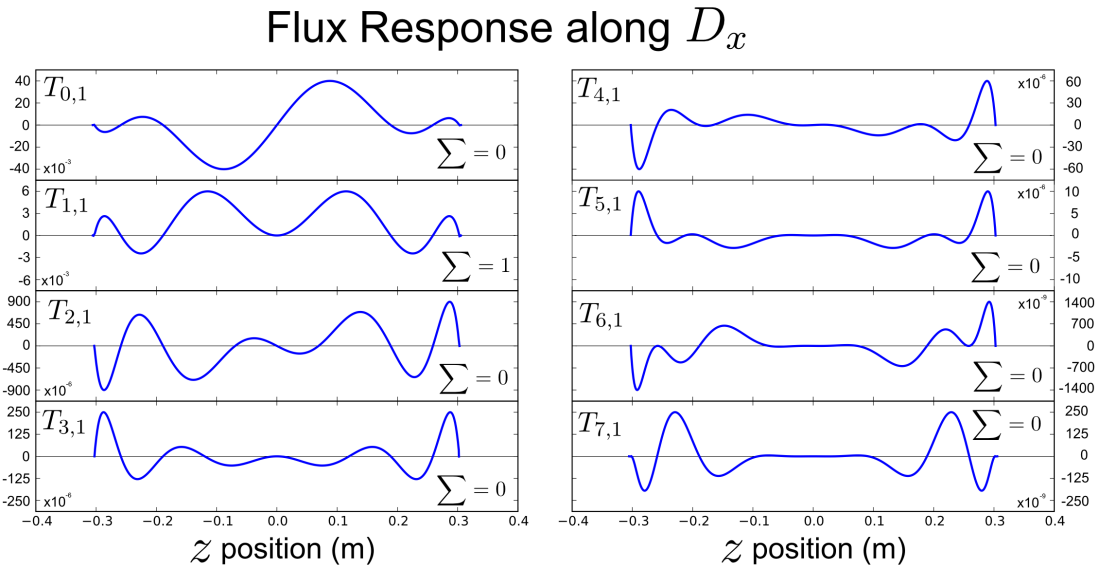

Figure 8.2: Flux comparison along the length of D_x

8.3 Mesh Detection Coils

A possible alternative detection coil design method, although not one based on the patterns discussed above, would be to form a virtual set of harmonic detection coils by combining the outputs of a cylindrical mesh of simple wire loops, shown in figure 8.3, each with its own preamplifier. One could work out what weighted combination of these outputs is equivalent to the output of each of a set of actual harmonic detection coils and since the preamplifier outputs can be simultaneously included in several weighted combinations, a great many virtual detection coils could co-exist as part of a single cylindrical mesh.

In addition to the cost and complexity of precision combinatorial circuitry and an array of preamplifiers, the summation of noise poses a significant difficulty for this idea. Let us compare the signal S_m from the output of a monolithic harmonic detection coil (sK_D) followed by an integrator ($K_I/(s + \omega_I)$) to the signal S_v produced by a virtual detection coil formed by the weighted combination of simple loops each with its own integrator/preamplifier. Provided the harmonic H changes at frequencies much greater than ω_I, the signals from these coils are

$$S_m = K_I K_D H \quad \text{and} \quad S_v = K_I \left(\sum_i a_i k_{d,i} \right) H$$

where each $k_{d,i}$ is a flux linkage of the harmonic to a mesh element and the weighting coefficients $|a_i| \leq 1$ used to combine the integrator signals are chosen such that $S_v = S_n$ and thus $\sum_i a_i k_{d,i} = K_D$. Now the noise contribution to S_m is simply $N_m = K_I p_n$ where p_n is the preamplifier's noise signal referred to the integrator's input. However the noise power N_v^2 at the output of a virtual detection coil is produced from the

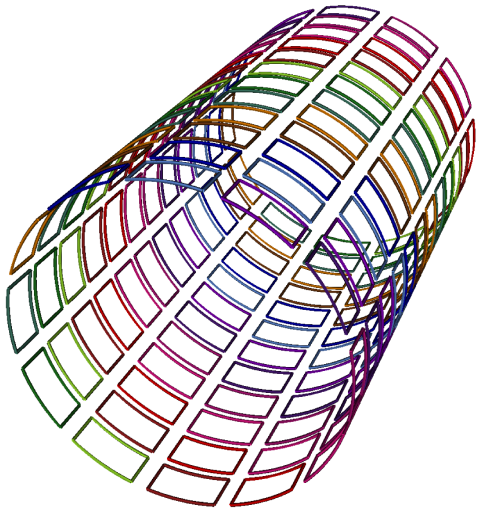

Figure 8.3: Mesh detection coil

sum of squares of the noise powers from the integrators/preamplifiers in each element such that

$$N_v = \sqrt{\sum_i K_I^2 k_{d,i}^2 p_n^2} = K_I p_n \sqrt{\sum_i a_i^2}$$

where $\sqrt{\sum_i a_i^2} > 1$. Therefore the signal to noise ratio of a virtual detection coil is always less than that of a normal detection coil and probably much less since many of the coefficients a_i will be near ± 1. Unfortunately building up virtual detection coils from such a mesh is inadvisable.

8.4 Detection Coils and Bore Space

The use of detection coils introduces a significant drawback for dynamic pre-emphasis: the coils require space within the magnet's bore. However detection coils have two features that make this problem much less severe than it initially seems. The first is that the detection coils are connected to a high impedance and thus carry essentially zero current and experience very little Lorentz force. For these reasons the detection coils need not be made from heavy wire and do not require extreme mechanical stability like the gradient coils. Instead they could be fabricated by etching minute wires on paper thin layers laminated together to form a detection coil set; magnet wire was only used for the coils in figure 6.6 to facilitate winding by hand. But even very thin detection coils must be placed on a coil former and if the radius of this former is less than those of the gradient and shim coils, as it is in our experiments, then bore space is reduced.

8.4.1 Production Coils Interspersed with or Surrounded by Detection Coils

It may be possible either to intersperse the detection coils with the field production coils or place them in the space between those coils and the cryostat; in either case bore space would not be limited at all. To see how this might work, first consider what happens as a detection coil's radius approaches that of its corresponding field production coil. Looking at the field plots of the G_x coil in figure 6.4c-d, we see that over a large region the field can be described with a single harmonic ($B_{za,1,1}$) and although the field descriptions in ever larger regions require that higher order harmonics have greater amplitudes, the original harmonic $B_{za,1,1}$ remains important. Let us define the region of interest, with respect to our G_x coil, as a sphere of radius 4 cm where the field is primarily $B_{za,1,1}$. If a detection coil fits entirely within this region the harmonics it experiences are those produced intentionally by the field production coils – including the G_x coil – and unintentionally by the eddy currents. However, as a detection coil's size increases it increasingly experiences spurious harmonics produced directly by the field production coil since those harmonics are part of the field description in the larger region surrounding the larger detection coil. Fortunately detection coils are designed to reject all but one harmonic and thus dynamic pre-emphasis will not be immediately affected.

Now if the detection coil's radius is increased further, eventually the extra harmonics in the field description may become so large that they overwhelm the detection coil's minimum harmonic rejection ratio. At this point the mutual inductance between the detection and production coils is no longer a measure of a single field harmonic in the region of interest and dynamic pre-emphasis can no longer function. But all is not lost since we are primarily interested in the fields arising from the eddy currents and even if the detection coil's radius approaches that of the gradient/shim coils it is still much less than that of the cryostat.

To see how this is helpful we conceptually split the eddy currents into a superposition of current distributions which each produce only a single harmonic of the B_z field within the small region of interest, just as in section 5.1.2. Without specifying precisely what these distributions are, we nonetheless know that the detection coil is inductively coupled primarily to only one unless the detection coil's radius is very close to that of the cryostat. Whatever the actual shape of one of these eddy current distributions, if it produces a single harmonic within the region of interest then that harmonic will remain important, but not necessarily dominant, in the field description over larger regions associated with this eddy current distribution. Thus ignoring the field production coils, a detection coil is inductively coupled primarily to that component of the eddy currents responsible for a single field harmonic within the region of interest provided that the detection coil's radius does not become so close to the cryostat's radius that the coupling to other field components overwhelms the detection coil's harmonic rejection ratio.

From equation 3.1.2 we remember that the harmonics of the field in the region of interest arise from both the field production coils and the eddy currents according as $B_{zab,n,m}(t) = B^{\text{coil}}_{zab,n,m}(t) - \sum_j E_{jab,n,m} e^{-t/\tau_j}$.

Therefore as long the detection coil for $B_{za,1,1}$ remains inductively coupled primarily to its one component of the eddy currents, the voltage V induced in it is

$$V = \left[s \sum_k M_k i_{c,k} \right] + [sK_D H_e] \tag{8.4.1}$$

where M_k is the mutual inductance between the detection coil and the k^{th} field production coil while $H_e = -K_c \frac{s/\omega_{es}}{1+s/\omega_e}$ (see equation 5.1.6) is the contribution of the eddy currents to $B_{za,1,1}$; a similar expression could be made for any harmonic. Therefore to recover the desired expression

$$V = sK_D G i_c \tag{8.4.2}$$

from equations 5.1.6 and 5.1.1, we must adjust the mutual inductances such that $\sum_k M_k i_{c,k} = K_D K_c i_c$. This may be accomplished by using a matrix of air-core transformers between the detection and field production coils placed outside the bore of the magnet. The number of turns on each side of each transformer can be adjusted until equation 8.4.2 holds and then dynamic pre-emphasis may be applied once again.

8.4.2 Computing the Spherical Harmonics Without a Sphere

To move this discussion beyond mere speculation, we now attempt to see – at least roughly – how the harmonics that a detection coil experiences change as its radius approaches that of the cryostat. First of all we do not know what set of orthogonal eddy current distributions should be considered. However our G_x coil, for example, *does* produce a single harmonic within the region of interest and was designed for minimum power dissipation. Therefore since eddy currents follow the path of least resistance (minimum power dissipation), we shall use our G_x coil as a very rough approximation of the eddy current distribution which produces $B_{za,1,1}$.

To find the spherical harmonics experienced by the detection coil as a result of this eddy current distribution we can use the Biot-Savart law to compute the magnetic field on points over the surface of a sphere surrounding the detection coil and then perform the spherical harmonic transform. But as the detection coil's radius approaches that of the cryostat, the sphere surrounding the detection coil intersects the eddy currents and thus only part of the region within the sphere obeys Laplace's equation. Using field points outside the cryostat to compute the spherical harmonics inside the cryostat is not correct. However one may still draw a region entirely within the cryostat – where Laplace's equation still applies – that encompass the detection coil. We must compute the spherical harmonics within such a region using field points on its surface.

As shown in figure 8.4a-d, one such region can be formed by starting with a sphere just encompassing the detection coil and then cutting away every part of that sphere outside the cylindrical surface that is radially half-way between the cryostat and detection coil. The cylinder's radius is $R_{\text{cut}} =$

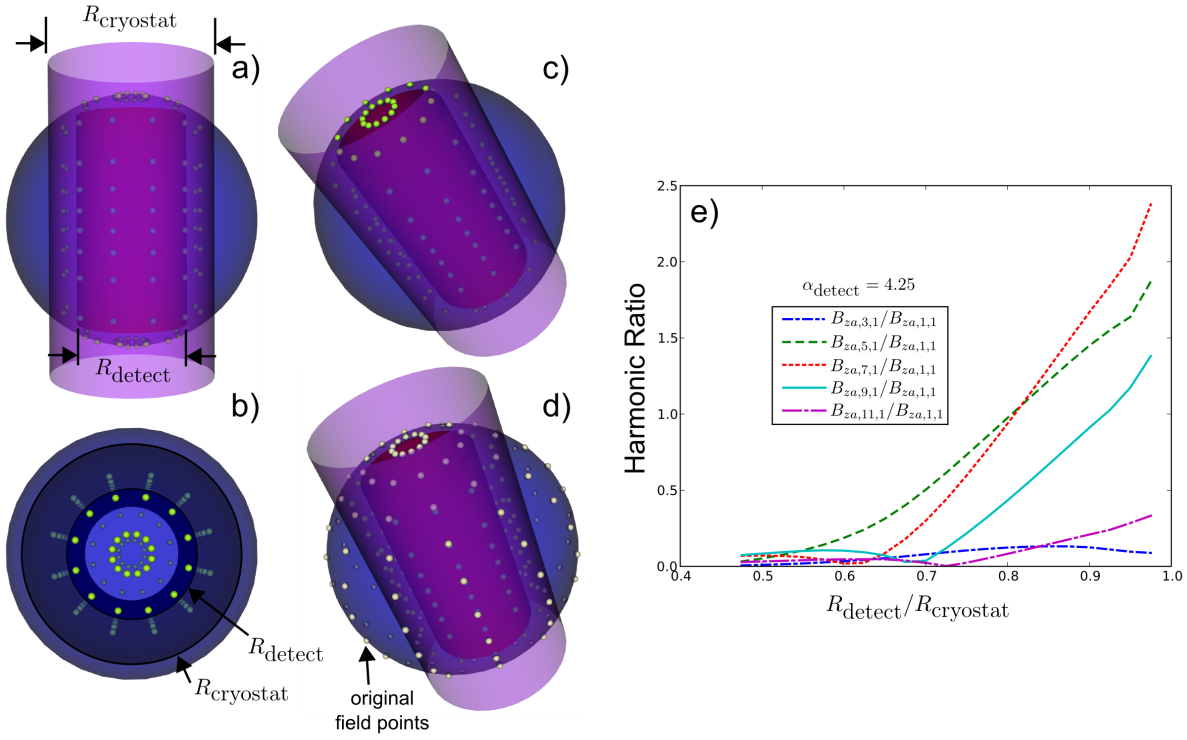

Figure 8.4: Part a) shows a sample detection coil former placed within a cylindrical cryostat. The spherical region which just surrounds the detection coil ($R_{\text{sphere}} = R_{\text{detect}}\sqrt{1+\alpha^2_{\text{detect}}/4}$) is shown as well as the field points used for the cylindrically restricted spherical harmonic transform. Parts b) and c) show the same setup first looking down the cylinders and then from an angle. In part d) the original field point locations on the sphere are also shown. Finally the plot in e) shows that as the region of interest increases so does the influence of higher order harmonics.

$(R_{\text{detect}} + R_{\text{cryostat}})/2$ and the sphere's radius is

$$R_{\text{sphere}} = R_{\text{detect}} \sqrt{1 + \alpha^2_{\text{detect}}/4}, \qquad \alpha_{\text{detect}} = L_{\text{detect}}/R_{\text{detect}}$$

where α_{detect} is the detection coil's aspect ratio while R_{detect} and L_{detect} are the detection coil's radius and length and R_{cryostat} is the cryostat's radius. Then for any R_{detect}, R_{cryostat}, and α_{detect} values we can define field points on this surface by starting with the ones given for the spherical harmonic transform and moving those outside the cylinder with radius R_{cut} until they lie on that cylinder; this can be done by sliding the points in the cylindrically radial direction. Given these new field points our task is to use them to compute the field's spherical harmonics, a task which we shall call the cylindrically restricted spherical harmonic transform or CRSHT.

Let us define this task more precisely: given the field values at points described above we wish to find the set of harmonic coefficients that best re-produces those field values. By 'best' we mean that the sum of the square errors between the actual field values and those produced by the harmonic coefficients should be at a minimum. If we want to find the harmonics up to and including $n = 5, m = 5$ (that is 36 coefficients) the fast spherical harmonic transform that we have been using [110, 65] requires 144 points and thus so will the CRSHT. Now given a set of harmonic coefficients it is a straightforward calculation to determine the field value at any point so we can setup the CRSHT as a rectangular matrix problem

$$\mathcal{F} = C\,\mathcal{H}$$

where $\mathcal{F}$ is a vector of field values, $\mathcal{H}$ is a vector of harmonic coefficients, and C is the straightforward mapping of coefficients to field values given the point positions and equation 2.1.31. To solve this problem for $\mathcal{F}$ we can impose the extra constraint that the harmonic coefficients be simple in that the sum of their squares be a minimum and thus use the pseudo-inverse to invert C. This process provides an alternative method for finding the spherical harmonic transform that works for points on the surface of a sphere but is not restricted to using such points. When using field points on a sphere, the results found using the CRSHT agree to those found using the fast spherical harmonic transform to within 0.01%.

Using our G_x coil as an approximation of the eddy current distribution responsible for producing $B_{za,1,1}$ and a detection coil aspect ratio $\alpha_{\text{detect}} = 4.25$, the results of performing the CRSHT with various values for R_{detect} are shown in figure 8.4e. As can be seen, higher order harmonics become more important than $B_{za,1,1}$ as $R_{\text{detect}}/R_{\text{cryostat}}$ approaches unity but the influence of the highest order harmonics only becomes relevant at the closest proximity. Since our D_x detection coil has a minimum harmonic rejection ratio of 47 dB (section 8.1) and $B_{za,7,1}/B_{za,1,1} < 2.5$, the detection coil is still inductively coupled primarily to the harmonic $B_{za,1,1}$ produced by the eddy current fields. These approximate and preliminary findings suggest that the detection coils will still be useful even if placed in close proximity with the cryostat

($R_{\text{detect}}/R_{\text{cryostat}} \sim 0.975$) provided that a matrix of transformers is used to adjust the mutual inductances between the detection and field production coils.

Chapter 9

Conclusion

9.1 Overview

Regarding the hypothesis that coils of wire can be shaped to sense distortions of the gradient field and that the resulting information can be used to correct the distortions as they unfold, we have shown that this is indeed the case. We have developed a method to design spherical harmonic detection coils which each produce a voltage proportional to the rate of change of a single spherical harmonic component of the B_z field. Since the induced voltages depend on vector potential, a pre-requisite of the design method was to determine what potentials and fields are associated with each spherical harmonic of B_z. These relationships are not limited to the design of spherical harmonic detection coils and may be useful wherever the quasi-static approximation is appropriate.

We have also investigated – both theoretically and experimentally – the use of harmonic detection coils in negative feedback loops each designed to control a single harmonic of the gradient field. The theoretical work allows detailed simulations and reveals that the feedback path in each loop should be split at a characteristic frequency ω_I between a high frequency branch capable of detecting the field directly and a low frequency branch providing stability at zero frequency. The choice of ω_I and the coil preamplifier are both critically important to system performance since eddy current effects at frequencies less than ω_I cannot be corrected but lowering ω_I increases the preamplifier's contribution to the system's offset and noise. For a given preamplifier, a numerical technique was developed to optimize ω_I with respect to the MRI image.

Experimentally, three feedback loops were constructed to simultaneously control the x, y, and z field gradients within a test apparatus surrounded by an aluminium tube. By using a small probe to plot the field within the apparatus as a function of time and then performing a spherical harmonic transform, the time courses of the various harmonics were determined. These results demonstrate that the feedback loops dynamically correct the gradient coil currents such that the effect of eddy currents on the field harmonics is effectively cancelled. The current waveforms are the same ones that static pre-emphasis would have applied,

but dynamic pre-emphasis generates them automatically without calibration or computation. Moreover when the feedback loops are operated simultaneously, they do not interfere with one another.

9.2 Future Applications

The advancement of MRI technology is not driven by engineering acumen but first by medical/biological curiosity and then by the desire to apply the fruits of that curiosity to health care. In the long term, this creates a demand for MRI machines with ever higher spatial and temporal resolution and thus ever higher B_0 field strength (section 2.3.4). One of the many problems associated with higher field strength is the B_0 inhomogeneity due to the patient's magnetic susceptibility. However the use of dynamic shimming means that this inhomogeneity need not unduly distort the final image: since the shim coils are unshielded, their dynamic use produces significant eddy current effects whose correction by static pre-emphasis is particularly difficult. Since the correct shim coils settings vary from patient to patient, so do the correct pre-emphasis waveforms. Thus we expect that developing dynamic pre-emphasis to a commercial standard will eventually become desirable, but it is doubtful that using dynamic pre-emphasis on only three channels would ever be superior to static pre-emphasis due to the extra hardware complexity. However, since no direct comparison with static pre-emphasis has been made and no MRI images have been acquired, we have not found the point at which dynamic pre-emphasis becomes preferable. Rather we have focused on demonstrating that dynamic pre-emphasis is indeed possible, leaving the details to others.

To find this tipping point, two significant questions still need to be answered: can dynamic pre-emphasis function with the detection coils near or outside the gradient/shim coils and what cross-over point and pre-amplifier/integrator technology are required to improve image quality? Answering these questions will undoubtedly require a close relationship with an MRI manufacturer and the ability to re-arrange the gradient system in an operational high field MRI. Therefore if the problem of bore space can be removed concurrent to an improvement in image quality, dynamic pre-emphasis will have a clear technical advantage over static pre-emphasis. However, even with a clear technical advantage, dynamic pre-emphasis will not become widely used unless the reduction in calibration time and the gains in image quality are sufficient to justify the added hardware complexity. Of course the location of this tipping point depends on the application; imaging techniques that struggle with eddy currents or those which employ dynamic shimming to correct magnetic susceptibility effects stand to benefit the most from dynamic pre-emphasis. Moreover, since the magnetic susceptibility effects and the gradient strength for a constant signal to noise ratio per voxel both increase with the field strength, so does the benefit of using dynamic pre-emphasis.

Despite the fact that dynamic pre-emphasis is not yet ready to replace static pre-emphasis, a significant advancement has been made. Although many have developed methods to measure the field and compute static calibrations, an alternative approach now exists. This work has demonstrated that pre-emphasis

currents can be generated dynamically in response to the eddy currents as they unfold; possibly with significant advantages over the static case.

Bibliography

[1] M. Abramowitz and I. A. Segun, editors. *Handbook of Mathematical Functions*. Dover, 1968.

[2] B. Aksel, B.D. Collick, L. Marinelli, W.D. Barber, P.A. Bottomley, and C.J. Hardy. Local planar gradients with order-of-magnitude strength and speed advantage. *International Society for Magnetic Resonance in Medicine Book of Abstracts*, page 780, 2006.

[3] Andrew M. Blamire, Douglas L. Rothman, and Terry Nixon. Dynamic shim updating: A new approach towards optimized whole brain shimming. *Magnetic Resonance in Medicine*, 36:159–165, 1996.

[4] N.I. Avdievich, J.W. Pan, J.M. Baehring, D.D. Spencer, and H.P. Hetherington. Short echo spectroscopic imaging of the human brain at 7 T using transceiver arrays. *Magnetic Resonance in Medicine*, 62(1):17–25, 2009.

[5] Christoph Barmet, Nicola De Zanche, and Klaas P. Pruessmann. Spatiotemporal magnetic field monitoring for MR. *Magnetic Resonance in Medicine*, 60:187–197, 2008.

[6] Adi Ben-Isreal and Thomas N. E. Greville. *Generalized Inverses, Theory and Applications*. Springer, New York, second edition, 2003.

[7] H. Benoit-Cattin, G. Collewet, B. Belaroussi, H. Saint-Jalmes, and C. Odet. The SIMRI project: a versatile and interactive MRI simulator. *Journal of Magnetic Resonance*, 173:97–115, 2005.

[8] Matt A. Bernstein, Kevin F. King, and Xiaohong Joe Zhou. *Handbook of MRI Pulse Sequences*. Elsevier, 2004.

[9] Yoshitaka Bito, Satoshi Hirata, Takayuki Nabeshima, and Etsuji Yamamoto. Echo-planar diffusion spectroscopic imaging. *Magnetic Resonance in Medicine*, 33(1):69–73, 1995.

[10] F. Bloch. Nuclear induction. *Physical Review*, 70:460–474, 1946.

[11] F. Bloch. Nuclear induction. *Physical Review*, 70:474–485, 1946.

[12] Michael A. Brideson, Larry K. Forbes, and Stuart Crozier. Determining complicated winding patterns for shim coils using stream functions and the target-field method. *Concepts in Magnetic Resonance*, 14(1):9–18, 2002.

[13] Robert W. Brown and Shmaryu M. Shvartsman. Supershielding: Confinement of magnetic fields. *Physical Review Letters*, 83(10):1946–9, 1999.

[14] Michael J. J. Buckingham. *Noise in Electronic Devices and Systems*. John Wiley and Sons, 1983.

[15] William Elwood Byerly. *An Elementary Treatise on Fourier's Series*. Boston:Ginn & Co., 1893.

[16] Bruce Carter and Thomas R. Brown. *Handbook of Operational Amplifier Applications - SBOA092A*. Texas Instruments, 2001.

[17] B.L.W. Chapman and P. Mansfield. Quiet gradient coils: active acoustically and magnetically screened distributed transverse gradient designs. *Meas. Sci. Technol.*, 6:349–54, 1995.

[18] C-N Chen and David I. Hoult. *Biomedical Magnetic Resonance Technology*. Adam Hilger, Bristol; Philadelphia, 1989.

[19] Blaine A. Chronik and Brian K. Rutt. Constrained length minimum inductance gradient coil design. *Magnetic Resonance in Medicine*, 39(2):270–8, 1998.

[20] S. Crozier, L. K. Forbes, and D. M. Doddrell. The design of transverse gradient coils of restricted length by simulated annealing. *Journal of Magnetic Resonance A*, 107:126, 1994.

[21] Rhodri Cusack, Matthew Brett, and Katja Osswald. An evaluation of the use of magnetic field maps to undistort echo-planar images. *NeuroImage*, 18:127–142, 2003.

[22] J. Delannoy, Ching-Nien Chen, R. Turner, R. L. Levin, and D. Le Bihan. Noninvasive temperature imaging using diffusion MRI. *Magnetic Resonance in Medicine*, 19(2):333–339, 1991.

[23] R. H. Dicke. Coherence in spontaneous radiation processes. *Phys. Rev.*, 93(1):99, Jan 1954.

[24] P.A.M. Dirac. *The Principles of Quantum Mechanics*. Oxford University Press, fourth edition, 1958.

[25] Richard Dorf and Robert Bishop. *Modern Control Systems*. Prentice Hall, Upper Saddle River, New Jersey, ninth edition, 2001.

[26] R. L. Driscoll and P. L. Bender. Proton gyromagnetic ratio. *Phys. Rev. Lett.*, 1(11):413–414, Dec 1958.

[27] C. D. Eccles, S. Crozer, M. Westphal, and D. M. Doddrell. Temporal spherical-harmonic expansion and compensation of eddy-current fields produced by gradient pulses. *Journal of Magnetic Resonance*, 103:135–141, 1993.

[28] Karl T. Edler and David I. Hoult. Spherical harmonic inductive detection coils for dynamic pre-emphasis. *Magnetic Resonance in Medicine*, 60:277–287, 2008.

[29] Karl T. Edler and David I. Hoult. A transverse gradient detection coil for dynamic pre-emphasis. In *17th Annual Meeting of the ISMRM*, page 1859, Honolulu, Hawaii, 2009.

[30] M. Galassi et al. *GNU Scientific Library Reference Manual*. second edition, 2004.

[31] Thomas C. Farrar and Edwin D. Becker. *Pulse and Fourier Transform NMR*. Academic Press, 1971.

[32] Farhad Farzaneh, Stephen J. Reiderer, and Norbert J. Pelec. Analysis of T2 limitations and off-resonance effects on spatial resolution and artefacts in echo-planar imaging. *Magnetic Resonance in Medicine*, 14:123–139, 1990.

[33] FDA. Guidance for industry and FDA staff: Criteria for significant risk investigations of magnetic resonance diagnostic devices, 2003.

[34] Lawrence K. Forbes and Stuart Crozier. A novel target-field method for finite-length magnetic resonance shim coils: III. shielded zonal and tesseral coils. *J. Phys. D: Appl. Phys.*, 36(2):68–80, 2002.

[35] Marcel J. E. Golay. Field homogenizing coils for nuclear spin resonance instrumentation. *Review of Scientific Instruments*, 29(4):313–315, 1958.

[36] C. J. Gorter and L. J. F. Broer. Negative result of an attempt to observe nuclear magnetic resonance in solids. *Physica*, 9:591–596, June 1942.

[37] David J. Griffiths. *Introduction to Electrodynamics*. Prentice Hall, third edition, 1999.

[38] Frederick W. Grover. *Inductance Calculations: Working Forumulas and Tables*. D. Van Nostrad Company Inc., New York, 1946.

[39] E.A. Guggenheim. *Thermodynamics: An Advanced Treatment for Chemists and Physicists*. Elsevier, seventh edition, 1985.

[40] E. L. Hahn. Spin echos. *Physical Review*, 80:580–594, 1950.

[41] C. L. G. Ham, J. M. L. Engels, G. T. van de Wiel, and A. Machielsen. Peripheral nerve stimulation during MRI: Effects of high gradient amplitudes and switching rates. *Journal of Magnetic Resonance Imaging*, 7(5):933–937, 1997.

[42] O. Heid, M. Vester, and P. Beasley. A novel concept for gradient coil and magnet integration. *International Society for Magnetic Resonance in Medicine Book of Abstracts*, page 895, 2005.

[43] Carl W. Helstrom. *Probability and Stochastic Processes for Engineers*. Macmillan Publishing Company, second edition, 1991.

[44] Mark A. Horsfield. Mapping eddy current induced fields for the correction of diffusion-weighted echo planar images. *Magnetic Resonance Imaging.*, 17(9):1335–1345, 1999.

[45] D. I. Hoult. Sensitivity and power deposition in a high-field imaging experiment. *Journal of Magnetic Resonance Imaging*, 12:46–67, 2000.

[46] D. I. Hoult. The origins and present status of the radio wave controversy in NMR. *Concepts in Magnetic Resonance Part A*, 34:193–216, 2009.

[47] D. I. Hoult and B. Bhakar. NMR signal reception: Virtual photons and coherent spontaneous emission. *Concepts in Magnetic Resonance*, 9:277–297, 1997.

[48] D. I. Hoult and N.S. Ginsberg. The quantum origins of the free induction decay signal and spin noise. *Journal of Magnetic Resonance*, 148:182–199, 2001.

[49] D. I. Hoult and Paul C. Lauterbur. The sensitivity of the zeugmatographic experiment involving human samples. *Journal of Magnetic Resonance*, 34:425–433, 1979.

[50] David I. Hoult and Roxanne Deslauriers. Accurate shim-coil design and magnet-field profiling by a power minimization-matrix method. *Journal of Magnetic Resonance A*, 108:9–20, 1994.

[51] Vasiliki N. Ikonomidou and George D. Sergiadis. Improved Shinnar-Le Roux algorithm. *Journal of Magnetic Resonance*, 143:30–34, 2000.

[52] John David Jackson. *Classical Electrodynamics*. Wiley, third edition, 1999.

[53] P. Jehenson and A. Syrota. Correction of distortions due to the pulsed magnetic field gradient-induced shift in B_0 field by postprocessing. *Magnetic Resonance in Medicine*, 12:253–256, 1989.

[54] P. Jehenson, M. Westphal, and N. Schuff. Analytical method for the compensation of eddy-current effects induced by pulsed magnetic field gradients in NMR systems. *Journal of Magnetic Resonance*, 90:264–278, 1990.

[55] Dye J. Jensen, William W. Brey, Jean L. Delayre, and Ponnada A. Narayana. Reduction of pulsed gradient settling time in the superconducting magnet of a magnetic resonance instrument. *Medical Physics*, 14(5):859–862, 1987.

[56] Peter Jezzard and Robert S. Balaban. Correction for geometric distortion in echo planar images from B_0 field variation. *Magnetic Resonance in Medicine*, 34:65–73, 1995.

[57] D. Healy Jr., D. Rockmore, P. Kostelec, and S. Moore. FFTs for the 2-sphere - improvements and variations. *The Journal of Fourier Analysis and Applications*, 9(4):341–385, 2003.

[58] Jun Shen, Douglas L. Rothman, Hoby P. Hetherington, and Jullie W. Pan. Linear projection method for automatic slice shimming. *Magnetic Resonance in Medicine*, 42:1082–1088, 1999.

[59] Walter G. Jung. *IC Op-Amp Cookbook*. Howard W. Sams I & Co., Inc., Indianapolis, Indiana, second edition, 1974.

[60] Walter G. Jung. *Op Amp Applications*. Analog Devices, 2002.

[61] Kevin F. King and Daniel J. Schaefer. Spiral scan peripheral nerve stimulation. *Journal of Magnetic Resonance Imaging*, 12:164–170, 2000.

[62] Charles Kitchin and Lew Counts. *A Designers Guide to Instrumentation Amplifiers*. Analog Devices, second edition, 2004.

[63] Charles Kittel and Herbert Kroemer. *Thermal Physics*. W. H. Freeman and Company, second edition, 2000.

[64] P. Kostelec, D. Maslen, D. Rockmore, and Jr. D. Healy. Computational harmonic analysis for tensor fields on the two-sphere. *Journal of Computational Physics*, 162:514–535, 2000.

[65] P. J. Kostelec and D. N. Rockmore. FFTs on the rotation group. *The Journal of Fourier Analysis and Applications*, 14:145–179, 2008.

[66] E.E. Kriezis, Theodoros D. Tsiboukis, Stavros M. Panas, and John A. Tegopoulos. Eddy currents: Theory and applications. *Proceedings of the IEEE*, 80(10), 1992.

[67] Kenneth K. Kwong, John W. Belliveau, David A. Chesler, Inna E. Goldberg, Robert M. Weisskoff, Brigitte P. Poncelet, David N. Kennedy, Bernice E. Hoppel, Mark S. Cohen, Robert Turner, Hong-Ming Cheng, Thomas J. Brady, and Bruce R. Rosen. Dynamic magnetic resonance imaging of human brain activity during primary sensory stimulation. *Proc. Natl. Acad. Sci. USA*, 89:5675–5679, 1992.

[68] L. Martyn Klassen and Ravi S. Menon. Robust automated shimming technique using arbitrary mapping acquisition parameters (RASTAMAP). *Magnetic Resonance in Medicine*, 51:881–887, 2004.

[69] P. C. Lauterbur. Image formation by induced local interactions: Examples employing nuclear magnetic resonance. *Nature*, 242:190–191, 1973.

[70] J. Leggett, D. Green, and R. Bowtell. Insert dome gradient coils for brain imaging. *International Society for Magnetic Resonance in Medicine Book of Abstracts*, page 779, 2006.

[71] Shizhe Li, Bernard J. Dardzinski, Christopher M. Collins, Qing X. Yang, and Michael B. Smith. Three-dimensional mapping of the static magnetic field inside the human head. *Magnetic Resonance in Medicine*, 36:705–714, 1996.

[72] Shizhe Li, Gerald D. Williams, Timothy A. Frisk, Blake W. Arnold, and Michael B. Smith. A computer simulation of the static magnetic field distribution in the human head. *Magnetic Resonance in Medicine*, 34:268–275, 1995.

[73] Zhi-Pei Liang and Paul C. Lauterbur. *Principles of Magnetic Resonance Imaging - A Signal Processing Perspective*. IEEE Press, 2000.

[74] David R. Lide, editor. *CRC Handbook of Chemistry and Physics*. CRC Press, 89th edition, 2009.

[75] Stephen Maas. *Noise in Linear and Nonlinear Circuits*. Artech House Publishers, second edition, 2005.

[76] Ron Mancini, editor. *Op Amps For Everyone*. Texas Instruments, 2002.

[77] P Mansfield. Multi-planar image formation using NMR spin echoes. *Journal of Physics C: Solid State Physics*, 10:L55–L58, 1977.

[78] P. Mansfield and B.L.W. Chapman. Active magnetic screening of coils for static and time-dependent magnetic field generation in NMR imaging. *J. Phys. E: Sci. Instrum.*, 19(7):1080–4, 1986.

[79] P. Mansfield and B.L.W. Chapman. Multishield active magnetic screening of coil structures in NMR. *Journal of Magnetic Resonance*, 72(2):211–223, 1987.

[80] J. Matwiy, B. Matwiy, P. Unger, and D. I. Hoult. A high-accuracy field plotting rig. In *11th Annual Meeting of the ISMRM*, page 2405, Toronto, Canada, 2003.

[81] J. C. Maxwell. On governors. *Proceedings of the Royal Society of London*, 16:270–283, 1868.

[82] Otto Mayr. *The Origins of Feedback Control*. MIT Press, Cambridge, MA, USA, 1970.

[83] Paul J. McCracken, Armando Manduca, Joel Felmlee, and Richard L. Ehman. Mechanical transient-based magnetic resonance elastography. *Magnetic Resonance in Medicine*, 53:628–639, 2005.

[84] Graeme McKinnon. System design trade-offs. In *17th Annual Meeting of the ISMRM - Weekend Syllabus*, page 01.19, Honolulu, Hawaii, 2009.

[85] Jagdish Mehra, editor. *The Physicist's Conception of Nature*. D. Reidel, 1973.

[86] G. Morrell and D. Spielman. Dynamic shimming for multi-slice magnetic resonance imaging. *Magnetic Resonance in Medicine*, 38:477–483, 1997.

[87] G. Morrow. Progress in MRI magnets. *IEEE transactions on applied superconductivity*, 10:744–751, 2000.

[88] Philip M. Morse and Herman Feshbach. *Methods of Theoretical Physics*. McGraw-Hill, New York, 1953.

[89] Raja Muthupillai, Phillip J. Rossman, David J. Lomas, James F. Greenleaf, Stephen J. Riederer, and Richard L. Ehman. Magnetic resonance imaging of transverse acoustic strain waves. *Magnetic Resonance in Medicine*, 36:266–274, 1996.

[90] Douglas C. Noll, Jonathan D. Cohen, Craig H. Meyer, and Walter Schneider. Spiral k-space MR imaging of cortical activation. *Journal of Magnetic Resonance Imaging*, 5(1):49–56, 1995.

[91] Hans C. Ohanian. *Classical Electrodynamics*. Infinity Sciences Press, second edition, 2007.

[92] Nikolaos G. Papdakis, Kay M. Martin, John D. Pickard, Laurance D. Hall, T. Adrian Carpenter, and Christopher L.H. Huang. Gradient preemphasis calibration in diffusion-weighted echo-planar imaging. *Magnetic Resonance in Medicine*, 44:616–624, 2000.

[93] R.K. Pathria. *Statistical Mechanics*. Butterworth-Heinemann, second edition, 1996.

[94] John Pauly, Patrick Le Roux, Dwight Nishimura, and Albert Macovski. Parameter relations for the Shinnar-Le Roux selective excitation pulse design algorithm. *IEEE Transactions on Medical Imaging*, 10:53–63, 1991.

[95] Andrew M. Peters, Matthew J. Brookes, Frank G. Hoogenraad, Penny A. Gowland, Susan T. Francis, Peter G. Morris, and Richard Bowtell. T2* measurements in human brain at 1.5, 3 and 7 T. *Magnetic Resonance Imaging.*, 25:748–753, 2007.

[96] Robert D. Peters, Eric Chan, John Trachtenberg, Serge Jothy, Linda Kapusta, Walter Kucharczyk, and R. Mark Henkelman. Magnetic resonance thermometry for predicting thermal damage: An application of interstitial laser coagulation in an in vivo canine prostate model. *Magnetic Resonance in Medicine*, 44(6):873–883, 2000.

[97] Labros S. Petropoulos. Finite size disc gradient coil set for open vertical field magnets. *Magnetic Resonance Imaging.*, 18:615–24, 2000.

[98] Sergio Pissanetzky. Minimum energy MRI gradient coils of general geometry. *Meas. Sci. Technol.*, 3:667–73, 1992.

[99] M. Poole. *Improved Equipment and Techniques for Dynamic Shimming in High Field MRI*. PhD thesis, University of Nottingham, 2007.

[100] M. Poole and R. Bowtell. Novel gradient coils designed using a boundary element method. *Concepts in Magnetic Resonance Part B: Magnetic Resonance Engineering*, 31:162–175, 2007.

[101] Alexander D. Poularikas, editor. *The Transforms and Applications Handbook*. CRC Press, second edition, 2000.

[102] Bogdan Povh, Klaus Rith, Christoph Scholz, and Frank Zetsche. *Particles and Nuclei: An Introduction to the Physical Concepts*. Springer, fourth edition, 2004.

[103] Manfred G. Prammer, John C. Haselgrove, Meir Shinnar, and John S. Leigh. A new approach to automatic shimming. *Journal of Magnetic Resonance*, 77:40–52, 1988.

[104] E. M. Purcell, H. C. Torrey, and R. V. Pound. Resonance absorption by nuclear magnetic moments in a solid. *Phys. Rev.*, 69(1-2):37–38, Jan 1946.

[105] I. I. Rabi. Space quantization in a gyrating magnetic field. *Phys. Rev.*, 51(8):652–654, Apr 1937.

[106] I. I. Rabi, J. R. Zacharias, S. Millman, and P. Kusch. A new method of measuring nuclear magnetic moment. *Phys. Rev.*, 53(4):318, Feb 1938.

[107] Devesh Raj, Derek P. Paley, Adam W. Anderson, Richard P. Kennan, and John C. Gore. A model for susceptibility artefacts from respiration in functional echo-planar magnetic resonance imaging. *Physics in Medicine and Biology*, 45:3809–3820, 2000.

[108] T. G. Reese, O. Heid, R. M. Weisskoff, and V. J. Wedeen. Reduction of eddy-current-induced distortion in diffusion MRI using a twice-refocused spin echo. *Magnetic Resonance in Medicine*, 49:177–182, 2003.

[109] Robin A. de Graff, Peter B. Brown, Scott McIntyre, and Douglas L. Rothman. Dynamic shim updating (DSU) for multislice signal acquisition. *Magnetic Resonance in Medicine*, 49:409–416, 2003.

[110] D. N. Rockmore. www.cs.dartmouth.edu/ geelong/sphere/.

[111] Francoise Roméo and David I. Hoult. Magnet field profiling: Analysis and correcting coil design. *Magnetic Resonance in Medicine*, 1:44–65, 1984.

[112] LN Ryner, P. Stroman, T. Wessel, David I. Hoult, and J.K. Saunders. Effect of oscillatory eddy currents on MR spectroscopy. In *6th Annual Meeting of the ISMRM*, page 1903, Sydney, Australia, 1998.

[113] J. Sabate, L. J. Garces, P. M. Szczesny, Qiming Li, and W.F. Wirth. High-power high-fidelity switching amplifier driving gradient coils for MRI systems. In *Power Electronics Specialists Conference, 2004. PESC 04. 2004 IEEE 35th Annual*, volume 1, pages 261–266, June 2004.

[114] J. J. Sakurai. *Modern Quantum Mechanics*. Addison-Wesley, revised edition, 1994.

[115] H. Sanchez, F. Liu, A. Trakic, E. Weber, and S. Crozier. Three-dimensional gradient coil structures for magnetic resonance imaging designed using fuzzy membership functions. *IEEE Transactions on Magnetics*, 43(9):3558–3566, 2007.

[116] H. Lopez Sanchez, M. Poole, F. Liu, and S. Crozier. Equivalent magnetization current method applied to the design of gradient coils for magnetic resonance imaging. *IEEE Transactions on Magnetics*, 45:767–775, 2009.

[117] Giovanni Sansone. *Orthogonal Functions*. Interscience, rev. english edition, 1959.

[118] Vincent J. Schmithorst and Bernard J. Dardzinski. Automatic gradient preemphasis adjustment: A 15-minute journey to improved diffusion-weighted echo-planar imaging. *Magnetic Resonance in Medicine*, 47:298–212, 2002.

[119] Frank G. Shellock. *Reference Manual for Magnetic Resonance Safety, Implants, and Devices*. Biomedical Research Publishing Group, 2005.

[120] Sh. M. Shvartsman, R. W. Brown, Y.-C.N. Cheng, T. P. Eagan, H. Fujita, M. A. Morich, L. S. Petropoulos, and J. D. Willig. Application of the SUSHI method to the design of gradient coils. *Magnetic Resonance in Medicine*, 45:147–55, 2001.

[121] Pekka Sipil*ä*, Rolf F. Schulte, Gerhard Watchutka, and Florian Wiesinger. Digital multiband receiver for magnetic resonance. *Concepts in Magnetic Resonance Part B: Magnetic Resonance Engineering*, 35B:210–220, 2009.

[122] C. P. Slichter. *Principles of Magnetic Resonance*. Springer, third edition, 1996.

[123] Steven W. Smith. *The Scientist and Engineer's Guide to Digital Signal Processing*. California Technical Publishing, 1997.

[124] Tony Stocker, Kaveh Vahedipour, and N. Jon Shah. HPC simulation of magnetic resonace imaging. *Parallel Computing: Architectures, Algorithms, and Applications*, 38:155–164, 2007.

[125] *MAGNETOM Trio a Tim System - Operator Manual*, syngo MR 2006t edition, 2005.

[126] A.M. Takahashi and R.S. Hinks. Measurement of cross-axis gradient eddy currents. *International Society for Magnetic Resonance in Medicine Book of Abstracts*, page 1374, 2006.

[127] *Techron 7570 Power Supply Amplifier: Technical Manual*, rev 0. edition, 1988.

[128] J.A. Tegopoulos and E.E. Kriezis. *Eddy Currents in Linear Conducting Media*. Elsevier, 1985.

[129] R. Turner. A target field approach to optimal coil design. *J. Phys. D: Appl. Phys.*, 19:L147, 1986.

[130] R. Turner. Minimum inductance coils. *J. Phys. E: Sci. Instrum.*, 21(10):948–952, 1988.

[131] R. Turner. Gradient coil design: a review of methods. *Magnetic Resonance Imaging.*, 11(7):903–920, 1993.

[132] R. Turner and R.M. Bowley. Passive screening of switched magnetic field gradients. *J. Phys. E: Sci. Instrum.*, 19(10):876, 1986.

[133] Mikhail Veshtort and Robert G. Griffin. SPINEVOLUTION: A powerful tool for the simulation of solid and liquid state NMR experiments. *Journal of Magnetic Resonance*, 178:248–282, 2006.

[134] Peter T. While, Larry K. Forbes, and Stuart Crozier. 3d gradient coil design - toroidal surfaces. *Journal of Magnetic Resonance*, 198(1):31 – 40, 2009.

[135] E. R. Williams and P. T. Olsen. New measurement of the proton gyromagnetic ratio and a derived value of the fine-structure constant accurate to a part in 107. *Phys. Rev. Lett.*, 42(24):1575–1579, Jun 1979.

[136] E.R. Williams, Jr. Jones, G.R., S. Ye, R. Liu, H. Sasaki, P.T. Olsen, W.D. Phillips, and H.P. Layer. A low field determination of the proton gyromagnetic ratio in water. *Instrumentation and Measurement, IEEE Transactions on*, 38(2):233–237, Apr 1989.

[137] Alen H. Wilman and Peter S. Allen. The response of the strongly coupled AB systm of citrate to a typical ^{1}H MRS localization sequence. *Journal of Magnetic Resonance B*, pages 25–33, 1995.

[138] Eric C. Wong, A. Jesmanowicz, and James S. Hyde. Coil optimization for MRI by conjugate gradient descent. *Magnetic Resonance in Medicine*, 21(1):38–48, 1991.

[139] Nicola De Zanche, Christoph Barmet, Jurek A. Nordmeyer-Massner, and Klaas P. Pruessmann. NMR probes for measuring magnetic fields and field dynamics in MR systems. *Magnetic Resonance in Medicine*, 60:176–186, 2008.